

Antarctic Meteorites XXVIII

Papers presented to the
Twentyeighth Symposium
on Antarctic Meteorites



June 1-3, 2004

NATIONAL INSTITUTE OF POLAR RESEARCH

TOKYO

国立極地研究所

南極隕石研究センター

28th Symposium on Antarctic Meteorites
June 1-3, 2004
National Institute of Polar Research, Tokyo, Japan

Tuesday, June 1, 2004

0930-1200 Registration Auditorium (6th Floor)

Oral sessions will be held in the auditorium, 6th floor of the Main Building.

** denotes speaker.*

0955-1000 **Watanabe O.** (Director-General, NIPR)
Opening Address

Chairs: Noguchi T. and Tomiyama T.

- | | | |
|-----------|---|----|
| 1000-1015 | Noguchi T.* , Imae N. and Kimura M.
Petrology and mineralogy of Asuka 881020: A preliminary report of the first CH chondrite found among the Japanese Antarctic meteorite collection | 62 |
| 1015-1030 | Hiyagon H.* and Kimura M.
Chemical composition, cathodoluminescence images and oxygen isotopes of FeO-poor isolated olivine grains from the Murchison CM2 chondrite | 15 |
| 1030-1045 | Sugita M.* and Tomeoka K.
Sodium-metasomatism in CAIs in the anomalous carbonaceous chondrite Ningqiang: Evidence for parent-body processes | 77 |
| 1045-1100 | Yamamoto Y.* , Okazaki R. and Nakamura T.
Aqueous alteration effects on argon-rich noble gases in the Ningqiang carbonaceous chondrite: An experimental study | 91 |
| 1100-1115 | Zolensky M. E.* , Tonui E. K., Bevan A. W. R., Le L., Clayton R. N., Mayeda T. K. and Norman M.
Camel Donga 040: A CV chondrite genomict breccia with unequilibrated and metamorphosed material | 95 |
| 1115-1130 | Ishizaki N.* and Tomeoka K.
Silicate darkening in CK chondrites: Verification of the cause by vesicular olivine | 21 |
| 1130-1145 | Yamashita K.* , Nakamura N. and Heaman L. M.
Pb isotopic study of Kobe (CK4) meteorite | 93 |
| 1145-1300 | —Lunch— | |

1300-1315	Kitajima F.* , Kitajima Y., Nakamura T. and Mase K. A XAFS study on degrees of alteration/metamorphism of carbonaceous matter in carbonaceous chondrites in their parent bodies	35
1315-1330	Kimura M.* , Hiyagon H., Nakajima H. and Weisberg M. K. Spinel group minerals in LL3 chondrites: Primary and secondary features	31
1330-1345	Tomiyama T.* and Misawa K. Thermal history of Yamato 86753	87
1345-1400	Osawa T.* and Nagao K. Noble gas compositions of gas-rich and gas-poor polymict breccias	70
1400-1415	Jagoutz E.* , Jotter R., Kubny A., Zartman W. and Dreibus G. U-Th-Pb systematics in chondrites	23

Chairs: Kita N. T. and Tachibana S.

1415-1430	Ninagawa K.* , Imae N., Kojima H. and Yanai K. Thermoluminescence study of Japanese Antarctic Meteorites VIII	58
1430-1445	Kusakabe M.* , Maruyama S. and Kojima H. $^{17}\text{O}/^{16}\text{O}$ and $^{18}\text{O}/^{16}\text{O}$ ratio measurement using laser fluorination with application to some Antarctic meteorites	41
1445-1515	—Coffee Break—	
1515-1530	Sugiura N.* and Miyazaki A. CL images of anorthite in meteorites	79
1530-1545	Kita N. T.* , Kimura M. and Morishita Y. The Al-Mg system in chondrules from the most primitive H chondrite Y82038	33
1545-1600	Tachibana S.* , Huss G. R., Miura H. and Nakamoto T. Heating conditions of chondrule precursors during shock-wave heating: Constraints from sulfur isotopic compositions of chondrule troilites	81
1600-1615	Nakamoto T.* , Kita N. T. and Tachibana S. Chondrule age distribution and degree of heating for chondrule formation	54
1615-1630	Miura H.* and Nakamoto T. Thermal history of chondrules during shock-wave heating	48

12

Wednesday, June 2, 2004

Chairs: Ebihara M. and Nishiizumi K.

1000–1015	Takeda H.* , Bischoff A. and Yamaguchi A. Magnesian granulitic clasts in some lunar meteorites from the feldspathic highlands	83
1015–1030	Karouji Y.* , Ebihara M. and Yamaguchi A. Chemical characteristics of lunar meteorites, Yamato 86032 and Dhofar 489	29
1030–1045	Chokai J.* , Mikouchi T., Arai T., Monkawa A., Koizumi E. and Miyamoto M. Mineralogical comparison between LAP02205 and lunar mare basalts	4
1045–1100	Sasaki T. , Sasaki S.*, Watanabe J., Sekiguchi T., Kawakita H., Fuse T., Takato N., Yoshida F., Dermawan B. and Ito T. Presence of mature and fresh surfaces on new-born asteroid Karin	75
1100–1115	Kitazato K.* , Abe M., Nakamura A. M., Saito J. and Fujiwara A. Hapke parameter properties of bidirectional reflectance for Yamato-75102 L6 chondrite	37
1115–1130	Jull A. J. T.* , McHargue L. R., Johnson J. A. and Nishiizumi K. Terrestrial ¹⁴ C ages of Yamato meteorites	25
1130–1145	Nishiizumi K.* and Hillegonds D. J. Exposure and terrestrial histories of new Yamato lunar and martian meteorites	60
1145–1200	Funaki M.* and Syono Y. Magnetization of the impact-generated plasma and shock induced magnetization under the pressure 5, 10 and 20 GPa	14
1200–1215	Ozima M.* , Miura Y. N., Podosek F. A. and Seki K. Early earth evolution recorded in lunar soils? A case for geomagnetic field	72
1215–1330	—Lunch—	

Chairs: Jagoutz E. and Koizumi E.

1330–1345	Koizumi E.* , Mikouchi T., Miyamoto M., McKay G., Monkawa A. and Chokai J. Experimental and computational studies of the olivine-phyric shergottite Yamato 980459	39
1345–1400	Ikeda Y.* and Shimoda G. Major-element trend for shergottite melts and their source materials	17
1400–1415	Fritz J.* , Greshake A. and Stöfler D. Micro Raman spectroscopy of plagioclase and maskelynite in Martian meteorites: Evidence for progressive shock metamorphism	10
1415–1430	Monkawa A.* , Mikouchi T., Koizumi E., Sugiyama K. and Miyamoto M. Oxidation state of iron in martian kaersutites: A micro-XANES spectroscopic study	52
1430–1445	Mikouchi T.* , Monkawa A., Tachikawa O., Yamada I., Komatsu M., Koizumi E., Chokai J. and Miyamoto M. Electron back-scatter diffraction (EBSD) and fore-scatter electron (FSE) image analyses of nakhlites	46
1445–1500	Imae N. An experimental study of the phase equilibrium using a parent magma composition formed nakhlites	19
1500–1515	Dreibus G.* and Jagoutz E. Similarities and diversities of nakhlites	8
1515–1545	—Coffee Break—	

—Special Talk—

Chair: Miyamoto M.

1545–1645	McKay G.* , Le L., Schwandt C., Mikouchi T. and Koizumi E. Redox state and petrogenesis of martian basalts: Clues from experimental petrology	44
1700–1900	Welcome Party (6th Floor)	

Thursday, June 3, 2004

Chairs: Nyquist L. E. and Park J.

1000-1015	Kaiden H.* and Buchanan P. C. Comparison of Fe-Mg interdiffusion coefficients in orthopyroxene: Implication for metamorphism of the Petersburg polymict eucrite	27
1015-1030	Yamaguchi A.* and Mikouchi T. Heating experiments of the HaH262 eucrite	89
1030-1045	Okamoto C.*, Ebihara M. and Yamaguchi A. Geochemical study of metal-rich eucrites from Antarctica	68
1045-1100	Nyquist L. E.*, Shih C.-Y. and Takeda H. Chronology of Eucrite Petrogenesis from Sm-Nd and Rb-Sr Systematics	66
1100-1115	Park J.* and Nagao K. Noble gas study of eucrites Asuka-880702, -880761, -881388	73
1115-1130	Miura Y. N.*, Sugiura N., Kusakabe M. and Nagao K. Noble gases in Northwest Africa 1670, a new angrite, and oxygen isotopes of this angrite and some achondrites	50
1130-1145	Nakamuta Y. Morphologies of graphite in ureilites: Implications for the petrogenesis of ureilites	56
1145-1200	Tamaki M.*, Misawa K., Yamaguchi A., Ebihara M. and Takeda H. Petrologic study of eucritic enclaves in mesosiderites, Mt. Pudbury and Vaca Muerta	85
1200-1215	Noguti M., Matsuzaki H., Setoguchi M., Honda M.* and Nagai H. Depth profile of cosmogenic nuclides in large iron meteorites	64
1215-1230	Fukushi Y., Tazawa Y.*, Fukuoka T., Saito Y. and Yada T. Chemical composition of individual micrometeorites collected from Antarctic ice	12

Poster Session

Bérczi Sz., Fabriczy A., Földi T., Hargitai H., Hegyi S., Hudoba Gy., Illés E., Kovács Zs., Kereszturi A., Mörtl M., Sik A., Józsa S, Szakmány Gy., Weidinger T., Roskó F. and Tóth Sz. Analog site studies in planetary science on Eötvös University, Hungary (Unusual guidebook, terrestrial field work and microenvironmental studies)	1
--	---

Abstract only

Christen F., Busemann H., Lorenzetti S. and Eugster O. Mars-ejection ages of Y-000593, Y-000749, and Y-000802 (paired nakhlites) and Y-980459 shergottite	6
Marakushev A. A., Zinovieva N. G., Bobrov A. V. and Granovsky L. B. The nature of diamond in ureilites and carbonaceous chondrites	42

ABSTRACTS

ANALOG SITE STUDIES IN PLANETARY SCIENCE ON EÖTVÖS UNIVERSITY, HUNGARY (UNUSUAL GUIDEBOOK, TERRESTRIAL FIELD WORK AND MICROENVIRONMENTAL STUDIES)

Bérczi Sz.¹, Fabriczy A.², Földi T.³, Hargitai H.⁴, Hegyi S.⁵, Hudoba Gy.⁶, Illés E.⁷, Kovács Zs.⁸, Kereszturi A.⁴, Mörtl M.⁹, Sik A.⁴, Józsa S.¹⁰, Szakmány Gy.¹⁰, Weidinger T.¹¹, Roskó F.¹², Tóth Sz.¹².

¹Eötvös University, Dept. G. Physics, H-1117 Budapest, Pázmány 1/a, Hungary, (bercziszani@ludens.elte.hu),
²Eötvös University, Teachers Tr. College, H-1126 Budapest Kiss. J. altb. u. 42, Hungary, ³FOELDIX, Budapest, Irinyi J. u. 36/b. Hungary, ⁴Eötvös University, Dept. Phys. Geography, Budapest, Pázmány 1/c, ⁵Pécs University, Dept. Informatics/ Technology, H-7625 Pécs, Ifjúság u. 6. Hungary, ⁶Budapest Polytechnic, Kandó Kálmán College of Engineering, 6000-Székesfehérvár, Budai út. Hungary, ⁷Konkoly Observatory, H-1525 Budapest, Pf. 67. Hungary, ⁸Berzsenyi College, Dept. Technology, H-9700 Szombathely, Károlyi G. tér 4. Hungary, ⁹Eötvös University, Dept. G. Chemistry, H-1117 Budapest, Pázmány 1/a, Hungary, ¹⁰Eötvös University, Dept. Petrology and Geochemistry, Budapest, Pázmány 1/c, Hungary, ¹¹Eötvös University, Dept. Meteorology, Budapest, Pázmány 1/a, ¹²eWorld Hungary Kft., 1026 Budapest, Garas u. 1.

Introduction: Various analog planetary geology studies were organized on Eötvös University, Cosmic Materails Space Research Group. First we show that a field work was organized in petrology to study rocks transported by Danube to Dunavarsány, Hungary. We compared analog site situation of Martian Pathfinder's rock observations where on the landing site the floods of the Ares Vallis river transported the rock types of the southern highlands onto the Chryse Planitia. Second: We compiled a new atlas in the series of the Solar System Research [1] with Microenvironmental Studies of landers on Planetary Surfaces. The main chapters were: a) field petrology and geography of the deserts, b) rock surface textural studies, c) landing on Venus, d) impacts around the landers, e) characteristics of water formed surface on Mars, f) man on the Moon: Apollo, g) micrometeorological measurements on Earth and Mars, h) electrostatics of the thin planetary atmospheres, i) measurement of the atmospheric chemical composition, j) biological measurements of Vikings [2]. With this little atlas our aims were to give background for construction of Hunveyor experiments on the basis of succesful programs of Surveyors, Lunas, Vikings, Apollos, Veneras, and the Pathfinder and to show details of some of their main experiments. But the main benefit of this booklet is that experiments and impressions in **any terrestrial geological and petrological field work studies in this human size and scale can be used up for comparisons to the observations of the planetary landers:** panorama studies, rock size frequency, visible textures of hand specimens, positions reached by geological process, etc.

Analog site petrology field works in Dunavarsány, Hungary: Field work of petrologic study of pebbles of the polymict gravel in the Dunavarsány mine (U-Pleistocene), south of Budapest. The South Pest Plain Pliocene-Pleistocene Suite surface gravel formation has 20-100 m thickness in this region, consisting of the sediments of the terraces of Danube [3]. Various rocks from the middle and upper flow of the Danube: quartzite from the Alps, (ca. 500 km of transporting distance), andesite (Miocene age, from the Börzsöny Mts. ca. 50 km transp. dist.), and sedimentary rocks,

however, it contains also eclogite, granulite, amphibolite of unknown locality, probably more than 500 or as far as 1000 kilometers of transporting distance. The samples were collected in the gravel pit of the Aqua Ltd., near Kisvarsány, on a gravel hill. Generally 5-10 cm sized pebbles can be found here, however sometimes some decimeter sized boulders were also found.

Classification of pebbles according to their transporting length in the river: The rock pebbles can be grouped into two groups. These groups are well separated on the basis of the shape and size of the pebbles. In one group there are the well abraded, well rounded smaller (less the 20 centimeter sized) grains. Most of the pebble rock types described occur in this group. In the other group we can find the larger pebbles, sometimes boulder sized rocks (they even may reach the 1 meter size). These larger rock fragments are more angular, worse abraded rocks. This group represents only a small part of the transported rocks of the river. Their rock type is mainly andesite (50 %), and many granite, granulite and gneiss boulders occur among them and rarely amphibolite. Sedimentary rocks were: limestones from triassic or jurassic, from eocene and miocene, sandstones or sandy limestones.

Considering their rounded and abraded shape the members of the first group could be transported from larger distances. They may origin from older conglomerate which later was resedimented and settled here. The members of the second group can not come from farther then some ten kilometers. But only part of these rock types are known in the near vicinity of the gravel pit or from drilling cores in this region. Probably a mountain was on the surface in the pleistocene nera this place and this mountain has been covered and the basin was filled in by the sediments of various sources since pleistocene and recently only the boulders represent the remnants of this mountain mixed with the pebbles transported from farther distances by the river.

Planetary comparisons of Dunavarsány field works: Rock types on a lunar Apollo expedition or in

the MPF landing site are mixed from the near or farther rock fragments delivered on the site by various processes. On the Moon the main process was the impact ejection. On Mars MPF case the flooding of the Ares Valley river was the main transporter of rocks. In any case the distance of transportation could be in the range of one 10s of kilometers till as far as 1000 kilometers. The great variability among the rock types can be seen on the Pathfinder's landing site where various rock surface textures were described [4,5,6]. In the MPF landing site- as on the Dunavarsány gravel pit - both igneous and sedimentary rocks occur. Camera resolution approaches the visual resolution in a field work observer's one. Identification of rock types was increased in the laboratory, in the thin section studies, however the field work estimation is in the range of the space probe camera's resolution capability. The positions on the MPF site are also informative and the stratigraphic relations in a gravel pit may also add some information of the sedimentation process. The field work with preparation from the planetary surface knowledge adds some point of view which will not arise without planetary landers geologic knowledge. These are: 1) Estimation the textures from various distances. (Approaching to the boulder may increase the exactness of the identification of the rock texture.) 2) Identification of minerals in the rock textures.

Field petrology and geography little atlas

a) Petrology and geography of the deserts: Comparison of the landing site rocky garden around Surveyor-7 and Pathfinder allows to study the size frequency of rocks, the analysis of rock surface textures and to imply the processes which formed these rocks. While on these two landing sites for Surveyor-7 on the Moon impact fragmentation and ejection was the main process [7], for Pathfinder on Mars the floods of the Ares Valley transported and rounded the rocks [8].

b) Rock surface textural studies: The good resolution of the Pathfinder images made it possible to find various rock forming processes to imply. There were found vesicular rocks (probably igneous origin) stratified textures (metamorphic or sedimentary origin) and brecciated textures (impact brecciation?). Comparison with rock surfaces in terrestrial deserts (Arizona Desert rocks i.e.) made it evident that strong winds with transported sand may scrape many of the surface pattern on the Pathfinder's rocks. Comparison with the wind-tails and dune directions in the vicinity of the landing site showed their origin from winds in the past [9].

c) Landing on Venus: Surface rocks and panoramas on Venus were studied by the Venera space probes. Considering the rocky surface desert photographic panorama of Venera 9 it is rather similar two that of Pathfinder's with scattered eroded rocks embedded in the soil. However the great refraction in the dense atmosphere produces different perspective as

compared to Mars. Two other Venera probes (17, 18) landed on lava flow surfaces [10]. Data of their X-ray fluorescence measurements referred tholeiitic and in the other landing site komatiitic composition. These reference were used when we compiled the rock gardens in the test-terrain of our Hunveyor experimental university landers [11].

d) Impacts around the landers: In this chapter we give wide range of descriptions and comparisons where terrestrial field works (with shatter cones) were also involved (Haughton, Vredefort, Tswaing). Field Works on Analog Sites, as known programs on Devon Island and impact related meteorite collections on Antarctica and other cold and in the hot deserts. [12, 13, 14]

e) Characteristics of water formed surfaces on Mars: In our human panorama scale this chapter is a vision: what kind of phenomena can be observed by a rover which travels along a Martian riverbed. It begins its route at the river's upper flow and observes with its camera the fresh slides on the riverbank from some tens of meter distance and at the same time observes the characteristics of the sediments below its wheels in some centimeters distance. Then it studies the events which can be observed while going along the river during the some 100 kilometers of the planned trip from the origin of the river till its delta (this chapter foresees the next volume of the series which will study the rover missions to the planets).

f) Man on the Moon: Apollo: This chapter is describing a real field work on another planetary surface. Many details of the field works are told in this chapter about Apollo astronaut's activities and many details of the lunar regolith, rock samples, their textures, types, formation processes. In the back cover rock samples and astronaut tools show more details and - at the same time - give (indirectly) list about tools necessary to a good field trip for students in preparations for their terrestrial field works [15].

g) Micrometeorological measurements on Earth and Mars: A terrestrial meteorologic station is standing in the Bugac Puszta in Kiskunság, Great Plain, Hungary and this station is measuring 25 parameters continuously. Its structure and data resembles in many instruments to those measured by Pathfinder's Sagan Memorial Station on Mars or earlier Vikings. Not only the terrestrial and Martian atmospheric boundary layer models are compared, but the temperature runs for some days/sols on the higher (1.4 m Pathf. and 1 m Bugac) and on the lower (0.9 m Pathf. and 0.1 m Bugac) measuring levels. On the basis of data and models the renormalized scale height for the boundary layers (about 3 times higher on Mars as compared to the Earth's atmospheric corresponding structures) can be shown [16].

h) Electrostatics of the thin planetary atmospheres: After describing the pioneering measurements of Surveyor-5 and the Apollo LEAM experiment we show the main transport processes [17,

18]. We also describe that instrument which is based on these processes, however not with such a "random electrodes" like in the case of charged particles of the lunar quasiatmosphere. That instrument is Foeldix-1, which is shown in another works, i.e. [19].

i) Measurement of the atmospheric chemical composition: This chapter gives a detailed description of the gaschromatograph and the mass-spectrometer unit which is the most frequently used instrument in atmospheric composition measurements. Although not strongly connected to classic field work activities this chapter foreruns the planetary geology age when the Apollo type field works will be the most exciting for students, with various instrumental technologies.

j) Biological measurements of Vikings: Biology is among the main programs on Mars. This was initiated by the Viking experiments. This way the last chapter has many roles. It shows the most complex new discipline in planetary activities and also it connects the geological type planetary field works to the yet not prepared but in the future planned biological planetary field work atlas. In this chapter we show the 3 experiments [20] and at the end we propose students to plan participation in space science education programs from biology side: cellular biology is the next to be involved in lander experiments on Hunveyor too. Finally we mention that next year hopefully 3 landers on the Mars shall extend this last chapter very much. When closing this abstract the MER-1 Spirit is successfully beginning its work.

Summary: The analog planetary geology studies not only connects the planetary petrographic and geologic field works with those of the laboratory Hunveyor robotic construction and its Husar rover program but gives a new approach possibility to the recent terrestrial geologic field works too teaching students by seeing back to the Earth from the planetary surfaces, with robotic landers.

Acknowledgments: This work has been supported by the MUI-TP-190/2003 and 154/2003-2004 funds

References: [1] Bérczi Sz., Fabriczy A., Hargitai H., Hegyi S., Illés E., Kabai S., Kovács Zs., Kereszturi A., Opitz A., Sik A., Varga T., Weidinger T. (2003): Alas Series of the Solar System (5 booklets) and other Works for Education and Public Outreach by Cosmic Materials, Planetology and Hunveyor Groups of the Eötvös University, Budapest. In LPSC XXXIV, #1305, LPI Houston (CD-ROM).; [2] Bérczi Sz. Hargitai H., Illés E., Kereszturi Á., Sik A., Földi T., Hegyi S., Kovács Zs., Mörtl M., Weidinger T. (2003): *Kis Atlasz a Naprendszeröl (6): Bolygófelszíni mikrokörnyezetek atlasza.* (Microenvironmental Studies of landers on Planetary Surfaces). ELTE TTK Koszmos Anyagokat Vizsgáló Űrkutató Csoport, UNICONSTANT, Budapest-Püspökladány; [3] Zsemle F., Török K., Józsa S., Kázmér M. (2001): Granulite pebbles from the Upper Pleistocene terrace of the Danube at

Délegyháza, Hungary. *Földtani Közlöny*, 131/3-4, 461-474.; [4] Basilevsky, A.T.; Markiewicz, W.J.; Thomas, N.; Keller, H.U. (1999): Morphology of the APXS Analyzed Rocks at the Pathfinder Site: Implications for Their Weathering Rate and Distance of Transportation. LPSC XXX, #1313, LPI, Houston, (CD-ROM); [5] Bridges, N.T.; Greeley, R.; Kuzmin, R.O.; Laity, J.E. (2000): Comparison of Terrestrial Aeolian Rock Textures to Those at the Mars Pathfinder Landing Site. LPSC XXXI, #2066, LPI, Houston, (CD-ROM); [6] Parker, T.J.; Moore, H.J.; Crisp, J.A.; Golombek, M.P. (1998): Petrogenetic Interpretations of Rock Textures at the Pathfinder Landing Site. LPSC XXIX, #1829, LPI, Houston, (CD-ROM); [7] Shoemaker E. M. et al. (1968) NASA-JPL Techn. Report 32-1264, Part II. p.9-76; [8] Yingst, R.A., Haldemann, A.F.C., Lemmon, M.T. (2003): Classification of Mars pathfinder Rock Surfaces ... LPSC XXXIV, #1081, LPI, Houston (CD-ROM); [9] Bridges, N.T., Greeley, R., Kuzmin, R.O., Laity, J.E. (2000): Comparison of Terrestrial Aeolian Rock Textures to those at the Mars Pathfinder Landing Site. LPSC XXXI, #20666, LPI, Houston (CD-ROM); [10] Florensky, C.P., Basilevsky, A.T., Kruichkov, V.P., Kuzmin, R.O. et al. (1983): Venera 13 and Venera 14 - Sedimentary Rocks on Venus? *Science*, 221, 57.; [11] Sz. Bérczi, B. Drommer, V. Cech, S. Hegyi, J. Herbert, Sz. Tóh, T. Diósy, F. Roskó, T. Borbola. (1999): New Programs with the Hunveyor Experimental Lander in the Universities and High Schools in Hungary. LPSC XXX, #1332, LPI, Houston, (CD-ROM); [12] Lee, P. (1997): A Unique Mars/Early Mars Analog on Earth The Haughton Impact Structure, Cevon Island, Canadian Arctic. Early Mars. Proc. Conf. 50.; [13] Sharpton, V.L., Dressler, T.O., Sharpton, T.J., (1998): Mapping the Haughton Impact Crater, Devon Island, .. LPSC XXIX, #1867, LPI, Houston, (CD-ROM); [14] Wieland, F., Reimold, W.U. (2003). Field and Laboratory Studies on Shatter Cones in the Vredefort Dome, South Africa. MAPS 38, #5016, [15] NASA Apollo 17 team: (1973): *Apollo 17 Preliminary Science Report*, JSC, NASA SP-330. Washington D.C.; [16] Larsen, S.E., Jorgensen, H.E., Landberg, L. Tillman, J.E. (2002): Aspects of the Atmospheric Surface Layers on Mars and Earth. *Boundary-Layer Meteorology* 105, 451-470; [17] Criswell, D. (1972): Horizon glow and motion of Lunar dust. *Lunar Science III*. p. 163. LPI, Houston; [18] Horányi M., Walch, B., Robertson, S. (1998): Electrostatic charging of lunar dust. LPSC XXIX. LPI, CD-ROM, #1527; [19] Földi, Sz. Bérczi (2001): Measurements on the ion-cloud levitating above the Lunar surface: Experiments and modelling on Hunveyor experimental lander. *MAPS*, 36, Supplement, p.A59; [20] NASA Viking Team (1976): Viking 1 early results. NASA SP-408. Washington, D.C.

MINERALOGICAL COMPARISON BETWEEN LAP02205 AND LUNAR MARE BASALTS: J. Chokai¹, T. Mikouchi¹, T. Arai², A. Monkawa¹, E. Koizumi¹ and M. Miyamoto¹ ¹Department of Earth and Planetary Science, Graduate School of Science, University of Tokyo, Hongo, Tokyo 113-0033, Japan (chokai@eps.s.u-tokyo.ac.jp), ²Lunar Exploration Technology Office, Japan Aerospace Exploration Agency (JAXA), 2-1-1 Sengen, Tsukuba, Ibaraki, 305-8505, Japan.

Introduction:

LAP02205 is a non-brecciated lunar meteorite recently recovered from the LaPaz ice field, Antarctica. Because most lunar meteorites are brecciated, this crystalline rock will offer useful information to understand crystallization of lunar mare basalt. In this study, we compare petrology and mineralogy of LAP02205 with those of other lunar meteorites and Apollo lunar rocks to explore their petrogenetic and crystallization relationships.

Petrology and Mineralogy of LAP02205:

The thin section studied (LAP02205, 34) shows a medium-grained subophitic texture with evidence for moderate shock metamorphism. The modal abundances of minerals are 53.1% pyroxene, 30.4% plagioclase, 6.9% olivine, 4.4% ilmenite, 2.2% silica, 1.3 % Si-, K-rich glass, 1.2% fayalite, 0.2% spinel, 0.2% Fe sulfide, and 0.1% others. Most pyroxenes are subhedral and ~0.5mm in size. Pyroxenes are extensively zoned and their compositions are generally Fe-rich. The zoning pattern in a single grain is irregular, but the most inner core is usually pigeonite ($\text{En}_{55}\text{Fs}_{30}\text{Wo}_{15}$) and partly mantled by augite ($\text{En}_{40}\text{Fs}_{25}\text{Wo}_{35}$). Then, outer parts are zoned to nearly Mg-free compositions. Plagioclase grains are equant to lath-shaped (~1mm long). Most plagioclase grains show clear birefringence, some plagioclase grains have been partly or completely maskelynitized. The plagioclase composition ranges from $\text{An}_{91}\text{Or}_0$ to $\text{An}_{80}\text{Or}_7$. Olivine grains are rounded and up to 1mm in size. They are usually present as clusters of a few composite grains. Olivine is remarkably zoned (Fo_{67-48}) as pyroxenes.

Comparison with other lunar meteorites:

LAP02205 is the 5th crystalline lunar meteorites. Only four samples have been known so far. They are Yamato 793169, Asuka 881757, NWA032/479, and Dhofar 287A. LAP02205 shows some similarities to all of these meteorites. However, Yamato and Asuka lunar meteorites are clearly different from LAP02205 in that they do not contain olivine [e.g., 1]. NWA032/479 is different in that they show a very fine-grained groundmass texture distinct from LAP02205, suggesting faster cooling history [2]. However,

they have similar mineral compositions to those of LAP02205 [2] and the bulk composition of LAP02205 is also nearly identical to those of NWA032/479 in major and minor elements [2]. When we take account of texture, LAP02205 is most similar to Dhofar 287A [3]. Olivine and pyroxene compositions of these two meteorites are similar, but Dhofar 287A lacks magnesian pigeonite unlike LAP02205. The modal abundance of olivine in Dhofar 287A is ~20%, which is clearly higher than that in LAP02205 (~7%), but the presence of abundant mesostasis of fayalite with Si-, K- rich glass is remarkably similar to LAP02205 [3]. Although LAP02205 contains ~2% silica, it is rare in Dhofar 287A because it is clearly olivine-normative. The difference is also apparent in that spinels in LAP02205 show wide range of Fe/(Fe+Mg) ratio ($fe\#$) (0.70-1.0) (Fig. 1), but in Dhofar 287A, the lowest $fe\#$ of spinels is about 0.90 [3]. Thus, LAP02205 is different from any other lunar meteorite found so far although they are similar to NWA032/479 in chemistry and Dhofar 287A in mineralogy, respectively.

Comparison with the Apollo lunar rocks:

When we compare LAP02205 with the Apollo lunar rocks, we found that LAP02205 is most similar to Apollo 12 ilmenite basalt [e.g., 4,5]. Apollo 12 ilmenite basalt shows a modal variation from quartz-normative to olivine-normative depended upon olivine control [4,5]. 12056 is subophitic basalt showing many similar features to LAP02205 [5]. The mineral assemblages and compositions of pyroxene, olivine and plagioclase in LAP02205 and 12056 are quite similar. The presence of the mesostasis and its unique texture is also identical. The abundances of olivine (10.8%) and silica (0.8%) in 12056 are slightly higher and lower than those in LAP02205, respectively [5]. Probably, LAP02205 became slightly more silica-rich because it contains less olivine phenocryst than 12056. In this respect, NWA032/479 and Dhofar 287A are also similar to olivine-normative member of this basalt series.

The Fe/Mg ratio and K abundance in plagioclase are function of olivine abundance and cooling rate [5]. Among olivine-normative Apollo 12 ilmenite basalt, 12005 has the highest Fe/Mg ratio and K abundance of plagioclase, suggesting

slowest cooling. In contrast, low Fe/Mg ratio would be responsible for the abundant presence of mesostasis due to faster cooling. Plagioclase in LAP02205 is identical to that in 12056 in these abundances, suggesting similar cooling history.

Is LAP02205 an Apollo 12 ilmenite basalt?:

Thus, LAP02205 is similar to Apollo 12 ilmenite basalt, especially 12056. Nevertheless, apparent differences are present between LAP02205 and 12056. Fe-Ni metal is very rare in LAP02205 and rather present as Fe sulfide. The ilmenite composition of LAP02205 is also different from 12056 in its very low Mg and Cr abundances. Spinel grains in the Apollo rocks are also different from those in LAP02205. The Cr/(Cr+Al) ratio of LAP02205 decreases as *fe#* increases, whereas that of the Apollo rocks shows smaller changes as *fe#* increases (Fig. 1). Spinel grains in LAP02205 range in composition from near endmember ulvöspinel to chromite. The high Fe/(Fe+Mg) grains imply that they are the result of Fe-Mg reequilibration between spinel and the Fe-rich residual liquid.

Apollo 12 ilmenite basalt is known to show clear correlation between the bulk *fe#* (indicating differentiation degree) and cooling rate (Fig. 2) [4]. Because LAP02205 shows mineralogical similarities to Apollo 12 ilmenite basalts (12056, 12063, 12054, 12051 and 12047 [5]), they would

experience similar cooling rates. However, the low *mg#* (0.33-0.35) [6-9] of the bulk LAP02205 composition with olvine-bearing petrology suggest slightly different parent magma from the Apollo 12 ilmenite basalt suite (Fig. 2). Dhofar 287A has a similar cooling rate to LAP02205, but its *mg#* is much higher than that of LAP02205. Thus, LAP02205 is a little bit different from either Apollo 12 ilmenite basalts or Dhofar 287A. NWA032 experienced faster cooling history than LAP02205 as discussed above. Because the bulk compositions are similar between them, LAP02205 and NWA032 may form a similar suite to the Apollo 12 ilmenite basalt such as 12056 and 12008.

References: [1] Takeda H. et al. (1993) *Proc. NIPR Symp. Antarct. Meteorites*, 6, 3-13. [2] Fagan T. J. et al. (2001) *Meteorit. & Planet. Sci.*, 37, 371-394. [3] Anand M. et al. (2003) *Meteorit. & Planetary Sci.*, 38, 485-499. [4] Rhodes J. M. et al. (1977) *Proc. LSC 8th*, 1305-1338. [5] Dungan M. A. & Brown R. W. (1977) *Proc. LSC 8th*, 1339-1381. [6] Korotev R. L. et al. (2004) LPS XXXV, #1416. [7] Jolliff B. L. et al. (2004) LPS XXXV, #1438. [8] Anand M. et al. (2004) LPS XXXV, #1626. [9] Joy K. H. et al. (2004) LPS XXXV, #1545

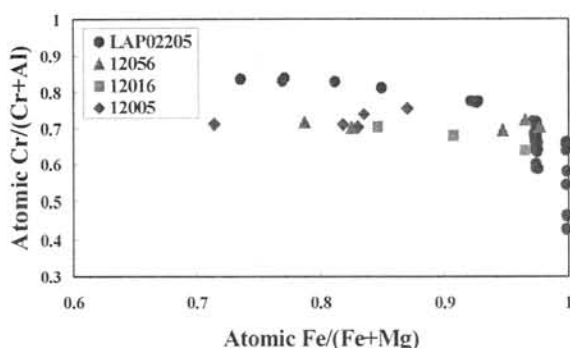


Fig. 1. Spinel compositions in LAP02205 compared with those of the Apollo 12 ilmenite basalts (12005, 12016 and 12056) [5].

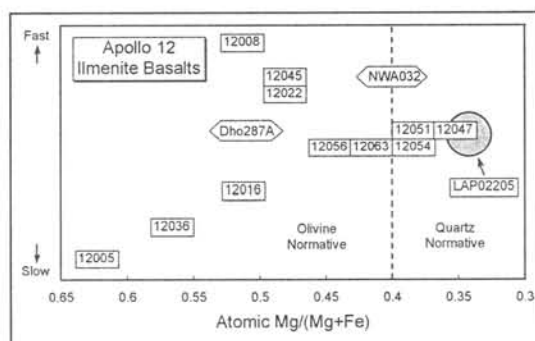


Fig. 2. The relationship between differentiation and cooling rate in lunar mare meteorites (LAP02205, NWA032 [2] and Dhofar 287A) and the Apollo 12 ilmenite basalts (12005, 12008, 12016, 12022, 12036, 12045, 12047, 12051, 12054, 12056 and 12063) [5].

Introduction

There is strong evidence that meteorites are ejected as small objects from the martian surface and come directly to Earth without secondary breakup in space [1]. Hence, the ejection age, T_{ej} , of a meteorite is the sum of its cosmic-ray exposure (CRE) age and its terrestrial age (T_{terr}). Presently, there are about 30 unpaired martian meteorites in our collections, representing five different petrographic and mineralogical types of martian surface areas. The value of these meteorites stems from the fact that they come from surface areas that were not sampled by automated missions. The distribution of the ejection ages indicates that up to eight different events are responsible for ejecting the dated martian meteorites.

Results

We measured the isotopic abundances of the noble gases in the Yamato-980459 shergottite recovered by the Japanese Antarctic Research Expedition (JARE) in 1998 and in the two paired nakhlites Yamato-000593 and Yamato-000749 collected by JARE-41 in 2000. The main purpose of these analyses is the determination of the CRE-ages, the Mars ejection ages and their comparison with the T_{ej} of the other known martian meteorites. For details of the analytical procedure see [1]. The isotopic compositions of the analyzed samples will be given in a forthcoming publication.

Cosmic-ray exposure ages

In this abstract we discuss, in particular, the CRE ages of the investigated meteorites. For calculating the ^3He , ^{21}Ne , ^{38}Ar , and ^{81}Kr - ^{83}Kr ages we adopted the method proposed by [2]. The abundances of the target elements responsible for the production of the cosmogenic nuclides in Y-980459 were taken from [3] and [4], and for the nakhlites from [4–7]. Shielding corrections, taking care of the meteorite's geometry, were based on the cosmogenic ratio $^{22}\text{Ne}/^{21}\text{Ne}$ and the formula given by [2]. Tables 1 and 2 give the CRE ages obtained in this work and those reported by other workers.

For Y-980459 the agreement among the CRE ages obtained from the different nuclides (Table 1) is not very good, perhaps due to the relatively low abundances of the cosmogenic noble gases and possibly due to ^3He loss [8]. The average value calculated from all determinations is 2.5 Ma. If we take T_{terr} of ≤ 0.3 Ma into account [1] an ejection age from Mars of 2.6 ± 0.4 Ma is obtained. This is in good agreement with the average T_{ej} of 2.7 ± 0.3 Ma for several basaltic shergottites (Los Angeles,

NWA 480/1460, NWA 856, NWA 1068, QUE 94201, Shergotty, and Zagami).

Excellent agreement among all available results for the paired nakhlites Y-000593, Y-000749, and Y-000802 is found. All samples given in Table 2 yield an average CRE age of 11.0 Ma. As the T_{terr} is < 0.04 Ma [9], we obtain $T_{ej} = 11.0\pm 1.0$ Ma, close to the average $T_{ej} = 10.7\pm 1.0$ Ma for the other nakhlites (Governador Valadares, Lafayette, Nakhla, and NWA 817). It is remarkable that the five (unpaired) nakhlites dated until now show ejection ages in the range of 10.0 – 11.9 Ma, indistinguishable from that for Chassigny of 11.1 Ma. The conclusion, that the same impact event on Mars in a chemically diverse area may have ejected the nakhlites and Chassigny [10] is, thus, confirmed.

Acknowledgements We thank NIPR for providing the meteorite samples. This work was supported by the Swiss National Science Foundation.

References [1] Eugster O., Busemann H., Lorenzetti S., and Terribilini D. (2002) Meteorit. Planet. Sci. **37**, 1345. [2] Eugster O. and Michel T. (1995) Geochim. Cosmochim. Acta **59**, 177. [3] Misawa K. (2003) Internat. Symp. Evolution of Solar System Materials: A New Perspective from Antarctic Meteorites, NIPR Tokyo. Abstract pp. 84-85. [4] Dreibus G., Haubold R., Huisl W., and Spettel B. (2003) Internat. Symp. Evolution of Solar System Materials: A New Perspective from Antarctic Meteorites, NIPR Tokyo. Abstract pp. 19-20. [5] Shirai N., Oura Y., and Ebihara M. (2002) Lun. Planet. Sci. abstract # 1134. [6] Imae N., Ikeda Y., Shinoda K., Kojima H., and Iwata N. (2003) Antarctic Meteorite Research **16**, 13. [7] Oura Y., Shirai N., and Ebihara M. (2003) Antarctic Meteorite Research **16**, 80. [8] Nagao K. and Okazaki R. (2003) Internat. Symp. Evolution of Solar System Materials: A New Perspective from Antarctic Meteorites, NIPR Tokyo. Abstract p. 94. [9] Okazaki R., Nagao K., Imae N., Kojima H. (2003) Antarctic Meteorite Research **16**, 58. [10] Nyquist L. E., Bogard D. D., Shih C.-Y., Greshake A., Stöffler D., and Eugster O. (2001) Space Science Reviews **96**, 105. [11] Murty S. V. S., Mahajan R. R., Das J. P., Sinha N., and Goswami J. N. (2003) Internat. Symp. Evolution of Solar System Materials: A New Perspective from Antarctic Meteorites, NIPR Tokyo. Abstract pp. 90-91. [12] Mathew K. J., Marty B., Marti K., and Zimmermann L. (2003) Earth Planet. Sci. Lett. **214**, 27.

Table 1. CRE age (Ma) of the Y-980459 basaltic shergottite

Sample (system) ¹⁾	T ₃	T ₂₁	T ₃₈	T _{av} ²⁾	Remarks	Ref.
Y-980459 (B)	1.6	4.0	2.7	2.8	total melt	this work
(C)	1.7	2.7	3.5	2.6	step heating	this work
Y-980459	1.6	2.5	2.1	2.1	step heating	[8]
Y-980459 (average)				2.5		

1) Mass spectrometer system used.

2) Typical experimental error of T_{av} about 10 %.

Table 2. CRE ages (Ma) of Y-000593, Y-000749, and Y-000802

Sample (system) ¹⁾	T ₃	T ₂₁	T ₃₈	T ₈₁	T _{av} ²⁾	Remarks	Ref.
Y-000593 (B)	12.4	11.3	10.1	–	11.3	total melt	this work
(C)	8.1	10.3	12.8	12.5	10.9	step heating	this work
	12.6	11.4	8.5	–	10.8	step heating	[9]
	12.6	11.9	8.3	11.8	11.2	total melt	[9]
	9.1	13.5	9.1	–	10.6	total melt	[11]
	11.5	13.5	8.5	–	11.2	total melt	[11]
Y-000749 (B)	12.7	10.7	9.4	–	10.9	total melt	this work
(C)	8.2	11.7	12.0	8.8	10.2	step heating	this work
	12.3	11.9	8.6	–	10.9	step heating	[9]
Y-000802	14.3	13.0	8.4	–	11.9	step heating	[9]
All samples (average)					11.0		
Nakhlites (average)					10.7		[10, 12]

1) Mass spectrometer system used.

2) Typical experimental error of T_{av} about 10 %.

Introduction:

Nakhrites are a small group among Martian meteorites with until today altogether 6 meteorites: Nakhla, Lafayette, Governador Valadares, NWA 817, NWA 998, and the two paired samples Y-000593 and Y-000749. Nakhrites are augite and olivine cumulates of similar chemical composition and ages (1.3 Ga). Only Nakhla itself is an observed fall, therefore for all other nakhrites the influence of chemical alterations during their residence time on Earth must be considered. In anticipation of studying the chemistry and radiogenic isotopes of the recently discovered nakhrites from hot (North West Africa = NWA) and cold (Antarctica = Y) deserts we are carrying out an intensive investigation of minerals in Nakhla meteorite.

Chemistry:

The major and minor element compositions of all 6 nakhrites reveal only small variations. Differences are found in the concentrations of trace elements. However, we have to be carefully distinct between terrestrial contamination and intrinsic concentrations. Furthermore, all nakhrites display evidence for pre-terrestrial aqueous alterations in form of iddingsite. After the discovery of huge amount of Br in a soil-free and abraded rock, Mazatzal, at the Gusev crater by the Mars Exploration Rover–A mission [1] the Br enrichment in Nakhla veins measured by [2] could be related to an influence of Martian aqueous alteration. A good indicator for a terrestrial alteration is a subchondritic La/U ratio in the finds. Uranium⁶⁺ formed soluble compounds which could easily contaminate the meteorite and could influence the Pb isotope systematics. Fig. 1 shows our results of the REE, Th, and U determination by INAA for some of the nakhrites together with the data of NWA 817 from [3]. The shape of this incompatible element pattern is similar for all nakhrites; however, the absolute concentrations are different. NWA 817 with its higher modal proportion of mesostasis compared to other nakhrites contains the highest REE abundances [3]. The nearly chondritic La/U ratios of all these meteorites indicate a weak influence of terrestrial weathering. The halogen concentrations in our investigated nakhrites show great differences. The extremely high Cl (880 – 1900 ppm) and Br (3.5 – 8.4 ppm) concentrations in Nakhla were discussed conflictingly by various authors [2, 4, 5]. Lafayette, Y-000593, Y-000749, and NWA 998 have a Cl content of about 100 ppm and the measured Br content is 0.59 ppm in Lafayette, 0.060 – 0.078 ppm in the Yamato nakhrites, and 0.17 ppm in NWA 998. Only the La/Br ratio of Lafayette matches the La/Br ratio measured in Chassigny, the basaltic shergottites, and lherzolitite shergottites. An explanation for the low Br content in the Yamato nakhrites might be a possible interaction

of Antarctic ice respectively water, which could extract a salt component from this meteorite.

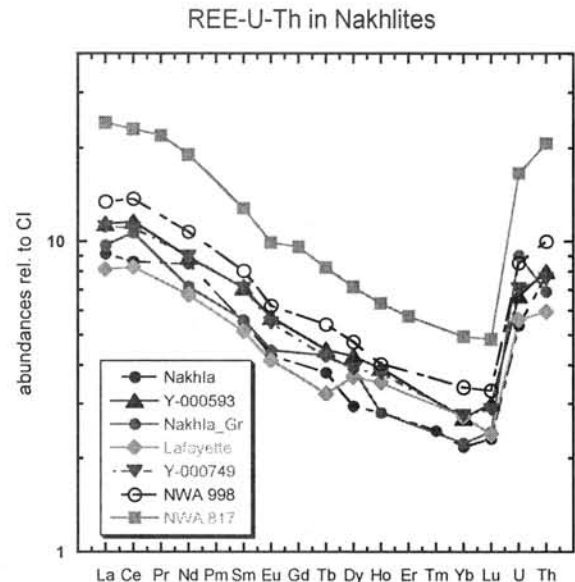


Fig. 1: Abundances of REE, U, and Th in nakhrites (NWA 817 from [3]).

Isotopes:

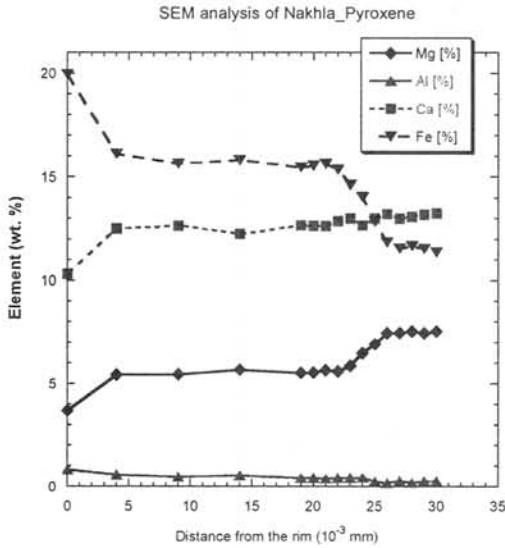
The measured positive ¹⁴²Nd anomaly in Nakhla, NWA 998, and Lafayette and their primitive Sr isotopic composition indicates a common, isotopic source, which was depleted since about 4.3 Ga [6]. The Rb-Sr and Sm-Nd mineral ages of all nakhrites are about 1.3 Ga [7, 8]. However, the ultra clean pyroxene and olivine separates of Nakhla together with two leaches and one of the residues in the Sm-Nd isochron plot are not co-linear within analytical uncertainty [7]. The leach and residue points alone align along a 1.38 Ga isochron; a least squares fit to all the data gives a distinctly younger age of 1.29 Ga.

In 2001, we started the investigation of the U-Pb isotopes in all SNC (Shergottites, Nakhrites, Chassigny) meteorites with an excess of ¹⁴²Nd [9]. The initial Pb isotopic composition of several SNC meteorites plots generally close to the geochron of 4.55 Ga and gives a further confirmation of the early depleted isotopic reservoir for the nakhrites. The first isotopic U-Pb data of Nakhla were reported by [10, 11]. The different steps of acid-leached portions and the residue in our U-Pb measurements of Nakhla yield similar to the Sm-Nd isotopic systematic no co-linear plot. The Nakhla Pb-Pb isotopic data in Fig.3 scatter considerably and the combined leach and residue fractions have ²⁰⁷Pb-²⁰⁶Pb ages >2 Ga. However, the ²³⁸U-²⁰⁶Pb age measured on the U-rich, baddelyite-containing residue is about 1.3 Ga [9].

From the Scanning Electron Microscope (SEM) images of Nakhla the olivine and augite are seen to be

zoned, which was also observed in the nakhlites from cold and hot deserts [12]. A backscattered electron analysis (Fig. 2) of a typically zoned pyroxene in Nakhla shows a high Fe content of 20 wt. % at the outermost rim of 3 μm , followed by a constant lower Fe amount of 14 wt. %

Fig. 2



At 22 μm distance from the rim a rapid decreasing of the Fe concentration from 14 to 11 wt. % in the center was measured. A complementary behaviour was observed for Mg with its 5.5 wt. % content in the rim and 7.5 wt. % in the center. Ca and Al show no variations between rim and core. The step step in Fig. 2 between center and rim in the Fe- and Mg concentrations could not be explained by a continuous evolution of pyroxenes during the crystallization process.

Pb-Pb-Isochron of Nakhlites

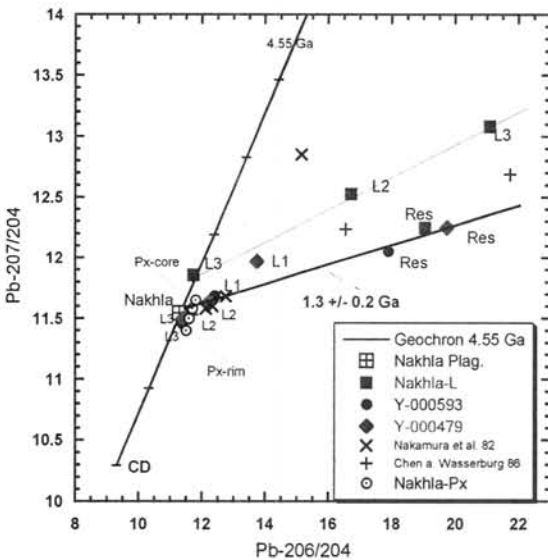


Fig. 3: Pb-Pb isochron of minerals, leaches and residues from Nakhla and Yamato nakhlites.

This was also confirmed by the Pb isotopic pyroxene composition of ultra clean Fe-poor and Fe-rich pyroxene separates, which plot close to the geochron (Fig. 3).

The pyroxene separates show variations in initial isotopic composition with the low-iron center parts implying a higher source μ than the iron-rich rim. A fluid infiltration along grain boundaries as visible in the SEM imagery could explain this isotopic variability.

Our Pb-Pb leach residue isochron of the two Yamato nakhlites, Y-000593 and Y-000749, gives an age of 1.3 Ga and show no scatter. Whereas, the detailed Pb isotopic analyses of whole rocks and mineral separates from Y-000593 by [13] show a considerable scatter.

Conclusions:

The chemical composition and the initial Nd, Sr, and Pb isotopic systematics indicate that the nakhlites share similar parental melt sequences. This melts originated from a very early depleted source in the Martian mantle and interacted with an LREE enriched phase. The internal or mineral ages of nakhlites are obscured by the effects of multiple superimposed processes. Penetration of fluids during the crystallization process, aqueous alteration on their parent body and terrestrial weathering are possible causes of the observed disturbance to the isotopic systems.

References:

[1] Gellert R. et al, (2004) *Science*, in press..
 [2] Sutton S. R. et al. (2002) *LPS XXXIII*, Abstract # 1278.
 [3] Sautter V. et al. (2002) *EPSL 195*, 223–238.
 [4] Gooding J. L. et al. (1991) *Meteoritics 26*, 135..
 [5] Bridges J. C. and Grady M. M. (2000) *EPSL 176*, 267–279.
 [6] Jagoutz E. (1991) *Space Sci. Rev. 56*, 13–22.
 [7] Jagoutz E. and R. Jotter (2000) *LPS XXXI*, Abstract # 1609.
 [8] Shih et al. (1999) *Meteoritics 34*, 647–655.
 [9] Jagoutz E. et al. (2001) *LPS XXXII*, Abstract # 1307.
 [10] Nakamura N. et al. (1982) *GCA 46*, 1555–1573.
 [11] Chen J. H. and G. J. Wasserburg. (1986) *GCA 50*, 955–968.
 [12] Wadhwa M. and G. Crozaz (2003) *Intern. Symp. NIPR Tokyo*, 144–145, abst.
 [13] Yamashita K. et al. (2003) *Intern. Symp. NIPR Tokyo*, 151–152, abst.

Micro Raman spectroscopy of plagioclase and maskelynite in Martian meteorites: Evidence for progressive shock metamorphism. J. Fritz, A. Greshake, and D. Stöffler, Institut für Mineralogie, Museum für Naturkunde, Humboldt Universität zu Berlin, Invalidenstraße 43, 10115 Berlin, e-mail: joerg.fritz.1@rz.hu-berlin.de

Introduction: The rapidly growing group of SNC's now contains 49 samples of 30 unpaired Martian meteorites. In addition to the opportunity to study the geological evolution of Mars, these unique samples provide insights to the interplanetary exchange of matter, including a possible transfer of life.

Released by a hypervelocity impact from the gravity field of Mars, all Martian meteorites experienced a certain degree of shock metamorphism. As part of a comprehensive study of the p/T launch conditions for all Martian meteorites, we measured the shock pressure dependent reduction of the refractive index of plagioclase [2, 3], which is the most sensible record for the equilibrium shock pressure in the range between 14 to 45 GPa [4]. Based on these results, the shock induced transformation of plagioclase is investigated by Raman spectroscopy to record systematic variations indicative for increasing equilibrium shock pressure.

Method: Micro-Raman spectroscopy (MRS) was carried out at the Museum für Naturkunde in Berlin using a notch filter system based Dilor LabRam with a HeNe laser of 632 nm wave length, and a 100x microscope lense. For the final spectra 20 single spectra were accumulated each recorded with a collecting time of 5 sec.

Results: The birefringent plagioclase in the weakly shocked Nakhilites Y 000593 and Lafayette displays no reduction of the refractive index while for Nakhla and Governador Valadarez a slight shock induced decrease of the refractive index was detected [2, 3]. Raman spectra of plagioclase of Y-000593 show prominent bands at 290, 480, 510 and 570 cm^{-1} (Fig. 1). These band positions show a slight shift compared to unshocked oligoclase (290, 483, 509, 575 cm^{-1}) and also minor peak broadening. Comparable spectra were obtained for plagioclase of Lafayette, Governador Valadarez, and Nakhla.

The dunite Chassigny contains birefringent and partly isotropic plagioclase as well as fully isotropic maskelynite. With increasing shock pressure the deformation of the plagioclase crystal lattice leads to a pronounced broadening of the Raman bands and the peak intensity tails off in the luminescence background. Band modifications from unshocked oligoclase to diaplectic plagioclase in Chassigny are also documented by the 100% increase of the full width at half maximum (FWHM) of the bands 483 and 510 cm^{-1} . For the diaplectic plagioclase characteristic Raman spectra are still observable, but bands shift to 270, 475, 515 and 585 cm^{-1} . The tendency of peak broadening and intensity reduction continues during the shock transformation from

plagioclase to maskelynite. Minor bands dwindle in the luminescence background. The prominent plagioclase peaks of 483 and 510 cm^{-1} shift to 475 and 515 cm^{-1} . Finally, peak broadening leads to a uniform Raman band at 505 cm^{-1} . Correspondingly, the Raman band at 575 cm^{-1} shows a higher intensity and a slight shift to higher wave numbers at 590 cm^{-1} (Fig. 1).

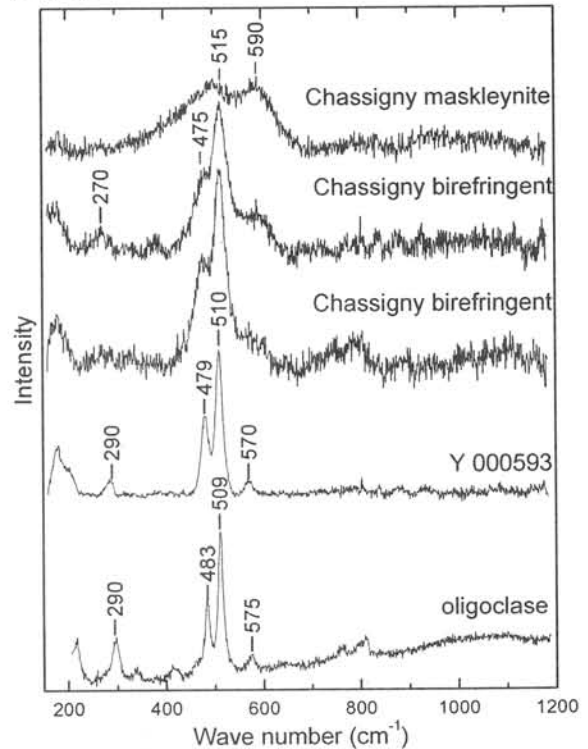


Fig. 1 Raman spectra of plagioclase from unshocked oligoclase (Ytterby, Sweden) and weakly shocked plagioclase of Y 000593 (5-14 GPa), moderately shocked plagioclase, and maskelynite from Chassigny (>26 GPa), showing the transition from plagioclase to maskelynite.

In Fig. 2 the Raman spectra of maskelynite and plagioclase glass are plotted in the order of increasing equilibration shock pressures determined by [2, 3]. The maskelynite spectra with a characteristic double band and high intensities at 505 and 590 cm^{-1} are recorded in Chassigny, Shergotty, Zagami, EET 79001, Dhofar 019, and ALH 84001, i.e., in maskelynite of all investigated Martian meteorites shocked between 25 and 40 GPa. Similar spectra additionally showing broad Raman bands at ~ 800 and ~ 1000 cm^{-1} were previously reported for maskelynite of Shergotty [5]. In our measurements these bands could not be identified unequivocal due to the high luminescence background. In Chassigny and Dhofar 019 the Raman spectra of maskelynite show slightly different positions reflecting the

different An-content of plagioclase in both meteorites (Chassigny, An_{29} ; Dhofar 019, An_{68} ; Fig. 2). For ALH84001, the relative intensity of the Raman band at 505 cm^{-1} is high compared to 590 cm^{-1} . The reduced intensity of the Raman band at 590 cm^{-1} relative to Raman band at 510 cm^{-1} seems to be indicative of strong shock metamorphism above 35–40 GPa. Raman spectra obtained from maskelynite in DaG 476, SaU 005, Los Angeles, QUE 94201, Y-793605, and LEW 88516 document the increase of 505 cm^{-1} peak relative to 590 cm^{-1} peak (Fig. 2).

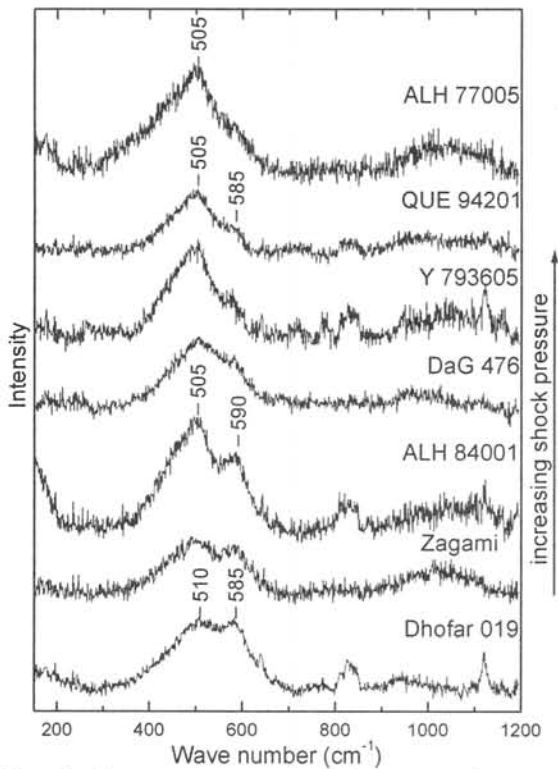


Fig. 2 Raman spectra of maskelynite and normal plagioclase glass (ALH 77005) in Martian meteorites. Spectra are plotted with increasing equilibration shock pressure determined by [2, 3].

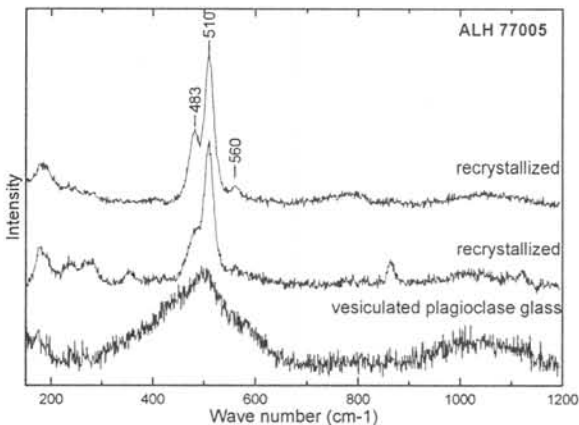


Fig. 3 Raman spectra of plagioclase glass and recrystallized birefringent rim in ALH77005.

In ALH77005, normal plagioclase glass is often surrounded by a recrystallized plagioclase rim which displays undulatory extinction. The Raman spectra

recorded from these phases allow to distinguish different stages of back transformation from glass to birefringent plagioclase (Fig. 3). With increasing degree of recrystallization the broad Raman band at 505 cm^{-1} which is characteristic for the vesiculated plagioclase glass separates in two sharp Raman bands at 483 and 510 cm^{-1} with FWHM comparable with weakly shocked plagioclase in Nakhilites. Similar to the weakly shocked Nakhilites, the Raman band 575 cm^{-1} for unshocked plagioclase, shifts to lower wave numbers in the recrystallized rim.

Conclusion: A systematic variation of Raman spectra could be recorded, documenting the shock induced transformation from plagioclase to diaplectic plagioclase glass (maskelynite) and normal plagioclase glass. Modified Raman bands in plagioclase of all investigated Nakhilites with respect to unshocked oligoclase furthermore indicate that all Martian meteorites experienced at least some degree of shock metamorphism.

For Y-793605 no data of the refractive index from plagioclase are available, but Raman spectra indicate a high equilibration shock pressure above 35–40 GPa. The obtained Raman spectra of maskelynite in Chassigny correspond to vibrational Raman spectra of experimentally shocked oligoclase above 32 GPa [6].

In the combined study of shock induced reduction of the refractive index in plagioclase [2, 3] and MRS investigations we could demonstrate that Raman spectra of shocked plagioclase and maskelynite show characteristic variations with progressive shock metamorphism. This calibration could possibly be used in future space missions for in situ identification of different shock stages. The usefulness of in situ Raman analysis for planetary landers has been discussed first by [7]. Since lander and rover got increasingly important instruments in solar system exploration, remote Raman systems are currently developed [8]. However, further work is needed to constrain a shock pressure calibration based on MRS on plagioclase normative phases.

Acknowledgements: The authors gratefully acknowledge the generous supply of the samples by the Natural History Museum, London the NASA Meteorite Working Group, Museum National d’Histoire Naturelle, Paris, the Max-Planck-Institut für Chemie, Mainz, Institute of Geophysics and Planetary Physics, Los Angeles, National Institute of Polar Research, Tokyo and the finder of DaG 476.

References: [1] Nyquist L. et al. (2001) *Space Sci. Rev.*, 96, 105–164. [2] Fritz J. et al. (2002) *LPSC XXXIII*, #1504. [3] Fritz J. et al. (2003) *LPSC XXXIV*, #1335. [4] Stöffler D. et al. (1986) *GCA*, 50, 889–903. [5] Chen M. and El Goresy A., (2000) *EPSL*, 179, 489–502. [6] Heymann D. and Hörz F., *Phys. and Chem. of Minerals*, 17, 38–44., [7] Stopar J.D. et al., (2003) *LPSC XXXIV*, #1450. [8] Wang et al., (1995) *JGR* 100, 21189–21199.

Chemical Composition of Individual Micrometeorites collected from Antarctic Ice

Yuusuke Fukushi¹, Yuji Tazawa², Takaaki Fukuoka¹, Yuko Saito³
and Toru Yada⁴

¹Department of Environmental Systems, Faculty of Geo-Environmental Science, Rissho University, Kumagaya 360-0194, Japan

²Department of Physics and Astronomy, Graduate School of Science, Kyoto University, Kyoto 606-8502, Japan

³Radio Isotope Laboratory, College of Science and Engineering, Aoyama Gakuin University, Sagamihara 229-8551, Japan

⁴Department of Earth and Planetary Science, University of Tokyo, Tokyo 113-0033, Japan

Introduction

Micro particles of cosmic origin collected from the Earth have been investigated as one of the important components of the Solar System for more than a century [e.g., 1, 2]. They generally have been affected more or less by heating during the Atmospheric entry and weathering after the settling on the Ground or the Deep sea floor. They lost their features inherited until the entry, and typical of them are fully molten droplets called "Cosmic Spherules (CSs)" [2]. Scarcely affected extra-terrestrial particles were mass-collected from the Stratosphere [3, 4] and the Polar Regions [5, 6, 7], typical of which are fragile aggregates of chondritic constituents, called "Interplanetary Dust Particles (IDPs)" thought as of cometary origin, and "Antarctic Micrometeorites (AMMs), especially, Unmelted Micrometeorites (UMMs)". AMMs have been examined widely in recent years [8, 9, 10, 11]. The UMMs may include unique samples of pristine, fragile, and weak-bound masses unknown in either IDPs or microscopic constituents of conventional meteorites.

Instrumental neutron activation analysis (INAA) is one of the most effective means to measure abundances of many elements of a single microscopic sample (smaller than 0.1 mm in size or 1 μ g in weight) in quantitative, simultaneous, and non-destructive ways. So far, we have been studying chemical compositions of individual AMMs and Deep sea Spherules (DSs) by means of INAA [11, 12, 13, 14]. We report here recent INAA results of AMMs.

Samples

AMMs studied in this work are ten stony type spherules (SSs) provided by National Institute for Polar Research (NIPR), which were collected from the bare ice around the N7 point (68°55.3' S, 39°51.0' E) near Tottuki Point on the Soya Coast by JARE-41 in 2000[15]. Assortments and preliminary investigations of the AMM collection have been also performed by the AMM initial examination team organized by NIPR.

INAA

INAA were performed on the individual MMs and tiny chips

of standard materials; i.e., glass made from a geological standard rock sample, JB-1, for lithophile elements (LPEs: Na, Mg, Al, Ca, Sc, Ti, V, Cr, Mn, Fe, Co, La, Ce, Sm, Eu, Yb, Lu, etc.) and metal wire, Al-Au (IRMM-530) and Pt (SRM- 680a) for siderophile elements (SPEs: Au, Ag, Ir, Os, etc.). Each of the samples was weighed by an electro micro-balance prior to the INAA. The procedures were applied correspondingly to [14].

INAA for short half-life nuclides: Each of the MMs and the standards was heat-sealed in each small (ca. 2 x 2 mm) bag made with ultra pure polyethylene sheet and irradiated by neutron for 10 min at 2×10^{13} neutrons/cm²/sec in a pneumatic pipe PN-3 of the reactor JRR-3M, Japan Atomic Energy Research Institute (JAERI). The first count series were done individually for 400 sec, after 2~10 min cooling, using a gamma-ray counting facility at PN-3. The second count series were done individually for 1000 sec at several hours after the first series using a facility at the Inter-University Laboratory for the Joint Use of JAERI Facilities, Research Center for Nuclear Science and Technology (RCNST, Tokai Branch), University of Tokyo. In these procedures, Na, Mg, Al, K, Ca, Ti, V, Mn, and Dy are determined.

INAA for long half-life nuclides: After the end of the SN series mentioned above, the samples were picked out from the polyethylene bags and encased again individually in ultra-pure synthetic quartz vials. Then they were irradiated again by neutrons for 100 hr at 1×10^{14} neutrons/cm²/sec in a hydraulic rabbit irradiation facility HR-1 of the JRR-3M. After the irradiation, each of them was unsealed and put on a small plastic plate for setting into a well type detector. They were counted sequentially according to the half-lives and activities of nuclides used to determine abundances of elements, e.g., (Na, K), Cr, Fe, Sc, rare earth elements (REEs: La, Ce, Nd, Sm, Eu, Tb, Yb, Lu), SPEs (Co, Au, Ir, Os), etc., using gamma-ray counting facilities of the Aoyama Gakuin University. Counting durations and cooling times were about for 2~12 hours after 4~8 days (1st sequence), for 6~24 hours after 2~3 weeks (2nd sequence), 1 day~1 week after more than 1 month (3rd sequence), respectively.

Results

Results of INAA, *i.e.*, abundances of 16 elements, are listed together with their weights in Table 1. Unfortunately, NS7 was lost during sample preparation for the second irradiation, therefore the long half-life nuclides, *e. g.*, Cr, Fe, Sc, REEs, SPEs, *etc.*, could not be determined. All the MMs analyzed here are confirmed to be S-type MMs; *i.e.*, (1) in all the MMs K and Dy are not detected, (2) except for SPEs and Na, abundances of elements (relative to Cl) are distributing around 1 within a range between 0.25 and 3.5, (3) in especial, those of N15 and NS5 agree in 15 elements except Au, (4) and also ND7, NA6, NO7, and NR6 show similar abundance.

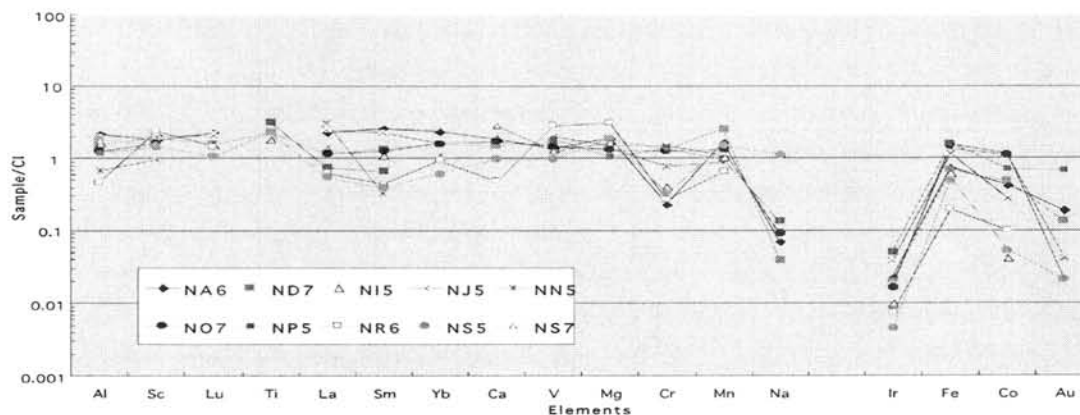
References: [1]Nordenskjöld N.A.E. (1874) Philos. Mag. ser.

4, 48, 546-547. [2]Murray J. and Renard A.F. (1883) Proc. Roy. Soc. Edinburgh 12, 474-495. [3]Brownlee D.E. *et al.* (1976) NASA Tech. Mem. TMX-73152, 1-42. [4]CDPET (1981-1996) Cosmic Dust Catalog, NASA/JSC, Vol. 1-16. [5]Maurette M. *et al.* (1986) Science, 233, 869-872. [6]Maurette M. *et al.* (1991) Nature, 351, 44-47. [7]Nakamura T. *et al.* (1999) Antarct. Meteorite Res., 12, 183-198. [8]Noguchi T. and Nakamura T. (2000) Antarct. Meteorite Res., 13, 285-301. [9]Nakai I. *et al.* (2000) *ibid.* 302-310. [10]Osawa T. *et al.* (2000) *ibid.* 322-342. [11]Fukuoka T. *et al.* (1999) Antarct. Meteorites XXIV, 24-25. [12]Fukuoka T. *et al.* (2000) Antarct. Meteorites XXV, 10-11. [13]Tazawa Y. *et al.* (2003) Int. Sym. Evolution of solar System Materials, Sept. 3-5, 138-139. [14]Fukuoka T. and Tazawa Y. (1996) Antarct. Meteorites XXI,33-34. [15]Iwata N. and Imae N. (2002) Antarct. Meteorite Res., 15, 25-37.

INAA Results of Abundances of Elements in Antarctic Micrometeorites										
Sample Name	NA6	ND7	N15	NJ5	NN5	NO7	NP5	NR6	NS5	NS7
Weight μg	6.4	20.5	14.9	4.7	5.1	4.5	10.8	13.3	24.4	7.3
Element										
Na	% 0.062(21)	0.014(36)	0.574(4)	-	-	0.050(30)	0.073(12)	-	0.565	-
Mg	% 19.0(6)	18.5(6)	17.7(6)	15.0(7)	13.4(7)	13.0(7)	10.6(6)	30.6(6)	18.8(6)	16.2
Al	% 1.93	1.34	1.43	1.75	0.586	1.10	1.05	0.415	1.64	1.57
K	% -	-	-	-	-	-	-	-	-	-
Ca	% 1.7(16)	1.4(10)	1.8(11)	-	-	1.6(19)	-	0.45(21)	0.92(12)	2.6(13)
Sc	ppm 10.4	11.2	131	11.6	5.68	9.55	8.39	13.9	8.84	*
Ti	% -	0.1(20)	0.08(25)	-	-	-	0.14(14)	-	0.1(10)	-
V	ppm 77.2(5)	93.1	78.4(4)	115(4)	80.3(4)	83.7(5)	103	164	54.7(4)	71.0(5)
Cr	ppm 613	3540	1090	3900	2120	3390	3710	726	899	*
Mn	% 0.331	0.51	0.304	0.217	0.181	0.263	0.197	0.134	0.296	0.207
La	ppm 0.540(4)	0.276(8)	0.314(9)	0.594(5)	0.718(6)	0.27(13)	0.18(15)	0.15(12)	0.13(17)	*
Sm	ppm 0.385	0.199	0.161	0.332	0.049(10)	0.188	0.099(4)	0.065	0.058(5)	*
Dy	ppm -	-	-	-	-	-	-	-	-	-
Yb	ppm 0.383(4)	0.256(5)	0.174(9)	0.27(10)	-	0.263(9)	-	0.154(5)	0.10(12)	*
Lu	ppm 0.056(7)	0.038(8)	0.038(11)	0.052(17)	-	-	-	0.036(8)	0.026(12)	*
Fe	% 14.07	13.06	12.16	22.03	26.53	29.18	30.43	3.77	9.54	*
Co	ppm 211	247	21.1	140	566	568	359	50.4	27.1	*
Ir	ppb 11	9.6	5.0	18	9.0	8.1(4)	25	3.7	2.2	*
Au	ppb 27	19(4)	-	-	6(12)	3(26)	97	-	3(24)	*

Note Experimental errors (% errors) larger than 3% are shown in parentheses at the end of values.

Cl Normalized Abundances of Antarctic UMMs



Magnetization of the impact-generated plasma and shock induced magnetization under the pressure 5, 10 and 20 GPa. Minoru FUNAKI¹ and Yasuhiko SYONO^{2, 1} National Institute of Polar Research, Japan, ²Institute for Materials Research, Tohoku University, Japan

Introduction

A collision under the ultra-hyper velocity induces the magnetization in the shocked samples, as reported by Pohle et al. (1975) and Cisowski and Fuller (1978). However, the reason was not well understood. An impact-generated magnetic field proposed by e.g. Crawford and Schultz (1991) is the most plausible acquisition mechanism, but the induced field during shocks is only several tens nT, which may not be enough intensity for remagnetization of the high coercive force magnetic grains.

We carried out the experimental study in order to confirm the remagnetization in the weak magnetic field by impact-generated plasma using samples consisting of Co precipitated (mostly single domains) in Cu matrix. One sample (inner sample) of 1cm in diameter was set in a sample holder at 6mm depth from the collided surface and another one (outer sample) was set beside 2mm from a limb of the surface. A single stage propellant gun was employed and the shock pressures to 5, 10 and 20GPa were loaded to the sample holder. The samples were demagnetized by AF field to 100mT prior to the shock loading. The magnetic field around the sample holder was reduced to 0.0077mT by a mu-metal magnetic shield pipe.

Experiments

In case of the inner samples, the magnetization in the range of 5.20×10^{-4} to 1.61×10^{-3} Am²/kg after AF demagnetization increased to 3.86×10^{-3} , 3.47×10^{-3} and 1.38×10^{-2} Am²/kg (7.42, 2.15 and 21.33 times) by shocks to 5 GPa, 10 GPa and 20 GPa respectively. The directions after shock loading scattered in the low inclination, perpendicular against shock direction. The outer samples showed almost same intensities (9.35×10^{-4} to 1.74×10^{-3} Am²/kg) after AF demagnetization and they increased to 9.06×10^{-4} , 2.92×10^{-3} and 3.39×10^{-3} Am²/kg (1.03, 1.68 and 3.58 times) after shocks to 5 GPa, 10 GPa and 20 GPa respectively (Fig. 1). Their directions scattered widely with the high to low inclinations. The outer sample shocked to 5GPa showed almost no change of the intensity and direction. Namely, the inner samples acquired the magnetization efficiently than the outer samples.

When the inner samples were divided into 8 subsamples, their intensities were increased to 1.2×10^{-2} to 1.3×10^{-1} Am²/kg for the samples shocked to 5, 10 and 20 GPa, but they were demagnetized smoothly to less than 1/20 up to 100mT. The directions scattered widely, but the low inclination was dominant after the demagnetization. On the contrary, the divided samples of the outer samples shocked to 5 GPa, 10 GPa and 20 GPa did not

drastically change the intensities compared with their parents. The intensity demagnetization curves for many subsamples were much stable (Fig. 2) and the directions were also stable in many cases. Namely, the outer samples seem to not be acquired to the strong magnetization by shocks, keeping the magnetization after AF demagnetization.

Discussion

From these experimental results, the outer samples did not acquire the significant magnetization, even if the distance was 2mm from the edge of collided surface. However, the inner samples located 6mm deeper from the collided surface acquired strong magnetization. Therefore, we concluded that the magnetization by the magnetic field resulting from the impact-generated plasma was minor, but the other phenomena affected strongly the inner samples for the acquisition of magnetization.

Reference

Cisowski, S.M. and Fuller, M. (1978), *JGR*, 83, B7, 3441-3458. Crawford and Schultz (1991), *J. Geophys. Res.* 96, 3, 18807-18817. Pohl, J., Bueil, U. And Hornemann, U. (1977), *J. Geophys.* 41, 23-41.

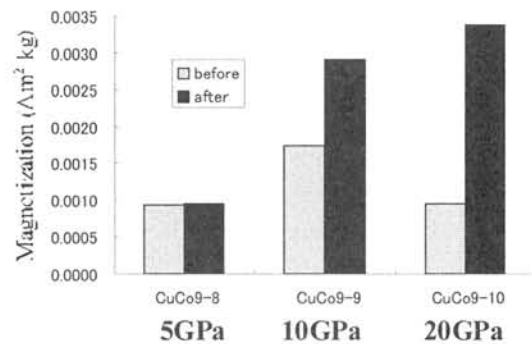


Fig. 1 Intensity changes of the magnetization before and after shocks for the outer samples

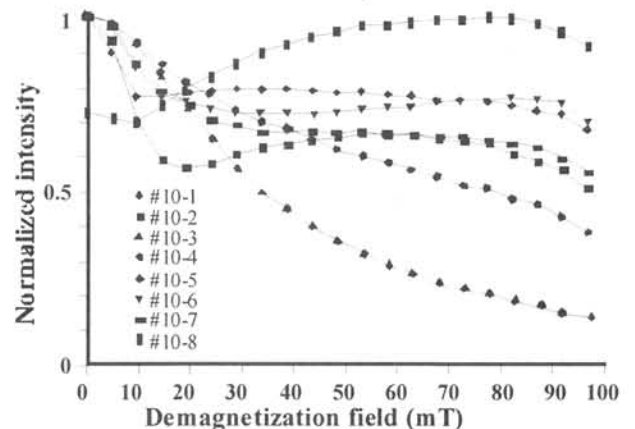


Fig. 2 AF demagnetization curves of the intensity for divided samples #9-10 (20GPa)

Chemical compositions, cathodoluminescence images and oxygen isotopes of FeO-poor isolated olivine grains from the Murchison CM2 chondrite. H. Hiyagon¹ and M. Kimura²,
¹Department of Earth and Planetary Science, Graduate School of Science, The University of Tokyo, Tokyo 113-0033, Japan, ²Faculty of Science, Ibaraki University, Mito 310-8512, Japan.

Introduction:

Forsteritic olivine with bright (blue) cathodoluminescence (CL) often occurs as isolated grains in the matrix in carbonaceous chondrites (CCs), unequilibrated ordinary chondrites (UOCs) and even in R-chondrites. It has high abundance of refractory lithophile elements (RLEs; CaO, Al₂O₃, TiO₂, REEs, etc.) and is also referred to as refractory forsterite. There are two models for the origin of refractory forsterite grains: they formed through direct condensation from the solar nebula [e.g., 1-3] or they formed from chondrule melts [e.g., 4-6]. Recently, Pack et al. [7] proposed a model, in which they formed in a melt directly condensed from the nebula. In order to better understand the origin of FeO-poor isolated olivine grains, we conducted chemical, CL, and O-isotopic studies on isolated olivine grains separated from the Murchison CM2 chondrite.

Sample preparation and analytical conditions:

A 9.85 gram piece of Murchison meteorite was freeze-thaw disaggregated. Isolated olivine grains, both FeO-poor and FeO-rich, as well as chondrules were handpicked under an optical microscope, fixed on a slide glass (25mm in dia.) with epoxy together with San Carlos olivine and synthetic forsterite for O-isotope standards, and polished together. The samples were first observed under an optical microscope, then carbon-coated and examined with a SEM (JEOL-5310) -EDS (Oxford Co.). Cathodoluminescence (CL) images were observed using a MiniCL (Gatan Inc.) attached to the SEM. Oxygen isotopes were analyzed with a CAMECA ims-6f ion microprobe using analytical conditions similar to those described in [8]. Beam size was about 10 μ m in diameter, so that spinel inclusions (typically <20 μ m in size) found in some of the isolated olivine grains could be analyzed as single phases. The samples were further analyzed with an EPMA for more precise determinations of minor element abundances in olivine (Ca, Al, Ti, Cr, Mn, etc.).

CL images and chemical compositions:

All the FeO-poor isolated olivine grains show bright CL emissions and have high abundances of RLEs (e.g., 0.4-0.8 wt% CaO), consistent with previous reports. Some grains show irregular-shaped bright CL regions in the center surrounded by darker CL regions in the margin. The boundary is very sharp. A good correlation is observed between the CL intensity and chemical compositions: the bright

regions are CaO-rich (0.4-0.8 wt%) while darker CL regions are CaO-poor (\leq 0.2 wt%). Some of the isolated olivine grains also contain euhedral to subhedral spinel grains.

Oxygen isotopes:

We have measured O-isotopes, so far, in the four isolated olivine grains: MCFH-04, -06, -18 (Fig.1) and -24 (not shown here). All of them have irregular-shaped bright CL regions in the core and dark CL regions surrounding them. Three of them (MCFH-04, -18 and -24) contain spinel in the bright CL regions. Oxygen isotopic compositions were measured for all the phases: bright CL olivine, dark CL olivine, and spinel.

The results are shown in Fig.2. Also shown for comparisons are terrestrial fractionation (TF) line and carbonaceous chondrite anhydrous minerals (CCAM) line. All the data fall in a rather narrow region approximately on the CCAM line with $\delta^{17}\text{O}$ and $\delta^{18}\text{O} = -9\pm 3$ and -6 ± 2 permil, respectively. No difference is observed in O isotopes among the bright CL regions, dark CL regions and even spinel grains. Only spinel in MCFH-24 shows a slightly ¹⁶O-rich composition than the host olivine, but the difference is only marginal and it disappears if we take 2-sigma errors.

The cause for the complicated CL structures is not well known, but they cannot be produced by a simple secondary diffusion and primary crystallization processes because boundaries are very sharp. Some kind of partial melting events may be necessary; the dark CL regions might have lost their RLEs by partitioning of these elements into other phases (possibly, a melt phase). Indistinguishable O isotopic compositions among bright and dark CL regions of olivine and spinel suggest that all these phases formed from a single O-isotopically homogeneous reservoir. Spinel is not a relict but formed *in situ* with olivine.

References:

- [1] Grossman L. and Olsen E. (1974) *GCA*, 38, 171-187.
- [2] Steele I. M. (1989) *GCA*, 50, 1379-1395.
- [3] Weinbruch S., Palme H. and Spettel B. (2000) *Meteorit. Planet. Sci.*, 35, 161-171.
- [4] McSween H. Y. Jr. (1977) *GCA*, 41, 411-418.
- [5] Jones R. H. (1992) *GCA*, 56, 467-482.
- [6] Jones R. H., Saxton J. M., Lyon I. C. and Turner G. (2000) *Meteorit. Planet. Sci.*, 35, 849-857.
- [7] Pack A., Yurimoto H. and Palme H. (2004) *GCA*, 68, 1135-1157.
- [8] Hiyagon H. and Hashimoto A. (1999) *Science*, 238, 828-831.

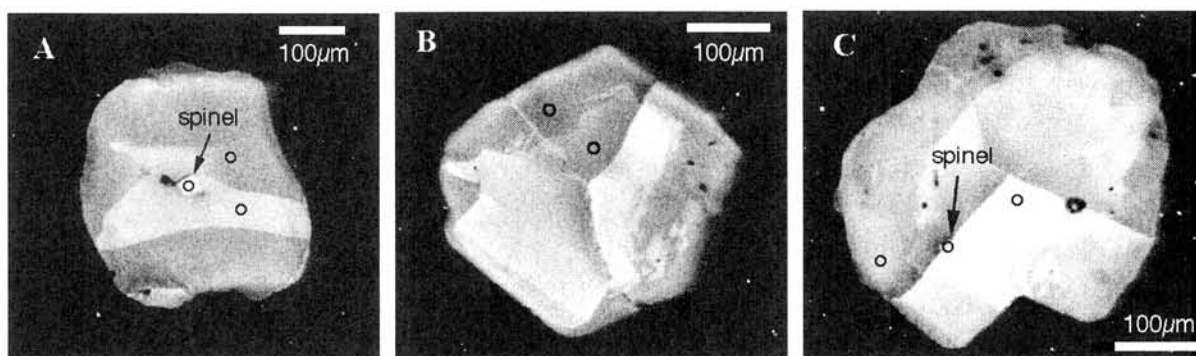


Fig.1 Cathodoluminescence (CL) images of some isolated olivine grains from Murchison: (A) MCFH-04, (B) MCFH-06 and (C) MCFH-18. Very bright regions with irregular boundaries are noticeable in these olivines. Spinel grains exist in MCFH-04, -18 and -24 (not shown here). Ion microprobe analysis spots are shown by open circles (about 10 μ m in diameter).

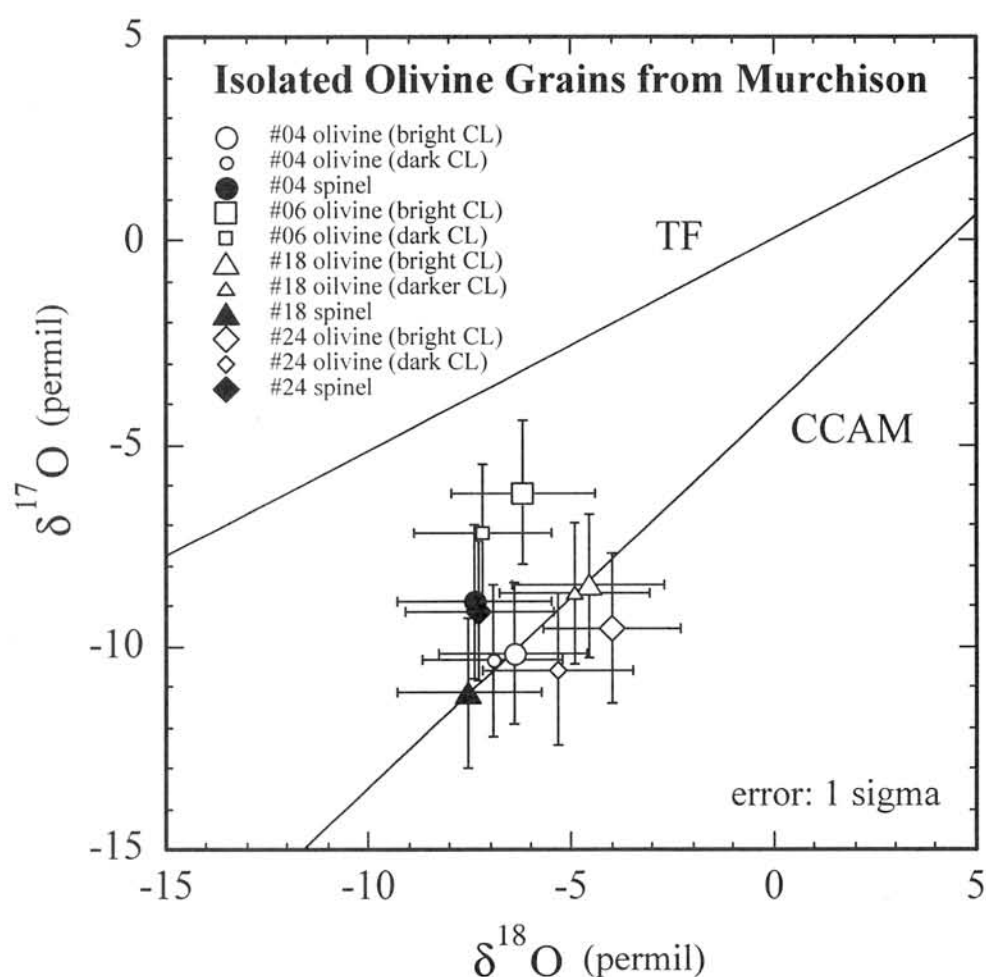


Fig.2 Oxygen isotopic compositions of olivine with different CL brightness and spinel inclusions in four isolated olivine grains from Murchison.

Major-element Trend for Shergottite Melts and Their Source Materials. Y. Ikeda¹ and G. Shimoda², ¹Ibaraki University, Mito 310-8512, ²Geological Survey of Japan, Tsukuba 305-8567.

Shergottite Melt Trend:

The major-element compositions of the parental and fractionated melts for the shergottites have been estimated by many authors using the follow methods. (1) The bulk compositions of some shergottites represent the parental magmas on an assumption that cumulus phases or xenocrysts are absent or minor in them. (2) For the case that cumulus phases or xenocrysts are common, the parent magmas are estimated by subtraction of them from the bulk compositions. (3) The groundmass (or mesostasis) in some shergottites may represent the fractionated melts. (4) Magmatic inclusions occur in some SNC meteorites, and they are used to obtain the initial trapped melts. (5) Parental melt compositions are calculated by using the partition coefficients between the constituent minerals and the coexisting melts, and the experimental results are also used.

The estimated melt compositions for shergottites are shown in Fig. 1, which indicates that all shergottites form a Shergottite Melt Trend. The melts for olivine(Ol)-phyric shergottites are more magnesian than the basaltic shergottites, suggesting that the basaltic shergottites are late differentiates of the Ol-phyric shergottites. Otherwise, both have derived from the same source materials with different degrees of the partial melting. The later hypothesis may be plausible, because their crystallization ages range widely from 150 to 600 m.y. The lherzolitic shergottites seem to have formed as cumulative rocks. from melts similar to the Ol-phyric shergottite melts or their differentiates.

Comparison of melts for nakhlites and chassignite to the Shergottite Melt Trend:

The major-element compositions of the parental and fractionated melts for nakhlites and chassignite are compared with the Shergottite Melt Trend. The chemical compositions of melts for chassignite are well coincident with the Shergottite Melt Trend, although the melts for nakhlites are more depleted in Al₂O₃ and more enriched in FeO, indicating that the nakhlite melts do not coincide with the Shergottite Melt Trend.

Comparison of terrestrial basalts, lunar basalts and eucrites with the Shergottite Melt Trend:

The FeO contents of the Shergottite Melt Trend are high, and the Al₂O₃ contents are low in comparison to terrestrial basalts and kamatiites, indicating that the terrestrial rocks are dissimilar to the shergottite melts. Lunar marie basalts with low TiO₂ and eucrites are rather similar to the Shergottite Melt Trend, although their alkali contents are too low .

Source materials for the Shergottite Melt Trend:

The major-element composition of the source materials for the Shergottite Melt Trend is estimated by the following two constraints. (1) The parental magmas of some Ol-phyric shergottites are the most magnesian and they are situated in the olivine liquidus field of the Ol-Qz-Pl pseudoternary system. Therefore, the compositions of the source materials should be between the parental magmas for magnesian Ol-phyric shergottites and the olivine residue. (2) The parental magma of Shergotty has a complimentary trace-element pattern to that of Nakhla, suggesting that they have been derived by remelting the same source at different times [1]. As the source materials of the parent magmas for nakhlites may have contained spinel or garnet instead of plagioclase [2], the remelting may take place at deeper mantle for nakhlite melts than the melts for shergottites.

A plausible source material for the shergottites is estimated under the above -stated two constraints on an assumption that the original source materials is very similar to the composition of Mars mantle (+crust) obtained by [3]. It is obtained as a crossing point of two lines in the Ol-Qz-Pl pseudoternary system. First is a tie line between the parental magmas of the magnesian Ol-phyric shergottites and a relic olivine. The relic olivine is taken to be the most magnesian phenocrystic olivine in Ol-phyric shergottites. Second is an extension line of the Mars mantle connecting with the parental magmas of nakhlites.

The source material obtained is a depleted lherzolitic peridotite with Mg/(Mg+Fe) atomic ratio around 0.78, and the parental melts for shergottites are produced by partial melting of the source material with various degrees.

References:

- [1] McSween H.Y. (1994). 92, 757-779. [2] Treiman A. H. (1986), GCA,50,1061-1070. [3] Wanke H. and Dreibus G. (1988) Phil. Trans. R. Soc. Lond. A325, 545-557.

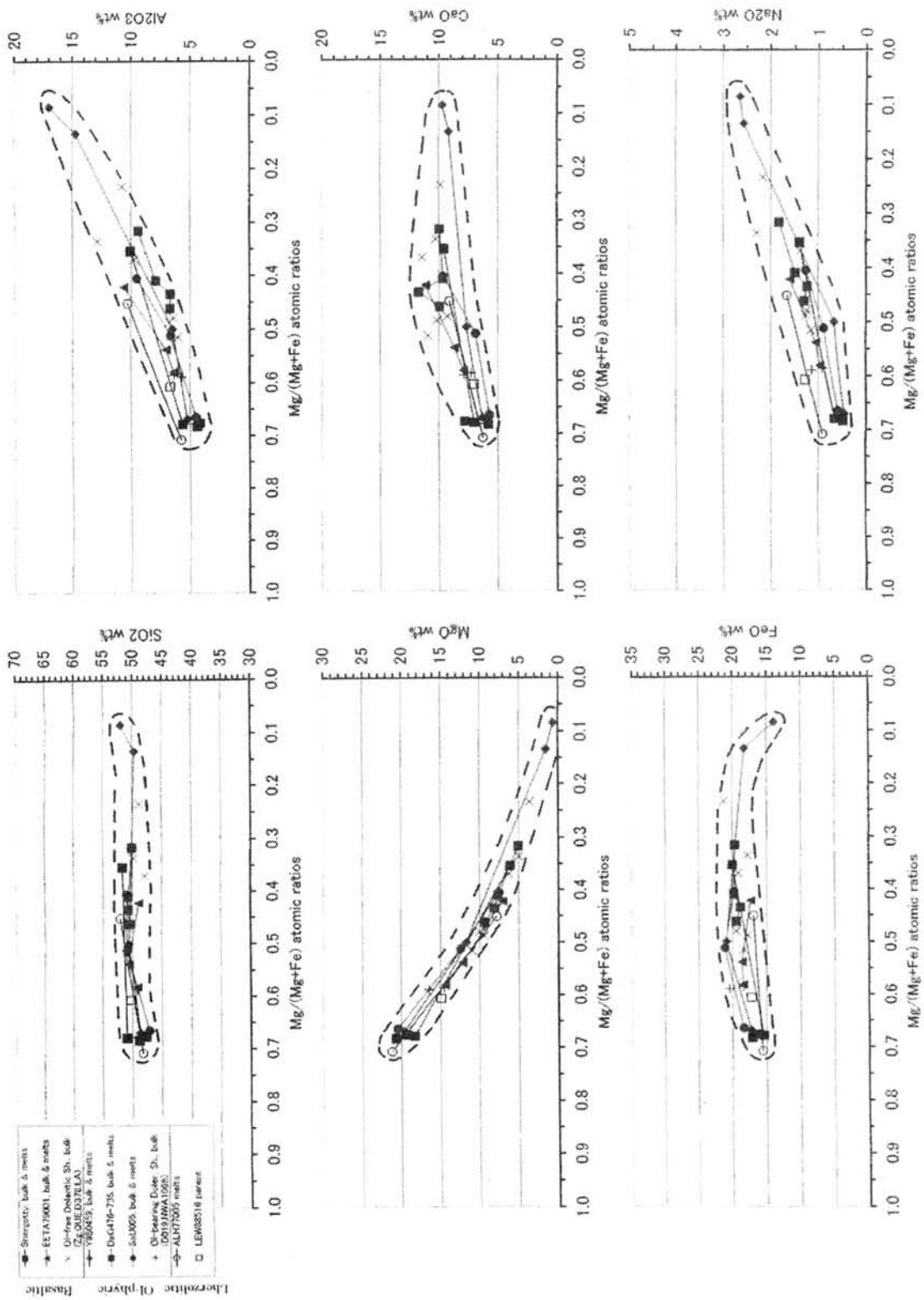


Fig. 1. Shergottites Melt Trend

An experimental study of the phase equilibrium using a parent magma composition formed nakhlites. N. Imae. National Institute of Polar Research, 9-10, Kaga 1-chome, Itabashi-ku, Tokyo 173-8515, Japan.

Introduction: Nakhlites are one class of Martian meteorites petrographically classified into clinopyroxenites. The most characteristic is that these are a cumulate igneous rock, suggesting that nakhlites experienced a fractional crystallization between solid and melt in lava flow or sill under the condition of the Martian gravity field. Parent magma compositions of nakhlites have been obtained [1-3]. However, the experimental studies of the phase relationship using a parent magma composition have not been sufficiently carried out [4]. I examined it using the "NIM" composition obtained by [1] in detail, which is important in understanding the crystallization processes of the parent magma formed nakhlites.

Experiments: A gas mixing vertical furnace using H₂ and CO₂ newly set up at NIPR was used for the experiments. Glasses with the composition of "NIM" [1] were prepared using the reagent grade powder: SiO₂ (46.46wt%), MgO (5.62wt%), FeO (22.4wt%), CaO (9.24wt%), Al₂O₃ (7.9wt%), TiO₂ (3.93wt%) Na₂O (1.42wt%), and K₂O (1.57wt%). Powdered glass was pressed into the pellet, held with Pt-wire loop of 0.2 mm in diameter, and put into the furnace under the FMQ condition at fixed temperature. 13 among 23 experiments were successfully carried out at temperatures ranging from 1010 to 1265 °C for durations ranging from 13 to ~100 h. 10 runs was failed because the droplet was separated from Pt-wire loop during the run or the duration is too short. Each run was finished by putting a charge into a water bath, after the charge was pulled out from the furnace. The charges were mounted into epoxy resin, and polished sections were made. These were studied using an optical microscope, an electron probe microanalyzer (JXA-8200) and a secondary electron microscope (JSM-5900LV). Modal abundances of constituting minerals and glass were determined by the point counting method using grid under the images on a display monitor.

Results: The phase relationship of "NIM" composition is summarized in Fig. 1. A run product is shown in Fig. 2. The first phase appeared below 1240 °C, corresponding to liquidus temperature, is euhedral abundant small titanomagnetites of 2 μm in size (Fig. 1 and Fig. 2). The TiO₂ content is 20 ~ 30 wt% (Fig. 3). The second phase appeared below 1140 °C is euhedral abundant small augites of 2~5 μm in size. The composition is En₁₄₋₃₇Fs₂₁₋₅₅Wo₃₀₋₄₂ (Fig. 3 and Fig. 4). The third phase appeared below 1130 °C is irregular shaped scarce larger olivines of 10 μm in size. The composition is Fa₅₀₋₇₃ (Fig. 3).

The fourth phase appeared below 1050 °C is plagioclase of rectangular shape. At 1050 °C, the composition is Ab₃₇An₅₆Or₆, and at 1040 °C it is Ab₃₈An₅₅Or₇. Titanomagnetites, augites, olivines and plagioclases in a run are compositionally homogeneous, irrespective of grains. The difference of the crystallization temperature of augite and olivine is small to be 10 °C (Fig. 1). Augites trap smaller sized titanomagnetites of a few μm. Olivines trap larger sized interstitial melts of 20 μm as well as small titanomagnetites. Solidus temperature is 1030 °C.

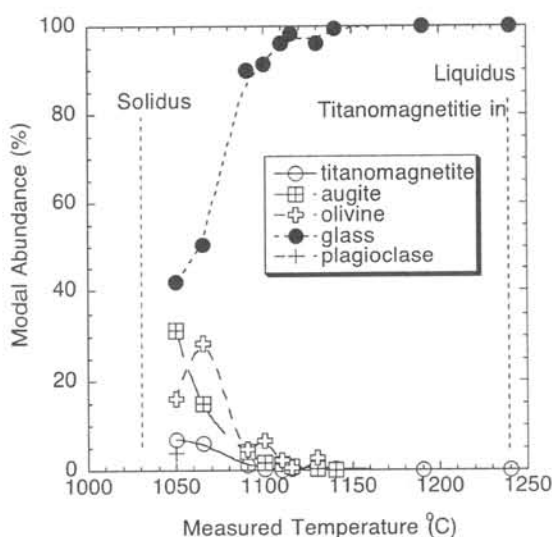


Fig. 1. Modal abundances of run products.

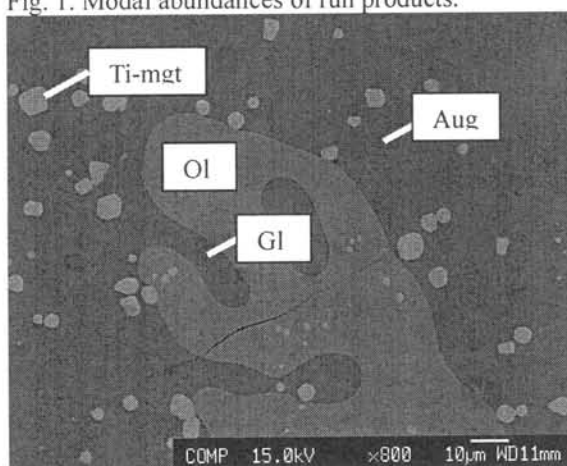


Fig. 2. A run product at 1065 °C and for 93 hr under the FMQ condition. An ameboid large grain including trapped melt is olivine. Bright small grains are titanomagnetite. Small grains are augite. Remains are glass.

In runs with high degree of melting (> 1090 °C), the position of formed crystals in the pellet is deviated to one side periphery of the pellet,

suggesting that these crystals are accumulated into these areas due to the gravity.

Discussions: There are common characteristics between the run products in some runs and nakhlites: morphologies, constituting minerals and the compositions of these. The crystallization of three cumulative minerals of augites, olivines and titanomagnetites has been reproduced. The composition of augites is $En_{34-37}Fs_{19-26}Wo_{39-42}$ at the run on the condition of 1065–1130 °C. It is nearly identical with the composition of augite phenocryst cores in nakhlites ($En_{36}Fs_{25}Wo_{39}$) [5]. Therefore this temperature region corresponds to main crystal growth temperature after the nucleation at higher temperature. At the similar temperature range, olivine crystallized, and the composition was Fa_{50-60} , which is more magnesian compared with those of nakhlites. Olivines in nakhlites experienced diffusional modification during the cooling.

The Fe/Mg partitioning coefficients between augite and melt, and between olivine and melt are $K_D^{aug/melt}=0.22$ [6] and $K_D^{ol/melt}=0.33$ [7], respectively. Both partition coefficients obtained from experiments are independent of temperature, nearly consistent values with reference data (Fig. 5), suggesting that experiments are under the equilibrium.

Trapped melts in olivines observed in many runs may correspond to the rounded vitrophyric inclusion in nakhlites [1], though augites and titanomagnetites have not been formed in the inclusion in the run products, due to the experiments at fixed temperature. It is thus necessary to carry out the cooling experiments in order to test the reproduction of these inclusions. Small titanomagnetite inclusions observed in augites in many runs are also seen in nakhlites.

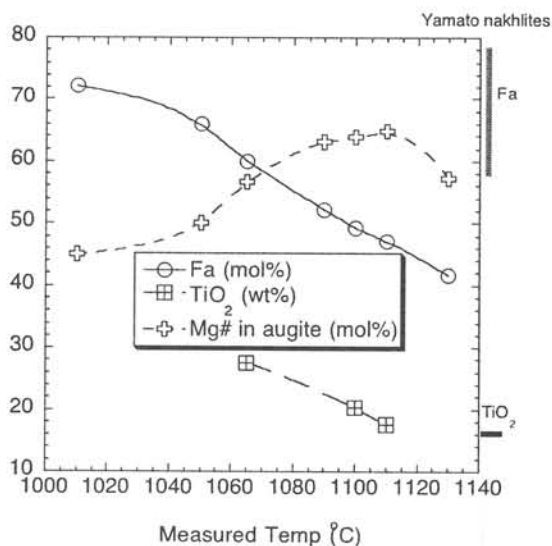


Fig. 3. The Fa contents of olivines and TiO_2 contents in titanomagnetites for runs. Mg# shows $Mg/(Mg+Fe)*100$ (mol%) in augites. Fa is less ferroan and TiO_2 in titanomagnetites is poorer, in

runs at higher temperature. For reference, the compositions of Yamato nakhlites are shown on the right side of the figure.

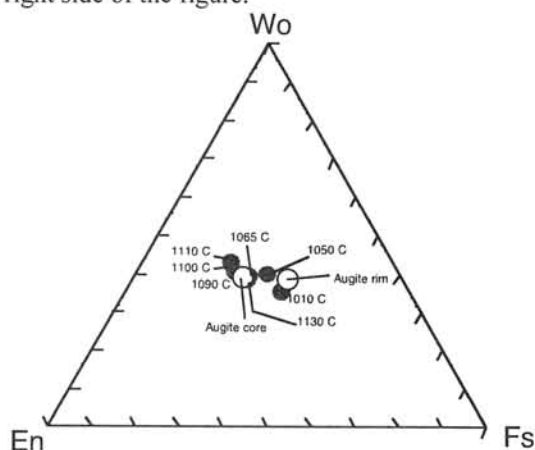


Fig. 4. The composition of augites for products and Yamato nakhlites. The compositions of augites in runs at more than 1065 °C are consistent with that of augite cores in nakhlites.

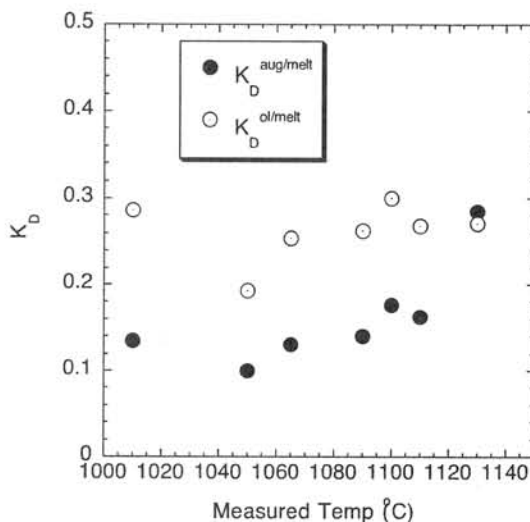


Fig. 5. Observed partition coefficients for products. These are consistent with $K_D^{aug/melt} = 0.22$ [6] and $K_D^{ol/aug}=0.33$ [7].

Acknowledgments: I am grateful to Prof. A. Tsuchiyama in Osaka University and Dr. N. Shimobayashi in Kyoto University for their suggestions for setting up the gas-mixing furnace.

References: [1] Harvey R. and McSween H. 1992. *EPSL*, 111: 467-482. [2] Treiman A. H. 1986. *GCA*, 50, 1061-1070. [3] Imae N. et al. 2003. *LPSC*, XXXIV Abstract#1520. [4] Longhi J. and Pan V. 1989. Proc. 19th Lunar and Planetary Science Conference, 451-464. [5] Imae N. et al. 2003. *AMR*, 16, 13-33. [6] Grove T. L. and Bence A. E. 1977. Proc. 8th Lunar and Planetary Science Conference, 1549-1579. [7] Longhi J. et al. 1978. *GCA*, 42, 1545-1558.

Silicate darkening in CK chondrites: Verification of the cause by vesicular olivine.

Noriko Ishizaki and Kazushige Tomeoka

Department of Earth and Planetary Sciences, Faculty of Science

Kobe University, Nada, Kobe 657-8501, Japan.

Correspondence authors' e-mail address: 031s401n@y03.kobe-u.ac.jp

Introduction:

Most CK chondrites have been thermally metamorphosed to various degrees to yield petrologic types from 4 to 6. A striking feature of the CK chondrites is that their chondrules and matrices show a dark, dusty appearance, when their thin sections are observed in transmitted light. Most previous workers suggested that the silicate darkening resulted from shock metamorphism [1-6], but the true cause of the darkening has long been unknown. It has been thought that Fe-Ni sulfide and metal were mobilized by shock-induced melting and injected into pre-existing fractures in silicates, and resultant opaque fracture fillings caused darkening [5, 6]. However, a recent study of the Kobe CK4 chondrite [7] revealed that it contains abundant unusual olivine in matrix and chondrules, which contains numerous small vesicles and grains of magnetite and pentlandite. The authors suggested that the vesicular olivine resulted from recrystallization of partially melted olivine by shock and it is the principal cause of the silicate darkening in Kobe. We undertook a survey of other CK chondrites that show various degrees of silicate darkening in order to examine whether vesicular olivine is also the cause of their silicate darkening and to determine how vesicular olivine formed. We here present the results of detailed petrographic and scanning electron microscope (SEM) observations of Karoonda (CK4), ALH85002 (CK4), Y693 (CK5) and LEW87009 (CK6) chondrites.

Petrography and Mineralogy:

Karoonda and ALH85002 show similar high degrees of silicate darkening, but Y693 shows a lower degree of darkening. Silicate darkening in the three chondrites is observed in both matrix and chondrules, but it is more pronounced in matrix. Chondrule mesostases are distinctly more darkened than phenocrysts. The matrix generally shows heterogeneous darkening and exhibits a mottled appearance; the heterogeneity in the Y693 matrix is especially strong. Darkened silicates are olivine, plagioclase and pyroxene, but olivine shows distinctly stronger darkening than other silicates. Optical microscopy of these three chondrites indicates that olivine grains exhibiting weak to moderate undulatory extinction are common, but olivine grains exhibiting planar fractures are rare. Based on these features, all the three CK chondrites are assigned to shock stage S2, being consistent with

the previous estimate [6, 8].

Backscattered electron images of highly dark regions in the matrices of the three CK chondrites show that vesicular olivine fills interstices of subhedral and anhedral nonvesicular olivine crystals, exhibiting a complex network of veinlets (5-50 μm wide). Vesicular olivine also occurs within mesostases in chondrules, commonly together with plagioclase. The vesicular olivines in the three chondrites exhibit common characteristics, i.e., they contain numerous small spherical vesicles (<0.1-5 μm in diameter) and spherical grains (<0.1-8 μm) of magnetite and pentlandite as well as anhedral grains of plagioclase, low-Ca pyroxene and diopside. There is a tendency that a region having a higher volume proportion of vesicular olivine to exhibit a darker and dustier appearance in transmitted light.

LEW87009, the only CK6 chondrite, has a highly recrystallized granular texture with no discernable chondrules. Branching glassy to microcrystalline shock veins (10-150 μm in width) filled with small globules of magnetite and pentlandite are observed. Compared to the three CK4-5 chondrites described above, LEW87009 shows a much lower degree of silicate darkening. Olivine exhibits almost no darkening. However, in places, plagioclase exhibits noticeable darkening. Backscattered electron imaging shows no vesicular olivine. However, plagioclase grains, which exhibit darkening, contain numerous small spherical vesicles and spherical grains of magnetite and pentlandite. Optical microscopy indicates that this meteorite is assigned to shock stage S3, higher than the three CK4-5 chondrites described above.

Discussion:

Our study has revealed that vesicular olivine occurs pervasively in matrix and chondrule mesostases in Karoonda, ALH85002 and Y693 that exhibit pronounced silicate darkening. Vesicular olivine is particularly abundant in regions of matrix and chondrules that exhibit a high degree of darkening. These characteristics closely resemble those in the Kobe CK4 chondrite [7]. On the other hand, vesicular olivine is totally absent in LEW87009 that exhibits much less darkening than the three chondrites. Curvilinear trails of opaque mineral blebs, which Rubin [6] suggested to be the cause of silicate darkening in CK and ordinary chondrites, are absent or rare in vesicular olivine-rich regions. From these observations, we conclude that

vesicular olivine is the principal cause of the silicate darkening in the Karoonda, ALH85002 and Y693 CK chondrites.

The internal texture of the vesicular olivine closely resembles those of local melts produced in the matrices of experimentally shocked [9, 10] and naturally shocked [11] carbonaceous chondrites. We suggest that the vesicular olivine in CK chondrites formed from melts that were produced from fine-grained olivine in the matrix by shock. The matrix was probably heated heterogeneously upon shock, and so temperatures locally exceeded the melting point of the Fe-rich olivine. Heating must have been instantaneous and followed by rapid cooling, and so the melted materials essentially remained *in situ*. This process caused the heterogeneous distribution of vesicular olivine on the extremely small scales in the matrix. During melting, numerous small vesicles were produced in the melts, and the melts trapped numerous droplets of melted magnetite and pentlandite as well as fragmented grains of other minerals.

The CK chondrites having vesicular olivine (Karoonda, ALH85002, Y693) exhibit light shock effects (e.g., undulatory extinction in olivine) that are consistent with shock stage S2, which is too low to account for shock-induced melting. On the other hand, LEW87009 exhibiting higher shock effects than the three chondrites contains no vesicular olivine. These results appear to be contradictory to our interpretation that the vesicular olivine was produced from shock-induced melts. We suggest that the vesicular olivine was produced by shock at the state where the meteorite was heated to a high temperature. The results of recent shock-recovery experiments on Allende preheated to 600-800°C have indicated that vesicular melts are indeed produced in

interstices of unmelted olivine grains in matrix at peak pressures of 20-25 GPa [12]. The results suggest that the vesicular olivine in CK chondrites was produced in a region (or regions) of the parent body where it was heated to a temperature higher than 600°C and shocked at a pressure lower than 25 GPa. Therefore, mechanical effects on olivine such as fractures and deformation, which currently serve as principal indicators for shock intensities, were relatively minor, but heating was strong enough to cause partial melting of matrix olivine.

References:

- [1] Heymann D. (1967) *Icarus* 6, 189-221.
- [2] Dodd R.T. (1981) *Meteorites—A Petrologic-Chemical Synthesis*. Cambridge Univ. Press, 368pp.
- [3] Ehlmann A.J. et al. (1988) *Proc. Lunar Planet. Sci. Conf. 18th*, 545-554.
- [4] Kallemeyn G.W., Rubin A.E. and Wasson J.T. (1991) *Geochim. Cosmochim. Acta* 55, 881-892.
- [5] Stöffler D., Keil K. and Scott E.R.D. (1991) *Geochim. Cosmochim. Acta* 55, 3845-3867.
- [6] Rubin A.E. (1992) *Geochim. Cosmochim. Acta* 56, 1705-1714.
- [7] Tomeoka K., Ohnishi I. and Nakamura N. (2001) *Meteorit. Planet. Sci.* 36, 1535-1545.
- [8] Scott E.R.D., Keil K. and Stöffler D. (1992) *Geochim. Cosmochim. Acta* 56, 4281-4293.
- [9] Tomeoka K., Yamahana Y. and Sekine T. (1999) *Geochim. Cosmochim. Acta* 63, 3683-3703.
- [10] Kiriyama K., Tomeoka K. and Sekine T. (2000) (abstract). *Meteorit. Planet. Sci.* 35 (Suppl.), A88.
- [11] Ohnishi I. and Tomeoka K. (2002) *Meteorit. Planet. Sci.* 37, 1843-1856.
- [12] Kiriyama K., Tomeoka K. and Sekine T. (2001) (abstract) *Antarctic Meteorites* 26, 55-57.

U-Th-Pb Systematics in Chondrites

E. Jagoutz, R. Jotter, A. Kubny, W. Zartman G. Dreibus
Max Planck Institut für Chemie Planetology
jagoutz@mpch-mainz.mpg.de

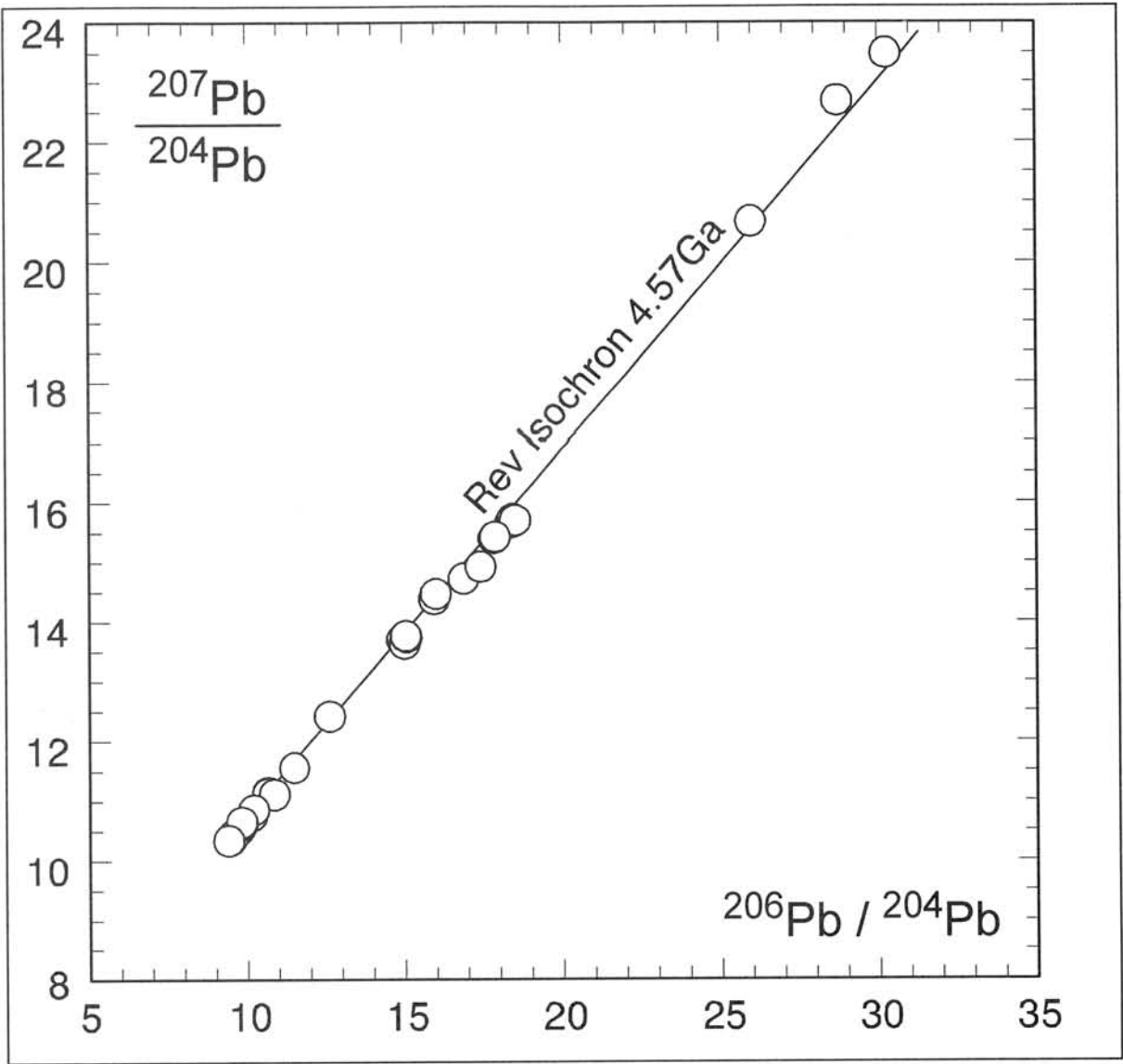
Over the past 30 years continuous improvements have been made in the analytical capabilities to measure Pb isotopic composition. Since the return of the first lunar samples by the Apollo 11 mission, chemistry Pb blanks have been lowered from ~1 ng to ~1 pg. Also, the increased sensitivity of the mass spectrometer now makes it possible to measure quite precisely the isotopic composition of 100 pg of Pb. However, most of the existing U-Th-Pb data for meteorites were obtained prior to these significant improvements, and mainly on bulk rock samples before very clean mineral separates were available.

U-Th-Pb isotope systematics in chondrites have always presented us with an unsolved problem in cosmochemistry. Although their Pb-Pb isochrons give ages close to 4.55 Ga, the U-Pb and Th-Pb systems are heavily disturbed. In most cases they contain more radiogenic Pb than can be accounted for by the present U and Th concentrations. The origin of this so-called excess Pb component has been under discussion for many years.

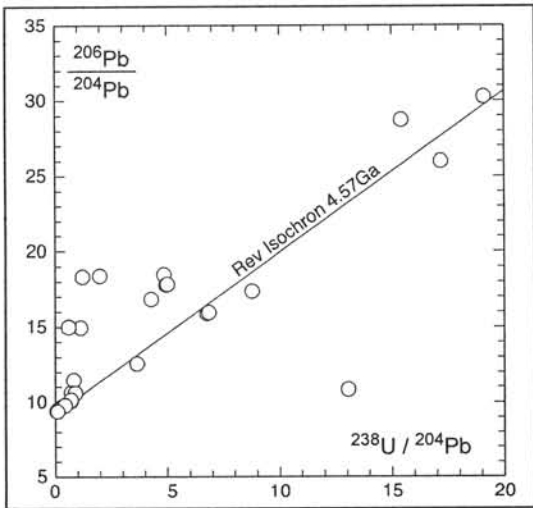
We present here the results of a study, in which we have measured U, Th, and Pb isotope systematics in fragments and mineral concentrates from four different chondrites (Pantar H5, Leighton H3/5, Rumuruti and Zag). In particular, we designate the fragments as being of dark or light lithology, and identify the mineral concentrates as plagioclase or sulfide. Also, included are the fused crusts of two of the chondrites. Although the dark lithology has been shown to be enriched in volatile elements, such as K, J, Br, compared to the light lithology, we do not find the dark lithology to be preferentially enrichment in radiogenic Pb.

While on a $^{207}\text{Pb}/^{204}\text{Pb}$ vs. $^{206}\text{Pb}/^{204}\text{Pb}$ diagram (A) the samples lie close to a 4.57 Ga Pb-Pb isochron, they are heavily disturbed on a $^{206}\text{Pb}/^{204}\text{Pb}$ vs. $^{238}\text{U}/^{204}\text{Pb}$ diagram (B). In the latter diagram about half of the data plot above a 4.55 Ga reference isochron, indicating that the Pb is more radiogenic than would be produced by the measured $^{238}\text{U}/^{204}\text{Pb}$ ratio. However, at least one sample does plot significantly below the reference isochron and suggests the possibility of some internal re-distribution of Pb. In the $^{208}\text{Pb}/^{204}\text{Pb}$ versus $^{232}\text{Th}/^{204}\text{Pb}$ diagram (C) the samples plot only on or above the reference isochron, implying that disturbed systems only gained radiogenic Pb.

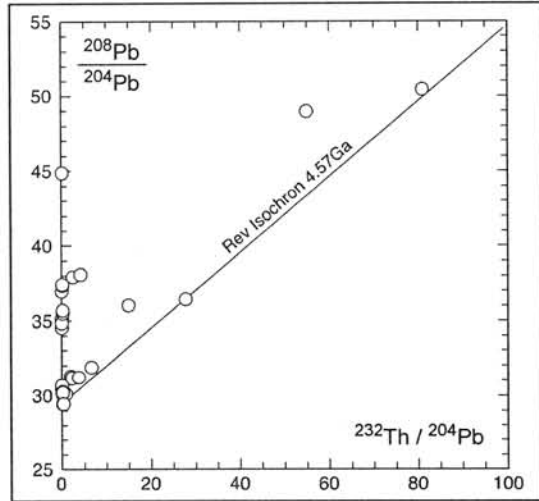
While some of the excess Pb could be explained by the infiltration of terrestrial Pb into the chondrites, many aspects of these data cannot be explained this way. Nonetheless, the Pb re-distribution must be a young event, possible related to shock metamorphism at the time of excavation from the parent body. Such data hold promise of giving better insight into the mechanism and timing of Pb re-distribution. We plan to extend this study to other meteorites and an examination of the relationships within coexisting mineral suites.



A



B



C

Terrestrial ^{14}C ages of Yamato meteorites. A. J. T. Jull¹, L. R. McHargue¹, J. A. Johnson¹ and K. Nishiizumi². ¹NSF-Arizona AMS Laboratory, The University of Arizona, 1118 East Fourth St, Tucson, AZ 85721, USA. ²Space Science Laboratory, University of California, Berkeley, CA 94720, USA.

Introduction: We have investigated the terrestrial ages, or residence times, of meteorites from the Yamato region, Antarctica. This information can be applied to studies of infall rates, meteorite distributions, weathering of meteorites and meteorite concentration mechanisms. The study of the terrestrial ages of meteorites gives us useful information concerning the storage and weathering of meteorites and the study of fall times and terrestrial age. We would expect that weathering of meteorites and their eventual destruction would be a function of the terrestrial age. In addition, weathering is expected to affect trace-element and isotopic compositions [1]. would affect trace-element composition. However, a direct connection of weathering rates to the terrestrial survival times of meteorites was initially shown by Wlotzka et al. [2] and later by Bland et al. [3].

Terrestrial ages of meteorites have been determined by the concentration of ^{36}Cl , ^{14}C or ^{41}C , measured independently or also in combination. With measurement of more than one radionuclide, we can correct for shielding effects [4-6]. At our laboratory, we make measurements of ^{14}C and $^{14}\text{C}/^{10}\text{Be}$. We have obtained ~ 239 ^{14}C terrestrial ages on various Antarctic meteorites, from many different sites. This number includes 24 Yamato meteorites [7,8]. We previously also investigated $^{14}\text{C}/^{10}\text{Be}$ dating on the grounds that this production ratio should be reasonably constant at ~ 2.5 to 2.6 [9,10]. Recently, Jull et al. [11] have also discussed new modeling calculations to determine if we can assume a constant production rate of ^{14}C and ^{10}Be .

New Measurements on Yamato meteorites. In this paper, we present new results on 17 Yamato meteorites. The results are summarized in table 1. Our results show a range of terrestrial ages of Yamato meteorites. We compare these and earlier Yamato terrestrial ages to those from the Allan Hills Far Western Icefield and various "hot" desert environments. The interesting result at Yamato is that, although the meteorites with terrestrial ages $<45\text{ka}$ have a similar distribution to the other sites studied, such as the Far Western Icefield and "hot" deserts, $\sim 35\%$ of the Yamato meteorites have ages (measured by ^{81}Kr or ^{36}Cl) from 55 to 270ka. This suggests that the older part of the Yamato distribution is more analogous to the Allan Hills Main Icefield, where there are few meteorites $<45\text{ka}$ and the mean life of meteorites is closer to 150ka. Indeed, 2 meteorites of $\sim 2\text{Ma}$ residence times have been reported [13, 14]. This is characteristic of Antarctic meteorites, where it is known some achondrites can survive for up to 270 ± 40 ka [12].

Table 1: Some new terrestrial ages for Yamato meteorites.

Meteorite	Class	^{14}C (dpm/kg)	^{14}C age (ka)
Y74037	Diogenite	11.6 ± 0.4	13.8 ± 1.3
Y791186	Eucrite	22.2 ± 1.0	8.3 ± 1.4
Y791217	H4	<0.49	>38
Y791406	H5	22.7 ± 0.5	5.9 ± 1.3
Y791422	Diogenite	3.0 ± 0.3	25.0 ± 1.6
Y791452	L5	<0.39	>40
Y791482	H4	1.0 ± 0.4	31.5 ± 3.0
Y791477	H4-5	<1.7	>27
Y791486	L6	6.4 ± 1.2	17.2 ± 2.0
Y791630	L4	43.0 ± 1.0	1.4 ± 1.3
Y791960	Eucrite	$32 \pm 11^*$	5.3 ± 3.3
Y791962	Eucrite	0.78 ± 0.48	>32
Y792510	Eucrite	0.58 ± 0.24	>35.5
Y983885	Lunar	<0.8	>36
Y981651	Eucrite	3.4 ± 0.4	23.7 ± 1.6
Y000593	Nakhlite	0.8 ± 0.3	>34.7
Y000749	Nakhlite	<0.7	>35.8

* - very small sample 0.05g.

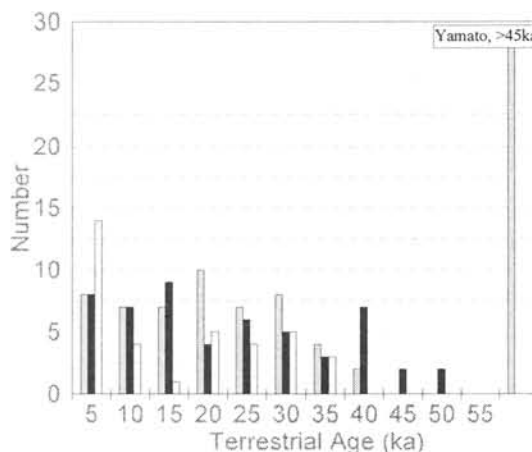


Figure 1: Distribution of terrestrial ages of meteorites from Yamato (left, gray) [7,8], the Allan Hills Far Western Icefield (solid color) [5] and the deserts of Western Australia (right, stippled gray) [13].

The <45ka age distribution at Yamato generally shows a younger age distribution, typical of recent infall at this site [4-5], yet there is also a population with much longer terrestrial ages. This indicates that the Yamato meteorite population is a mixture of falls directly onto the ice (as at the Far Western icefield) and meteorites transported some distance by the ice [13].

References: [1] E. Gnos et al., 2003, *Meteoritics & Planetary Science*, **48**, A26. [2] F. Wlotzka et al., 1995, *Lunar & Planetary Institute Technical Report 95-02*, 72. [3] P. A. Bland et 1996. al., *Monthly Notices, Royal Astronomical Society* **238**, 551. [4] A. J. T. Jull, 2000. in "Accretion of extraterrestrial matter throughout Earth's history" (eds. B. Peuker-Ehrenbrink and B. Schmitz), Kluwer Academic/Plenum Publishers, New York., pp. 241-266 [5] A. J. T. Jull et al., 1998. *Geological Society of London Special Publication* **140**, 75. [6] K. C. Welten et al., 2003. *Meteoritics & Planetary Science* **38**, 499. [7] A. J. T. Jull et al., 1993, Proc. NIPR Symposium on Antarctic Meteorites, **6**, 374. [8] A. J. T. Jull et al., Antarctic Meteorites XIV, 62. [9] D. A. Kring, et al., 2001. *Meteoritics & Planetary Science*, **36**, 1057. [10] K. C. Welten et al. 2001. *Meteoritics & Planetary Science*, **36**, 301. [11] K. J. Kim et al. 2003, abstract #1191, *35th Lunar & Planetary Science Conference*. [12] Y. Miura et al., 1991, *26th Symposium on Antarctic Meteorites*, Tokyo, p. 129. [13] P. A. Bland et al., 2000, *Quaternary Research*, **53**, 131. [14] P. Scherer et al., 1997, *Meteoritics & Planetary Science*, **32**, 769. [15] K. C. Welten et al., 1997, *Meteoritics & Planetary Science*, **32**, 775.

Comparison of Fe-Mg interdiffusion coefficients in orthopyroxene: Implication for metamorphism of the Petersburg polymict eucrite. H. Kaiden^{1,2} and P. C. Buchanan¹,
¹National Institute of Polar Research, Tokyo 173-8515, Japan. E-mail: kaiden@nipr.ac.jp.
²Department of Polar Science, School of Multidisciplinary Sciences, The Graduate University for Advanced Studies, Tokyo 173-8515, Japan.

Introduction:

The compositional zoning of minerals contained in igneous and metamorphic rocks provides us with clues about the thermal history of these rocks. Orthopyroxene is a common mineral in both terrestrial rocks and meteorites, but there are fewer studies about Fe diffusion properties of orthopyroxene than those of olivine (*e.g.* [1]). Here, we compare two different sets of diffusion coefficients taking into account the abundance of Fe and the oxygen fugacity. Using these diffusion coefficients, we also model the metamorphic redistribution of Fe at the edges of mineral fragments of magnesian orthopyroxene in the polymict eucrite Petersburg (Fig. 1). Previously [2], we suggested that this partial re-equilibration might have been caused by contact metamorphism. We initially suspected that these two sets of diffusion coefficients would provide different time periods for metamorphism. In fact, the results are quite similar.

Calculations:

In the present study, we assumed that the compositional gradient of Mg# (=100 × Mg / (Mg + Fe), molar) at the edges of these orthopyroxene fragments was controlled by atomic diffusion. In order to obtain cooling rates, calculated diffusion profiles were numerically fit to the observed zoning profiles using calculation procedures similar to those in Miyamoto *et al.* [3].

Diffusion coefficients:

Ganguly and Tazzoli (G&T) [4] mathematically described the average Fe-Mg interdiffusion coefficient along the *c* and *b* axes of orthopyroxene as a function of temperature and composition with the following equation:

$$D_{Fe} = \exp(-12.8 + 0.060C_{Fe}) \exp\left(-\frac{57.306}{RT}\right) \quad (1)$$

where D_{Fe} , C_{Fe} , R , and T are the diffusion coefficient (cm^2/s), abundance of Fe (mol%), gas constant ($\text{kcal}\cdot\text{mol}^{-1}\cdot\text{K}^{-1}$), and temperature (K), respectively. The diffusion coefficients in Fe-bearing silicate minerals, such as olivine [5], orthopyroxene [4], and garnet [6], have been reported to depend on oxygen fugacity, fO_2 , and to vary approximately as $(fO_2)^{1/6}$. Hence, we modified eq. (1), which is valid at fO_2 ranging from the iron-wüstite (IW) buffer to 0.8 log units above the IW buffer, by incorporating the fO_2 dependence as follows [3]:

$$D_{Fe} = (fO_2)^{1/6} \exp(-15.3 + 0.060C_{Fe}) \exp\left(-\frac{36.561}{RT}\right). \quad (2)$$

Miyamoto and Takeda (M&T) [7] estimated the diffusion coefficient in orthopyroxene to be $1 \times 10^{-14} \text{ cm}^2/\text{s}$ at 1200 °C. They approximated the activation energy for Fe diffusion in pyroxene to be 100 kcal/mol for temperatures >1100 °C and 25 kcal/mol for temperatures <1100 °C from the experimental data by Fujino *et al.* [8]. Using these estimates, the Fe-Mg interdiffusion coefficient in orthopyroxene is expressed by the equation:

$$D_{Fe} = 7.9 \times 10^{-12} \exp\left(-\frac{25}{RT}\right). \quad (3)$$

Several workers (*e.g.* [9]) have experimentally determined redox conditions for volcanic materials in HED meteorites. We assumed similar redox conditions for metamorphism, *i.e.*, fO_2 of 1 log unit below the IW buffer. We used the fO_2 versus temperature relationships for the IW buffer reported by Eugster and Wones [10]:

$$\log(fO_{2(IW)}) = -\frac{27215}{T} + 6.57. \quad (4)$$

Results and Discussion:

We evaluated the C_{Fe} and fO_2 dependence of the diffusion coefficient defined by eq. (2). The effect of fO_2 is very small, whereas abundance of Fe has a greater effect (Fig. 2). We also compared the two sets of diffusion coefficients by G&T [4] and M&T [7]. In the temperature range ~1000 °C to ~800 °C, values are similar; however, at ~500 °C, the value suggested by M&T [7] is nearly three orders of magnitude higher than that of G&T [4] (Fig. 2). We calculated the compositional profile of a diagenetic orthopyroxene fragment in Petersburg resulting from Fe-Mg interdiffusion caused by cooling over the same temperature range (850 °C to 400 °C) as Buchanan and Kaiden [2] using the two sets of diffusion coefficients. The diffusion coefficients of G&T [4] give the best fit profile at a cooling rate of 0.12 °C/year (a period of ~4000 years) (Fig. 3), and the diffusion coefficients of M&T [7] give the best fit profile at a cooling rate of 0.25 °C/year (~2000 years).

Conclusions:

Although the diffusion coefficient suggested by M&T [7] is not reported to be dependent on C_{Fe} and fO_2 , the values are very close to those of G&T [4] for

$f_{O_2} \approx IW$ and $C_{Fe} \approx 10-50$ mol% at relatively high temperatures of $\sim 800^\circ C$. Despite significant differences in the suggested diffusion coefficients at low temperatures, the calculated cooling rates are very similar and are within the range expected for wall rock near a laccolith intruded into the crust of 4 Vesta [2]. This similarity in calculated zoning profiles suggests that diffusion at maximum temperatures during metamorphism is the most important factor in determining the character of the zoning profile.

References:

[1] Miyamoto M. et al. (2002) *Antarct. Meteorite Res.*, 15, 143–151. [2] Buchanan P. C. and Kaiden H. (2004) *LPSC XXXV*, #1502. [3] Miyamoto M. et al. (1986) *JGR*, 91, 12804–12816. [4] Ganguly J. and Tazzoli V. (1994) *American Mineralogist*, 79, 930–937. [5] Buening D. K. and Buseck P. R. (1973) *JGR*, 78, 6852–6862. [6] Chakraborty S. and Ganguly J. (1991) *Advances in Physical Geochemistry*, 8, pp. 120–175, Springer-Verlag. [7] Miyamoto M. and Takeda H. (1994) *JGR*, 99, 5669–5677. [8] Fujino K. et al. (1990) *EOS*, 71, 943–944. [9] Jurewicz A. J. G. et al. (1993) *GCA*, 57, 2123–2139. [10] Eugster H. P. and Wones D. R. (1962) *J. Petrol.*, 3, 82–125.

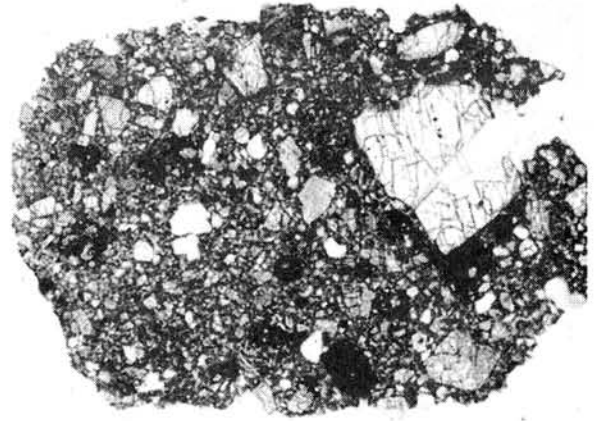


Fig. 1. Photomicrograph taken with transmitted light of a thin section of the breccia of Petersburg with a large fragment of diagenitic orthopyroxene. Field of view is 2.5 mm.

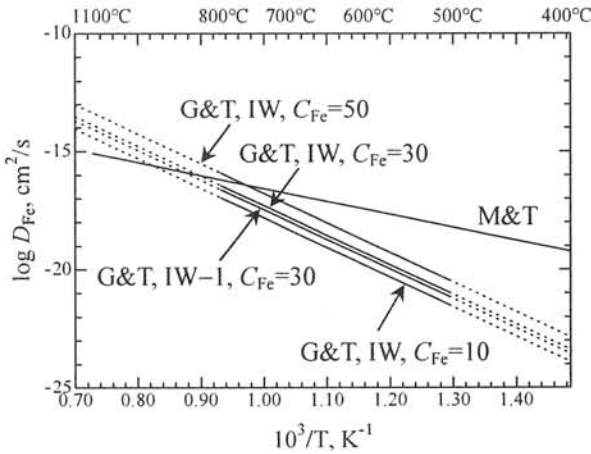


Fig. 2. An Arrhenius plot of the Fe-Mg diffusion coefficients in orthopyroxene by Ganguly and Tazzoli (G&T) [4] and Miyamoto and Takeda (M&T) [7]. For G&T, the oxygen fugacity $f_{O_2}=IW$ and $IW-1$, and the abundance of Fe $C_{Fe}=10, 30$, and 50 mol% are calculated for comparison. The diffusion coefficient by G&T is valid between $500^\circ C$ to $800^\circ C$ [4].

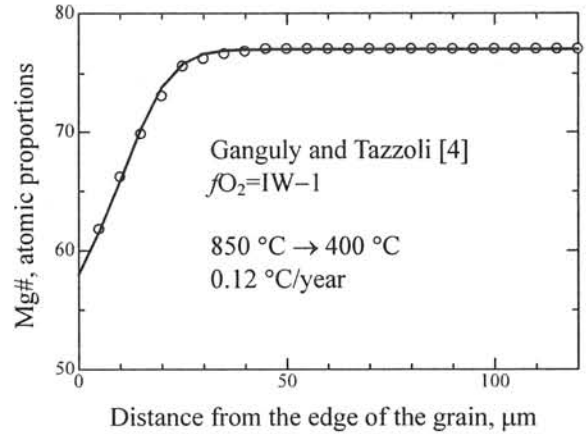


Fig. 3. Calculated (solid curve) and observed (open circles) zoning profiles for Mg# at the edge of a fragment of orthopyroxene in the Petersburg breccia. Calculated profile is obtained with the diffusion coefficient of Ganguly and Tazzoli [4] for $f_{O_2}=IW-1$ and cooling from $850^\circ C$ to $400^\circ C$.

Chemical Characteristics of lunar meteorites, Yamato 86032 and Dhofar 489. Y. Karouji¹ M.Ebihara^{1,2} and A. Yamaguchi², ¹Graduate School of Science, Tokyo Metropolitan University, Hachioji, Tokyo 192-0397, Japan, ²National Institute of Polar Research, Itabashi, Tokyo 173-8515, Japan.

Introduction:

Yamato (Y) 86032 is a lunar meteorite which was found on Antarctica in 1986. This meteorite was classified into feldspathic lunar highland breccia [1, 2]. One ferroan anorthosite clast of Y86032 has a very old Ar-Ar age of ~4.35-4.4 Ga [3]. This meteorite is composed of at least three lithologies, white and light feldspathic lithology, dark-gray matrix (hereafter DG) and black impact melt veins (B) [4]. Dhofar (Dho) 489 is a lunar meteorite recently found in Oman in 2002, and was classified into feldspathic crystalline matrix breccia [5]. This lunar meteorite also has an old Ar-Ar age of ~4.27 Ga [6].

In this study, we determined major, minor and trace elements compositions of Y86032 and Dho489 by using several analytical methods and aimed to characterize these meteorites chemically as well as petrographically in comparison with those for other lunar highland meteorites and lunar rocks returned by the Apollo mission.

Samples and analytical methods:

We analyzed three fragments of Y86032; Y86032,34 (81.9mg), Y86032,36 (92.8mg) and Y86032,131 (238.6mg) (values in parentheses indicate weight of samples allocated to us). Both ,34 and ,36 are black impact melt (B) and ,131 is dark-gray lithology (DG) [4]. For Dho489, we analyzed four fragments; Dho489a, b, c and d. Dho489a (143.5mg) and Dho489b (31.0mg) are bulk materials, Dho489c (36.0mg) is pure anorthosite material, and Dho489d (9.2mg) is matrix fragment. Samples were first analyzed by neutron-induced prompt gamma-ray analysis (PGA), for which lump samples were used. Following PGA, instrumental neutron activation analysis (INAA) was performed. Except for Dho489d, lumps were ground in a clean agate mortar and some aliquants were used in INAA. We also used inductively coupled plasma mass spectrometry (ICP-MS) for the determination of rare earth elements (REEs), Th and U.

Results and Discussion:

Table 1 shows major, minor and trace element composition of the two lunar highland meteorites analyzed in this study. Our data of three fragments of Y86032 are mostly consistent with those of Palme et al. (1991) [7] except for such elements as Na, Al, V, Cr, Mn and heavy-REEs (HREEs), indicating that this meteorite is heterogeneous in chemical composition in a scale of g-size. The chemical composition of Y86032 is almost indistinguishable from those of other lunar highland meteorites except for incompatible elements, which are systematically

lower in Y86032. Compared with other lunar highland meteorite, Dho489 is characterized by even lower concentrations of Sc, V, Cr, Mn, Co, Ni and REEs (e.g., [7]) and much higher mg# (atom Mg/(Mg + Fe)).

Texture and mineralogy of mafic components in anorthosite of lunar highland meteorites are complex, and, in most cases, modified by regolith processes and shock and thermal metamorphisms, being evidenced by the presence of glassy materials and granulitic breccias. Nevertheless, lunar highland meteorites follow relatively simple chemical trends in terms of some major elements [7]. Figure 1 shows a TiO₂ versus Al₂O₃ correlation for lunar highland meteorites and rocks. In this figure, individual values for Y86032 and Dho489 are shown, while average compositions of the other lunar highland meteorites are plotted. We have calculated such average values from the following sources and other references cited therein: Jolliff et al. (1991) [8], Koeberl et al. (1989, 1990) [9, 10], Korotev et al. (1996) [11], Palme et al. (1991) [7] and Warren and Kallemeyn (1991) [12]. As shown in Fig. 1, lunar meteorites, except for Dho489, show a trend with negative slope, which is not overlapped with that for Apollo 16 highland rocks.

Figure 2 shows chondrite-normalized REE abundance patterns for lunar highland meteorites analyzed in this study. The REE pattern of Y86032,34 (B) is very similar to the pattern of ,131 (DG), with ,36 (B) being slightly enriched in HREE. The REE abundance of Dho489 is much lower than those of other lunar highland meteorites including Y86032. A U/Th ratio of Dho489 is much higher than those of other lunar highland meteorites, and must have been increased by weathering in the hot desert. Similarly, negative anomaly of Ce seen in the REE abundance patterns of Y86032 and Dho489 could have been caused by weathering in cold and hot deserts. Dho489a and Dho489b represent bulk samples of this meteorite and their REE abundance patterns are similar to each other. Their REE abundances are the lowest among those of other lunar highland meteorites. Considering this fact and that other incompatible element abundances are similarly lower in Dho489 compared with those of other lunar highland meteorites, Dho489 must have come from a site with long distance from Mare Imbrium, highly probably from the far-side of the moon. However, the source region of Y86032 whose REE abundance is not so low as that for Dho489 needs not necessarily be the far-side of the moon.

References:

- [1] Tanaka H. et al (1990) *Proc. Lunar Planet. Sci. Conf.* 20, 91-100. [2] Tanaka H. et al. (2002)

LPS.XXXIII, Abstract #1267. [3] Bogard D. D. et al. (2002) LPS XXXIII, Abstract #1267. [4] Yamaguchi A. et al. (2004) LPS XXXV, Abstract #1474. [5] Takeda H. et al. (2003) LPS XXXIV, Abstract #1284. [6] Takeda H. et al. (2004) LPS XXXV, Abstract #1222. [7] Palme H. et al. (1991) GCA 55, 3105-3122. [8] Jolliff B.L. et al. (1991) GCA 55, 3051-3071. [9] Koeberl C. et al. (1989) Proc. NIPR Symp. Antarct. Meteorites 2, 15-24. [10] Koeberl C. et al. (1990) Proc. NIPR Antarct. Meteor. 3, 3-18. [11] Korotev R.L. et al. (1996) MAPS 31, 909-924. [12] Warren P.H. and Kallemeyn G.W. (1991) Proc. NIPR Antarct. Meteor. 4, 91-117.

Acknowledgements:

We thank H. Takeda for valuable discussion.

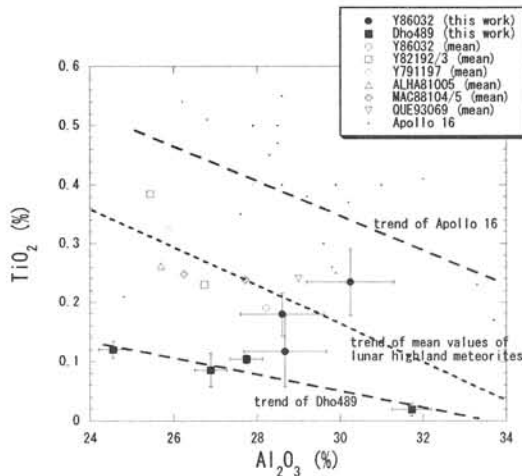


Fig.1 TiO₂ vs. Al₂O₃ for Lunar highland meteorites and Apollo 16 rocks.

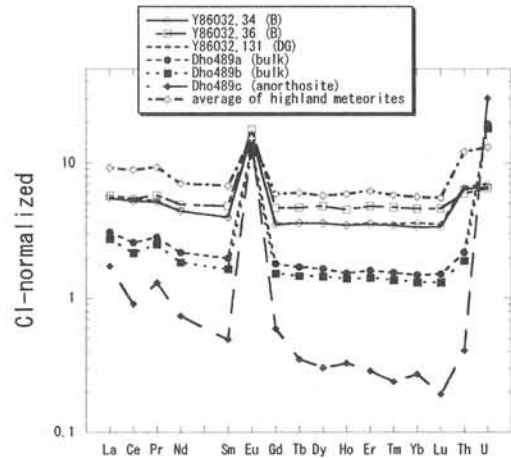


Fig.2 Chondrite-normalized REE abundance patterns for lunar highland meteorites.

Table 1 Chemical composition of Y86032 and Dho489.

	Yamato 86032						Dhofar 489								
	.34 (B)		.36 (B)		.131 (DG)		a (bulk)		b (bulk)		c (anorthosite)		d (matrix)		
		error		error		error		error		error		error		error	
Na	%	0.344	0.003	0.397	0.004	0.373	0.004	0.275	0.001	0.267	0.001	0.356	0.001	0.307	0.001
Mg	%	3.79	0.37	3.36	0.36	3.34	0.33	3.93	0.28	3.37	0.41	1.43	0.18	5.25	0.58
Al	%	15.2	0.5	15.1	0.5	16.0	0.6	14.7	0.2	13.0	0.2	16.8	0.3	14.2	0.2
Si	%	21.3	0.7	20.8	1.0	20.6	0.6	20.3	0.4	20.5	0.6	19.9	0.6	20.8	1.0
K	%	0.0367	0.0097	0.0107	0.0075	0.0401	0.0155	0.0300	0.0098	0.0589	0.0210	0.0232	0.0180		
Ca	%	11.0	0.8	11.0	0.8	11.3	0.8	11.2	0.7	10.3	0.8	13.2	1.0	10.4	0.9
Sc	ppm	8.56	0.02	10.32	0.03	10.34	0.03	4.77	0.02	4.02	0.03	0.71	0.01	4.94	0.03
Ti	%	0.070	0.036	0.108	0.022	0.140	0.034	0.0622	0.0044	0.0720	0.0084	0.0115	0.0066	0.0514	0.0169
V	ppm	35.1	4.9	18.5	3.0	38.8	3.9	14.1	2.7	5.59	2.43				
Cr	%	0.0648	0.0003	0.0605	0.0003	0.0752	0.0003	0.0441	0.0002	0.0386	0.0003	0.0055	0.0001	0.0470	0.0003
Mn	%	0.0527	0.0022	0.0529	0.0022	0.0586	0.0022	0.0366	0.0015	0.0291	0.0020	0.0088	0.0009	0.0356	0.0026
Fe	%	3.43	0.02	3.46	0.02	3.89	0.02	2.55	0.02	2.20	0.02	0.36	0.01	2.56	0.03
Co	ppm	16.2	0.2	14.0	0.1	16.3	0.2	10.1	0.1	8.8	0.2	1.6	0.1	10.4	0.2
Ni	ppm	130	10	110	10	115	12	57.3	7.0						
Ga	ppm	3.65	0.69	2.86	0.64										
Ba	ppm	41.0	0.6	48.2	0.3	44.8	1.1	28.4	0.6	25.4	0.4	219	2		
La	ppm	1.28	0.02	1.34	0.03	1.30	0.02	0.727	0.023	0.645	0.012	0.405	0.010	0.659	0.053
Ce	ppm	3.15	0.01	3.26	0.04	3.25	0.06	1.56	0.03	1.31	0.02	0.545	0.010		
Pr	ppm	0.456	0.007	0.509	0.012	0.464	0.008	0.251	0.006	0.224	0.006	0.116	0.004		
Nd	ppm	1.99	0.02	2.21	0.05	2.00	0.03	0.986	0.029	0.831	0.023	0.333	0.016		
Sm	ppm	0.586	0.012	0.708	0.015	0.584	0.014	0.291	0.009	0.241	0.013	0.072	0.010	0.328	0.009
Eu	ppm	0.894	0.008	0.988	0.012	0.928	0.008	0.718	0.019	0.668	0.011	0.802	0.015	0.743	0.041
Gd	ppm	0.692	0.012	0.915	0.012	0.702	0.013	0.353	0.010	0.300	0.020	0.117	0.010	1.28	0.72
Tb	ppm	0.129	0.003	0.168	0.005	0.129	0.003	0.0613	0.0027	0.0525	0.0031	0.0126	0.0008		
Dy	ppm	0.870	0.008	1.16	0.01	0.873	0.020	0.400	0.017	0.351	0.012	0.074	0.003		
Ho	ppm	0.194	0.002	0.253	0.005	0.194	0.004	0.0857	0.0049	0.0781	0.0027	0.0184	0.0011		
Er	ppm	0.559	0.007	0.760	0.007	0.570	0.010	0.254	0.010	0.225	0.012	0.046	0.002		
Tm	ppm	0.0827	0.0012	0.113	0.002	0.0847	0.0016	0.0371	0.0015	0.0327	0.0016	0.0057	0.0005		
Yb	ppm	0.547	0.008	0.747	0.005	0.589	0.012	0.241	0.012	0.214	0.003	0.045	0.003		
Lu	ppm	0.0813	0.0011	0.111	0.003	0.0844	0.0025	0.0360	0.0007	0.0315	0.0022	0.0046	0.0004		
Hf	ppm	0.454	0.032	0.408	0.027	0.400	0.043	0.173	0.020						
Th	ppm	0.185	0.003	0.171	0.006	0.191	0.004	0.0634	0.0021	0.0551	0.0030	0.0118	0.0009		
U	ppm	0.0530	0.0024	0.0518	0.0016	0.0564	0.0026	0.156	0.004	0.143	0.006	0.241	0.011		

Errors are due to counting statistic (1σ) in γ-ray counting except for Ba, REE, Th, and U, whose errors indicate standard deviation (1σ: n=5) in ICP-MS.

Spinel group minerals in LL3 chondrites: Primary and secondary features. M. Kimura¹, H. Hiyagon², H. Nakajima¹ and M.K. Weisberg^{3,4}, ¹Faculty of Science, Ibaraki University, Mito 310-8512, Japan, ²Dept. Earth and Planet. Science, University of Tokyo, Tokyo 113-0033, Japan, ³Department of Physical Sciences, Kingsborough College of the City University of New York, Brooklyn, NY 11235, ⁴Department of Earth and Planetary Sciences, American Museum of Natural History, New York, NY10024, USA.

Introduction:

The chemical composition of spinel group minerals is a useful indicator of chemical group and petrologic type in ordinary chondrites. Recently, Kimura [1] and Tomiyama et al. [2] showed that spinel composition varies with the petrologic subtype of LL and L chondrites, respectively. Here we report the results of our systematic study of spinel group minerals in two LL3.0 and six LL3.1-3.9 chondrites. We suggest that the characteristic features of the spinel group minerals are not only sensitive to thermal metamorphism, but also shed light on chondrule formation.

Chemical composition of spinel group minerals in LL3.0-3.9:

In spite of petrologic subtype, LL3 chondrites always contain tiny spinel group minerals, 3-85 microns in size. They are encountered as phenocryst and inclusion in olivine in chondrules, as isolated minerals in the matrix, and in close association with Fe-Ni metal and troilite grains in the matrix. The atomic Mg/(Mg+Fe) and Al/(Al+Cr) ratios of the spinels range from 0.006-0.995 and 0.001-0.995 in types 3.0-3.3, to 0.03-0.61 and 0.001-0.995 in types 3.5-3.9 (Fig. 1). In type 3.0-3.3, the spinel chemistry strongly depends on its textural setting; Near pure chromite (<0.5% Al₂O₃ and <0.5 MgO) typically occurs as isolated grains in the matrix, and associated with opaque minerals. On the other hand, Mg and Al-rich spinel (Al/(Al+Cr)>0.25) occurs only within chondrules. Therefore, the chemistry of spinel and its textural settings is a good indicator of petrologic subtype, and spinel in subtypes 3.0-3.3 preserve their primary compositions.

Crystallization of spinel in chondrules:

We obtained bulk compositions of chondrules that contain spinel in LL3.0-3.3 chondrites. These chondrules are not Al-rich, but are common ferromagnesian chondrules. In many chondrules spinel is expected to have crystallized after olivine, based on phase equilibria. This is consistent with the petrographic observation that euhedral to subhedral spinel, 10 to 40 microns in size, is present in the groundmass. In a few chondrules, the crystallization sequence expected from the bulk composition is inconsistent with the presence of spinel, 5 to 25 microns in size, completely enclosed in olivine. The addition of Cr drastically expands the liquidus field of spinel on some phase diagrams [3]. However, if we take Cr into account, the spinel enclosed in

olivine can not be explained by crystallization from the chondrule melt. Therefore, we suggest that such spinel is relict, and was incorporated into the chondrule precursor material before melting. Olivine surrounding the relict spinel in the chondrules studied here is not refractory forsterite [4].

Oxygen isotopic composition and formation of spinel:

We measured oxygen isotopic compositions of spinel and coexisting phases by the CAMECA-6F ion microprobe. Olivine and euhedral to subhedral spinel in chondrule, plot around the terrestrial fractionation (TF) line, supporting *in situ* crystallization of the spinel. On the other hand, a relict spinel (0.6% Cr₂O₃ and 1.2% FeO) in a ferromagnesian chondrule (WE-S3) is enriched in ¹⁶O ($\delta^{17}\text{O} = -5.06 \pm 1.64\text{‰}$ and $\delta^{18}\text{O} = -2.47 \pm 3.15\text{‰}$), and has significantly lighter oxygen than the coexisting olivine, which plots on the TF line (Fig. 2).

Diffusion of oxygen into spinel is very slow [5], and thus, it is difficult for the oxygen isotopic composition of the relict spinel to completely equilibrate with that of the surrounding olivine, during chondrule formation by flash heating [e.g., 6]. Thus, it is unlikely that the relict spinel completely lost its primordial oxygen isotopic compositions during chondrule formation. The oxygen compositions of the spinels are evidently different from the ¹⁶O-rich spinels in CAI and the spinels in refractory forsterite of ordinary chondrites [4]. However, the relict spinel resembles that in Al-rich chondrules [7]. Al-rich chondrules are an intermediate component between CAIs and ferromagnesian chondrules [8]. Our discovery of relict spinel in a ferromagnesian chondrule is an indication of the complexities in the early solar nebula processes that ranged from CAI, through Al-rich chondrule, to ferromagnesian chondrule formation. Some of the early-formed minerals like spinel may have been incorporated into the subsequent components.

References:

- [1] Kimura M. (2000) *LPS XXXI*, #1213. [2] Tomiyama T. et al. (2001) *Antarc. Meteorites XXVI*, 145-147. [3] Onuma K. (1984) *J. Japan. Assoc. Min. Petr. Econ. Geol.*, 79, 387-393. [4] Pack A. et al. (2004) *GCA*, 68, 1135-1157. [5] Ryerson F.J. and McKeegan K.D. (1994) *GCA*, 58, 3713-3734. [6]

Lofgren G.E. (1996) in *Chondrules and the Protoplanetary Disk*, 187-196. [7] Russell S.S. et al. (2000) *EPSL*, 184, 57-74. [8] MacPherson G.J. et al. (2000) *LPS XXXI*, #1796.

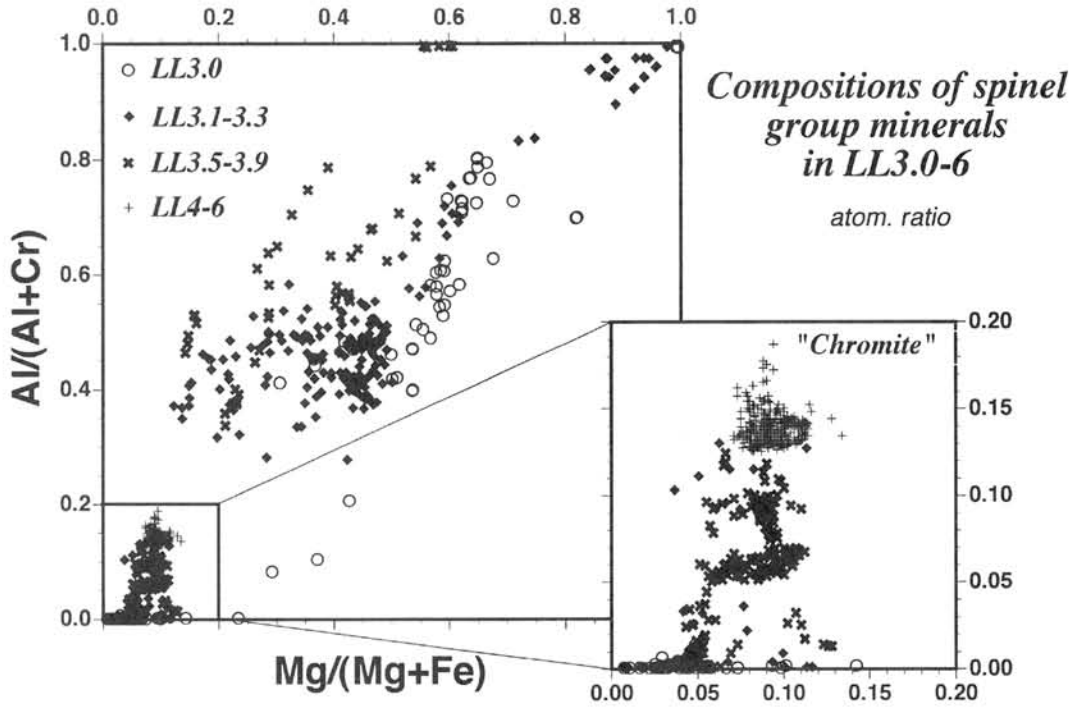


Fig. 1. Compositions of spinel group minerals in LL3.0-3.9 chondrites, in comparison with those in LL4-6.

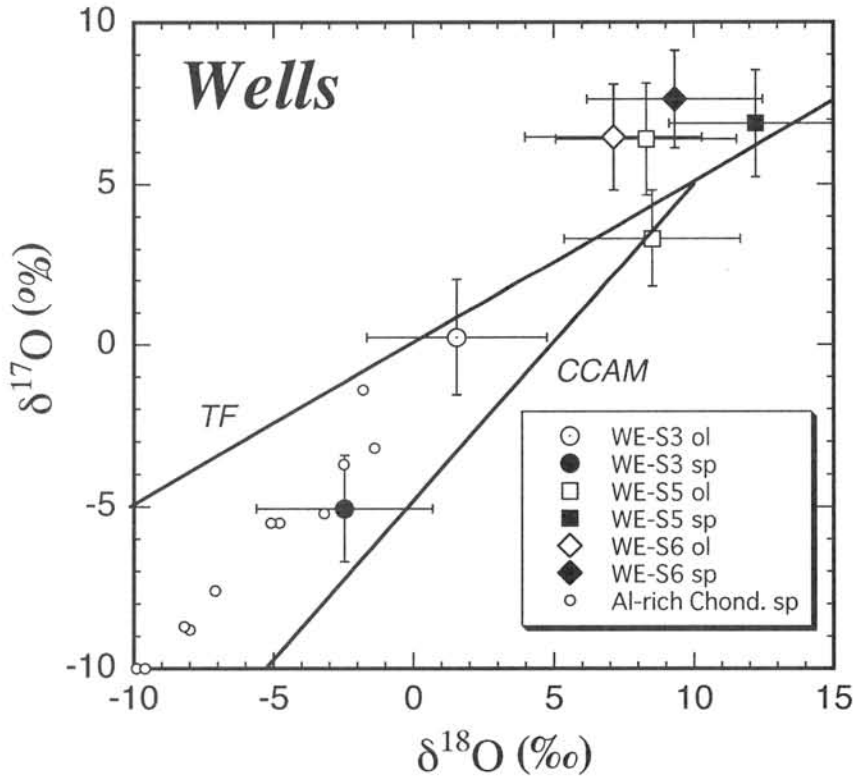


Fig. 2. Oxygen isotopic compositions of olivine (ol) and spinel (sp) in chondrules of Wells (LL3.3), in comparison with spinels in Al-rich chondrites in ordinary chondrites [7].

The Al-Mg system in chondrules from the most primitive H chondrite Y82038. N. T. Kita¹, M. Kimura² and Y. Morishita¹, ¹Geological Survey of Japan, AIST, ²Ibaraki University.

Introduction:

The Al-Mg ages of ferromagnesian chondrules have been obtained from the least equilibrated ordinary chondrites (LL3.0-3.1; Semarkona, Bishunpur, and Krymka), showing the ages of 1-2.5 Myr younger than CAIs [1-2]. As these data are obtained only from LL chondrites, it is not clear if the same results would be obtained from other types of chondrites. Unfortunately, most H3 chondrites are classified as type 3.5 or higher, in which the Al-Mg system might be heavily disturbed during the parent body metamorphism. Recently Y82038 is recognized as a H3.2 chondrite from the petrology and chemistry [3] and TL sensitivity [4]. This is one of the most primitive H chondrites known to date. For this reason, we started systematic study on the Al-Mg age determination of chondrules in Y82038, to see if they preserve the undisturbed Al-Mg systems since the time of chondrule formation and further if there are any systematical difference between ages of chondrules in H and LL chondrites.

Method:

We used a thin section of Y82038, 61-3, from the NIPR Antarctic meteorite collection. Among many chondrules studied previously in the same section [3], we selected several chondrules that contain Al-rich mesostasis suitable for the Al-Mg study. These samples are first observed with EPMA (JEOL JXA-733 and JXA-8900) to examine the chemical compositions and mineral phases in the mesostasis. The Al-Mg age determination was carried out using ims-1270 at Geological Survey of Japan with analytical conditions similar to the previous studies [1-2, 5].

Compositions of mesostasis:

Selected chondrules are mostly type I chondrules (Fo>90) either with glassy groundmass and/or nepheline. Three of them are glassy chondrules, consisted of Na-rich glass containing magnesian mafic minerals (Fig. 1a). The chemical composition of glass in these chondrules are enriched in alkali and depleted in MgO (<0.3%) and CaO (<0.1%). Another chondrule (F2, Fig. 1b) shows a typical type IA texture, containing euhedral forsteritic olivine enclosed in glassy groundmass. The chemical composition of glassy groundmass is unusually low in MgO (0.3-0.5%) and CaO (0.1%) compared to the typical type IA in LL3.0 chondrite Semarkona [6]. The glass inclusion in olivine shows the chemical composition higher in MgO (~2%) and

CaO (~22%) and lower in alkali contents. Other chondrules contain nepheline, from partly to completely replacing the mesostasis area. We also observed mesostasis in type II chondrules in the same section. They contain microcrystallites that is typical to type II chondrules in Semarkona [7]. However, surrounding groundmass seems to be devitrified into sub-micron scale crystals.

Results of SIMS analyses :

At present we obtained preliminary data from a type IA chondrule F2. We analyzed two positions in mesostasis, one is near the center of the chondrule and the other is near the edge. In spite of high ²⁷Al/²⁴Mg ratio ~100, we only observed a small ²⁶Mg excesses in the level of ~1‰ (Fig. 2). By assuming the normal Mg isotopic ratio as initial, the slope of the isochron corresponds to the ²⁶Al/²⁶Al ratio of ~1×10⁻⁶, which is 10 times lower than those observed in chondrules from LL3.0-3.1 chondrites. The apparent relative age inferred from the data is 4.1(-0.5/+0.8) Myr after CAIs by assuming canonical value of CAIs to be 5×10⁻⁵ [8].

Discussion:

The preliminary result indicates the Al-Mg age of chondrule F2 is much younger than those of ferromagnesian chondrules in LL3.0-3.1 [1-2]. Even though the Y82038 is the most primitive H chondrite and contains glassy mesostasis and sharply defined chondrules, it also shows alteration products, such as nepheline in both refractory inclusions and chondrules [3]. The ²⁷Al/²⁴Mg ratios in mesostasis in type IA chondrules in Semarkona (LL3.0) are less than 10 [6]. Both low MgO contents and small ²⁶Mg excess in the mesostasis of F2 imply that Mg was lost from glass later than 4 Myr. If the chondrule originally formed at ~2Myr after CAIs with the initial ²⁶Al/²⁶Al=1×10⁻⁵ and the original glass had the ²⁷Al/²⁴Mg ratio=10, the ²⁶Mg excess in glass is expected to be ~1‰. In this case, Mg was lost from glass without isotopic re-equilibration after the ²⁶Al had almost completely decayed to its daughter, which should be much later than 4 Myr after CAIs.

Previously, lack of ²⁶Mg excess or low initial ²⁶Al/²⁷Al ratios (<1×10⁻⁶) among chondrules in type 3 chondrites were considered to be the extended chondrule formation time more than 5Myr [9]. It also means that the life of the proto-planetary disk was longer than 5Myr. However, recent Al-Mg data in chondrules from type 3.0-3.1 chondrites show a limited range of Al-Mg ages (1.5-3Myr [1-2, 5]). Further, a plagioclase-olivine inclusion in Ningqiang

carbonaceous chondrite, which is only mildly metamorphosed, showed disturbed Al-Mg isochron, indicating both the original formation time (2.5Myr) and the lower limit of secondary event (>4Myr) [10]. Therefore, it is very likely that the Al-Mg system is easily disturbed even in only mildly metamorphosed type 3 chondrites. Further Al-Mg analyses in chondrule mesostasis in Y82038 may help us to understand the time and process of elemental and isotopic re-distribution during the parent body metamorphism.

References:

[1] Kita N. T. et al. (2000) *GCA*, 64, 3913-3922. [2] Mostefaoui et al. (2002) *Meteorit. Planet. Sci.*, 37, 421-438. [3] Kimura M et al. (2002) *Meteorit. Planet. Sci.*, 37, 1417-1434. [4] Benoit P. H. et al. (2002) *Meteorit. Planet. Sci.*, 37, 793-805. [5] Kurahashi et al. (2004) *LPS XXXV*, #1476. [6] Jones R. H. and Scott E. R. D. (1989) *Proc. 19th LPSC*, 523-536. [7] Jones R. H. (1996) *GCA*, 60, 3115-3138. [8] MacPherson G. J. et al. (1995) *Meteoritics*, 30, 365-386. [9] Russell S. S. et al. (1996) *Science*, 273, 757-762. [10] Kita et al. (2004) *LPS XXXV*, #1471.

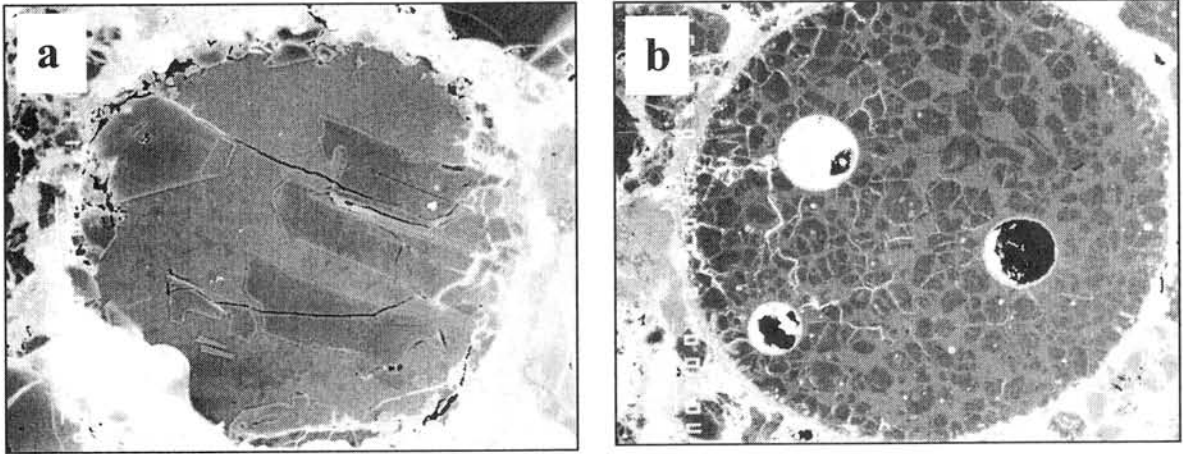


Fig. 1. Mesostasis-rich chondrules in Y82038. (a) glassy chondrule (200µm in diameter), (2) type IA chondrule (1mm in diameter).

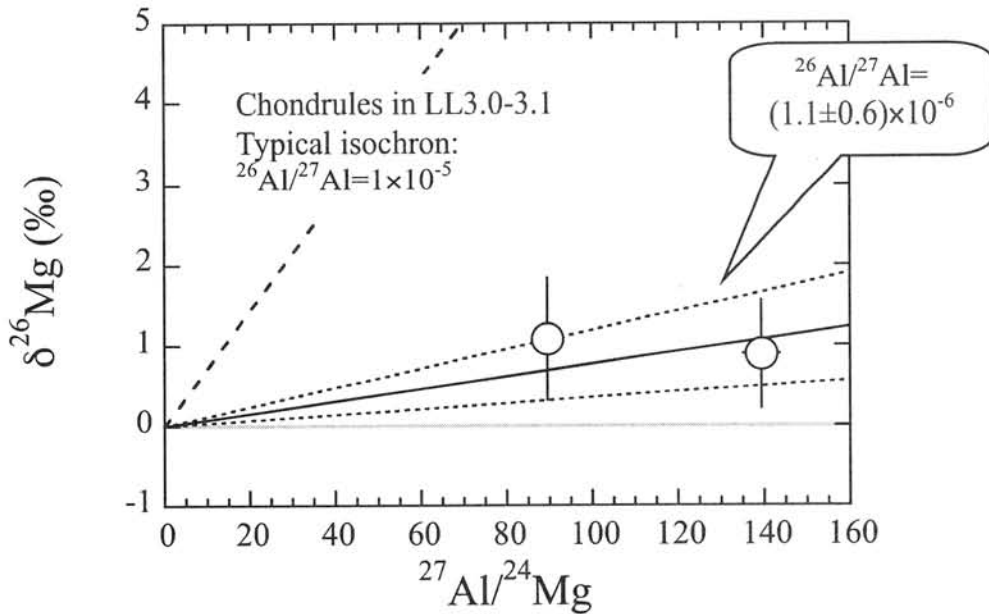


Fig. 2. The Al-Mg isochron diagram of Type IA chondrule F2 in Y 82038.

A XAFS study on degrees of alteration/metamorphism of carbonaceous matter in carbonaceous chondrites in their parent bodies.

F. Kitajima¹, Y. Kitajima², T. Nakamura¹, and K. Mase²

¹Department of Earth and Planetary Sciences, Faculty of Sciences, Kyushu University, Hakozaki, Fukuoka, 812-8581, Japan (kitajima@geo.kyushu-u.ac.jp).

²KEK-PF, Tsukuba, Ibaraki, 305-0801, Japan.

Introduction:

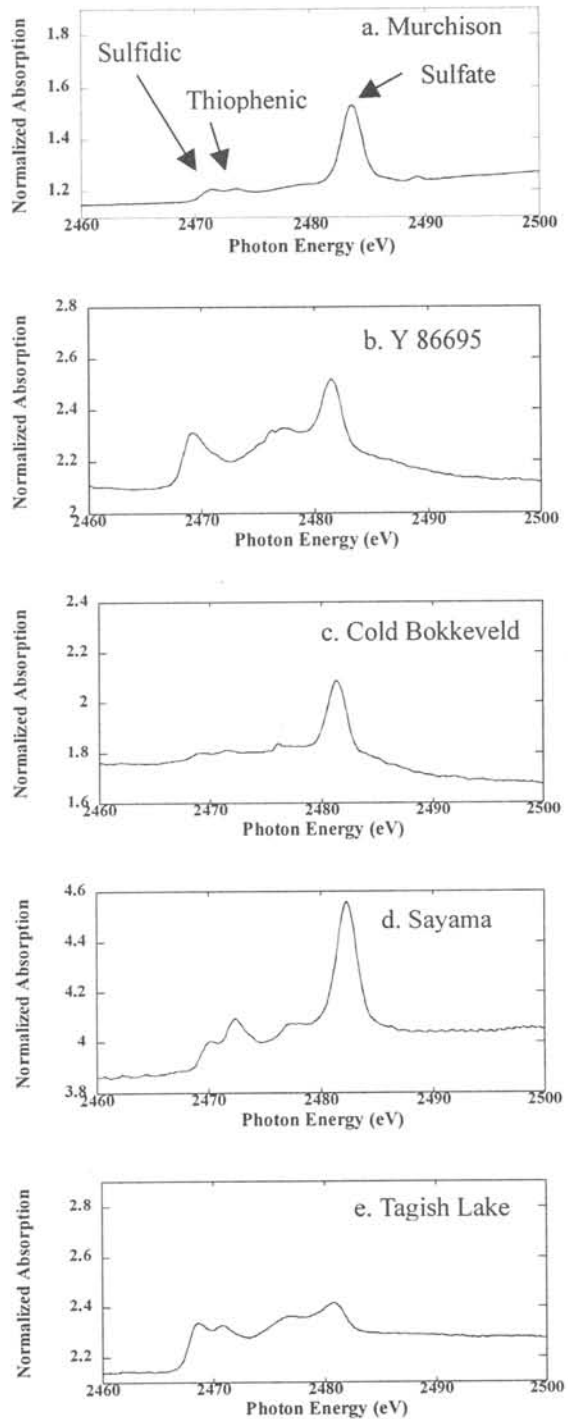
X-ray absorption fine structure (XAFS) spectroscopy has been applied to characterization of some extraterrestrial carbonaceous materials by several investigators [1, 2, 3]. Insoluble macromolecular matter is the major fraction of carbonaceous matter in carbonaceous chondrites, and it reflects the degree of thermal metamorphism and/or aqueous alteration that chondrites suffered [4]. In this investigation, we tried to evaluate the degree by using XAFS technique. The carbonaceous macromolecular matter has sulfur-containing heterocycles such as thiophene [5]. We therefore observed sulfur *K*-edge XAFS spectra, and chose the thiophenic (it means organic sulfur) absorption as an index of the degree of thermal metamorphism and/or aqueous alteration in their parent bodies.

Samples and methods:

XAFS analyses were performed at the High Energy Accelerator Research Organization (KEK). An aliquot of powdered samples (*ca.* 2-3 mg each) were pressed onto stainless plates, and the plates were set in the chamber at the beamline BL-11B. Spectra were obtained by TEY (total electron yield) method. Results of some chondrites have been previously reported [6, 7]. Here, we report some additional results including Tagish Lake.

Results and discussion:

Fig.1 shows the sulfur *K*-edge XAFS spectra of several carbonaceous chondrites. The spectra of CM chondrites show sulfidic, sulfate and thiophenic (organic) absorptions such as Murchison (Fig.1a). The CM chondrites suffered thermal metamorphism strongly can be distinguished by relatively weak thiophenic absorption (Y 86695; Fig.1b) from the unheated or weakly heated CM chondrites. This suggests that the thiophenic portion of the carbonaceous matter must be gradually lost during thermal metamorphism. Sayama (Fig. 1d) that suffered extensive aqueous alteration shows relatively strong thiophenic absorption. Tagish Lake (Fig.1e) also shows relatively strong thiophenic absorption, and weak sulfate absorption is another characteristic of this sample. The CV (Allende; Fig.1f) and CO (Ornans) chondrite show quite different spectra from the CM chondrites. The spectra did not show thiophenic and sulfate absorptions.



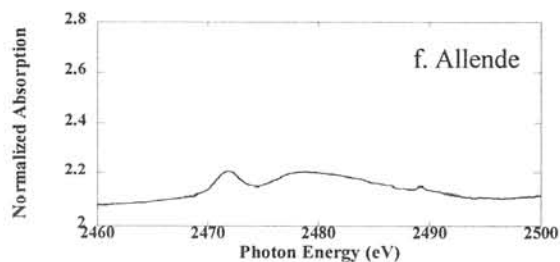


Fig. 1. Sulfur K-edge XAFS spectra of carbonaceous matter in carbonaceous chondrites.

Acknowledgments:

We thank Dr. Shigekazu Yoneda, National Science Museum, for providing us with the Sayama sample.

References:

- [1] Cody G. D. III, Alexander C. M. O'D and Tera F. (1999) *Meteorit. Planet. Sci.* **34**, A25-A26.
- [2] Keller L. P., Messenger S., Flynn G. J., Jacobsen C. and Wirick S. (2000) *Meteorit. Planet. Sci.* **35**, A86.
- [3] Derenne S., Behar F., Robert F., Rouzaud J.-N., Gourier D. and Largeau C. (2001) *Meteorit. Planet. Sci.* **36**, A49.
- [4] Kitajima F., Nakamura T., Takaoka N., and Murae T. (2002) *Geochim. Cosmochim. Acta* **66**, 163-172.
- [5] Shimoyama A., and Katsumata H. (2001) *Chem., Lett.*, 202-203.
- [6] Kitajima F., Kitajima Y., Nakamura T., and Mase K. (2003) *Meteorit. Planet. Sci.* **38**, A114.
- [7] Kitajima F., Kitajima Y., Nakamura T., and Mase K. (2003) *KEK Photon Factory Activity Report, Part B, Users' Report.* **20**, 38.

Hapke Parameter Properties of Bidirectional Reflectance for Yamato-75102 L6 chondrite. K. Kitazato^{1, 2}, M. Abe², A. M. Nakamura³, J. Saito⁴, and A. Fujiwara²,
¹Department of Earth and Planetary Science, Graduate School of Science, University of Tokyo, Hongo, Bunkyo, Tokyo 113-0033, Japan, ²Department of Planetary Science, Institute of Space and Astronautical Science, Japan Aerospace Exploration Agency, Yoshinodai, Sagami-hara, Kanagawa 229-8510, Japan, ³Graduate School of Science and Technology, Kobe University, Nada, Kobe, Hyogo 657-8501, Japan, ⁴Nishimatsu Construction Co., Shimotsuruma, Yamato, Kanagawa 242-8520, Japan.

Introduction:

Laboratory measurements of scattered light by particulate surface and photometric observations of planetary surfaces have been performed with a wide range of phase angle, which play an important role in estimating a planetary surface characterization. Spacecraft explorations also have enabled access to data sets with a much wider range of the phase angle. The HAYABUSA (MUSES-C) is a Japanese asteroid sample return mission [1]. The launch of the spacecraft succeeded by a Japanese M-V rocket on May 19 in 2003 and it will arrive at the target, near-Earth asteroid (25143) Itokawa, in summer 2005. Itokawa is considered an S-type asteroid and has similar spectra to LL class ordinary chondrite [2]. During the HAYABUSA rendezvous phase to the target, reflectance spectra of the target's surface materials with a wavelength range from 850 nm to 2100 nm are going to be observed by an on-boarded near-infrared spectrometer (NIRS). NIRS observation is planned to perform around the home position; where is about 6 km of the altitude from the asteroid surface, and can obtain the data with a wide range of phase angle due to investigate the surface material characterization [3]. For the purpose of comparison, further investigation about light-scattering properties of analogue materials to an asteroidal surface from laboratory study is required to interpret the data obtained by NIRS. Moreover, it would be available for initial analysis of returned samples by spectrometer.

Hapke's bidirectional reflection model, an approximate light-scattering model from radiative transfer theory, is the most widely used model in analyzing the photometric data of planetary surfaces with a regolith layer [4]. In the present study, we measured the bidirectional reflectance of Yamato-75102 L6 chondrite sample by changing incident and emission angles and derived Hapke's parameter properties dependent on wavelength using the Hapke's model.

Measurements:

The spectral bidirectional reflectance of the powdered surfaces at different angles were measured over the range 0.3-2.6 μm using the Shimadzu UV-3150 goniometric spectrophotometer at the Institute of Space and Astronautical Science, Japan Aerospace Exploration Agency. The light sources used are a

deuterium lamp at the UV wavelength range and a 50 W halogen lamp at the VIS-NIR. The aperture diameter is approximately 9 mm. The detectors are an R-928 photomultiplier at the UV-VIS wavelength range and a PbS photodiode at the NIR. The angles of interest are the zenith angle of the incident ray i , the zenith angle of the emission ray e , and the phase angle α , that is, the angle between the light source and the detector. This goniometric equipment has i , e and α ranges: $-60\sim 60^\circ$, $-60\sim 60^\circ$ and $15\sim 120^\circ$.

The sample prepared for the measurements is Yamato-75102 L6 chondrite. The sample was ground using a mortar and a pestle and was dry sieved to a size range of 250-590 microns. The sample powder was gently poured into a sample holder to form an optically thick layer with a depth of 5 mm and the surface was flattened by using the edge of a spatula to make it macroscopically smooth. To minimize the effects of the heterogeneity of the sample surface, four measurement sequences were performed. In the sequences, the position angles of the sample holder were 0° , 90° , 180° , and 270° : the sample holder was rotated horizontally in 90° steps. The standard deviation of these measurements was calculated to give an estimation of the experimental error.

Results and Discussion:

The reflectance spectra of Yamato-75102 L6 chondrite show common features, specifically low overall reflectance and broad absorption features in the 1 and 2 micron regions, which are considered to derive from olivine and pyroxene components.

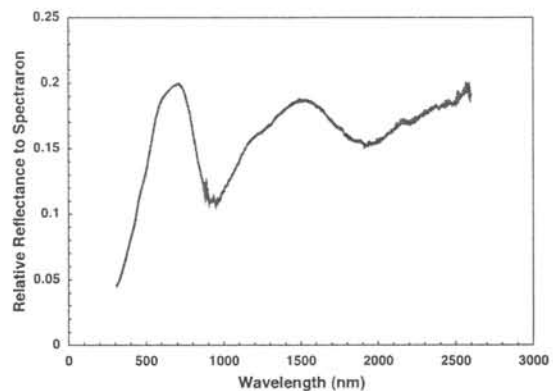


Fig. 1 Reflectance spectra of Yamato-75102 L6 chondrite at $i = 30^\circ$ and $e = 0^\circ$.

We determined the Hapke parameters — the single-scattering albedo ω , the opposition surge amplitude B_0 , the opposition surge angular width h , and the macroscopic roughness parameter θ — for all the data sets by using the double H-G phase function with the asymmetry parameters b and c . The bidirectional reflectance $r(i, e, \alpha)$ is then

$$r(i, e, \alpha) = \frac{\omega}{4\pi} \frac{\mu_{0e}}{\mu_{0e} + \mu_e} \left\{ [1 + B(\alpha, h)] p(\alpha) + H(\mu_{0e}) H(\mu_e) - 1 \right\} S(i, e, \alpha; \theta),$$

$$p(\alpha) = \frac{1-c}{2} \frac{1-b^2}{(1+2b\cos\alpha+b^2)^{3/2}} + \frac{1+c}{2} \frac{1-b^2}{(1-2b\cos\alpha+b^2)^{3/2}}$$

$$H(x) = \left[1 - \omega x \left(r_0 + \frac{1-2r_0x}{2} \right) \ln \frac{1+x}{x} \right]^{-1},$$

$$r_0 = \frac{1-\gamma}{1+\gamma},$$

$$\gamma = \sqrt{1-\omega},$$

where $\mu_{0e} \sim \cos i$, $\mu_e \sim \cos e$, $B(\alpha)$ is the opposition effect term, and $S(\theta)$ is the roughness function (see [1], [3]). We applied weighted non-linear least-squares fitting to each of the four measurement sequences that minimize the χ^2 squares defined as

$$\chi^2 = \sum_j \frac{[r_j - r]^2}{\sigma_j^2},$$

where the r_j , r , and σ_j are the laboratory data, the reflectance derived from the Hapke model, and the measurement error. A representative phase curve is shown in Fig. 2, which displays an opposition effect.

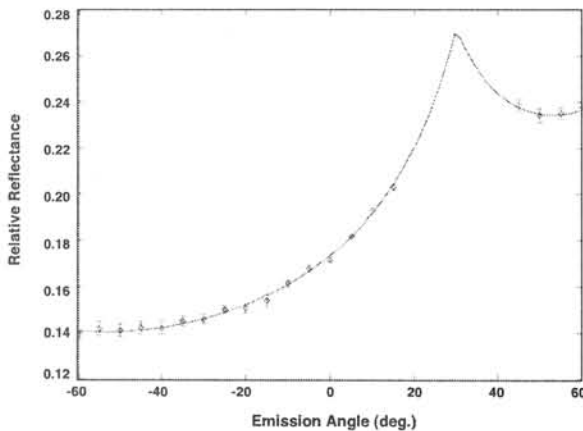


Fig. 2 Representative measurement of Yamato-75102 at a wavelength of 560 nm at fixed incident angle ($i = 30^\circ$). Solid curve is a model curve at best fitting.

We determined the Hapke parameters in the wavelength of 100 nm steps from 300 to 2600 nm to investigate the asymmetry parameters properties dependent on the wavelength.

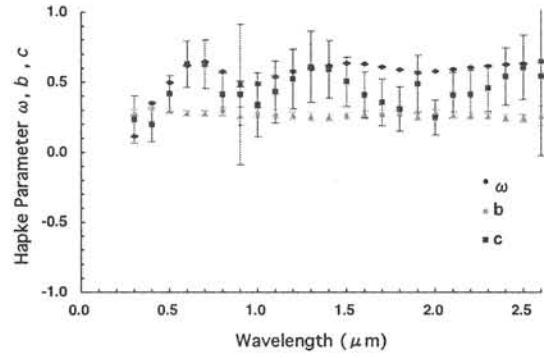


Fig. 3 Hapke Parameters (ω , b , c) values versus the wavelength.

For the present sample, asymmetry parameter b is approximately constant at overall wavelength and c , the parameter indicating the ratio of forward- and back-scattered light, has a positive correlation to the single scattering albedo ω . According to [6], Fig. 3 implies that the present sample would be high density of internal scatters and backscattering would dominate at high single scattering albedo.

Acknowledgements:

The Yamato-75102 sample was supplied by the National Institute of Polar Research through the open research proposal scheme.

References:

- [1] Fujiwara A. *et al.* (2000) *Adv. Space Res.*, 25, 231-238.
- [2] Binzel R.P. *et al.* (2001) *Meteorit. Planet. Sci.*, 36, 1167-1172.
- [3] Abe M. *et al.* (2004) *LPI*, 35,1724A.
- [4] Hapke B. (1993) *Theory of Reflectance and Emittance Spectroscopy*, Cambridge Univ. Press.
- [5] Hapke B. (2002) *Icarus*, 157, 523-534.
- [6] MucGuire and Hapke (1995) *Icarus*, 113, 134-155.

EXPERIMENTAL AND COMPUTATIONAL STUDIES OF THE OLIVINE-PHYRIC SHERGOTTITE YAMATO 980459. E. Koizumi¹, T. Mikouchi¹, M. Miyamoto¹, G. McKay², A. Monkawa¹ and J. Chokai¹, ¹Department of Earth and Planetary Science, University of Tokyo, Hongo, Bunkyo-ku, Tokyo 113-0033, Japan. ²Mail Code SR, NASA Johnson Space Center, Houston, TX 77058, USA. E-mail: koi@eps.s.u-tokyo.ac.jp.

Introduction:

Yamato 980459 (Y98) is a new martian meteorite showing close affinities to olivine-phyric shergottite, but having several clear different mineralogical features from other samples in this group. Y98 is a glassy rock displaying a porphyritic texture composed of olivine megacrysts and medium-grained pyroxene with abundant mesostasis. In contrast to all other martian meteorites, this meteorite contains neither plagioclase nor phosphates. Olivine megacrysts (Fo₈₆₋₇₉) are euhedral to subhedral and up to 2 mm in size. Olivine also exists in the groundmass (tens to hundreds of μm ; Fo₇₉₋₄₀) coexisted with zoned pyroxene (En₈₁Fs₁₇Wo₂ to En₂₂Fs₄₃Wo₃₅). The mesostasis is glassy, but contains small amounts of dendritic olivine and pyroxene with other minor minerals such as Fe sulfide [1-2]. Y98 is distinct from other shergottites because of the presence of highly magnesian olivine and the abundant glassy mesostasis without plagioclase. This is the first martian meteorite that contains no plagioclase. Therefore, investigating the formation process of this unique meteorite will give us the clue to the evolution of martian magma and the formation of the other shergottites. In this abstract, we discuss the origin of olivine megacrysts and the absence of plagioclase and calculated the cooling rate of this meteorite.

Crystallization of Y980459:

We used the MELTS software [3] in order to investigate the crystallization history of this meteorite. The calculation result shows that liquidus temperature is about 1450 °C for the bulk composition of Y98 and the liquidus phase is olivine [4]. The olivine composition at 1450 °C is Fo₈₈ [2] which is close to that of the core composition of olivine megacrysts in Y98 (Fo₈₆). According to the MELTS calculation, pyroxene started crystallizing at around 1360 °C. The pyroxene composition at this temperature is En₈₄Fs₁₄Wo₂. This composition is similar to that of the most magnesian pyroxene in Y98 (En₈₁Fs₁₇Wo₂). The calculated olivine composition in equilibrium with the pyroxene core is Fo₈₁ and this value is close to the core composition of the groundmass olivine (Fo₇₉) [1], indicating that olivine and pyroxene in the groundmass began to crystallize simultaneously.

We also performed crystallization experiments of Y98 to obtain more advanced understanding of its

crystallization history. Synthetic glass having a similar composition to the bulk Y98 was prepared. This glass is slightly more Fe-rich than the bulk composition of Y98, and the alkalis were depleted by volatilization due to high experiment temperatures. The experimental procedure is the same as in [5], and the glass was homogenized just above the liquidus temperature (1460 °C). We employed the oxygen fugacity of IW+1 that was estimated by [6]. At 1460 and 1450 °C, no minerals crystallized. Olivine was present at 1425 °C, and its composition was Fo₈₄. This composition is slightly more Fe-rich than that in Y98 (Fo₈₆) and the calculation result (Fo₈₈) probably because of Fe-rich composition of the starting material.

A cooling experiment was also performed with the bulk composition of Y98. Homogenized glass was cooled at the cooling rate of 2.5 °C/hr from 1460 °C to 1000 °C at IW+1. There are skeletal olivine grains, euhedral pyroxene and chromite in the run product although no plagioclase crystallized (Fig. 1). Pyroxene composition shows a similar zoning sequence to that of Y98 [7] and this cooling experiment could reproduce the zoning feature of Y98 pyroxene that the pigeonite core is surrounded by the augite rim (Fig. 2). Furthermore, the Al/Ti ratio of pyroxene shows good agreement between synthetic and Y98 pyroxene (Fig. 3).

These calculation and experimental results indicate that the olivine megacryst is a phenocryst, and the bulk composition of the meteorite represents a parent melt composition.

The absence of plagioclase, which is another unique feature of Y980459, can be explained by either (1) some processes removed plagioclase after it crystallized or (2) some processes prevented plagioclase crystallization. It is reported that the Al and Ti contents of pyroxene show monotonous increase with the increase of Fe#, suggesting that there was never any plagioclase crystallization [1]. The glassy mesostasis that includes dendritic olivine and pyroxene grains suggests a quenching origin. This fact is supported by the observation that the synthetic pyroxene from the cooling run showed no drop of Al/Ti ratio (Fig. 3) although it usually shows drop after plagioclase crystallization [5]. Thus, it is likely that plagioclase failed to nucleate due to significant undercooling by the rapid crystallization of the magma.

Cooling rate of olivine megacryst:

The texture of the synthetic olivines from the cooling experiment is different from that of the euhedral olivines in Y98, suggesting that the cooling rate of 2.5°C/hr in our experiment was faster than that of Y98. In contrast, pyroxene grains are comparatively larger than the olivine grains. These indicate that slower cooling history is required for the formation of olivine megacrysts.

We calculated the cooling rate of the olivine megacryst in Y98 considering both fractional crystallization and diffusional modification during crystal growth with a method similar to [8]. In this calculation, we supposed that olivine megacryst started crystallizing at 1460 °C (liquidus temperature of olivine megacryst), and stopped crystallizing at 1360 °C (temperature at which groundmass pyroxene started crystallizing), although the Fe-Mg diffusion continued to 1200 °C (just above the liquidus temperature of plagioclase). We assumed that the oxygen fugacity was at IW+1. The result of the best-fit cooling rate for the formation of the zoning of olivine megacryst is about 1 °C/hr (Fig. 4). We also tested that the fractional crystallization origin of the zoning of Y98 olivine megacryst using the Rayleigh equation (Fig. 4).

It is an important issue whether some quenching process at the late stage of crystallization is required to produce a porphyritic texture with glassy groundmass as observed in Y98. It is not clear whether 1 °C/hr linear cooling can suppress the plagioclase crystallization although 2.5 °C/hr cooling did not crystallize plagioclase when cooled to 1000 °C. This temperature is about 150 °C below the calculated liquidus temperature (1150 °C) of plagioclase. In the 0.7 °C/hr cooling run of QUE94201 [5] plagioclase crystallized at the temperature (1085 °C) that was about only 40 °C lower than the calculated plagioclase liquidus temperature (1125 °C). This difference is probably because of the difference of high crystallization temperature of Y980459, which caused more significant undercooling of the magma. Hence, it might be possible that 1 °C/hr linear cooling can produce significant undercooling that can suppress the plagioclase crystallization. If this is the case, we do not need to consider the quenching of the magma before crystallization of plagioclase.

References:

[1] Mikouchi T. et al. (2003) *NIPR Symp.*, 82-83. [2] McKay G. et al. (2003) *NIPR Symp.*, 76-77. [3] Ghiorso M. & Sack R. (1995) *Contrib. Mineral Petrol.*, 119, 197-212. [4] Misawa K. (2003) *NIPR Symp.*, 84-85. [5] Koizumi E. et al. (2002) *33rd LPSC*, #1442. [6] McKay G. et al. (2004) *35th LPSC*, #2154. [7] Koizumi E. et al. (2004) *35th LPSC*,

#1494. [8] Miyamoto M. (1999) *Meteoritics & Planetary Science* 34:A82.

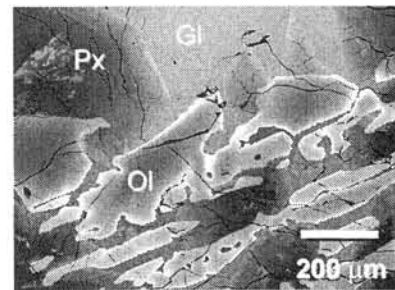


Fig. 1. BSE image of the run product from cooling experiment. Ol: olivine; Px: pyroxene; Gl: glass.

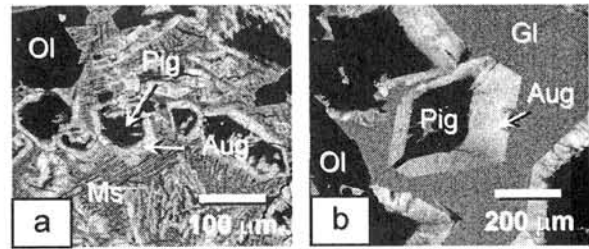


Fig. 2. Ca map of (a) 980459 and (b) the run product from cooling experiment. Pig: pigeonite; Aug: augite; Ol: olivine; Ms: mesostasis; Gl: glass.

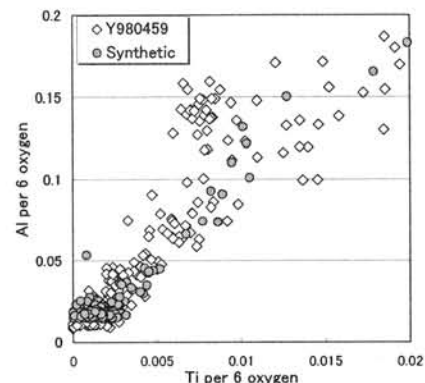


Fig. 3. Al/Ti ratio of pyroxene in Y980459 and cooling run product. Both Al and Ti were normalized by 6 oxygen.

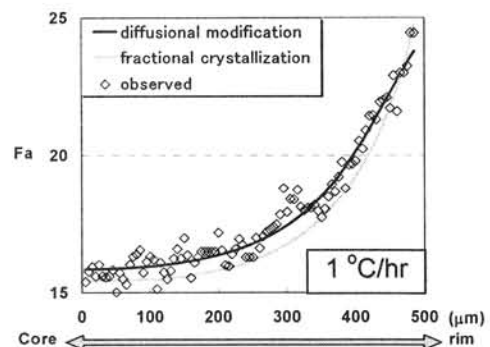


Fig. 4. The calculation result of the formation of olivine zoning with considering only fractional crystallization and both fractional crystallization and diffusional modification.

$^{17}\text{O}/^{16}\text{O}$ and $^{18}\text{O}/^{16}\text{O}$ ratio measurement using laser fluorination with application to some Antarctic meteorites. M. Kusakabe¹, S. Maruyama¹, H. Kojima². ¹Institute for Study of the Earth's Interior, Okayama University, Misasa, Tottori-ken 682-0193, Japan, ²Antarctic Meteorite Research Center, National Institute of Polar Research, Tokyo 173-8515, Japan.

Introduction:

Determination of $\delta^{17}\text{O}$ and $\delta^{18}\text{O}$ of meteorites has a special and unique importance in the meteoritic studies because the oxygen three-isotope systematics have been known to give information on the origins and processes during the early solar system and on classification of meteorite types [1]. Much work has been done by Clayton and his colleagues in this field [1, 2 and references therein] using a conventional fluorination technique. Recently secondary ion mass spectrometry is used to obtain the oxygen isotopic ratios with very high spatial resolution, although the analytical accuracy is poorer than that of the conventional fluorination technique [3]. In the present note we report an oxygen isotope analytical system for rocks and minerals using a CO_2 laser- BrF_5 fluorination technique that has been built at the Institute for Study of the Earth's Interior, Okayama University at Misasa, Japan. The system is basically for bulk rock $\delta^{17}\text{O}$ and $\delta^{18}\text{O}$ analysis using a few mg of silicate and oxide samples. Results for some terrestrial reference materials and Antarctic meteorites are discussed.

Analytical system:

The configuration of our system is basically similar to that described in the literatures [4, 5] but some modifications have been made. Oxygen is extracted from sample in the form of O_2 which is used as an analyzing gas for mass spectrometry. A silicate (or oxide) sample is decomposed to O_2 with CO_2 laser under BrF_5 atmosphere. A modified SIRA12 IRMS (Micromass, UK) is connected on-line to the extraction-purification system. Oxygen is purified through a series of cold traps and a KBr trap, and is collected in a liquid nitrogen cooled Molecular Sieve 13X cold finger next to the mass spectrometer inlet system. In reporting oxygen isotopic ratios in a SMOW scale a recommended $\delta^{18}\text{O}$ value of 5.80 ‰ for UWG2 [6] was used. $\delta^{17}\text{O}$ value for UWG2 was calculated from a relationship $\delta^{17}\text{O} = 0.52 * \delta^{18}\text{O}$ that is well accepted for terrestrial materials [1].

System performance:

We have measured $\delta^{18}\text{O}$ and $\delta^{17}\text{O}$ values of some terrestrial silicate minerals. Some of them are widely used as the international reference materials for oxygen isotopic measurement. Samples include San Carlos olivine, UWG-2 garnet, NBS-28 quartz, enstatite, augite, and magnetite.

A long term reproducibility of $\delta^{18}\text{O}$ and $\delta^{17}\text{O}$ determination of UWG2 garnet using our system is

shown in Fig. 1. More than 50 replicate analyses of UWG2 during the last 10 months indicate both $\delta^{18}\text{O}$ and $\delta^{17}\text{O}$ are stable and reproducible within 0.09 ‰ (1σ) without drift.

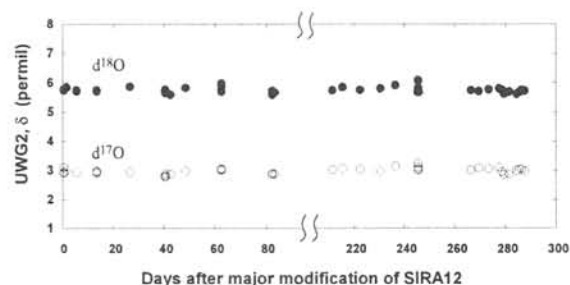


Fig. 1 $\delta^{18}\text{O}$ and $\delta^{17}\text{O}$ values of UWG2 garnet during the last 10 months. Reproducibility is within ± 0.09 ‰ for both $\delta^{18}\text{O}$ and $\delta^{17}\text{O}$.

Analytical results of some Antarctic meteorites from the collection of NIPR are plotted in Fig. 2 together with those of the terrestrial reference materials. The oxygen isotopic analyses generally support the classification of the Antarctic meteorites, for they fall in expected areas allocated to different meteorite types.

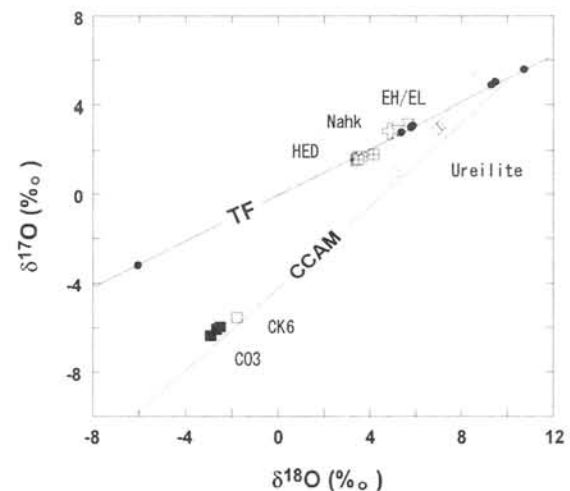


Fig. 2. Oxygen three-isotope plot of some Antarctic meteorites. Terrestrial reference materials are shown in closed circles.

References:

[1] Clayton, R.N. (1993) *Annu. Rev. Earth Planet. Sci.*, 21, 115-149. [2] Clayton, R.N. (2003) *Space Sci Rev.*, 106, 19-32. [3] Hiyagon, H. (1999) *Bull. Planet. Sci. Jpn.*, 8, 246-255. [4] Sharp, Z.D. (1990) *GCA*, 54, 1353-1357. [5] Elsenheimer, D. and Valley, J.W. (1990) *Chem. Geol.*, 101, 21-42. [6]

The nature of diamond in ureilites and carbonaceous chondrites. A. A. Marakushev¹, N. G. Zinovieva¹, A. V. Bobrov¹ and L. B. Granovsky¹, ¹Department of Petrology, Faculty of Geology, Moscow State University, Leninskie Gory, Moscow 119992, Russia.

Ureilites and carbonaceous chondrites are the most diamondiferous types of meteorites. According to oxygen isotopic pattern they belong to the single genetic family (C3—Ure). This family is characterized (Fig. 1) by light (plagioclase) and dark (pyroxene-olivine) inclusions in carbonaceous chondrites, and dark inclusions are similar to ureilites by oxygen isotopic characteristics.

Light plagioclase (anorthitic) inclusions are enriched in fassaite, spinel, melilite, and light oxygen isotope, and complimentary dark inclusions concentrate heavy oxygen isotopes. Compound chondrules in which the division of matter into light and dark material is observed were found in the Efremovka (C3) chondrite [3]: light matter forms daughter chondrules in dark olivine-rich substrate. Both the mineral and the bulk chondrule compositions are demonstrated in Fig. 1. The light chondrules fragments of Efremovka and Allende meteorites are corroded and intruded by veins of matrix matter containing numerous olivine chondrules [3]. The diagram also demonstrates isotopic correlations between light and dark inclusions of Efremovka and Allende meteorites and contains data on ureilites (primitive pyroxene-olivine achondrites), very similar to dark inclusions by the isotopic composition. This fact determines the genetic nature of ureilites representing a diamond-rich meteoritic type including in the family with the most diamondiferous carbonaceous chondrites. The diamond content ranges within 0.002—0.015 wt.% in ordinary and enstatite chondrites, reaches 0.5 wt.%, in carbonaceous chondrites, and the highest concentration up to 2 wt.% is registered in ureilites.

Relict diamond mineralization (diamond, moissanite, daubreelite and others), which is located in nickel-iron (kamacite, taenite) phase, is typical of all chondrite types, primitive achondrites (ureilites) and iron meteorites. The presence of diamonds provides evidence for their formation under high pressure. The fluid nature of this pressure is proved by (1) the low bulk density of diamond (2.22—2.23 g/cm³), resulting from a high gas saturation of diamond grains and (2) fluid influence of diamond-kamacite-graphite aggregates on silicate minerals, that causes reduction of iron to native state [4]. The content of gases in chondrite diamonds grows with an increase of its grain size.

Verchovsky with co-authors (1998) demonstrated the successive increase of noble gases content and the decrease of $\delta^{13}\text{C}$ from -26 to -33‰ in the Efremovka carbonaceous chondrite (C3) with an increase of diamond grain sizes ranging within 0.7—9.0 nm. The enlargement of diamond grains marks the transition to ureilites in which diamond

grains have larger sizes, though are similar to diamond from carbonaceous chondrites by morphology, abundance of fluid inclusions, some composition similarities of noble gases and others. But in ureilites with larger diamond crystals these regularities are observed only to some extent.

Diamonds from ureilites and carbonaceous chondrites are similar by the concentration of heavy noble gas isotopes (Ar, Kr, Xe), but differ by the concentration of light ones (He, Ne); the admixture of the latter is significantly higher in diamond from carbonaceous chondrites. Such a difference between diamonds by the concentration of light noble gases is well explained by our model of chondrite-ureilite magmatism [4], which reflects the injection position of diamond-rich graphite-kamacite mineralization of ureilites usually observed in intergrain interstices and veins. According to this model, diamond being presented by a fine emulsion of cubic crystals appeared in matrix kamacite melt under very high pressure of fluid envelopes of their parental giant planets. Loss of these envelopes under the influence of the Sun resulted in the formation of chondrite planets that either directly underwent explosive destruction with the formation of asteroids or were partially layered before the destruction. In the latter case plagioclase crusts (analogues of light inclusions in chondrites), ureilite mantles (analogues of dark inclusions in chondrites), and molten kamacite cores (analogues of carbon-kamacite matrix of chondrites) were formed in them (Fig. 1). Fluid nature of core melts controlled the endogenic activity of the planets preceding their explosive destruction to asteroids. The activity was reflected in the intrusion of carbon-kamacite melts to ureilite mantle by complex fluid-magmatic replacement with successive crystallization of kamacite-graphite assemblage. Small crystals (embryos) of diamond grew metastably in matrix melts. As a result, ureilite diamonds became different from that mineral in chondrite matrix: larger by a grain size and more depleted in mobile light noble gases. Metastable growth of diamond grains in ureilites occurred simultaneously with graphite crystallization in carbon-kamacite melt intruding ureilites.

The discussed model was directly proved by the find of the Dar al Gani 319 polymict ureilite [2], the silicate-rich matrices of which contain the metal-rich clast. The oxygen isotopic composition of it is the following (‰): $\delta^{18}\text{O} = 5.85$, $\delta^{17}\text{O} = 1.32$, $\Delta^{17}\text{O} = -1.72$; that is analogous to matrix of Allende C3 carbonaceous chondrite. Isotopic trend of the Dar al Gani 319 ureilite combines this meteorite with carbonaceous chondrites and melanocratic inclusion (Nilpena Dark Clast).

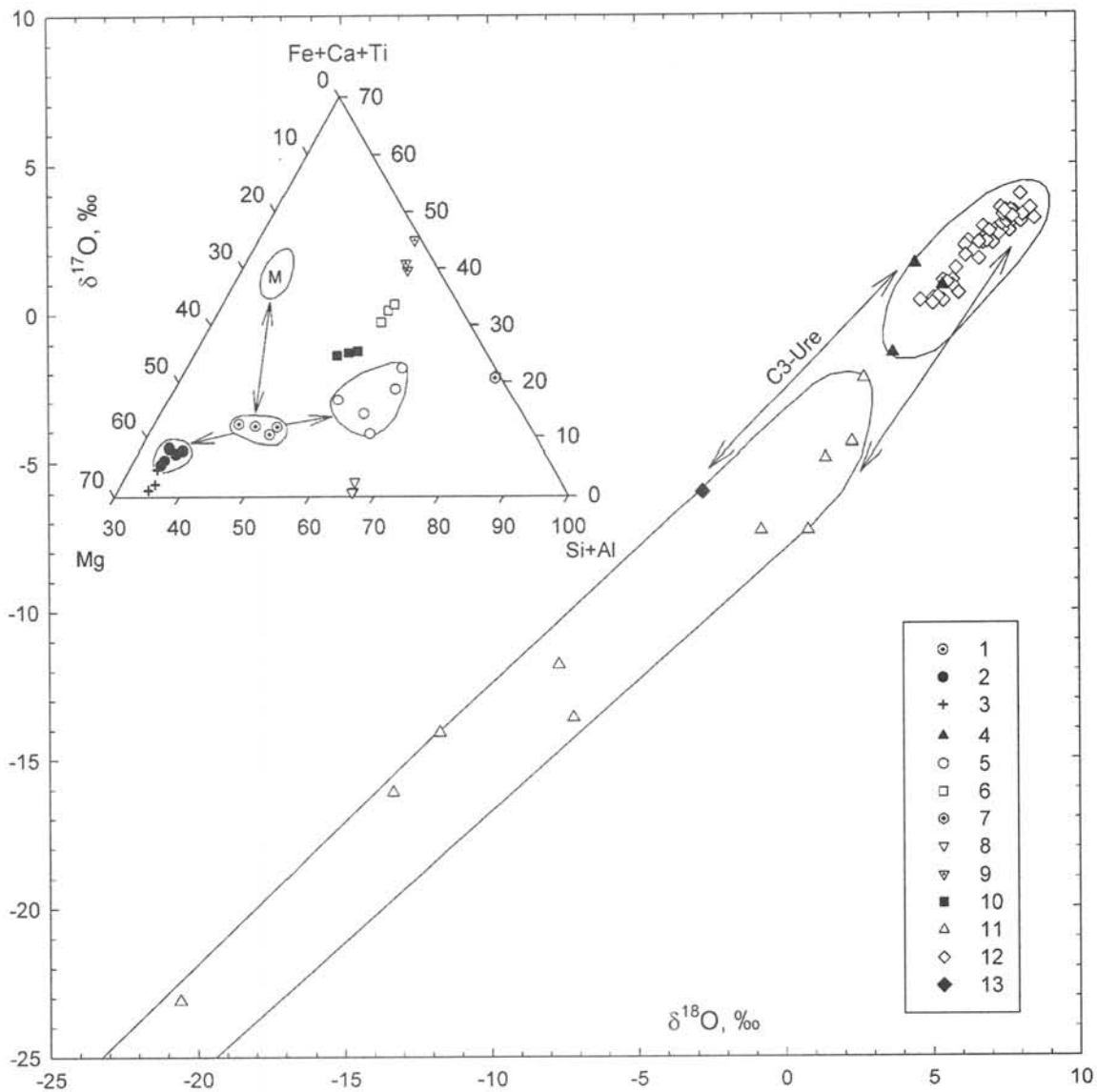


Fig. 1. Composition of light and dark inclusions in carbonaceous chondrites relatively to ureilites by oxygen isotopes [4].

(1) bulk composition of compound chondrule; (2) dark mafic phase; (3) olivine in its composition; (4) dark inclusions in Efremovka and Allende C3 chondrites; (5) light phase of compound chondrule; its minerals: (6) fassaite, (7) anorthite, (8) spinel, (9) melilite, and (10) secondary pyroxene; (11) light inclusions in Efremovka and Allende chondrites; (12) ureilites; (13) Eagle Station pallasite ($\delta^{17}\text{O} = -5,96$, $\delta^{18}\text{O} = -2,78$). Arrows on triangular diagram demonstrate the formation of mafic (analogues of dark inclusions) and silicic (analogues of light inclusions) phases at the expense of silicate matter in compound chondrule of Efremovka C3 chondrite. M is the composition of matrix

Acknowledgments:

This work was supported by the Russian Foundation for Basic Research, grant 04-05-64880; the Program "Universities of Russia - Basic Researches", grant UR.09.02.052; the Program "Support of Scientific Schools", grant 1301.2003.5.

References:

- [1] Verchovsky et al. (1998) *Science*, 281, 1165–1168. [2] Ikeda et al. (2003) *Antarctic Meteorite Research*, 16, 105–127; [3] Marakushev et al. (1992) *Kosmicheskaya Petrologiya*, Moscow, Moscow University-press, p. 325. [4] Marakushev et al. (2003) *Kosmicheskaya Petrologiya*, Moscow, Nauka-press, p. 387. [5] Mitreikina et al. (1995) *Proc. of NIRP Symp. on Antarct. Meteorites*, 8, 215–224.

Redox State and Petrogenesis of Martian Basalts: Clues from Experimental Petrology.

G. McKay¹, L. Le², C. Schwandt², T Mikouchi³, and E. Koizumi³, ¹Mail Code SR, NASA Johnson Space Center, Houston, TX 77058, USA, ²Lockheed Martin, 2400 NASA Parkway, Houston, TX 77058, USA, ³Dept. of Earth and Planetary Science, Univ. of Tokyo, 7-3-1 Hongo, Tokyo 113-0033, Japan.

Introduction:

Although the Mars Exploration Rovers determined the mineralogy and bulk composition of several basaltic rocks, these rovers have no instruments to determine detailed textures and mineral compositions. Thus we can gain only an imperfect understanding of the rocks' petrogenesis from MER data. Currently, Martian meteorites continue to provide our best clues to the magmatic evolution of Mars. This abstract addresses several things we have learned about the oxidation state, primitive nature, and petrogenesis of Martian meteorites from combined petrographic and experimental studies. We focus on two Antarctic basaltic shergottites, QUE 94201 (QUE) and Yamato 980459 (Y98).

Oxidation state of the Martian mantle:

One of the most important characteristics of a planet is the oxidation state of its mantle, as reflected in primitive basalts. Using completely different approaches (see below), Wadhwa [1] and Herd *et al.* [2] concluded that Martian basalts formed under a range of oxygen fugacities, suggesting complex petrogenetic processes. Moreover, correlations between oxygen fugacities and source region trace element and isotopic characteristics [1, 2] attest to the fundamental importance of the oxidation state of these basalts.

Both [1] and [2] reported a spread in oxygen fugacity of ~3 log units between the most oxidized and most reduced samples (Shergotty and QUE 94201, respectively). Herd *et al.* [2] reported values for individual samples that were about 1.5 log units higher than those reported by [1]. Thus, the value reported by [1] for QUE 94201 is $\sim IW-1$, while that reported by [2] is $\sim IW+0.5$. This discrepancy may reflect shortcomings of one or both techniques.

Techniques for determining oxidation state:

Wadhwa [1] used the depth of the Eu anomaly in pyroxenes to estimate the oxygen fugacity for several shergottites. This technique relies on using experimentally determined partition coefficients to calibrate the depth of the Eu anomaly against oxygen fugacity. Wadhwa [1] used the only calibration available at the time, by McKay *et al.* [3], in which partition coefficients were measured for highly aluminous angritic pyroxenes. One potential problem with results of [1] is that the large difference in pyroxene composition between shergottitic and angritic pyroxenes may result in systematic errors in inferred oxygen fugacity, although relative errors should be much less. Work is in progress to calibrate this technique for face compositions appropriate for shergottites [e.g., 4, 5].

Herd *et al.* [2] used electron microprobe analy-

ses of coexisting oxide minerals and mafic silicates to estimate oxygen fugacities for several shergottites. This approach also has drawbacks. Determination of ferric Fe in oxide minerals by stoichiometry requires very careful, accurate microprobe analyses. Moreover, oxides are known to equilibrate down to temperatures, and are highly susceptible to post magnetic oxidation. The good correlation of fO_2 with isotopic characteristics [2] suggests that random oxidation was not a problem with these samples. Nevertheless, the inferred oxygen fugacities may differ systematically from magmatic values because of equilibration to subsolidus temperatures.

We have used a slightly different approach to estimating the fO_2 for Y98. We conducted a series of experiments in which a synthetic Y98 composition was allowed to partially crystallize at a variety of oxygen fugacities. Ferric Fe content of resulting chrome spinel was determined by stoichiometry, and end-member mineral components were calculated including magnetite. Magnetite contents from these experiments were compared with the magnetite contents obtained for natural spinel from Y98. Results are shown in figure 1.

Results suggest that Y98 spinels crystallized at oxygen fugacities of about $\sim IW+0.5$. If the estimates of [2] are correct, the fO_2 for Y98 is similar to that for QUE. This is an important result, because both samples are among the most LREE-depleted shergottites. Thus the correlation of fO_2 with trace element characteristics holds for Y98.

This technique is ideal for use on Y98. This sample has only one oxide phase and thus the

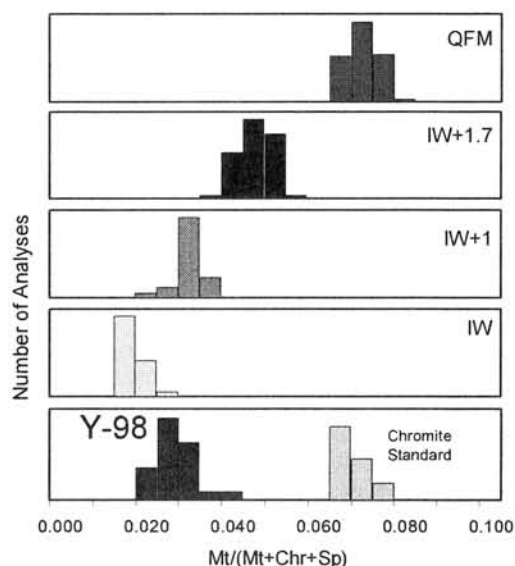


Figure 1. Magnetite contents of spinels from experimental runs and Y98.

2-oxide oxybarometer cannot be applied. Moreover Y98 cooled rapidly enough preserve a large fraction of interstitial glass and thus its oxide minerals are likely to retain their magmatic compositions.

Which samples are primitive?

One important issue is which of the shergottites, if any, are primitive basalts that accurately reflect their source regions. Experimental crystallization studies can indicate whether a sample represents a crystallized melt as opposed to a partial cumulate. If a composition representing a cumulate is experimentally crystallized, the composition of the initial mafic minerals will be more Mg-rich than the most magnesian olivine or pyroxene in the natural sample. This was the case for Shergotty [6]. On the other hand, if the synthetic minerals match the natural cores, this is a strong indication that the sample represents a crystallized liquid. We reported this to be the case for QUE [7]. Thus, QUE takes on added importance: It is one of the most reduced Martian meteorites, has depleted trace element and isotopic characteristics, and is also one of the few shergottites that can be demonstrated to be a melt composition.

Is QUE a primitive melt straight from the mantle? Most likely not. It is quite Fe-rich, and pyroxene is the liquidus phase rather than olivine [e.g., 7]. Thus it has probably undergone significant fractionation after partial melting.

Our recent results indicate that Y98 is much more likely than QUE to be a primitive melt. In fact, it appears to be the most primitive Martian magma [8]. It formed at low fO_2 and has depleted trace element and isotopic patterns. Although we have not yet measured the composition of the liquidus experimental olivine, the composition predicted by MELTS (Fo 88) closely matches the most magnesian olivine cores (Fo 86). Thus it is unlikely to be a cumulate. Moreover, it has an extremely high liquidus temperature ($\sim 1460^\circ\text{C}$ [8]).

The texture of Y98 is different from all other shergottites. It has a porphyritic texture, with olivine megacrysts set in a fine-grained groundmass of olivine and pyroxene (Fig. 2c). The groundmass has about 20% mesostasis consisting of glass with skeletal crystals of olivine and pyroxene. It is the only shergottite without plagioclase.

Does this texture indicate an unusual cooling history? Probably not. One of our experiments produced a texture that closely resembles that of the meteorite. This run was cooled at $5^\circ\text{C}/\text{hr}$ from 1460° to 900°C . The quenched charge contains large grains of olivine (Fig. 2A, bottom left), elongated pyroxene crystals, and interstitial glass. In some areas (Fig 2B), the glass contains skeletal mafic crystals resembling those in Y98. We have yet to study this charge in detail, but on the surface, it bears a remarkable resemblance to Y98, despite its simple cooling history.

Summary:

The Martian meteorites contain a profound re-

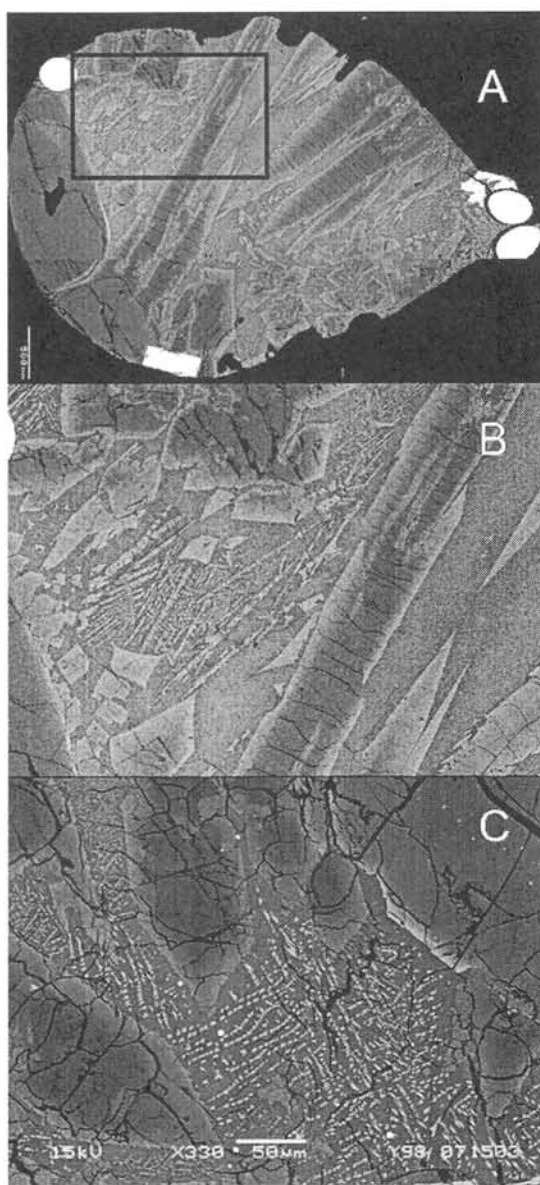


Figure 2. BSE Images of experimental Y98 charge (A and B) and natural Y98 (C).

cord of magmatic processes on Mars. Understanding how the correlated variation of trace element/isotopic characteristics and oxidation state originated is one of the fundamental problems in Martian evolution. Combined petrographic and experimental study can provide important insight into the nature and history of these samples, including oxidation state, thermal history, and the degree to which they represent unmodified melts from mantle source regions.

Acknowledgement: We thank NIPR for inviting us to participate in the Y98 consortium.

References:

- [1] Wadhwa (2001) *Science* 291, 1527.
- [2] Herd *et al.* (2002) *GCA* 66, 2025.
- [3] McKay *et al.* (1994) *GCA* 58, 2911.
- [4] Musslewhite *et al.* (2003), *MAPS*, in review.
- [5] McCanta *et al.* (2003) *GCA*, in review.
- [6] Stolper & McSween, 1979, *GCA* 43, 1475.
- [7] McKay *et al.* (2003) *LPSC XXXIV*, 2109.
- [8] McKay *et al.* (2004) *LPSC XXXV*, 2154.

ELECTRON BACK-SCATTER DIFFRACTION (EBSD) AND FORE-SCATTER ELECTRON (FSE) IMAGE ANALYSES OF NAKHLITES. T. Mikouchi, A. Monkawa, O. Tachikawa, I. Yamada, M. Komatsu, E. Koizumi, J. Chokai, M. Miyamoto, Dept. of Earth and Planetary Science, Graduate School of Science, University of Tokyo, Hongo, Bunkyo-ku, Tokyo 113-0033, JAPAN, E-mail: mikouchi@eps.s.u-tokyo.ac.jp

Introduction:

Electron back-scatter diffraction (EBSD) and fore-scatter electron (FSE) image analyses are newly emerged analytical techniques that enable us micro-area (~0.5 μm) crystallography on thin sections when combined with field emission gun scanning electron microscope (FEG-SEM) [e.g., 1-3]. In SEM, orientation contrast imaging in back-scattered electron (BSE) mode is possible by mounting a BSE detector in the FSE position that is underneath the EBSD detector. The contrast in the FSE image is related to the orientation of the crystals. The other merits of these techniques include easy sample preparation and analyses compared to conventional crystallographic techniques such as single crystal X-ray diffraction or transmission electron microscopy (TEM). In this abstract we report EBSD analysis of symplectites in olivines from three nakhlites (Nakhla, Governador Valadares, and Y000593) to study orientational relationship between the host olivine and exsolved phases. We also analyzed pyroxene twinning of Governador Valadares by combining FSE images and EBSD.

Result and Discussion:

Symplectite

Nakhlite olivines often contain fine-grained symplectic inclusions composed of augite and magnetite [4]. Symplectites in nakhlite olivines are present as either lamellar (several tens of μm long and a few μm wide) or blebs (a few tens of μm) (Fig. 1). Such symplectites are interpreted as exsolution products at high oxygen fugacity ($\log f_{\text{O}_2} \sim \text{QFM}$) [4,5]. We previously determined orientational relationships of the host olivine and exsolved symplectites in Nakhla olivine by TEM [4] and found that they are orientationally identical to the type I symplectites in terrestrial olivines [5]. It is also reported that symplectites in Y000593 have the identical orientation relationships [6].

In this study we obtained EBSD patterns from the host olivine and exsolved magnetite and augite in Nakhla, Governador Valadares and Y000593 olivines. Although olivines in Nakhla and Governador Valadares show a similar texture of symplectites, that in Y000593 is slightly different (Fig. 1). Because exsolved augite and magnetite in lamellar symplectites are so fine-grained and complexly intergrown in all nakhlites studied, we could not analyze them. Thus, the EBSD analyses here were performed for the bleb symplectites that contain more coarse-grained exsolved phases.

The obtained magnetite EBSD patterns from

several different blebs in Nakhla and Governador Valadares are identical in a single olivine grain, and (100), [001] and [010] of olivine are parallel to $\{111\}$, $\langle 110 \rangle$ and $\langle 112 \rangle$ of magnetite, respectively (Fig. 2). These relationships are identical to [4-6]. However, the EBSD patterns of exsolved augite show a few different patterns and we could not find clear orientational relationship between augite and olivine/magnetite, but one of them is close to the relationship that $[011]_{\text{augite}}$ is parallel to $[010]_{\text{olivine}}$ and $\langle 112 \rangle_{\text{magnetite}}$ (Fig. 2) [4-6].

In Y000593, the obtained magnetite EBSD patterns from most symplectite blebs in a single olivine grain are also identical. However, augite in each symplectite shows different patterns and we could not find clear orientational relationship. Furthermore, we have not been in successful to give proper indices for the EBSD pattern from the host olivine. As briefly described before, the symplectite textures of Y000593 are slightly different from those of Nakhla and Governador Valadares (Fig. 1). Some of the symplectites in Y000593 contain silica (which is amorphous because no EBSD pattern was observed) and laihunite is reported [6]. It seems that Y000593 olivine contains symplectites formed at different stages (Fig. 1). Thus, more detailed analysis is required for the Y000593 symplectites.

Pyroxene twinning

Optical microscopy of the cumulus augite in nakhlites shows broad twin bands and some twin bands are then polysynthetically twinned with spacing of a few to tens of μm possibly caused by moderate shock (Fig. 3). The wide twin and polysynthetic twin are believed to be parallel to (100) and (001), respectively. We analyzed cumulus augite in Governador Valadares by the FSE imaging system. Because FSE images provide contrast for different orientations even in a homogeneous phase as stated before [2], we could observe contrast in the FSE images of augite twins due to different orientations (Fig. 3). We then analyzed these different orientation areas by EBSD and confirmed that the broad (100) twin and polysynthetic (001) twin share b and c axes and a and b axes in common, respectively (Fig. 3).

References:

- [1] Prior D. J. et al. (1996) *Mineral. Mag.*, 60, 859-869.
- [2] Kogure T. (2002) *American Mineral.*, 87, 1678-1685.
- [3] Fliervoet T. F. et al. (1999) *Tectonophysics*, 303, 1-27.
- [4] Mikouchi T. et al. (2000) *Meteorit. & Planet. Sci.*, 35, 937-942.
- [5] Moseley D. (1984) *American Mineral.*, 69, 139-153.
- [6] Noguchi T. et al. (2003) *NIPR Symp.*, 105-106.

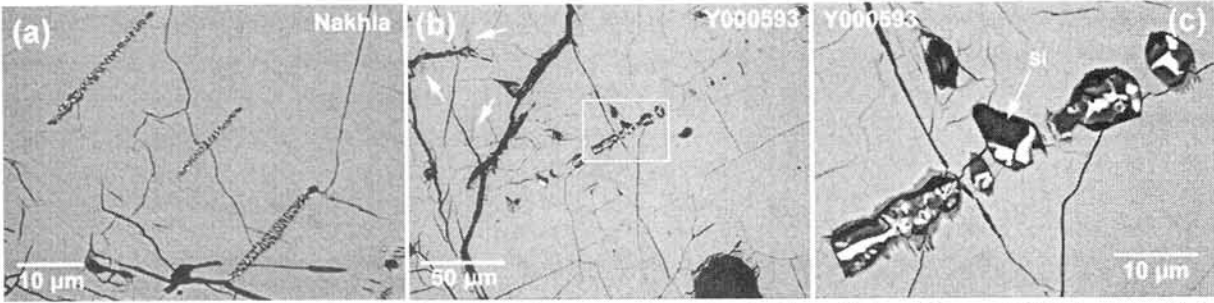


Fig. 1. BSE images of symplectites (mainly composed of magnetite and augite) in nakhlite olivines. (a) Nakhla. (b) and (c) Y000593. (c) is an enlarged area in (b). Arrows in (b) show lamellar symplectites similar to those in Nakhla (a). Si: silica.

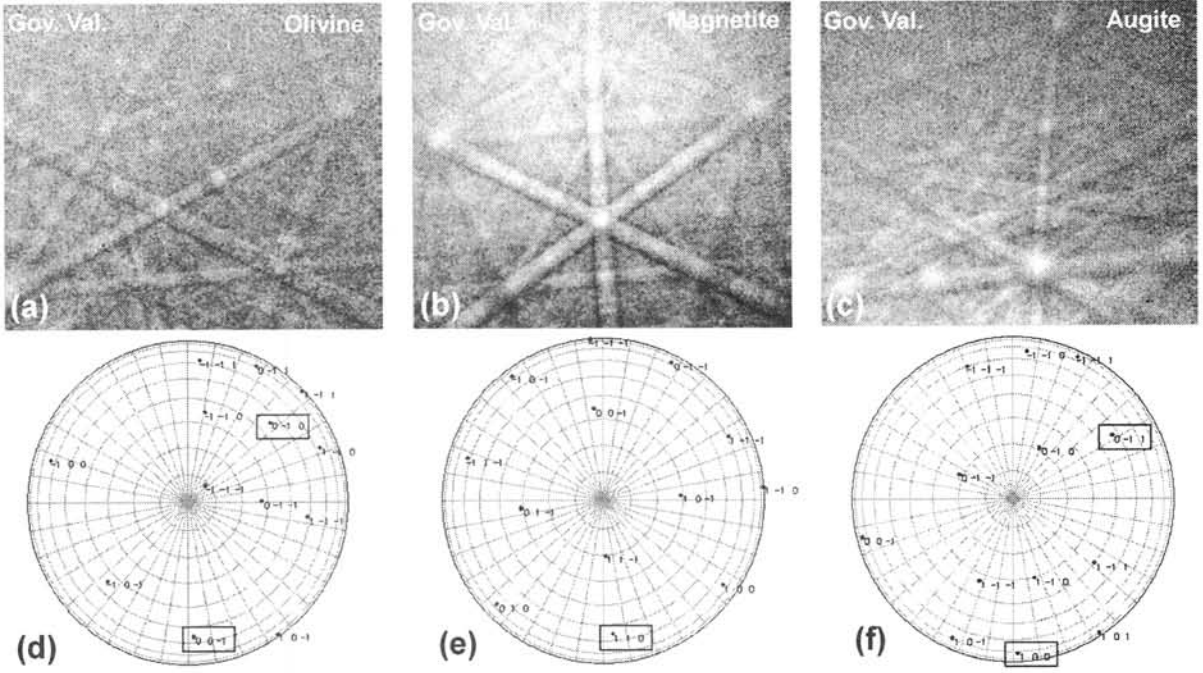


Fig. 2. Obtained EBSD patterns of (a) host olivine, (b) exsolved magnetite and (c) exsolved augite in Governor Valadares olivine. (d), (e) and (f) are stereo projections of (a), (b) and (c), respectively, after they were indexed by each mineral species. The results show their orientational relationship (see the text).

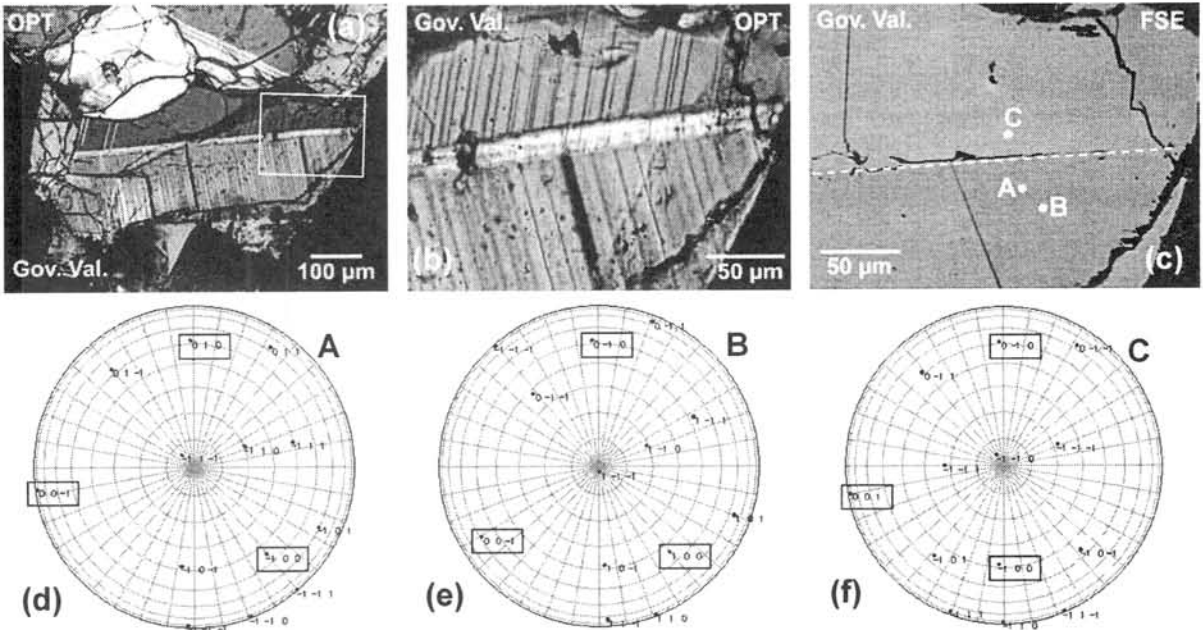


Fig. 3. (a) and (b) Optical photomicrographs (crossed nicols) and (c) FSE image of cumulus augite in Governor Valadares. Areas showing different orientations due to twinning show contrast in the FSE image of (c). (d), (e) and (f) are stereo projections of the EBSD patterns from A, B and C marked in (c), respectively.

Thermal history of chondrules during shock-wave heating. H. Miura^{1,2} and T. Nakamoto³,
¹Pure and Applied Sciences, University of Tsukuba, Japan, ²Research Fellow of the Japan Society for the Promotion of Science, ³Center for Computational Sciences, University of Tsukuba.

Introduction:

Chondrules are thought to be formed by melting and subsequent cooling of solid precursors. Evaporation during chondrule melting may have resulted in depletion of volatile elements in chondrules. The kinetic evaporation from a volatile melt leads to enrichment of heavy isotopes in an evaporation residue. However, no evidence for a large degree of heavy-isotope enrichment has been reported in chondrules. In order to explain this observed isotopic fractionation, the kinetic evaporation model suggests that a rapid heating rate of $> 10^4$ - 10^6 K/hr for a temperature range of 1273-1573 K is required (e.g., [1]).

One of the most appropriate heating mechanisms for chondrule formation is shock-wave heating model (e.g., [2]). The gas drag heating is so rapid that isotopic fractionation is expected to be suppressed ([1]). However, according to the simulations of shock-wave heating by [3], a dust particle in front of the shock front is heated by the thermal radiation of other dust particles. This effect is regarded as the blanket effect. In the case by [3], the heating rate of chondrules for a temperature range 1273-1573 K is about 300 K/hr. This is so slow that the isotopic fractionation will occur, this is not consistent with observations.

The blanket effect depends on the optical depth for dust thermal radiation. Obviously, the optically thinner the environment is, the less effective this effect becomes. Optical depth mainly depends on the dust/gas mass ratio, the dust size distribution, and the emission (absorption) coefficient of dust particle. In this study, we report the dust thermal history by shock-wave heating model including the radiative transfer effect. We pay attention to the effects of the size distribution of dust particles.

Our Shock-Wave Heating Model:

We assume that shock waves are generated in the solar nebula. We have developed the numerical model that simulates 1-dimensional plane-parallel steady shock flow including dust particles [4, 5]. In this model, the dynamics of the gas flow and the dust particles are treated in detail. The model takes into account following physical and chemical processes: hydrodynamics of gas flow, dynamics of dust particles in the gas medium, heating/cooling of gas by several processes (compressional heating, chemical reactions in gas phase, atomic/molecular radiative cooling/heating, and interaction with dust particles), non-equilibrium chemical reactions among 32 gas species, heating/cooling of dust particles by

the thermal interaction with gas and radiation, and evaporation of material from dust particles. The procedures for calculation are described in [4, 5]. In addition to those, in our current study, we also take into consideration the radiative transfer among dust particles. Details of the radiative transfer treatment are described in [3].

Optically Thick/Thin Environments:

In Figs. 1 and 2, we display the temperature profiles of gas and chondrule (T_g and T_c) and mean intensity (J) as a function of distance from shock front (x). We express the mean intensity using a radiation temperature T_{rad} which is given by $T_{rad} = (\pi J / \sigma_{SB})^{1/4}$, where σ_{SB} is the Stefan-Boltzmann constant. Shock front is assumed to be at $x = 0$. The difference between two figures is only the dust size distribution. In Fig. 1, we assume that the dust size distribution has a simple power-law form. The size is in a range $0.01\mu\text{m}$ - 1cm . In this case, since there are a lot of sub- μm -sized dust particles, the environment is optically thick. On the contrary, in Fig. 2, the dust size distribution is similar to that of measured chondrules (e.g., [6]), e.g. majority of dust mass is contained in chondrule-sized dust particles (diameter is about $600\mu\text{m}$). It corresponds to the optically thin environment.

Results:

Optically Thick Environment: In Fig. 1, chondrule temperature T_c rises up to about 1300 K in pre-shock region. Chondrules are irradiated by the line emissions from post-shock region and thermal radiation of other dust particles. Though we set the gas temperature T_g to 300 K at $x = -10^5$ km (boundary of chondrule-forming region we are considering now), it rises above 1000 K. Gas is mainly heated by the μm -sized dust particles. T_c is almost the same as radiation temperature T_{rad} , which is about 1300 K nearby the shock front. Behind the shock front, chondrules are heated up to 1536 K by the gas drag heating. The reason why T_c in front of the shock front becomes so high is that the thermal radiation of other dust particles is strong. The optical depth of the pre-shock region is 1.8, so the blanket effect works well. In such an optically thick environment, chondrule is kept at high temperature (> 1300 K) for a long time, so the isotopic fractionation will occur.

Optically Thin Environment: Fig. 2 shows results for an optically thin environment case. In pre-shock region, T_c is suppressed below 1200 K because T_{rad} is smaller than that of Fig. 1. Since T_g is lower than 400 K in the pre-shock region, it is not shown in

Fig. 2. The reason why T_{rad} is small is the optical depth is small. The optical depth of the pre-shock is about 0.3, so the blanket effect is not significant. Behind the shock front, chondrules are abruptly heated by the gas drag heating up to 1525 K. The heating rate of chondrule from $T_c=1273$ to the maximum temperature 1525 K is about 3×10^5 K/hr. It is rapid enough to be consistent with observed isotopic fractionation.

Discussion, to the Point in Cooling Rate:

The cooling rate of dust particles is important information for chondrule formation. After dust particles melt by the drag heating, they begin to cool. If $T_c > T_{rad}$, dust particles cool as the drag heating becomes weak. In this phase, the cooling rate is about 10^4 K/hr. If $T_c < T_{rad}$, heating is dominated by the radiation. In this phase, the cooling rate is of the order of 10^2 K/hr. Calculations of [3] show that the radiation dominates the drag heating through the crystallization temperature 1400-1730 K. However, the radiation temperature in the pre-shock region seems to be almost the same as that in the post-shock region. As a result, the dust particles in the pre-shock region slowly heated by radiation through these crystallization temperatures. We can estimate from figure 4(a) of [3] that the heating rate is about 300 K/hr. This is too slow to suppress isotopic fractionation because required heating rate is 10^4 - 10^6 K/hr or more in a temperature range of 1273-1573 K. Therefore, the radiation temperature should be lower than about 1273 K. Namely, the shock waves in an optically thin environment is consistent with observations of isotopic fractionation. In this case, the cooling rate should be about 10^4 K/hr because heating is dominated by the drag heating.

Finally, we would like to note that the value of cooling rate 10^4 K/hr is obtained for only a single shock condition (shock velocity is 7 km s^{-1} and pre-shock gas number density is $10^{14.5} \text{ cm}^{-3}$). Results for other shock conditions will be presented in our future paper.

Summary:

The appropriate shock waves for observations of isotopic fractionation should occur in the optically thin (not dusty) environment. If the environment is optically thick (dusty), the thermal radiation of other dust particles heats chondrules in the pre-shock region and keeps them high temperature for a long time, so isotopic fractionation will occur.

References:

- [1] Tachibana S. et al. (2004) *LPS XXXV*, 1549.
- [2] Boss A. P. (1996) In *Chondrules and Protoplanetary Disk*, 257. [3] Desch S. J. and Connolly H. C. Jr. (2002) *Meteorit. Planet. Sci.*, 37, 183. [4] Iida A. et al. (2001) *Icarus*, 153, 430. [5] Miura H. and Nakamoto T. (2004) submitted to

Icarus. [6] Nelson V. E. and Rubin A. E. (2002) *Meteorit. Planet. Sci.*, 37, 1361.

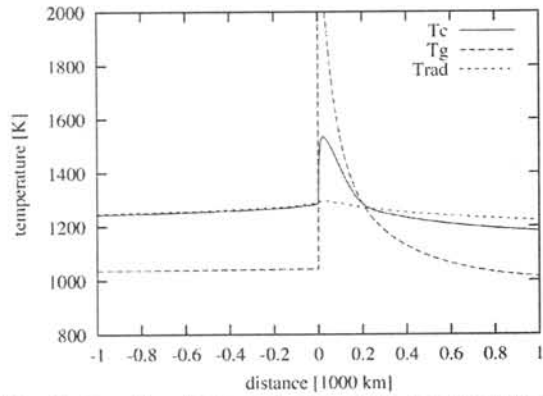


Fig. 1. Results of gas and chondrule temperature (T_g and T_c) and radiation temperature (T_{rad}) plotted as a function of distance from shock front. We assume a dusty environment (the dust size distribution is a power-law form between $0.01 \mu\text{m}$ - 1cm).

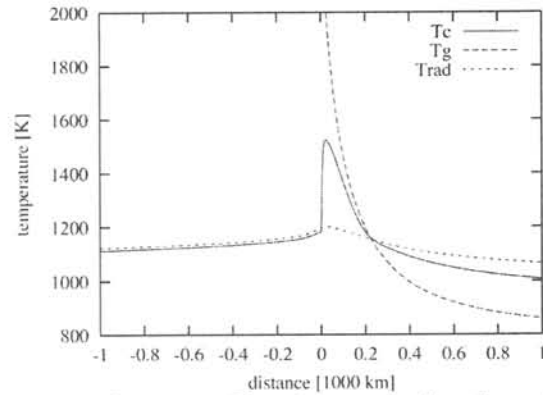


Fig. 2. Same as Fig. 1 except the dust size distribution. We assume the majority of dust mass concentrates chondrule-sized dust particles (diameter is about $600 \mu\text{m}$). This represents an optically thin environment case.

Noble gases in Northwest Africa 1670, a new angrite, and oxygen isotopes of this angrite and some achondrites. Y. N. Miura¹, N. Sugiura², M. Kusakabe³, K. Nagao⁴, ¹Earthquake Research Institute, University of Tokyo, Yayoi, Bunkyo-ku, Tokyo 113-0032, Japan. ²Department of Earth and Planetary Science, University of Tokyo, Hongo, Bunkyo-ku, Tokyo 113-0033, Japan. ³Institute for Study of the Earth's Interior, Okayama University, Misasa, Tottori 682-0913, Japan. ⁴Laboratory for Earthquake Chemistry, Graduate School of Science, Hongo, Bunkyo-ku, Tokyo 113-0033, University of Tokyo, Japan.

Introduction:

Six meteorites have been identified as angrite (Angra dos Reis, Asuka 881371, D'Orbigny, LEW 86010, LEW 87051 and Sahara 99555) [1, 2, 3]. Recently, another meteorite, Northwest Africa 1670 (NWA 1670), is classified into angrite [4]. This seventh angrite is a single stone of 29 g mostly covered by fusion crust with mm-sized pores [4]. We measured noble gases of NWA 1670 in order to investigate cosmic-ray exposure and thermal histories of the meteorite, and compare them with those of the other angrites. Oxygen isotopes were also determined for NWA 1670 to confirm genetic link to other angrites. Oxygen results for some other achondrites we measured recently are also presented here.

Experimental methods:

The bulk sample of NWA 1670 weighing 0.07646 g was used for noble gas analyses. Noble gas isotopic compositions including ⁸¹Kr were measured with a mass spectrometer system (modified VG5400) at Laboratory for Earthquake Chemistry, University of Tokyo. The sample loaded into a sample holder was preheated at 150 °C under ultra-high vacuum to remove adsorbed terrestrial atmosphere. Gases to be measured were extracted at the temperatures of 600 °C and 1750 °C. The analytical procedure is essentially similar to our standard one (e.g., [5]).

Oxygen isotope measurements were performed at ISEI, Okayama University. The system consists of oxygen extraction line with a CO₂-laser, a purification line and a mass spectrometer (modified VG-SIRA12). Details for apparatus and procedure were described in [6, 7]. Duplicated analyses were applied using about 2 mg samples (2.61 and 2.03 mg) for NWA 1670. For measurement of the other achondrites, we also used about 2 mg samples and adopted the same analytical procedure as NWA 1670.

Results and discussion:

Results on noble gases are presented in Table 1. Helium and Ne is mostly cosmogenic component with radiogenic ⁴He. Argon is a mixture of cosmogenic, trapped and radiogenic ⁴⁰Ar. The concentrations of cosmogenic ³He, ²¹Ne and ³⁸Ar were calculated to be 2.32×10^{-7} , 3.27×10^{-8} , 1.31×10^{-8} cm³STP/g, respectively. These concentrations are not similar to those of any other angrites. For

obtaining production rates of cosmogenic, we used equations proposed for eucrites [8], which are functions of target element abundances and the shielding parameter of ²²Ne/²¹Ne ratio. Since there is no available bulk chemical composition data on NWA 1670, we adopted averaged values of those for Asuka 881371 and LEW 87051 in accordance with close relation of NWA 1670 with the Asuka and LEW [9]. These three angrites are characterized by presence of magnesian olivine xenocrysts [9, 10], and bulk compositions are likely similar. T₃, T₂₁ and T₃₈ are obtained as 14.7, 16.5 and 8.1 m.y., respectively. Meteorites recovered from hot deserts often show partial loss of cosmogenic ³He and ³⁸Ar. The short T₃₈ of NWA 1670 is probably due to the terrestrial weathering. The ⁸¹Kr-Kr age is determined to be 17.6 ± 1.3 m.y. ($\lambda_{81} = 3.30 \times 10^{-6}$). From these data, we can constrain the exposure age of NWA 1670 is between 15 m.y. (T₃) and 18 m.y. by (T₈₁). The long T₈₁ may be for decay of ⁸¹Kr after fall to the Earth. Therefore, the average of T₃ and T₂₁ is considered as cosmic-ray exposure age for NWA 1670. The cosmic-ray exposure ages for all angrites are plotted in Fig. 1. Note that the cosmic-ray exposure age for LEW 86010 is re-calculated here (see also figure caption), because the production rates used in literature [11] seem to be too large compared with the currently adopted production rates. LEW 87051 gave only a lower limit of the exposure age due to intensive gas loss from the meteorite. NWA 1670 shows cosmic-ray exposure ages different from any other angrites. The seven angrites do not show characteristic peaks for cosmic-ray exposure ages, implying that most angrites were ejected by individual impact events. There seems to be at least five impact events at the angrite parent body that ejected the seven angrites.

We found fission derived Xe in NWA 1670. The concentration of fission ¹³⁶Xe is calculated to be 5.8×10^{-12} cm³STP/g. This is in the range reported for angrites ($3.9 - 19 \times 10^{-12}$ cm³STP/g), of which more than 90 % is estimated to be ²⁴⁴Pu-derived fission. From the observed fission Xe spectrum for NWA 1670 (¹³²Xe/¹³⁶Xe=0.76±0.16 and ¹³⁴Xe/¹³⁶Xe=0.938±0.104), majority of fission component seems to be ²⁴⁴Pu-derived fission (¹³²Xe:¹³⁴Xe:¹³⁶Xe=0.885:0.939:1). Therefore, it is expected that the angrite NWA 1670 also has an old ²⁴⁴Pu-Xe age and an ancient crystallization age as like other angrites.

Three isotope plot of oxygen is shown in Fig. 2. The oxygen isotopic compositions of NWA 1670 are

$\delta^{17}\text{O} = 2.01$ and $\delta^{18}\text{O} = 4.00$ (run #1) and $\delta^{17}\text{O} = 2.04$ and $\delta^{18}\text{O} = 3.97$ (run #2), respectively, which agree with $\delta^{17}\text{O} = 1.967$ and $\delta^{18}\text{O} = 3.887$ reported in [4] for this angrite. These data plot at an upper end of the area for angrites [12, 13]. NWA 1670 is abundant in Mg-rich olivine, whose origin is unclear (possibly exotic component related to the other class of meteorite [9]). Oxygen isotopic compositions slightly higher in $\delta^{17}\text{O}$ and $\delta^{18}\text{O}$ than other angrites may imply contribution of oxygen from the Mg-rich olivine which might be exotic. Other obtained results on oxygen isotopes are listed in the figure caption.

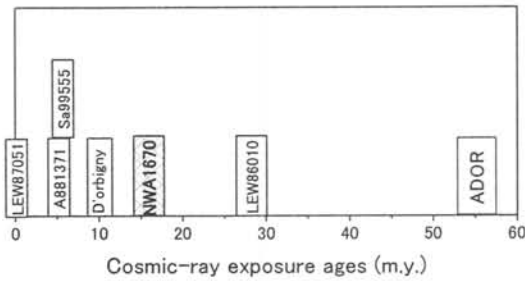


Fig. 1. Distribution of cosmic-ray exposure ages of angrites (NWA 1670 from this work, and the other angrites from ref [14] and references therein). For LEW 86010, we calculated the cosmic-ray exposure age using reported noble gas data [11] and production rates obtained by the same way as NWA 1670 in this work. LEW 87051 shows a very short cosmic-ray exposure age due to gas loss, which means a lower limit of the cosmic-ray exposure age. There seems to be at least five impact events at the angrite parent body that ejected the seven angrites.

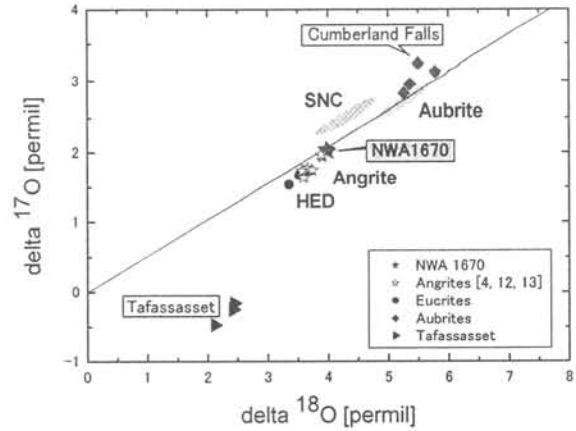


Fig. 2. Plot of $\delta^{17}\text{O}$ vs. $\delta^{18}\text{O}$, where $\delta^{17}\text{O} = ((^{17}\text{O}/^{16}\text{O})_{\text{sample}} / (^{17}\text{O}/^{16}\text{O})_{\text{SWOM}} - 1) \times 1000$. Three data for NWA 1670 (two solid star symbols determined in this work and the nearest open symbol taken from literature [4]) well agree each other. Other plotted data are as follows ($\delta^{17}\text{O}$, $\delta^{18}\text{O}$): DHO 007 eucrites (1.75, 3.61; 1.74, 3.69), Y-82066 eucrites (1.54, 3.35), Y-794002 eucrites (1.68, 3.52), Cumberland Falls aubrites (3.23, 5.50), Pena Blanca Spring aubrites (2.95, 5.37; 2.95, 5.36; 2.83, 5.26), Sallowater aubrites (3.12, 5.78) and Tafassasset primitive achondrite (-0.16, 2.44; -0.25, 2.42; -0.47, 2.12).

References:

[1] Grady M. M. et al. (2000) *Catalogue of Meteorites*, Cambridge Univ. Press. [2] Koblitz J. (2003) *Metbase*, CD-ROM. [3] Meteorit. Bulletin, No. 85, (2001). [4] Meteorit. Bulletin, No. 88 (2004) on web. [5] Miura Y. N. et al. (1998) *GCA*, 62, 2369-2387. [6] Jabeen I. et al. (1998) *Antarct. Meteorit. Res.* 11, 122-135. [7] Kusakabe M. et al. (2004) this volume. [8] Eugster O. and Michel Th. (1995) *GCA* 59, 177-199. [9] Mikouchi T. and McKay G. (2003) *GCA*, 67, A291. [10] Mikouchi T. and McKay G. (2003) *Meteorit. Planet. Sci.*, 38, A116. [11] Eugster O. et al. (1991) *GCA*, 55, 2957-2964. [12] Clayton R. N. and Mayeda T. K. (1996) *GCA*, 60, 1999-2017. [13] Bischoff A. et al. (2000) *Meteorit. Planet. Sci.*, 35, A27. [14] Kurat G. et al. (2004) *GCA*, 68, 1901-1921.

Table 1. Concentrations and isotopic compositions of He, Ne and Ar of the angrite NWA 1670.

	^4He	$^3\text{He}/^4\text{He}$	^{20}Ne	$^{20}\text{Ne}/^{22}\text{Ne}$	$^{21}\text{Ne}/^{22}\text{Ne}$	^{36}Ar	$^{38}\text{Ar}/^{36}\text{Ar}$	$^{40}\text{Ar}/^{36}\text{Ar}$
600°C	1660	0.06252 ±.00031	5.19	0.8538 ±.0031	0.8103 ±.0023	0.597	0.5331 ±.0041	294.15 ±1.32
1750°C	14370	0.00894 ±.00015	29.3	0.8141 ±.0017	0.7743 ±.0020	11.5	1.1705 ±.0068	41.85 ±.16
Total	16030	0.01449 ±.00014	34.5	0.8199 ±.0015	0.7795 ±.0017	12.1	1.1390 ±.0065	54.34 ±0.19

Concentrations are given in the unit of $10^{-9}\text{cm}^3\text{STP/g}$.

OXIDATION STATE OF IRON IN MARTIAN KAERSUTITES: A MICRO-XANES SPECTROSCOPIC STUDY. A. Monkawa, T. Mikouchi, E. Koizumi, K. Sugiyama M. Miyamoto. Department of Earth and Planetary Science, Graduate School of Science, University of Tokyo, 7-3-1 Hongo, Bunkyo-ku, Tokyo 113-0033, Japan

Introduction:

The presence of kaersutite (Ti-rich amphibole) in martian meteorites has been considered to indicate significant quantities of water in the pre-eruptive magmas [1-4]. Watson et al. [5] determined the D/H ratio and water content of kaersutite grains in Chassigny and Zagami by ion probe. The results show that these kaersutites have low water contents (0.1-0.2 wt%) with high D/H ratios. Therefore, it is doubtful whether the presence of kaersutite is direct evidence for water existence in martian parent magma. The low H content of martian kaersutite implies the presence of oxy-amphibole component (O^{2-} replaces OH in the O3 site of the amphibole crystal structure). Oxidation of Fe^{2+} in amphiboles behaves as the oxy-component. Fe^{2+} within an amphibole crystal structure can be oxidized to Fe^{3+} by the formation of oxy-amphibole and subsequent release of H. Fe^{3+} is accommodated within the amphibole crystal structure as an oxy-amphibole component.

The amounts of Fe^{3+} and Fe^{2+} are controlled by oxidation-dehydrogenation equilibrium. It is considered that oxidation-dehydrogenation of martian kaersutites occurred (1) during eruption of martian magma or (2) as a result of shock induced by a martian impact event. These models suggest that oxidation-dehydrogenation of originally H-rich kaersutite occurred as secondary alteration. The $Fe^{3+}/\Sigma Fe$ ratios of H-poor kaersutites in terrestrial rocks are usually higher than that of normal amphibole groups. This can be explained by oxidation-dehydrogenation in terrestrial kaersutites. If H content of martian kaersutites have changed by oxidation-dehydrogenation as well as terrestrial H-poor kaersutites, the $Fe^{3+}/\Sigma Fe$ ratio would be high. To elucidate the formation of low-H kaersutites in martian meteorites, it is necessary to determine their $Fe^{3+}/\Sigma Fe$ ratios. We determined the $Fe^{3+}/\Sigma Fe$ ratio by using synchrotron micro-XANES analysis.

Observation:

Kaersutites can be found as subhedral or euhedral small grains in magmatic inclusions of Chassigny olivines and both LEW88516 and Zagami pyroxenes. The size of Chassigny kaersutites is 50-80 μm (Fig. 1). This kaersutite has a high Ti content ($TiO_2 = \sim 7$ wt%). F and Cl abundances are low (F = 0.5 wt%, Cl = 0.1 wt%). LEW88516 kaersutite is up to 20 μm across and shows pleochroism from brownish orange to bright brown. This kaersutite is rich in Ti ($TiO_2 = 10$ wt%) and Al ($Al_2O_3 = 15$ wt%). Zagami kaersutite (10 μm across) is as small as that in LEW88516 and also rich in Ti ($TiO_2 = 10$ wt%).

Analytical method:

Fe-XANES spectra were recorded in fluorescence mode on Beamline 4A at the 2.5 GeV Photon Factory (KEK, Tsukuba, Japan) using bending magnet radiation. The transmitted and fluorescent X-rays were measured by an ionization chamber and a Si (Li) detector, respectively. The angle between the incident beam and the detector is fixed at 90° . Kirkpatrick-Baez geometry mirrors were used to focus the beam to a $5 \times 6.5 \mu m$ spot on the specimen. Spectra were recorded from 7103–7153 eV using a 0.13 eV step size for the pre-edge and edge regions. The energy was calibrated by defining the first derivative peak of Fe foil to be 7111 eV and standard kaersutite was measured at regular intervals to determine the energy reproducibility. Each energy interval was counted between 45 live seconds for a total XANES spectrum acquisition time of about 4 hours. We prepared a calibration line for martian kaersutites on the basis of XANES pre-edge positions in spectra of standard kaersutites whose Fe^{3+} contents were determined by wet chemistry. By using this calibration line, we measured Fe-XANES spectra of martian kaersutites (Chassigny, LEW88516 and Zagami).

XANES pre-edge positions of kaersutites depend on their crystallographic orientations [6]. In order to correct the pre-edge positions depended on different crystallographic orientation, we determined crystallographic orientations of martian kaersutites by EBSD equipped with FEG-SEM, and compared Fe-XANES spectra of martian kaersutites with those of standard kaersutites whose crystallographic orientations were determined by single crystal X-ray diffraction (precession camera).

Results:

XANES spectra of standard kaersutites ($Fe^{3+}/\Sigma Fe$ ratio = 0) recorded at the three different crystallographic orientations, are shown in Fig. 2 (A-C). A is spectrum acquired parallel to the stacking direction of the chains, B is spectrum polarized parallel to the direction across the chains, and C is spectrum acquired with the beam parallel to the length of the chains. Compared with these spectra, the main-edge features of A and C spectra are different from that of B, the pre-edge centroid of A and C spectra shift to lower energy than that of B. These result show that pre-edge centroid of kaersutite is constant when X-ray beam polarized in the *a-c* plane of the kaersutite. We determined crystallographic orientation of martian kaersutites by EBSD analysis, and selected kaersutites facing close to the *a-c* plane.

XANES pre-edge centroids of martian kaersutites are located at lower energy than those of Fe oxy kaersutites ($\text{Fe}^{3+}/\Sigma\text{Fe} = 0.5$ and 1). XANES pre-edges of kaersutites in both Chassigny and LEW88516 are located at almost the same position as standard kaersutite whose $\text{Fe}^{3+}/\Sigma\text{Fe}$ ratio is 0 (Fig. 3), suggesting that the Fe^{3+} contents of these martian kaersutites are low. In contrast, the XANES pre-edge centroid of Zagami kaersutite is closer to that of standard kaersutite whose $\text{Fe}^{3+}/\Sigma\text{Fe}$ ratio is 0.36.

Discussions:

Dyar et al. [6] reported the extent of X-ray anisotropy in biaxial minerals from measurement of Fe XANES spectra on single crystals of amphiboles with the X-ray beam polarized along the X, Y and Z optical orientations. We confirmed that Fe XANES spectrum of kaersutite depends on the crystallographic orientation, that XANES pre-edge centroid of kaersutite is constant in *a-c* plane. In order to correct error by extent of X-ray anisotropy, it is necessary to measure XANES spectra of standard and unknown kaersutite samples in the *a-c* plane. Although this analytical method can not correct all error in $\text{Fe}^{3+}/\Sigma\text{Fe}$ determinations by Fe XANES measurement, the method can minimize error in $\text{Fe}^{3+}/\Sigma\text{Fe}$.

The low H content of martian kaersutite implies the presence of oxy-amphibole component. Fe^{3+} is accommodated within the amphibole crystal structure as an oxy-amphibole component. On the basis of these estimated $\text{Fe}^{3+}/\Sigma\text{Fe}$ ratios of kaersutites in both Chassigny and LEW88516, oxidation-dehydrogenation is not responsible for low-H contents of these martian kaersutites. On the other hand, the H content in Zagami kaersutite may have changed by oxidation-dehydrogenation because Zagami kaersutite has a moderate amount of Fe^{3+} . However, based on the result of this study, the low H content in Zagami kaersutite can not be explained only by oxidation-dehydrogenation because the loss of H content in the kaersutite by oxidation-dehydrogenation is small. Therefore, it is unlikely that H in these martian kaersutites is lost by oxidation-dehydrogenation of kaersutite.

Ti is also accommodated within the amphibole crystal structure as an oxy-amphibole component. We found that martian kaersutite has a large Ti oxy-component based on the relationship between H and Ti of kaersutite from chemical analysis of terrestrial and martian kaersutites. This means that the H deficiency for martian kaersutite can be explained by Ti oxy-substitution. For the above reason, we propose that the H content of the martian kaersutites is low mainly due to the presence of Ti oxy-component rather than Fe oxy-component.

References: [1] Floran R. J. et al. (1978) *GCA*, 42, 1213-1229. [2] Treiman H. (1985) *Meteoritics*, 20, 227-242. [3] Johnson M. C. et al. (1991) *GCA*, 55,

349-366. [4] McSween H. Y. and Harvey R. P. (1993) *Science*, 259, 1890-1892. [5] Watson L. L. et al. (1994) *Science*, 265, 86-90. [6] Dyar M. D. et al. (2002) *Canadian Mineral.*, 40, 1375-1393.

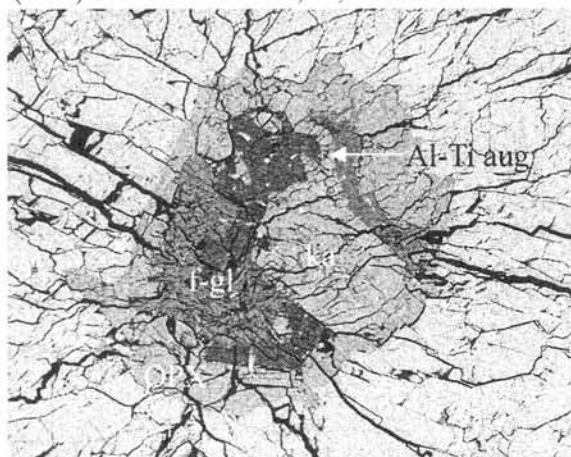


Fig. 1. Backscattered electron image of the magmatic inclusion in Chassigny. Phases in the inclusion include low-Ca pyroxene (OPX), Al-Ti rich augite (Al-Ti aug), kaersutite (ka) and feldspathic glass (f-gl).

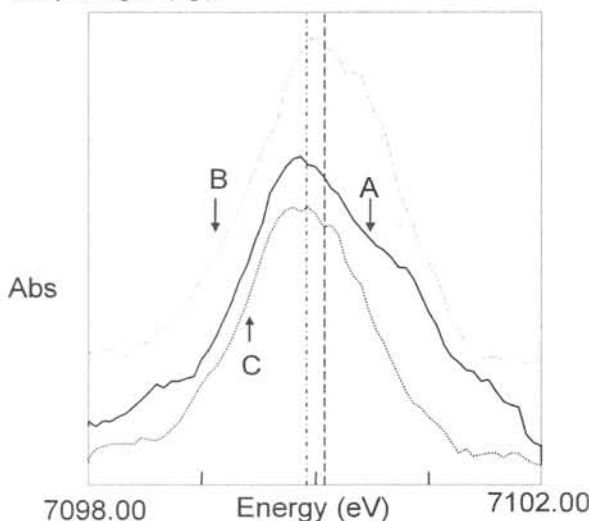


Fig. 2. XANES pre-edge spectra of standard kaersutites ($\text{Fe}^{3+}/\Sigma\text{Fe}$ ratio = 0) recorded at the three different crystallographic orientations

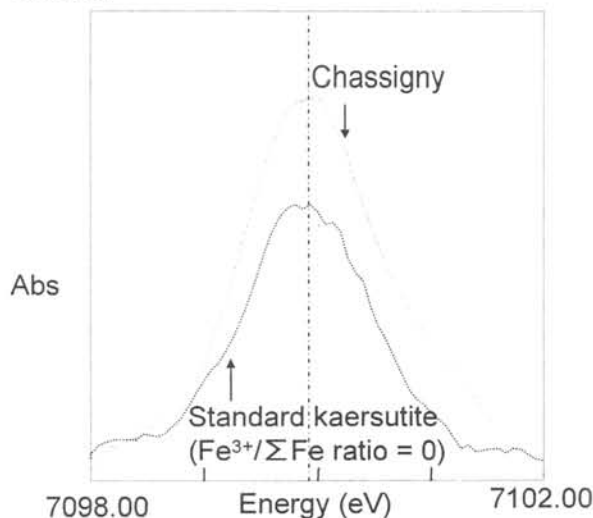


Fig. 3. XANES pre-edge spectra of standard kaersutites ($\text{Fe}^{3+}/\Sigma\text{Fe}$ ratio = 0) and Chassigny kaersutite.

Chondrule age distribution and degree of heating for chondrule formation.

T. Nakamoto¹, N. T. Kita², and S. Tachibana³, ¹Center for Computational Sciences, University of Tsukuba, ²Geological Survey of Japan, AIST, ³Department of Earth and Planetary Science, University of Tokyo.

Introduction:

Chondrules are believed to have formed through some of heating events in the early solar system. Although several heating mechanisms have been proposed to date, no one has been widely accepted. In this work, we attempt to reveal the gross feature of the heating events, especially the degree of heating, h , which is the fraction of material that experiences heating events per unit time, and its time variation. The degree of heating h can be deduced without specifying any particular heating mechanism by using the fraction of chondrules in chondrites and the age distribution of chondrules as constraints.

Since the age distribution of chondrules is not well-determined, we examine it first. Then, we make a simple model for chondrule formation and obtain h as a function of time by comparing model results with observations.

Age Distribution:

We compiled the ^{26}Al - ^{26}Mg ages of 22 UOC chondrules from type 3.0-3.1 ordinary chondrites [1-5]. We do not include data from UOCs with petrologic sub-types higher than 3.3 because there is a possibility of age resetting by the mild thermal metamorphism [2, 6]. From this data set, we obtain age variation somewhere between 1 Myr and 3 Myr (a time of zero is assigned to the formation time of CAI) with a peak near 1.8 Myr, though many data show a large age error of > 0.5 Myr, making it difficult to estimate detailed age distribution. We consider the age distribution, showing a peak at ~ 2 Myr, well represents the general trend among chondrules from LL chondrites, although detail distributions should not be considered seriously.

Mostefaoui and co-workers first indicated that there is a correlation between ^{26}Al -ages of LL3.0-3.1 chondrules and their pyroxene/olivine ratios in phenocrysts; younger chondrules tend to contain more pyroxene phenocrysts [4]. This is further recognized as a correlation between ^{26}Al -ages and bulk volatile (Si, Mn, Na)/Mg ratios by Tachibana et al. [7], indicating that chondrule bulk chemical compositions changed to Si- and volatile-rich compositions with time. If we assume this correlation to the whole population of chondrules, we can estimate age distribution by applying bulk Si/Mg distribution of chondrules. Recently, Tomomura et al. [5] obtained the bulk Si/Mg ratios of randomly selected 89 chondrules from two LL3.1 chondrites. They converted the Si/Mg distribution to the age distribution as shown in Fig. 1. We can see the peak at 1.8 Myr as in the case of measured data. The measured data show much wider distribution, mostly

to younger ages. It is probably due to large age errors spreading the real distribution, though there is also problem of the estimate of age-Mg/Si correlation line. Nevertheless, the measured chondrule data and the estimated age distribution both indicate that the ages of chondrules distribute between 1 Myr and 3 Myr with a peak at 1.8 Myr.

Chondrule Formation Model:

We make a simple phenomenological model for chondrule formation to examine the degree of heating h . Here, we do not specify any heating mechanism. We assume that all the chondritic material is categorized into two groups, for simplicity: "matrix material," which includes small dust particles consisting of matrix and large unheated dust aggregates, and "chondrules." Chondrule formation is modeled as follows: (1) all the material is in a closed volume where chondrule formation/destruction and accretion of chondrite parent bodies take place, (2) the process is a local event and affects only a minor fraction of material in the volume at a time, but occurs many times during the chondrule formation epoch, (3) a certain fraction of heated "matrix material" ("chondrule") is converted to "chondrule" ("matrix material") by the chondrule forming (destructing) heating events, and (4) the age of a chondrule, which is the last heating time of the chondrule, is reset by the heating event. The degree of heating h is defined as the fraction of the material in the volume affected by the heating events in a unit time. When we assume that conversion factors from heated "matrix material" ("chondrule") to "chondrule" ("matrix material") are constant during the chondrule formation epoch, the fraction of chondrules among all the material, the fraction of reheated chondrules, and the chondrule age distribution can be obtained as functions of $h(t)$.

Results:

Total amount of heating: The model shows that the total amount of heating, which is the time integration of the degree of heating $h(t)$ over the chondrule formation epoch, should be more than 1.2 times the total amount of material to reproduce the observed fraction of chondrules in ordinary chondrites (70% is the adopted value here). This means that a dust particle is averagely heated more than 1.2 times during the heating epoch. Thus, it is implied that a dust particle is heated about 1 time at every 10^6 yr. Interestingly, this result does not depend on the time variation of $h(t)$.

Fraction of reheated chondrules: The fraction of the reheated chondrules among all the chondrules is also

obtained as the function of the total amount of heating. It is suggested that about 60-95% (depending on the conversion factors) of chondrules should have been reheated, which is consistent with the idea of chondrule recycling.

Age distribution of chondrules: The age distribution of chondrules is dependent on the time variation of the degree of heating h . We used several cases of evolution of h (case 1: constant, case 2: linearly decreasing, case 3: sinusoidal with a peak, and case 4: exponential decreasing) to calculate the (last heated) age distribution of chondrules. Obtained distributions are displayed in Fig. 2. It is seen that three types of $h(t)$, i.e., linear, sinusoidal, and exponential cases produce age distributions similar to estimated one shown in Fig. 1.

Conclusions:

What we have found are summarized as follows.

(1) The age of chondrules in LL chondrites is estimated to be in a range from 1 Myr to 3 Myr after the CAI formation time with a peak around 2 Myr. (2) Each chondrule-forming event heated only a small fraction of dust material at a time and numerous heating events are necessary to produce abundant chondrules. (3) The average number of heating events experienced by a dust particle is more than 1.2 times. (4) More than half of the chondrules have been reheated. (5) The age distribution is well reconstructed by three types of $h(t)$, i.e., linearly decreasing, sinusoidal with a peak, and exponentially declining functions of time. The starting and ending times of chondrule formation are 0.4-1.5 Myr and 2.2-2.3 Myr after CAI formation. The total duration of chondrule formation epoch is 0.7-1.9 Myr. (6) The degree of heating $h(t)$ should decrease monotonically with time after the peak of the age distribution. (7) The peak of $h(t)$ is 0.1-0.8 Myr earlier than the peak of the age distribution of chondrules. (8) Chondrule-forming heating events seem to have started about 0.4 Myr (or more) after the CAI formation time, implying that chondrule formation events were different from CAI formation events. These constraints will help us elucidate the chondrule forming mechanism.

References:

[1] Hutcheon I. and Hutchison R. (1989) *Nature* 337, 238-241. [2] Kita N. T. et al. (2000) *GCA* 64, 3913-3922. [3] McKeegan K. D. et al. (2000) *LPS XXXI*, Abstract #2009. [4] Mostefaoui S. et al. (2002) *Meteoritics & Planet. Sci.* 37, 421-438. [5] Tomomura et al. (2004) *LPSC XXXV*, Abstract #1555. [6] Huss G. R. et al. (2001) *Meteoritics & Planet. Sci.* 36, 975-997. [7] Tachibana S. et al. (2003) *Meteoritics & Planet. Sci.* 38, 939-962.

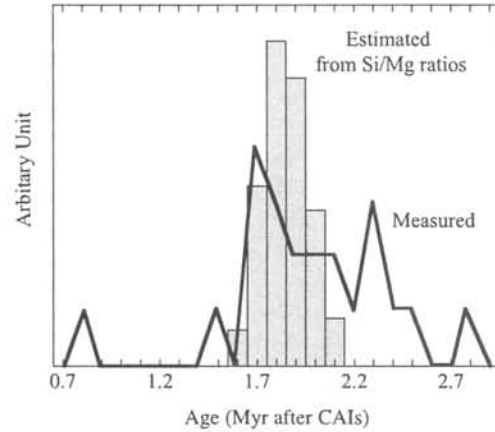


Fig. 1. Estimated age distribution of chondrules based on the correlation between ages and Si/Mg ratios [5]. "Measured" (a solid line) indicates the age distribution of porphyritic chondrules in LL3.0-3.1 chondrites (Data from [1-5]).

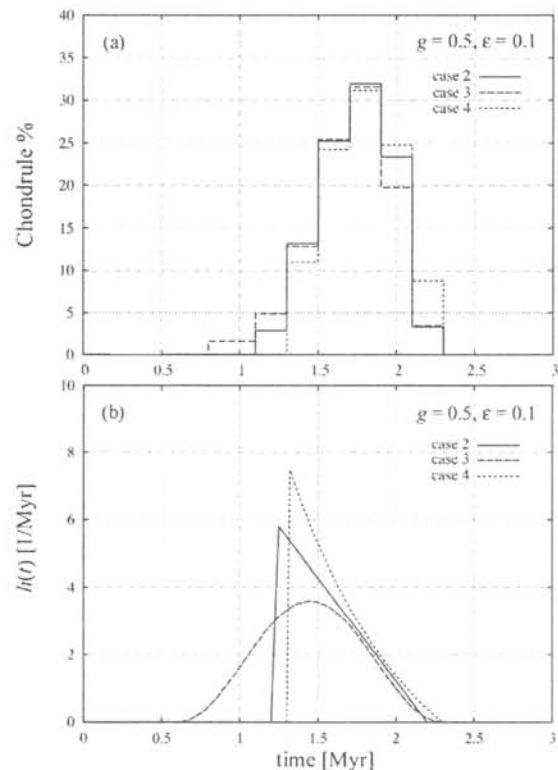


Fig. 2. Best fit age distributions (a) and the degree of heating $h(t)$ (b). The formation/destruction coefficients are chosen to be 0.5 and 0.1, respectively.

Morphologies of graphite in ureilites: Implications for the petrogenesis of ureilites.

Y. Nakamuta, Kyushu University Museum, Kyushu University, Fukuoka 812-8581, Japan,
e-mail address: nakamuta@museum.kyushu-u.ac.jp.

Introduction:

Ureilites comprise a meteorite group of achondrites, being mainly composed of olivine and pigeonite. They are unique among achondrites in containing relatively a large amount of primordial noble gases and carbon occurring as graphite and diamond. The primordial noble gases are thought to be exclusively contained in carbon minerals [1]. It has been a problem to reconcile the primordial natures as chondritic abundances of noble gases to igneous or metamorphic natures as coarse-grained recrystallized olivine and pyroxenes. To resolve the problem and give a constraint to the petrogenesis of ureilites it may be important to know the form and the mode of occurrence of carbon minerals in ureilites. So far, carbon minerals are thought to be interstitial material, often referred to as matrix or vein material together with metal, sulfide and minor fine-grained silicates.

Recently, large, mm-sized, euhedral graphite crystals were found in some ureilites [2] and diamond in ureilites was shown to have formed from well-crystallized graphite by shock at the time when the ureilite parent body or bodies broke up [3]. Then, it may be reasonable to think that graphite is a mineral that occurred through igneous or metamorphic processes together with olivine and pyroxenes, even though some parts of it were converted to diamond by a later shock-event. In this study, polished thin sections (PTSs) of ten Antarctic ureilites having variable olivine-core mg# ($\text{Mg}/(\text{Mg} + \text{Fe})$ molar%) were observed by an optical microscope in reflected light and the mode of occurrence and morphologies of graphite were described.

Experiments:

PTSs of ten Antarctic ureilites listed in Table 1 were observed by an optical microscope in reflected light. C-rich grains selected from disaggregated samples of each ureilite preserved in NIPR were X-rayed by using a Gandolfi camera and carbon minerals composing them were identified based on their X-ray powder diffraction patterns. Raman spectra were also obtained in order to identify tiny crystals in some PTSs by using a laser-Raman spectrometer with 1 micrometer-beam radius.

Results:

ALH 78019 and Y-8448 contain only well-crystallized graphite as a carbon mineral, Y-8448 and Y-74659 contain both well-crystallized graphite and grains composed of graphite and diamond, which are thought to have formed by partial conversion of graphite to diamond by a later

shock-event [3], and other six ureilites exclusively contain carbon grains composed of graphite and diamond.

Graphite in PTSs shows tan-gray color and metallic luster. Graphite that was partially converted to diamond shows black in color in PTSs, however, almost preserves external forms of primordial graphite. Then, the external forms of carbon grains composed of graphite and diamond were thought to represent the forms of primordial graphite. Graphite in ureilites occurs in olivine or pyroxene crystals or interstitially as blade-like, lath or amoeboid shapes. Photomicrographs of graphite in ALH 78019 and Y-82100 are shown in Fig. 1. Graphite in ALH 78019 shows exclusively lath shapes and that in Y-82100 shows amoeboid shapes. The morphologies of graphite in each PTS are summarized in Table 1 along with mg# of olivine reported for each ureilite in literatures. In Table 1, samples are arranged in the increasing order of mg#. Blade-like shaped graphite is minor but observed in all samples.

Discussion:

In Table 1, it is remarkable that graphite in low-mg# ureilites shows lath shapes and graphite in medium to high-mg# ureilites shows amoeboid shapes. The intimate relation between graphite shapes and olivine mg# strongly suggests that graphite crystallized during igneous or metamorphic processes together with olivine and pyroxenes. The lath-shaped graphite appears as euhedral crystals, but euhedral-appearing graphite crystals can also form during metamorphism, for example, graphite flakes in marble. It may be reasonable to think that lath-shaped graphite crystals were formed in a condition near to metamorphism since lath-shaped graphite occurs mainly at grain boundaries among silicate minerals. Amoeboid-shaped graphite can be thought to have formed in a condition where liquid phase was much abundant since rounded olivine crystals were enclosed in amoeboid graphite. The results may be consistent with high-temperature formation of high-mg# ureilites [4].

References:

- [1] Mittlefehldt D.W. (1997) *Planetary Materials*, 473-495.
- [2] Berkley J.L. and Jones J. H. (1982) *JGR*, 87, A353-A364.
- [3] Nakamuta Y. and Aoki Y. (2000) *Meteorit. Planet. Sci.*, 35, 487-493.
- [4] Shinha S. K. et al. (1997) *GCA*, 4235-4242.
- [5] Goodrich C.A. and Berkley J.L. (1986) *GCA* 50, 681-691.
- [6] Takeda H. et al. (1979) *Mem. NIPR Special Issue* 15, 54-73.
- [7] Takeda H. et al. (1988) *Proc. NIPR Symp. Antarct. Meteorites* 1, 145-172.
- [8] Takeda H. (1987) *EPSL* 81, 358-370.

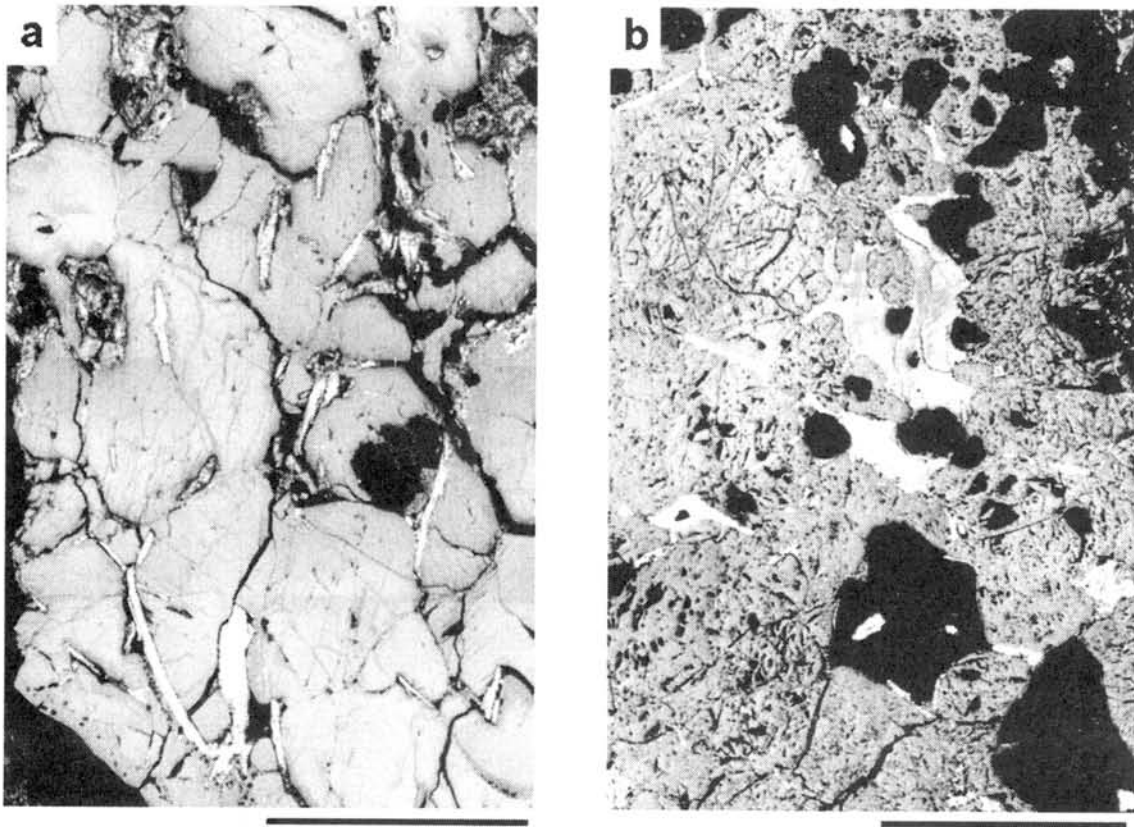


Fig. 1 Photographs of graphite (bright colors) in ALH 78019 (a) and Y-82100 (b) by an optical microscope in reflected light. Graphite in a and b-photographs show lath and amoeboid-shapes, respectively. Solid lines under photographs show 1 mm in length.

Table 1 Relative abundance and shapes of graphite in ureilites along with mg# of olivine.

Polished thin section	Relative abundance of graphite	Graphite shapes		Olivine composition	
		lath-shaped	amoeboid-shaped	mg#	reference
ALH 78019, 56-1	+++	○	—	76.2	[5]
Y-74130, 63-2	+++	○	—	77.1	[6]
MET 78008, 61-2	+++	○	△	77.3	[7]
ALH 78262, 83-2	++	○	—	77.7	[5]
Y-8448, 61-1	+++	○	—	78	[1]
Y-82100, 51-1	+++	—	○	81.8	[7]
Y-74123, 92-2	+++	—	○	86.2	[7]
ALH 77257, 73-1	+++	—	○	87.1	[8]
Y-791538, 71-1	+	—	○	91.8	[7]
Y-74659, 97-4	+	—	○	91.9	[8]

+++ : abundant, ++ : medium, + : rare, ○ : dominant, △ : subdominant, — : minor.

THERMOLUMINESCENCE STUDY OF JAPANESE ANTARCTIC METEORITES VIII

K. Ninagawa¹, N. Imae², H. Kojima², and K. Yanai³

¹Okayama University of Science, ²National Institute of Polar Research, ³Iwate University.

Natural TL (thermoluminescence), the luminescence of a sample that has received no irradiation in the laboratory, reflects the thermal history of the meteorite in space and on Earth. Natural TL data thus provide insights into such topics as the orbits of meteoroids, the effects of shock heating, and the terrestrial history of meteorites. Induced TL, the response of a luminescent phosphor to a laboratory dose of radiation, reflects the mineralogy and structure of the phosphor, and provides valuable information on the metamorphic and thermal history of meteorites. The sensitivity of the induced TL is used to determine petrologic type of type 3 ordinary chondrites.

As reliable pairing approach, TL properties within large chondrites were analyzed, taking advantage of the fact that serial samples from these meteorites is known to be paired [1]. Then a set of TL pairing criteria: 1) the natural TL peak height ratios, LT/HT, should be within 20%; 2) that ratios of raw natural TL signal to induced TL signal should be within 50%; 3) the TL peak temperatures should be within 20°C and peak widths within 10°C was proposed. This set of TL pairing criteria is less restrictive than previously used [1].

We have measured TLs of 82 Yamato and 101 Asuka unequilibrated ordinary chondrites so far [1,2,3,4,5]. This time we measured TL of more 30 Asuka chondrites. Twenty one of them are from 10km west of point A233 (D2), and 9 of them are from point A233 (D3) of around the Sør Rondane Mountains. The TL data of them are listed in Table. The petrologic subtype was determined from their TL sensitivity. Three chondrites, A-881408 (LL3), A-881607 (LL3), and A-881522 (L3) were primitive below subtype 3.3. However TL sensitivities of A-881494 (L3) and A-881558 (H3) conflicted with main trend of correlation between TL sensitivity and olivine heterogeneity as shown in figure 1. These chondrites would be received heavy shock or heavy weathering. In some cases, the TL sensitivity of the samples was increased by a factor of 10, although the typical increase was a factor of 2-3 for Antarctic meteorites [6]. The factor 10 makes increase of subtype only 0.3. We also found that A-881522 (L3) is in the lower cluster.

Above pairing criteria were also applied to the Asuka unequilibrated chondrites. A-881597 and A-881609 were paired in H3 chondrites.

References: [1] Ninagawa et al. (1998): Antarctic Meteorite Res., 11, 1-17. [2] Ninagawa et al. (2000): Antarctic Meteorite Res., 13, 112-120. [3] Ninagawa et al. (2002): Antarctic Meteorite Res., 15, 114-121. [4] Ninagawa et al. (2002): Papers presented to the twenty-seventh Symposium on Antarctic Meteorites, 128-129. [5] Mieda et al. (2003): Evolution of Solar System Materials: A New Perspective from Antarctic Meteorites, 80-81. [6] Benoit et al. (2002) Meteoritics & Planetary Science, 37, 793-805.

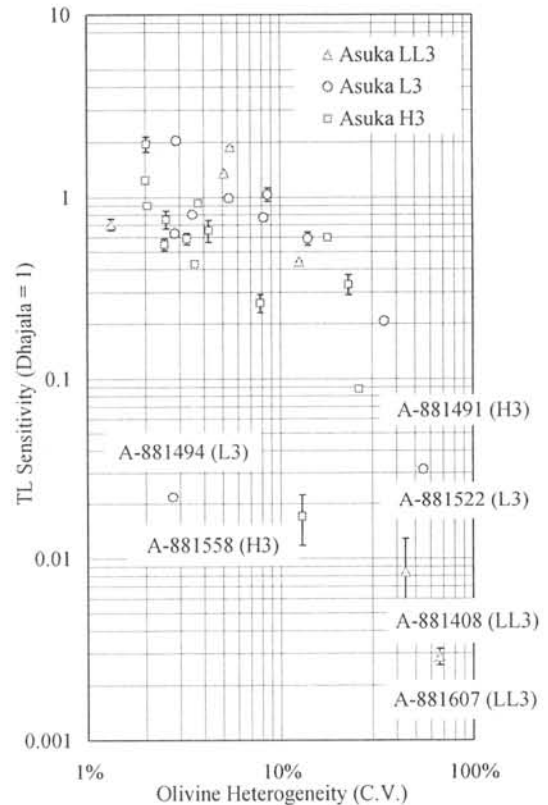


Fig.1. Correlation between TL sensitivity and olivine heterogeneity

Table Thermoluminescence data of Okayama for thirty unequilibrated Japanese ordinary chondrites

Meteorite	Class	Natural TL		Induced TL			L.T.		Low Ca-Py Heterogeneity (C.V.)†	Ol Heterogeneity (C.V.)‡	Ol Subtype	Recom- mended Subtype	Sampling site
		L.T/HT	L.T (10 ³ counts)	TL Sensitivity (Dhajala=1)	Peak Temp. (°C)	Width (°C)	TL Subtype	/TL Sens. (x10 ³)					
A-881405	L3	6.77 ± 0.05	251.3 ± 0.7	2.04 ± 0.01	137 ± 4	138 ± 0	3.8	123 ± 0	26%	3%		D2	
A-881408	LL3	3.99 ± 0.25	0.6 ± 0.1	0.008 ± 0.004	261 ± 140	186 ± 31	3.0-3.2	71 ± 38	73%	44%	3.5	D2	
A-881411	H3	6.92 ± 0.23	85.5 ± 10.5	0.65 ± 0.09	169 ± 5	140 ± 2	3.7	131 ± 24	9%	4%		D2	
A-881412	L3	3.07 ± 0.02	40.1 ± 1.4	0.63 ± 0.09	151 ± 0	158 ± 3	3.7	64 ± 2	38%	3%		D2	
A-881418	LL3	3.24 ± 0.03	95.6 ± 2.2	1.35 ± 0.00	160 ± 0	139 ± 2	3.8	71 ± 2	8%	5%	3.9	D2	
A-881420	H3	2.14 ± 0.08	73.4 ± 4.9	1.96 ± 0.19	161 ± 1	133 ± 0	3.8-3.9	37 ± 4	8%	2%		D2	
A-881436	L3	8.89 ± 0.46	171.4 ± 21.4	1.04 ± 0.09	159 ± 14	152 ± 5	3.7-3.8	165 ± 25	29%	9%	3.9	D2	
A-881437	L3	8.07 ± 0.15	159.3 ± 0.1	0.80 ± 0.02	161 ± 1	155 ± 2	3.7	199 ± 4	30%	3%		D2	
A-881460	H3	3.09 ± 0.09	18.1 ± 0.0	0.26 ± 0.03	179 ± 1	156 ± 2	3.5-3.6	69 ± 8	24%	8%	3.9	D2	
A-881484	L3	1.74 ± 0.06	0.2 ± 0.0	0.21 ± 0.00	175 ± 0	163 ± 0	3.5-3.6	0.9 ± 0.1	39%	35%	3.6	D2	
A-881491	H3	1.99 ± 0.04	2.8 ± 0.2	0.088 ± 0.003	114 ± 7	143 ± 10	3.4	32 ± 3	35%	26%	3.7	D2	
A-881492	H3	2.45 ± 0.04	16.3 ± 1.6	0.33 ± 0.04	177 ± 1	150 ± 2	3.6	50 ± 8	20%	23%	3.7	D2	
A-881493	H3	0.20 ± 0.00	1.9 ± 0.1	0.59 ± 0.04	170 ± 0	138 ± 3	3.7	3.2 ± 0.2	20%	3%		D2	
A-881494	L3	1.07 ± 0.00	2.6 ± 0.2	0.02 ± 0.00	174 ± 0	166 ± 2	3.2-3.3	117 ± 11	10%	3%		D2	
A-881498	L3	5.17 ± 0.35	170.6 ± 6.4	0.99 ± 0.03	160 ± 17	162 ± 7	3.7-3.8	172 ± 9	49%	5%	3.9	D2	
A-881512	LL3	0.39 ± 0.01	2.5 ± 0.2	0.44 ± 0.01	163 ± 10	176 ± 4	3.6-3.7	6 ± 1	47%	13%	3.8	D2	
A-881522	L3	1.33 ± 0.10	0.31 ± 0.0	0.031 ± 0.001	98 ± 0	115 ± 14	3.3	10 ± 0	90%	55%	<3.5	3.3	
A-881538	H3	2.14 ± 0.05	26.1 ± 1.9	0.90 ± 0.01	168 ± 5	159 ± 5	3.7	29 ± 2	18%	2%		D2	
A-881539	H3	2.32 ± 0.09	65.2 ± 1.0	1.24 ± 0.05	166 ± 4	164 ± 4	3.8	53 ± 2	21%	2%		D2	
A-881544	H3	0.19 ± 0.02	0.66 ± 0.00	0.43 ± 0.01	167 ± 3	166 ± 2	3.6	2 ± 0	25%	4%		D2	
A-881546	H3	2.27 ± 0.64	0.69 ± 0.02	0.55 ± 0.04	172 ± 2	165 ± 2	3.7	1 ± 0	9%	2%		D2	
A-881558	H3	0.49 ± 0.00	0.06 ± 0.01	0.017 ± 0.005	319 ± 29	235 ± 46	3.1-3.3	4 ± 1	40%	13%	3.8	D3	
A-881567	LL3	4.46 ± 0.22	195.8 ± 23.5	1.88 ± 0.01	160 ± 2	162 ± 0	3.8	104 ± 12	27%	5%	3.9	D3	
A-881597	H3	0.23 ± 0.02	1.9 ± 0.0	0.60 ± 0.02	165 ± 0	164 ± 4	3.7	3 ± 0	22%	18%	3.8	D3	
A-881607	LL3	0.94 ± 0.30	0.09 ± 0.02	0.0029 ± 0.0003	167 ± 1	183 ± 66	3.0	31 ± 7	82%	67%	<3.5	3.0	
A-881609	H3	0.24 ± 0.00	1.7 ± 0.1	0.75 ± 0.08	165 ± 3	169 ± 1	3.7	2 ± 0	25%	3%		D3	
A-881616	LL3	3.60 ± 0.02	46.4 ± 2.4	0.71 ± 0.05	163 ± 2	160 ± 5	3.7	66 ± 6	16%	1%		D3	
A-881621	L3	1.95 ± 0.00	46.7 ± 1.7	0.77 ± 0.02	174 ± 1	161 ± 0	3.7	61 ± 3	24%	8%	3.9	D3	
A-881622	L3	3.45 ± 0.07	54.4 ± 4.1	0.59 ± 0.05	183 ± 1	160 ± 2	3.7	92 ± 10	18%	14%	3.8	D3	
A-881626	H3	0.15 ± 0.00	1.3 ± 0.0	0.93 ± 0.02	164 ± 1	161 ± 0	3.7	1 ± 0	13%	4%		D3	

†: Coefficient of variation (σ as percentage of the mean) of ferrosilite in the low Ca pyroxene.

‡: Coefficient of variation (σ as percentage of the mean) of fayalite in the olivine.

EXPOSURE AND TERRESTRIAL HISTORIES OF NEW YAMATO LUNAR AND MARTIAN METEORITES. K. Nishiizumi¹ and D. J. Hillegonds², ¹Space Sciences Laboratory, University of California, Berkeley, CA 94720-7450, USA (kuni@ssl.berkeley.edu), ²CAMS, Lawrence Livermore National Laboratory, Livermore, CA 94550, USA.

Introduction:

Cosmogenic nuclide studies of lunar and Martian meteorites have contributed significantly to our understanding of these objects. By measuring a combination of cosmogenic stable- and radionuclides in these meteorites, it is possible to determine a number of important parameters of their exposure histories. Most lunar meteorites have complex cosmic ray exposure histories, having been exposed both at some depth on the lunar surface (2π irradiation) before their ejection, and as small bodies in space (4π irradiation) during transport from the Moon to the earth. On the other hand, we have not observed evidence of complex exposure history for Martian meteorites yet. These exposures were then followed by residence on Earth's surface, a time commonly referred to as the terrestrial ages. In addition to their complement of galactic cosmic ray (GCR) produced nuclides some lunar and Martian meteorites contain nuclides produced by solar cosmic rays (SCR). Unraveling the complex history of these objects requires the measurement of at least four cosmogenic nuclides. The specific goals of these measurements are to constrain or set limits on the following shielding or exposure parameters: (1) the depth of the sample at the time of ejection from the Moon or Mars; (2) the transit time from ejection off the lunar or Martian surface to the time of capture by the earth; (3) and the terrestrial residence time. The sum of the transit time and residence time yield an ejection age. The ejection age in conjunction with the sample depth on the Moon or Mars can then be used to model impact and ejection mechanisms.

We report here preliminary results for the cosmogenic radionuclides, ^{10}Be (half-life= 1.5×10^6 yr), ^{26}Al (7.05×10^5 yr), and ^{41}Ca (1.04×10^5 yr) in lunar meteorites, Yamato 981031 and 983885, shergottite, Yamato 980459, and nakhlites Yamato 000593, 000749, and 000802. Measurements of ^{36}Cl (3.01×10^5 yr) are in progress. The AMS measurements were performed at the Lawrence Livermore National Laboratory.

Results and Discussion:

Preliminary results of ^{10}Be , ^{26}Al , and ^{41}Ca concentrations in new Yamato lunar and Martian meteorites are shown in Table 1 along with ^{14}C results [1] in Yamato 983885, 000593, and 000749. The cosmogenic nuclide concentrations in the lunar meteorite Yamato 793274 and shergottites DaG 476/489/670/735 are also shown in the table as comparison. Although ^{36}Cl measurements are not yet completed, exposure and terrestrial histories of each meteorite could be drawn as following.

Yamato 981031/793274: Cosmogenic nuclide concentrations of lunar meteorite Y 981031 are very similar to Y-793274 [2]. Our results support that these two meteorites are a pair fall. The most probable scenario is that meteoroid, Y 981031/Y-793274 was ejected from a depth of 140-180 g/cm^2 in the lunar surface 32 ± 3 kyr ago. The terrestrial age for those meteorites is 20-35 kyr. Transition time from the Moon to the earth was less than 10 kyr.

Yamato 983885: Lunar meteorite Y 983885 was ejected from a depth of ~ 90 g/cm^2 at 45 ± 10 kyr ago. The terrestrial age is 45 ± 10 kyr and transition time from the Moon to the earth was less than 20 kyr.

Yamato 980459: The shergottite Y 980459 is covered by fusion crust and its recovered mass is 82 g. A higher concentration of ^{26}Al in the near-surface sample indicates that the meteorite contains SCR produced ^{26}Al and thus experienced low ablation during atmospheric entry. The preatmospheric radius was estimated less than 5 cm. The exposure age is calculated to be 1.1 ± 0.2 Myr based on ^{10}Be concentration. The age is similar to that of other shergottites, SaU 005 pairs, DaG 476 pairs, and NWA 1195. However, the age is significantly shorter than that of ^{21}Ne exposure age of 2.5 Myr [3], indicating it had SCR produced ^{21}Ne or a significant pre-exposure on the parent body.

Yamato 000593/000749/000802: Identical cosmogenic radionuclide concentrations in three nakhlites confirm pair falls. The terrestrial age is 55 ± 20 kyr based on ^{14}C and ^{41}Ca concentrations. Since the ^{21}Ne exposure age of the three Yamato nakhlites is 12.1 ± 0.7 Myr [4], Yamato nakhlites might be ejected with other nakhlites, Nakhla, Lafayette, Governador Valadares, and NWA 817 from the parent body at the same impact event. Slightly higher ^{26}Al concentration toward surface of Y 000593 is due to the chemical heterogeneity, higher concentration of target element Al, rather than SCR production.

References:

- [1] Jull A. J. T., et al. (2004) *28th Symposium on Antarctic Meteorites (this volume)*. [2] Nishiizumi K., et al. (1991) *16th Symp. Antarctic Meteorites*, 188-190.
- [3] Nagao K. and Okazaki R. (2003) *International Symposium: Evolution of Solar System Materials: A New Perspective from Antarctic Meteorites*, 94. [4] Okazaki R., et al. (2003) *Antarct. Meteorite Res.*, 16, 58-79. [5] Nishiizumi K., et al. (2001) *Lunar Planet. Sci.*, XXXII, CD ROM, #2117.

Table 1. Cosmogenic radionuclide concentrations in lunar and Martian meteorites (dpm/kg meteorite).

	¹⁰ Be	²⁶ Al	³⁶ Cl	⁴¹ Ca	¹⁴ C [1]	Reference
Lunar meteorites						
Y 981031,62 (0-2 mm)	7.78±0.11	37.7±0.9	8.77±0.17	83.0±4.0		This work
Y 981031,62 (3-5 mm)	7.66±0.11	35.1±1.4	9.18±0.20	90.5±4.1		This work
Y 981031,64 (interior)	7.79±0.18	40.0±1.0	9.43±0.20	81.5±4.3		This work
<i>Y-793274,65</i>	<i>8.16±0.25</i>	<i>32.7±1.6</i>	<i>8.95±0.42</i>	<i>91.2±2.3</i>		[2]
Y 983885,76 (exterior)	9.41±0.10	48.1±0.9		96.7±6.2		This work
Y 983885,70 (interior)	9.70±0.11	47.7±0.7		106.8±4.3	<0.8	This work
Martian meteorites						
Y 980459,58 (0-2 mm)	7.25±0.13	65.2±1.2		3.5±0.6		This work
Y 980459,58 (2-4 mm)	6.85±0.20	58.6±1.1		4.1±0.8		This work
Y 980459,58 (4-6 mm)	7.26±0.19	55.9±1.0		2.9±0.8		This work
Y 980459,56 (interior)	7.29±0.11	57.5±1.0		4.9±0.7		This work
<i>DaG 476/489/670/735</i>	<i>7.9 - 9.6</i>	<i>36 - 47</i>	<i>7.2-10.3</i>	<i>1.5 - 3.4</i>	<i><0.3</i>	[5]
Y 000593,59 (0-1.5 mm)	18.66±0.26	72.5±1.5		7.5±0.9		This work
Y 000593,59 (10-12 mm)	20.53±0.29	68.8±1.4		4.9±1.5		This work
Y 000593,60 (interior)	19.36±0.28	63.3±1.3		4.8±0.8	0.8±0.3	This work
Y 000749,50 (interior)	18.10±0.21	57.7±1.3		5.5±0.6	<0.7	This work
Y 000802,61 (5 mm)	19.38±0.25	58.1±1.2		6.2±0.8		This work

Petrology and mineralogy of Asuka 881020: A preliminary report of the first CH chondrite found among the Japanese Antarctic meteorite collection.

T. Noguchi^{1*}, N. Imae², and M. Kimura¹, ¹Department of Materials and Biological Sciences, Ibaraki University, Bunkyo 2-1-1, Mito 310-8512, Japan, ²National Institute of Polar Research, Kaga 1-9-10, Itabashi 173-8515, Japan. (*: tngc@mx.ibaraki.ac.jp)

Introduction:

CH chondrites are rare meteorites belonging to the CR clan (e. g., [1]). There are only 7 meteorites belonging to the CH chondrite group to date. CH chondrites contain abundant fine-grained (<100 μm across) chondrules, 24 vol. % Fe-Ni metal grains that preserve condensation processes in the solar nebula, and heavily altered clasts, and lack fine-grained opaque matrices (e. g., [1, 2, 3, 4]).

No meteorites belonging to the CH group have been found among the Japanese Antarctic meteorite collection. Last year, we recognized the first CH chondrite in the Japanese Antarctic meteorite collection. We performed SEM observation and EPMA analysis of this meteorite. Here we report the mineralogy and petrology of this meteorite.

Results:

General petrography: This meteorite composes mainly of fine-grained chondrules and abundant Fe-Ni metal grains. There is no fine-grained opaque matrix. Typical grain sizes of the chondrules are <100

μm across and cryptocrystalline chondrules are the most abundant. Chondrules whose sizes are as large as several hundred μm are relatively rare. There are many chondrules that contain silica. Silica-bearing microchondrules (<100 μm across) often have thin (<10 μm) Fe-rich olivine rims. There are many clasts that often contain lath-shaped pentlandite and framboidal aggregates of magnetite embedded in phyllosilicate dominant matrix (Fig. 1). Their sizes range from about 10 to 500 μm across. They occupy about 2-3 vol. % of this meteorite. The phyllosilicate-rich clast shown in Fig. 1 contains a dolomite that contains 2.70 wt % FeO and 3.72 wt % MnO. There is also another type of clasts that experienced aqueous alteration (Fig. 1). They are composed of unaltered cores (often have corroded forms) and altered rims. Their mode is lower than that of the heavily altered clasts. Refractory inclusions are small and rare. Their typical sizes are <30 μm . They often contain grossite, perovskite, spinel, and Ca-rich pyroxene, which are common to the other refractory inclusions in CH chondrites [1, 5].

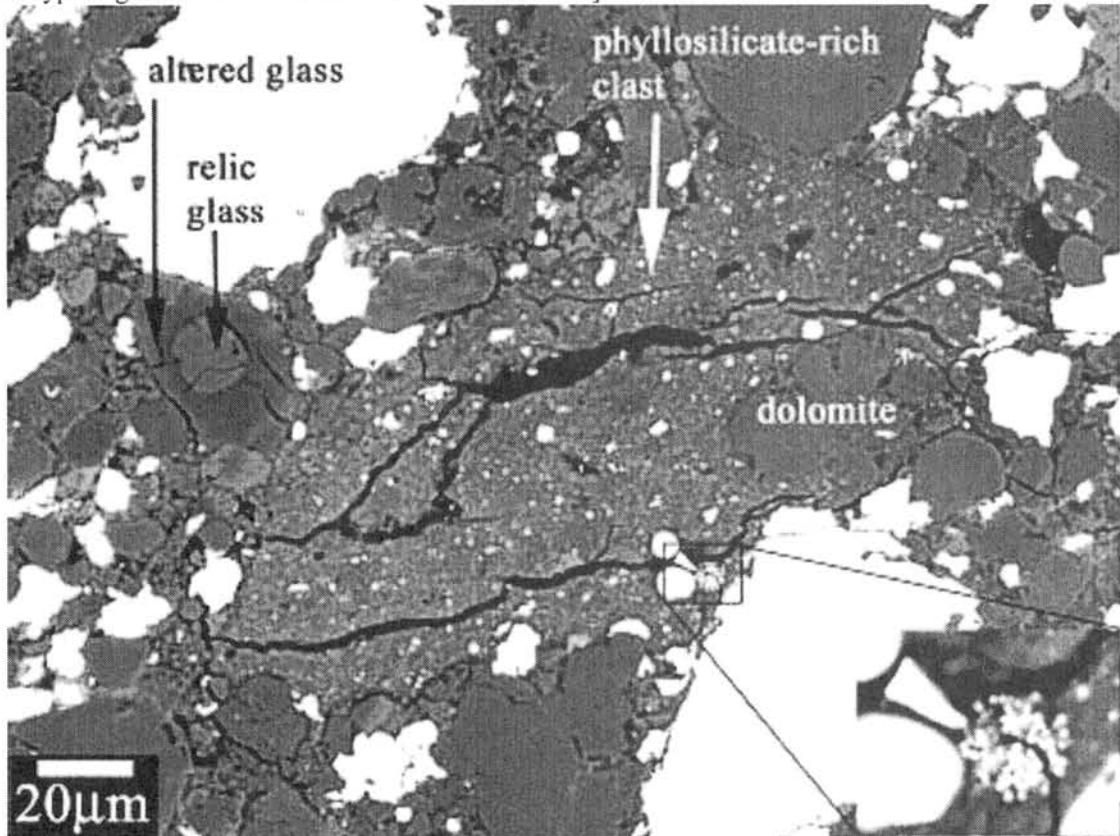


Figure 1 A back-scattered electron image of a phyllosilicate-rich clast and a clast that contains a relic glass core and an altered rim. The phyllosilicate-rich clast contains abundant Fe sulfides and magnetite. The lower right inset shows an enlarged image of a framboidal aggregate of magnetite.

Mineralogy: Most of the olivine crystals in this meteorite have $>F_{0.98}$. There are a small number of olivines with $F_{0.80}$ to $F_{0.55}$. Most of the low-Ca pyroxene has $>En_{90}$. Most of Ca-rich pyroxene is also magnesian. There are two types of Fe-Ni metal grains. Most of them show compositional zoning. Although they have Ni- and Co-rich cores and Ni- and Co-poor rims, their compositions overlap to each other. Ni and Co concentrations are positively correlated and plotted slightly above the line with the solar Ni vs Co ratio. There are another type of metal grains that have both Ni-poor and Ni-rich areas. Co concentrations of Ni-poor areas are higher than those of Ni-rich areas. Si-rich metal (6-15 wt % Si) occurs as fine-grained isolated grains and are relatively common. Iron sulfides occur as inclusions in Fe-Ni metal grains and isolated ones. Chromium content of one inclusion was 33.4 wt %, which suggests that the inclusion contains daubreelite.

[Si+Al]-Mg-Fe atomic ratios of phyllosilicate-rich clasts and clasts composed of altered glass and relic unaltered glass are plotted on ternary diagrams (Figs. 3 and 4). Major chemistry of the former clasts suggest that they are composed mainly of serpentine and Fe dominant phases (magnetite, pentlandite, and pyrrhotite) (Fig. 2). Their average $Mg/(Mg+Fe)$ ratio is 0.55.

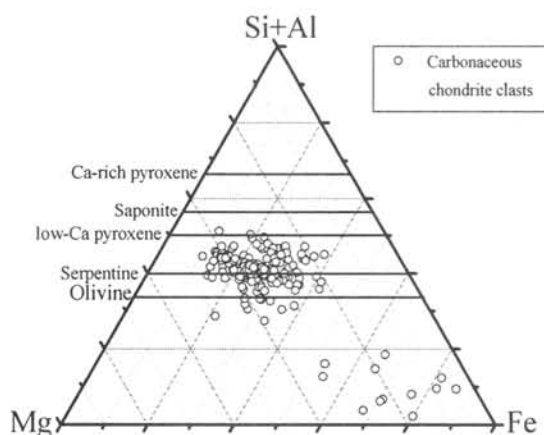
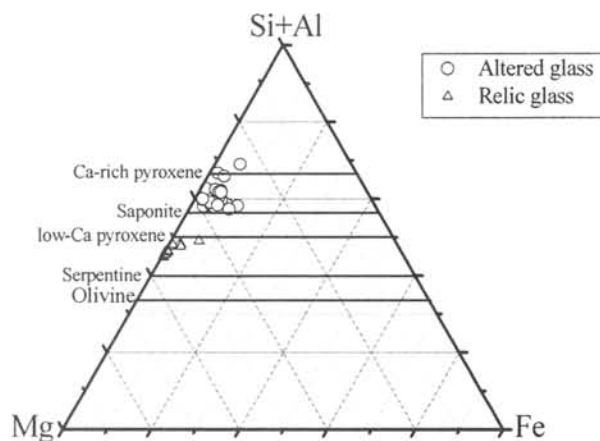


Figure 2 [Si+Al]-Mg-Fe atomic ratios of phyllosilicate-rich clasts

As described above, this meteorite is unique because there is another type of clasts that experienced aqueous alteration. Although partially altered microchondrules have been described [6], these newly recognized hydrated clasts do not have the shapes of chondrules or their fragments (Fig. 1). [Si+Al]-Mg-Fe atomic ratios of the relic cores and altered rims are plotted in Fig. 3. Chemical compositions of relic cores are similar to each other. They have enstatite-like (Fig. 3). Altered rims are richer in Si (and a lesser amount,

Fe) than those in the cores (Fig. 3). Iron is often enriched along narrow ($<2-3 \mu m$) veins. Chemical compositions of the altered glass suggest that they



contain abundant magnesian saponite. Figure 3 [Si+Al]-Mg-Fe diagram of clasts that contain altered glass and unaltered glass cores

Discussion and conclusions:

As described above, this meteorites have many features that are common to the other CH chondrites: abundant microchondrules and Fe-Ni metal grains, a positive correlation of Ni and Co in the metal, presence of minerals that were formed under reducing conditions, phyllosilicate-rich clasts that contain lath-shaped pentlandite and framboidal aggregates of magnetite, and fine-grained CAI that contain grossite. Therefore, it is clear that Asuka 881020 is a new member of CH chondrites.

This meteorite also has unique characteristics. First is another type of hydrated clasts. Because chemical compositions of the relic cores of the hydrated clasts overlap with those of microchondrules in the host meteorite, the clasts probably have a genetic relation with the host meteorite. It contrasts to the origin of another type of hydrated clasts, which do not have any genetic relationship to the host CHs [3]. Next are the compositions of Fe-Ni metal in this meteorite. They suggest that this meteorite experienced a slight thermal metamorphism based on their chemical compositions.

References: [1] Krot A. N. et al. (2002) *Meteorit. Planet. Sci.*, 37, 1451-1490. [2] Grossman J. N. et al. (1988) *EPSL*, 91, 33-54. [3] Greshake, A. et al. (2002) *Meteorit. Planet. Sci.*, 37, 281-293. [4] Ivanova, M. A. et al. (2001) *LPSC XXXII*, #1817. [5] Kimura, M. et al. (1993) *GCA*, 57, 2329-2359. [6] Krot, A. N. (1999) *Meteorit. Planet. Sci.*, 35, 1249-1258.

Depth Profile of Cosmogenic Nuclides in Large Iron Meteorites. M. Noguti¹⁾, H. Matsuzaki²⁾, M. Setoguchi³⁾, M. Honda¹⁾, and H. Nagai¹⁾. ¹⁾Dept. of Chemistry, Nihon University, Setagaya, Tokyo, 156-0045, ²⁾Res. Center for Nucl. Sci. and Tech., Univ. Tokyo. Tokyo, ³⁾Dept. of Chemistry, Tokyo Metropolitan Univ. Hachioji, Tokyo.

Introduction:

Many species of meteorites have been recovered on the earth. Among them, some iron meteorites have been realized to be much larger than stony meteorites. The most popular iron seems to be the one known as Canyon Diablo, IA. Pre-atmospheric size of the meteorite has been estimated by many investigators. The estimates have widely been scattered, due to the fatal difficulties. The considerable part of the meteoroid could be lost at the time of fall. The most reliable information in the recovered meteorites can be obtained from the cosmic ray induced nuclides that have been varied by the depth.

The depth profile of the contents of many cosmogenic nuclides in recovered large meteorites can be expressed by a simple exponential function. The profiles of the cosmogenic stable- and radionuclides seem inform us with their production records as the function of the depths from the surface.

The largest meteoritic object may be found in lunar surface samples as shown in lunar long core sample of Apollo 15, which informed us the depths profiles of the cosmogenic productions under a real 2 pi geometry of the materials. In the case of lunar stony materials about 140 g/cm² has been observed for various products. For large iron meteorites practically 2 pi geometry can also be applied, but slopes of the depth profile patterns in metallic objects must be studied separately.

The three dimensional distributions of cosmic ray induced products such as ³He in a large irons will give us a reasonable and commonly applicable data. Unfortunately, such a set of data has not been available yet, due to the empirical difficulties to collect useful data from a complete set out of suitably large specimens.

According to the model experiments employing GeV particles and large thick iron targets, the thickness of 22 cm for ²²Na and others, was corresponding to the mean absorption thickness (Honda, 1962). According to recent report by Masarik and Reedy (2002), the slope can be expressed employing exponential relation with 26 cm for ³⁶Cl in Campo del Cielo, IA. The estimates are important parameter to measure the size of the iron meteorites. However, the value has been derived by purely theoretically and it must be examined and confirmed directly with meteoritic observations.

Experimental:

Ideally three dimensional sets of samples must be obtained for this problem. In fact so far it

has been performed partially, using two dimensional samples. For example, a large plane sample of the cutting slice obtained from El Taco at Mainz, Germany, the large fragment of the Campo del Cielo. The contents of noble gases have been measured by many investigators (1969-1971). An apparent slope of the projection to the (x, y) plane is indicating the slope of 22 cm as the limit for the value. Using ¹⁰Be and ²⁶Al we determined that 23 cm is for the same data. The direction of the depth measured perpendicular to the surface is identical to that by noble gas data. These data indicate already that the real slope must be definitely lower, most probably at about 19 cm.

More than 50 tiny fragments of Gibeon, IVA (the other large iron recovered 21 tons, in South West of Africa) have been collected randomly, and some deep interior data have been observed by the AMS method at Univ. Tokyo. The deepest sample of the Gibeon seems to contain about 1/50000 levels of ¹⁰Be relative to those of the surface. The depth can be estimated at 200 cm below the surface. Less sensitively but a similar trend of ²⁶Al has been determined. The same can be expected for other nuclides, such as ³⁶Cl and ⁵³Mn. This has been extended with ²⁶Al in S target in troilite inclusions. This was because of the higher sensitivity for ²⁶Al by a lower delta A, 32-26 = 6. The contents of noble gases have also been determined by mass-spectrometry by Dr. Nagao.

The Fig.1 is illustrating the variations of the profile found with all samples of Gibeon as the function of depths. The plots have tentatively been performed assuming 20 cm for the slope.

Discussion.

In future studies, an extensive three dimensional measurements can be performed with a spherical fragment of larger than R = 20 cm. Several small samples of 1 gram size can be taken from the surface of the fragment. The sphere can be treated as the globe. The maximum ratio of the contents of the products may be by a factor of 5 or more. The value at the center may be commonly interpolated. Eventually we may conclude the real depth profiles of the products as the functions of depth perpendicular to the surface plane of the meteoroid in space.

Ref.:1). M. Noguchi et al. Cosmogenic Radionuclides in Large iron Meteorites. *Geochimica. Goldschmidt Conf.* S49, Sept. 2003, Kurashiki, Japan. 2). V. Buchwald, *Iron Meteorites* (1975). 3). Heymann et al. (1966) *JGR.*71, 619.. 4). N.Takaoka,

Priv. Communication (2003). 5). M. Honda et al. (2002) Meteoritics 37, 1711. 6). M.Honda (1962) JGR 67, 4847.

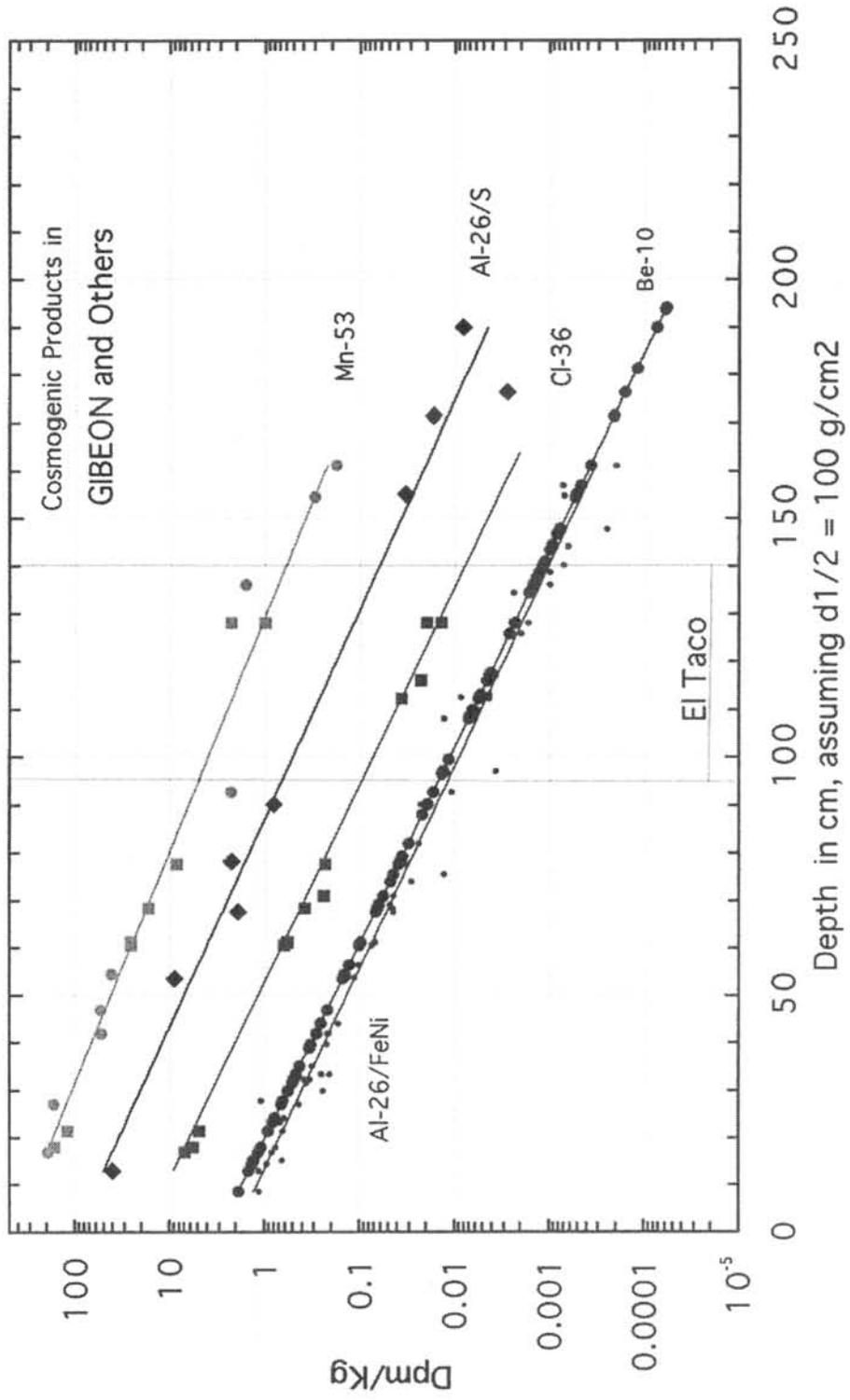


Fig.1. Distributions of Cosmogenic Nuclides in Gibeon and Others.

Chronology of Eucrite Petrogenesis from Sm-Nd and Rb-Sr Systematics. L. E. Nyquist¹, C.-Y. Shih², and H. Takeda³, ¹Mail Code SR, NASA Johnson Space Center, Houston, TX 77058, l.nyquist@nasa.gov, ²Mail Code C23, Lockheed-Martin Space Mission Systems and Service Co., Houston, TX 77058, ³Research Institute, Chiba Institute of Technology, Narashino 257-0016, Japan.

Introduction:

We apply Sm-Nd and Rb-Sr data from joint mineralogical and isotopic studies of several eucrites to constrain times of magma genesis and cooling.

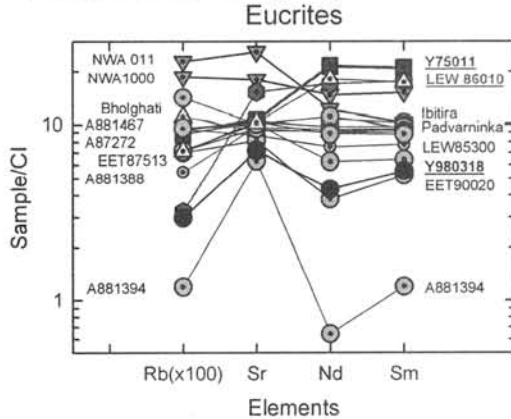


Figure 1. Rb, Sr, Sm, and Nd abundances in studied eucrites compared to those in angrite LEW86010 and the unique achondrite NWA 011.

Characterization of Studied Eucrites:

CI-chondrite-normalized Rb abundances in eucrites are depleted ~100X relative to more refractory Sr, Nd, and Sm, reflecting general alkali element depletion in the parent body (Fig. 1). With the exception of unique achondrite NWA 011 and of NWA 1000, Sr abundances are enriched ~6-10X over chondritic abundances. Rb and Sr abundances in NWA 011 and NWA 1000 are the highest among the studied meteorites, and are affected by terrestrial contamination. The ancient, unique eucrite A881394 [1] has a very low Rb/Sr ratio. Nd and Sm abundances in A881394 also are depleted relative to Sr, and to those of other eucrites in the figure. Although A881394 has the chemical characteristics of a cumulate eucrite [2], it does not contain orthopyroxene inverted from pigeonite [1] like most cumulate eucrites. Rb, Nd, and Sm are significantly more depleted in A881394 than in cumulate eucrite Y980318, but the Sm abundance in A881394 is similar to that of cumulate eucrites Moama and EET87548 [2]. The Sm abundance in Y980318 is similar to that of Moore County, highest among the cumulate eucrites for which data are summarized by [2]. Pristine eucrite clast Y75011,84 is most enriched in Nd and Sm, and with NWA 1000 as well as a clast from EET87513, may belong to the Nuevo Laredo or Stannern trends for evolved eucrites. The remaining eucrites have Nd and Sm abundances of ~6-10X chondritic, typical of Main Group eucrites. Nd and Sm abundances in NWA 011 are at the upper limit of

this range.

Sm-Nd Internal Isochrons: Fig. 2 shows a conventional ¹⁴⁷Sm-¹⁴³Nd internal isochron for the Y980318 cumulate eucrite. The determined age,

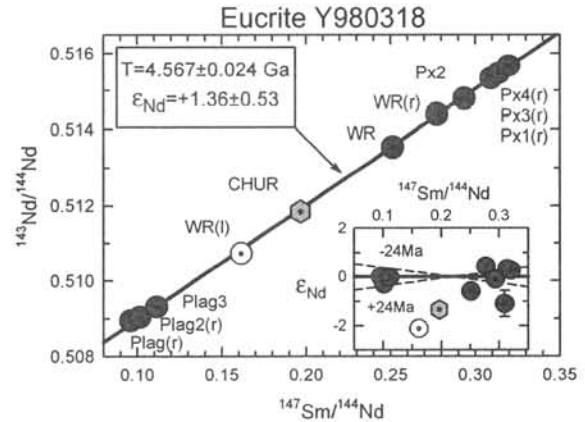


Figure 2. ¹⁴⁷Sm-¹⁴³Nd isochron for Y980318. The position of the CHUR (Chondritic Uniform Reservoir) datum is shown by the cyan hexagon. An HCl leachate, WR(l) was omitted from the fit.

4567±24 Ma (2σ) gives the time of isotopic closure of the Sm-Nd system. Within the error estimate, the age is the same as the ~4558 Ma Pb-Pb age of angrite LEW86010 [3], or the ~4567 Ma Pb-Pb age of CAI [4]. This age contrasts to apparently younger ages for some other cumulate eucrites [5].

A ¹⁴⁶Sm-¹⁴²Nd isochron gives ¹⁴⁶Sm/¹⁴⁴Sm = 0.0060±0.0009 in Y980318 at crystallization, slightly less than ¹⁴⁶Sm/¹⁴⁴Sm = 0.0076±0.0009 for LEW86010 [6]. The calculated time of ¹⁴²Nd/¹⁴⁴Nd isotopic equilibration is 4523±8 Ma assuming crystallization of the angrite at 4558 Ma [3].

Initial ¹⁴³Nd/¹⁴⁴Nd and Pyroxene Model Ages:

The ages determined from the ¹⁴⁷Sm-¹⁴³Nd and ¹⁴⁶Sm-¹⁴²Nd internal isochrons are slightly discordant. Moreover, the isochron passes above the CHUR (Chondritic Uniform Reservoir [7]) datum (Fig. 2 inset), resulting in elevated ε_{Nd} = +1.36±0.53. The internal isochron relies on data for both pyroxene and plagioclase. The pyroxene data are analytically most robust, and also least affected by post-crystallization events. Thus, Sm-Nd CHUR model ages could be more robust than internal isochron ages. They are subject to larger statistical errors than internal isochron ages because they are calculated for a smaller range in ¹⁴⁷Sm/¹⁴⁴Nd, but a comparison between internal isochron ages and pyroxene model ages is nevertheless instructive.

Fig. 3 shows isochron ages and ε_{Nd} for eucrites

studied in the JSC lab. All of the data plot above the CHUR datum [7] for ages near the accepted age of the solar system making CHUR inappropriate as a reference for our data set. The point labeled HED PB gives a revised $^{143}\text{Nd}/^{144}\text{Nd} = 0.511889$ for $^{147}\text{Sm}/^{144}\text{Nd} = 0.1967$, defining a new reference datum, HEDR (HED Reservoir).

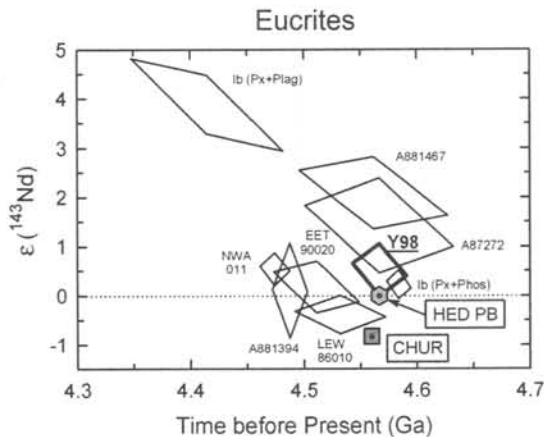


Figure 3. (T , ϵ_{Nd}) diagram for these eucrites.

Internal Isochron and Model Age Comparison:

Fig. 4 compares internal isochron ages to HEDR ^{147}Sm - ^{143}Nd model ages and CHUR ^{146}Sm - ^{142}Nd model ages. The good agreement between isochron and model ages shows no evidence that the Sm-Nd isotopic systematics of plagioclase separates were significantly affected by post-crystallization events. Of the twelve meteorites studied, the three types of Sm-Nd ages are concordant within $\sim 1\%$ for four: Y980318, EET90020, A881467, and EET87513. ^{147}Sm - ^{143}Nd model ages of pyroxene separates of some of the early-studied meteorites are not plotted in the figure because of large error limits due to pyroxene separates of inadequate purity. The majority of the meteorites with concordant Sm-Nd ages by all three methods suggest crystallization very close to 4558 Ma ago. The exception is EET90020, for which both types of model ages are in agreement with the 4510 ± 40 Ma internal isochron age [11]. The (T , ϵ_{Nd}) data of EET90020 suggest derivation from a reservoir of unfractionated relative REE abundances (Fig. 3). Other meteorites, including unique achondrite NWA 011 and A881394 have similar, or slightly lower internal isochron and ^{147}Sm - ^{143}Nd model ages suggesting a major thermal event(s) on the parent body(ies) ~ 4500 Ma ago corresponding to sharp isochronism in Ar-Ar ages of several unbrecciated and cumulate eucrites [8].

Rb-Sr Systematics of Eucrite Plagioclase:

Only a few precise, apparently undisturbed, Rb-Sr ages have been determined for eucrites. The Y75011,84 pristine clast [9], Bholghati [10], EET87513, and A881394 are exceptions. Y75011,84 has the oldest and most precisely determined Rb-Sr age of 4.56 ± 0.05 Ga ($\lambda_{87} = 1.402 \times 10^{-11} \text{ yr}^{-1}$). The

Rb-Sr data of plagioclase separates from the eucrites are robust against disturbance. Most give initial $^{87}\text{Sr}/^{86}\text{Sr} = 0.699004 \pm 10$ for age $T = 4.43 \pm 0.18$ Ga, higher than 0.698972 ± 8 for angrites [6] or 0.698934 ± 15 for Efremovka CAI E38 (JSC, unpub.). A few eucrite data, including those for Y75011, are consistent with the primitive CAI value, however.

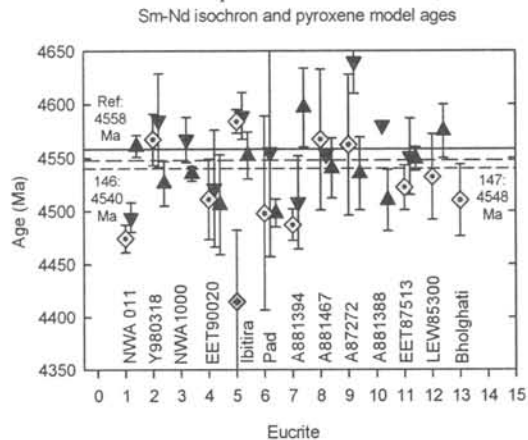


Figure 4. Internal isochron ages (yellow diamonds), ^{147}Sm - ^{143}Nd pyroxene model ages (red inverted triangles), and ^{146}Sm - ^{142}Nd model ages (blue triangles). Ibitira: yellow = px+leachates (phosphates), cyan = px+plagioclase

Conclusions:

Sm-Nd internal isochron and pyroxene model ages of the studied eucrites, including cumulate eucrite Y980318, show they formed ~ 4500 - 4560 Ma ago. The precisely determined Rb-Sr age of Y75011 suggests Rb-Sr ages should agree with the Sm-Nd ages for $\lambda_{87} = 1.402 \times 10^{-11} \text{ yr}^{-1}$, although Rb-Sr ages of some eucrites (not summarized here) appear to have been reset to lower values. The slightly elevated initial $^{87}\text{Sr}/^{86}\text{Sr}$ in most eucritic plagioclases suggests early isotopic evolution in reservoir (s) of higher Rb/Sr ratio than those of eucrites. The difference of ~ 0.000070 between $^{87}\text{Sr}/^{86}\text{Sr}$ for Efremovka E38 and that of most eucrites requires average $^{87}\text{Rb}/^{86}\text{Sr} \sim 0.005$ (Δt) $^{-1}$ for time interval Δt (Ga). Part of this evolution was at comparatively high nebular $^{87}\text{Rb}/^{86}\text{Sr} \sim 1$, but low apparent initial $^{87}\text{Sr}/^{86}\text{Sr}$ for some eucrites may suggest a period of global Rb loss following early parent body formation.

References:

- [1] Nyquist L. E. et al. (2003) *EPSL*, 214, 11-25.
- [2] Mittlefehldt D. W. and Lindstrom M. M. (2003) *GCA*, 67, 1911-1935.
- [3] Lugmair G. W. and Galer S. (1992) *GCA* 56, 1673-1694.
- [4] Amelin Y. et al., (2002) *Science*, 297, 1678-1683.
- [5] Carlson R. W. and Lugmair G. W. (2000) *Origin of the Earth and Moon*, pp. 25-44
- [6] Nyquist L. E. et al. (1994) *MAPS*, 29, 872-885.
- [7] Jacobsen S. B. and Wasserburg G. J. (1984) *EPSL* 67, 137-150.
- [8] Bogard D. and Garrison D. H. (2003) *MAPS* 30, 669.
- [9] Nyquist L. E. et al. (1985) *JGR*, 91, 8137-8150.
- [10] Nyquist L. E. et al. (1990) *GCA* 54, 2195-2206.
- [11] Yamaguchi A. et al. (2001) *GCA* 65, 3577-3599.

Introduction

Eucrites are basalts or gabbro composed of pyroxene and plagioclase with minor amounts of ilmenite, silica, Ca-phosphate, troilite and metallic phases. It is supposed that eucrites were formed in the upper layer of their parent planet by igneous activity, and their metallic abundances are generally very low. However, some eucrites have relatively high contents of metallic phases. There are two possible explanations for such anomalously high abundances of metallic phases; exogenous and endogenous processes. The former is due to incorporation of metallic phases by impact events. This would have caused contamination of projectile materials on the surface. Another possibility is endogenous. The Camel Donga eucrite contains about 2% metallic iron [1]. The origin of such a metallic phase can be explained by reduction of FeO and FeS, probably through loss of S₂ and SO₂ by impacts [1]. Thus, it is likely that metallic phases in eucrites give us information about impact-related events on the surface of the HED parent body and its formation process.

We conducted a geochemical study of six eucrites rich in metallic phases. Based on the chemical composition and mineralogical observation, we discuss the origin of metallic phases in these eucrites.

Samples and Experiments

We performed bulk chemical analyses of one monomict eucrite (EET92003) and five polymict eucrites (ALHA76005, EET92023, GRO95633, LEW85300 and LEW87026). A metallic grain having high concentrations of siderophile elements was observed in ALHA76005 [2]. EET92023 shows gabbroic texture and contains a significant amount of Fe-Ni metal (~0.5%) [3]. Fe-Ni metal grains were reported in the matrix of LEW85300 [4]. In GRO95633, a few metal grains are present, surrounded by brown limonitic staining [5]. LEW87026 has higher Re and Os concentrations than those for normal eucrites [6].

We used three nuclear analytical methods, prompt gamma-ray analysis (PGA), instrumental neutron activation analysis (INAA) and instrumental photon activation analysis (IPAA), and determined major, minor and trace elements in the six eucrites. Platinum group element contents are determined by ICP-MS.

Results and discussion

Major element contents of six eucrites analyzed in our study are shown in Table 1. GRO95633 has lower Al₂O₃ and CaO concentrations than those for

monomict eucrites, implying that GRO95633 has more diogenitic affinity. Based on mg# (= Mg/(Mg+Fe)) and Ti contents from our data, it is suggested that GRO95633 and EET92023 be classified into cumulate eucrites, and ALHA76005, EET92003 and LEW87026 be classified into noncumulate eucrites.

Figure 1 shows Ni and Co contents of the samples analyzed in this work and various meteorites. Our EET92023, EET92003 and GRO95633 samples have higher Ni and Co concentrations than the average values of Ni (7ppm) and Co (7ppm) for eucrites [7]. Among them, EET92023 has extraordinarily high abundances of Ni, Co and Ir. In contrast, siderophile contents of ALHA76005 and LEW87026 are within the range of polymict eucrites (e.g. Ni 5.7ppm, Co 11.8ppm) [8]. LEW85300 has much lower Ni and Co concentrations than those for our other samples. The variation of siderophile abundances in ALHA76005, LEW85300 and LEW87026 indicates that these samples have large heterogeneity in metallic phases.

Figure 2 shows a correlation between CaO and Co contents of eucrites and howardites. Although LEW85300 is a polymict eucrite, a Co content of our specimen is obviously lower than those of other polymict eucrites, and is plotted in the lower part of the range for monomict eucrites. LEW85300 was reported to have a wide range of Co contents [9], implying the heterogeneous distribution of Co. The CaO and Co contents of GRO95633 range within howardites (Fig. 2), suggesting that metallic phases in GRO95633 may have been brought by a projectile by which some howardites would have been produced.

Although EET92003 is classified into monomict eucrites [10], the bulk sample analyzed in this study has higher Ni and Co concentrations than those for other monomict eucrites. This suggests that the metallic material has remained in the parent liquid and has been taken in EET92003. It is more likely that EET92003 is a polymict breccia; polymict eucrites are, in some cases, misclassified into monomict eucrites. Further study is required for mineralogical observation of EET92003. Our Ni value of EET92023 is similar to its literature values [3, 11]. It is suggested that siderophile elements in EET92023 were brought by projectiles having fairly high Ni and Co contents. Recently, it was reported that EET92023 has a relationship to mesosiderites [3]. Further chemical and mineralogical studies are required to discuss this possibility.

References:

[1] Palme H. et al. (1988), *Meteoritics* 23, 49-57. [2] Fukuoka T. and Ikeda K. (1983) *Symp. Ant. Met., NIPR Tokyo*, 48. [3] Kaneda K. and Warren P. H. (1998) *Symp. Ant. Met., NIPR Tokyo*, 45-47. [4] Zolensky M. E. et al (1992) *Meteoritics* 27, 596-604. [5] *Antarctic Meteorite Newsletter* (1997) 20(2), 11. [6] Warren P. H. and Kallemeyn G. W. (1996) *Meteorit. Planet. Sci.* 31, 97-105. [7] Mason B. (1979) *Data of Geochemistry Sixth Edition*. U.S. Government Printing Office, Inc., Washington, B49-B52. [8] Barrat J. A. et al. (2000) *Meteorit. Planet. Sci.* 35, 1087-1100. [9] Mittlefehldt D. W. and Lindstrom M. M. (1991) *Geochim. Cosmochim. Acta* 55, 77-87. [10] *Antarctic Meteorite Newsletter* (1993) 16(2), 19. [11] Warren P. H. (1999) *Symp. Ant. Met., NIPR Tokyo*, 185-186. [12] Duku M. B. and Silver L. T. (1967) *Geochim. Cosmochim. Acta* 31, 1637-1665.

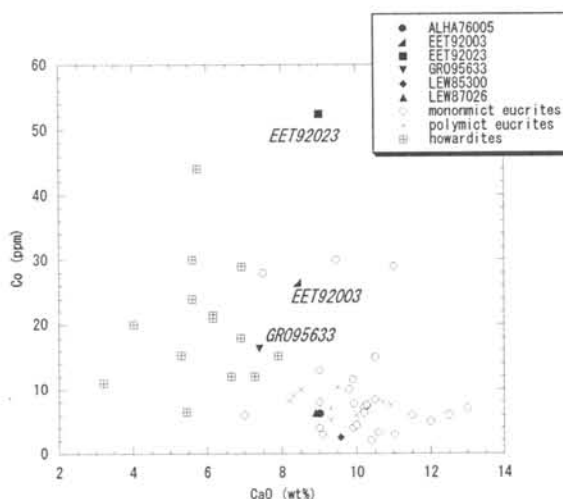


Fig. 2 CaO and Co contents for eucrites and howardites. LEW85300 is plotted in the lower part of the range for monomict eucrites. GRO95633 is plotted within the range of howardites.

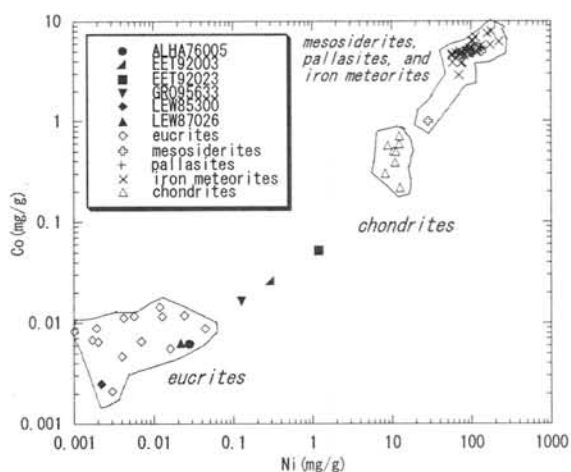


Fig. 1 Ni and Co contents in meteorites including eucrites. Closed symbols show values obtained in this work. Open diamonds designate eucrites. EET92023, EET92003 and GRO95633 have higher contents of Ni and Co than those for other eucrites.

Table 1. Major elemental composition (in wt%) for Antarctic eucrites, ALHA76005, EET92003, EET92023, GRO95633, LEW85300 and LEW87026

	ALHA76005		EET92003		EET92023		GRO95633		LEW85300		LEW87026		Range of eucrite analyses[12]	
	error*		error											
SiO ₂	47.7	1.7	45.6	1.7	47.7	1.7	48.8	1.7	46.0	1.3	49.4	1.5	48.6	- 49.6
TiO ₂	0.754	0.013	0.657	0.015	0.434	0.017	0.539	0.012	0.474	0.008	0.641	0.012	0.4	- 1.0
Al ₂ O ₃	12.0	0.2	11.0	0.2	11.3	0.2	9.3	0.1	12.5	0.2	10.9	0.2	11.7	- 13.9
Cr ₂ O ₃	0.333	0.001	0.301	0.001	0.310	0.002	0.572	0.002	0.279	0.001	0.395	0.001	0.06	- 0.9
FeO	18.4	0.1	19.3	0.1	18.4	0.1	17.6	0.1	19.2	0.1	18.1	0.1	15.8	- 20.1
MnO	1.17	0.06	1.12	0.06	1.15	0.06	1.16	0.06	1.15	0.06	1.11	0.06	0.3	- 0.8
MgO	7.45	0.57	8.94	0.60	9.29	0.55	11.78	0.72	5.74	0.44	8.75	0.55	5.4	- 7.4
CaO	9.02	0.20	8.45	0.21	9.00	0.20	7.40	0.17	9.58	0.17	8.90	0.18	8.6	- 11.5
Na ₂ O	0.500	0.005	0.531	0.004	0.446	0.004	0.350	0.003	0.488	0.004	0.417	0.004	0.4	- 0.9
K ₂ O	0.0832	0.0075	0.0638	0.0073	0.0251	0.0047	0.0275	0.0031	0.0346	0.0043	0.0411	0.0099	0.04	- 0.22
Total(%)	97.4		95.9		98.0		97.5		95.4		98.7			

* Errors are due to counting statistics (1 σ)

Noble gas compositions of gas-rich and gas-poor polymict breccias. T. Osawa¹ and K. Nagao¹, ¹Laboratory for Earthquake Chemistry, Graduate School of Science, The University of Tokyo, Hongo 7-3-1, Tokyo 113-0033, Japan.

Introduction:

Polymict breccias are stony meteorites including clasts of different meteorite groups or petrologic types. It is generally agreed on that the brecciated meteorites formed by gardening on asteroidal parent bodies [1]. Some polymict breccias have very high concentration of noble gases and are called regolith breccia. Regolith breccias are available for the research of early solar activity because they preserve plenty of solar noble gases implanted during asteroidal formation processes. Gerling and Levskii [2] first reported extremely high concentration of noble gases in Pesyanoe aubrite, and other gas-rich meteorites have been discovered subsequently (e.g., [3]). The gas-rich meteorites apart from carbonaceous chondrite group generally have the dark-light structure [4]. However, the prominent structure is not observed in some gas-rich meteorites belonging to ordinary chondrite, for example Y-75029 [5]. The solar noble gases are generally trapped in the dark matrix contrasting with the light inclusions, indicating the surface irradiation of solar wind. Meanwhile, cosmogenic products are predominant in the light inclusions.

In the present work, we performed noble gas measurements for 18 polymict breccias. 14 of them are Antarctic meteorites.

Samples and experimental procedure:

Meteorites measured in this work are follows: Asuka-87154 (L3), Asuka-87155 (L3), Asuka-87166 (L3), Asuka-87191 (H4), Asuka-87192 (H4), Asuka-87214 (H5), Asuka-87250 (LL3), Asuka-87289 (H3), Asuka-87341 (H4), Gladstone (H4), NWA869 (L5), Sahara98222 (L6), Willard (b) (H3.5-3.6), Yamato-74112 (H5), Yamato-790521 (LL), Yamato-791067 (LL), Yamato-791108 (LL5.6), and Yamato-791826 (Euc). All the meteorites are polymict breccias. In this work, we adopted four experimental techniques, such as (1) laser gas-extraction analyses for bulk samples, (2) laser spot analyses for a thin section, (3) laser gas-extraction analyses for small fragments of a meteorite, (4) stepwise heating analyses. We show here only the procedure of stepwise heating because it is tedious when all procedures are presented here. Polymict breccias were heated in a Ta oven at each temperature step for 20 min. Noble gases were extracted in each step and purified by two heated Ti-Zr getters in an ultra-high vacuum purification line to remove reactive gases. Ar, Kr, and Xe were trapped in a liquid-nitrogen-cooled charcoal trap and He and Ne were analyzed on a modified VG-5400 mass spectrometer (MS-II). Kr and Xe were trapped in a cryogenically cooled trap at 100 K and only Ar

was measured. Kr and Xe were released from the trap at 135 and 220 K, respectively. Sensitivity and mass discrimination effects were calibrated using an atmospheric noble gas standard, and a helium standard gas with $^3\text{He}/^4\text{He}=1.71\times 10^{-4}$. Neon mass interferences caused by $^{40}\text{Ar}^{++}$ and CO_2^{++} were corrected using experimentally determined $^{40}\text{Ar}^{++}/^{40}\text{Ar}^+$ and $\text{CO}_2^{++}/\text{CO}_2^+$ ratios. During Ne analysis, a liquid-nitrogen-cooled trap close to an ion source removed argon and carbon dioxide.

Results:

Regolith breccias are easily distinguishable from others by the presence of solar-He and Ne. 6 of 18 meteorites measured in the present work are regolith breccias and 5 of them are H chondrites. Only one L chondrite of 9 L and LL chondrites has solar noble gases. The result indicates that regolith breccias are relatively minor among polymict breccias. It is unclear why H chondrites occupy main population among the regolith breccias.

The highest concentrations of noble gases are detected for Willard (b), whose ^4He concentration is 5.8×10^{-3} cm³STP/g, ^{20}Ne is 1.4×10^{-5} cm³STP/g, and ^{36}Ar is 4.0×10^{-7} cm³STP/g. Although the concentrations are much lower than those of lunar regolith, elemental abundance ratios ($^4\text{He}/^{20}\text{Ne} = 418$, $^{20}\text{Ne}/^{36}\text{Ar} = 35$) are similar to the composition of the solar wind ($^4\text{He}/^{20}\text{Ne} = 550$, $^{20}\text{Ne}/^{36}\text{Ar} = 48.5$ [6]), indicating that the parent body of the meteorite has been prevented from severe heating and significant elemental fractionation did not occur. He and Ne isotopic compositions of the meteorite indicate the presence of solar wind and solar energetic particles (SEP) components. Total Ne isotopic composition ($^{20}\text{Ne}/^{22}\text{Ne} = 11.2$) is corresponding to that of SEP well.

Asuka-87191 (H4), Asuka-87214 (H5), NWA869 (L5), and Gladstone (H4) are also solar gas-rich meteorites. They have high concentrations of He, Ne, and Ar. Solar noble gases are mainly extracted at 600-1200°C steps. Noble gas elemental compositions of these polymict breccias are similar to the solar wind, showing these H and L chondrite parent bodies have been undergone quite different history of regolith formation from that of the moon, in which noble gases are heavily fractionated. The result might reflect the difference of the era of the solar irradiation between the polymict breccias and the moon.

Solar-derived noble gases are not detected in other thirteen polymict breccias and cosmogenic nuclides are dominant in them. The lowest noble gas concentrations are observed in Yamato-74112 (H5), whose ^4He concentration (2.2×10^{-7} cm³STP/g) is only 1/26000 of that of Willard (b). The gas-poor

meteorites are probably derived from deeper portion from the surface of parent bodies than gas-rich meteorites. The effect of neutron capture of Br is identified in Yamato-790521, which is consistent with the lack of solar noble gases because solar wind noble gases can be implanted into only the surface portion..

The measurements for 66 fragments of Asuka-87191 reveal the micro distribution of noble gases of regolith breccia. There is a correlation between ^4He concentrations and $^3\text{He}/^4\text{He}$ ratio (Fig. 1). Gas-rich fragments have solar-He and Ne, on the other hand, gas-poor fragments have no solar He and Ne and cosmogenic nuclides are relatively dominant. The most remarkable finding of the measurement is the clear correlation between ^4He and ^{20}Ne concentrations, and many fragments have $^4\text{He}/^{36}\text{Ar}$ and $^{20}\text{Ne}/^{36}\text{Ar}$ ratios higher than those of the solar wind of 30000 and 47. Since $^4\text{He}/^{20}\text{Ne}$ ratios of gas-rich fragments (400-550) are corresponding to the solar wind (550), relatively low abundance of ^{36}Ar might indicate that the composition of ancient solar wind is different from that of the current solar wind.

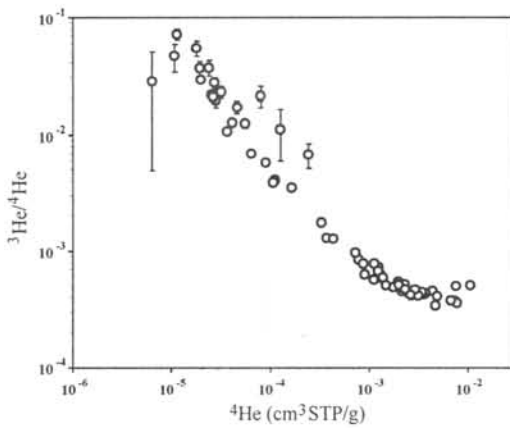


Fig. 1 ^4He concentrations and $^3\text{He}/^4\text{He}$ ratios of small fragments of Asuka-87191 regolith breccia.

References:

- [1] Housen K. R. *et al.* (1979) *Icarus* 39, 317-351. [2] Gerling E. K. and Levskii L. K. (1956) *Dokl. Akad. Nauk SSSR*, 110, 750. [3] Manuel O. K. and Kuroda P. K. (1964) *J. Geophys. Res.*, 7, 1413-1419. [4] Goswami J. N. *et al.*, (1984) *Space Sci. Rev.* 37, 111-159. [5] Nakashima D. *et al.*, (2002) *Antarct. Meteorite Res.* 15, 97-113. [6] Cerutti H. (1974) Ph.D. Thesis, Univ. Bern.

Early earth evolution recorded in lunar soils? A case for geomagnetic field. M. Ozima^{1*}, Y. N. Miura², F. A. Podosek³, and K. Seki⁴, ¹University of Tokyo, Tokyo, Japan (EZZ03651@nifty.ne.jp), ²Earthquake Research Institute, Tokyo, Japan, ³Washington University, St Louis, USA, ⁴Nagoya Univ. Toyokawa, Japan.

When did the geomagnetic field first appear? The question is directly relevant to core formation and to early earth evolution. Paleomagnetic studies trace the geomagnetic field back only to about 3.5 Ga ago [1] that suggested much weaker geomagnetic dipole. The geomagnetic field prevents any effective ion loss from the atmosphere [2], but if the geomagnetic field was absent or much weaker in the early Earth, the escape of ions from the ionosphere would be enhanced, and a substantial amount of terrestrial atmospheric ions may have been transported to lunar soils. We propose that close examination of the isotopic compositions of N and lighter noble gases in ancient lunar soils may resolve the evolution of the geomagnetic field and hence impose a constraint on early earth evolution.

The PVO (Pioneer Venus Orbiter) observations have suggested the loss of $10^6 - 10^8 \text{ O}^+ \text{ cm}^{-2}\text{s}^{-1}$ from the Venus atmosphere [3]. This substantial ion loss is understood to reflect direct interaction between the solar wind and the upper atmosphere in the absence of a permanent dipole field. For N^+/O^+ of about 0.02 around the ionopause [4], we would expect N^+ loss of about $2 \times 10^5 \text{ cm}^{-2}\text{s}^{-1}$. Venus's atmosphere may serve as a proxy for the primitive atmosphere in the early Earth, which was likely to consist predominantly of CO_2 [5]. We thus expect that a similar amount of N^+ would escape from the Earth if there were no geomagnetic field. Also considering that the Earth was much closer to the Moon in the first several hundred Ma [6], we infer from simple geometrical considerations that a few percent of escaping ions from the Earth's ionosphere may have directly hit the lunar surface. Isotopic inventory considerations suggest that this much of imported terrestrial N and possibly lighter noble gases could account for non-solar components of these elements that are observed in ancient lunar soils.

Comparing ancient lunar soils from the farside with those from the nearside can test the above proposal. It is known that the dynamical coupling between the Earth and the Moon has been so strong that the nearside of the Moon has remained facing the Earth for nearly the whole history of the Earth-Moon system [7]. Therefore, if our hypothesis is correct, terrestrial N and (possibly lighter noble gases) can only be observable in nearside lunar surface.

[1] Hale C.J. Nature, 399, 249-52, 1987. [2] Seki et al., Science, 291, 1847, 2001. [3] Kasprzak et al.

JGR, 11, 175, 1991. [4] Grebowsky et al. JGR, 9055, 1993. [5] Abe Y., Lithos, 30, 223-35, 1993. [6] Abe M. et al., Proc. 30th International Geological Conf., 26, 1-29. [7] Murray C.D. and Dermott, S.F., Solar System Dynamics, Cambridge Univ. Press, 592pp, 1999.

Noble gas study of eucrites Asuka-880702, -880761, -881388. J. Park¹ and K. Nagao¹,
¹ Laboratory for Earthquake Chemistry, Graduate School of Science, University of Tokyo, Hongo, Bunkyo-ku, Tokyo 113-0033, Japan. E-mail: jisun@eqchem.s.u-tokyo.ac.jp

Introduction:

Asuka-880702 (A-880702), Asuka-880761 (A-880761) and Asuka-881388 (A-881388), classified as Eucrites, have been studied for noble gas concentrations and isotopic compositions. These three meteorites were collected by Asuka wintering party of 29th Japanese Antarctic Research Expedition [1]. A-881388 is unbrecciated, fine-grained crystalline eucrite [2] and experienced the strong thermal metamorphism on the asteroid 4 Vesta, before the impact events [3]. And A-880702 and A-880761 are also similar as A-881388 petrologically [4].

We report the concentrations and isotopic ratios of noble gases of A-880702, -880761, -881388. K-Ar gas retention ages and the cosmic-ray exposure ages were calculated. Based on ⁸¹Kr-Kr ages, the terrestrial ages are also calculated. We discuss about their pairing.

Experimental Method:

Three eucrites were analyzed by using a mass spectrometric system (modified-VG5400/MS-II) at the Laboratory for Earthquake Chemistry, University of Tokyo. They were A-880702 (= 0.1734 g), A-880761 (= 0.1719 g) and A-881388 (= 0.1636 g).

At first, the noble gas experiment was organized at the temperature of 400 °C, in order to extract the adsorption of terrestrial gases in eucrites.

Then the eucrites samples were heated at the temperature of 1750 °C by total melting method for the radioactive isotope ⁸¹Kr. And, the gases were purified by using Ti, Zr getters. Four fractions of noble gases (He-Ne, Ar, Kr, and Xe) were measured separately; He and Ar were measured by using the Daly-multiplier system, and most of Ne and Kr, Xe by an ion-counting system.

Results and Discussion:

The concentration of the cosmogenic nuclides ³He, ²¹Ne, and ³⁸Ar (10⁻⁹ cm³STP/g) are (1) A-880702 = 220.1, 29.15, 10.47, (2) A-880761 = n.d., 54.71, 35.38, (3) A-881388 = 399.0, 52.54, 49.13, respectively (n.d.-not determined). K-Ar ages and cosmic-ray exposure ages, given in Table 1. The cosmic-ray exposure ages are calculated using the production rates for achondrite as function of target element concentrations [5]. A-880761 and A-881388 show similar cosmic-ray exposure ages about ~30 Ma, while that of A-880702 is about ~17 Ma, using T₂₁ exposure ages. K-Ar age is estimated by using ⁴⁰Ar concentrations and the average K concentrations of 124 ppm for A-881388 [2] and the other two, because of their petrological similarity [4]. K-Ar ages are longer than 4.5 Ga. Because of the sample's heterogeneity, the amount of K concentrations may be more than reported data [2].

Table 1. The cosmic-ray exposure ages and K-Ar ages

Eucrite	T ₃	T ₂₁	T ₃₈	K-Ar age
	Ma			Ga (K=124ppm ^[2])
A-880702	13.2	17.2	6.5	4.91±0.24
A-880761	n.d.	32.4	22.7	5.15±0.24
A-881388	24.0	31.0	30.7	5.57±0.24

(n.d.-not determined)

The calculated ⁸¹Kr-Kr apparent ages of A-880702, -880761, -881388 are 34.8, 59.3, 55.5 Ma, respectively, from the radioactive isotope ⁸¹Kr. Based on ⁸¹Kr-Kr apparent ages, the terrestrial age of A-880702, -880761, -881388 are also calculated as 0.22, 0.19 and 0.18 Ma, respectively. According to the terrestrial ages, A-880761 and A-881388 must have fallen on Antarctica at the same time.

Table 2. Cosmogenic Kr isotopic ratios.

	⁷⁸ Kr	⁸⁰ Kr	⁸¹ Kr	⁸² Kr	⁸³ Kr	⁸⁴ Kr	reference
A-880702	0.238	0.584	0.00602	0.790	= 1	0.366	this work
A-880761	0.181	0.502	0.00316	0.758	= 1	0.502	this work
A-881388	0.174	0.500	0.00333	0.767	= 1	0.519	this work
Stannern	0.179	0.495	-	0.765	= 1	0.63	[6]
Camel Donga	0.162	0.487	-	0.76	= 1	0.64	[5]
Millbillillie	0.154	0.48	-	0.75	= 1	0.6	[5]
	0.166	0.482	-	0.752	= 1	0.583	[7]
Y-75011	0.182	0.512	-	0.765	= 1	0.607	[8]
Y-793547	0.184	0.520	0.00262	0.766	= 1	0.494	[7]
Y-793548	0.183	0.524	0.00258	0.779	= 1	0.499	[7]
Y-793570	0.182	0.520	0.00313	0.767	= 1	0.498	[7]

calculated assuming (⁸⁶Kr/⁸³Kr)_c = 0.015

Since the $^{81}\text{Kr-Kr}$ ages do not calculated by absolute production rates [9,10], the uncertainty of cosmic-ray exposure age is small and reliable. This calculation uses the isotopic ratios of cosmogenic Kr (Table 2). Those of A-880761 and A-881388 show the same pattern with the typical eucrites such as Stannern, Camel Donga and Millbillillie.

On the basis of noble gas data A-880761 and A-881388 are paired, but A-880702 is not, although these eucrites, A-880702, -880761, -881388, seems to have similar petrology [4]. The $^{40}\text{Ar}/^{36}\text{Ar}$ isotopic ratios of A-880702, -880761, -881388, which are 1386.5 ± 22.5 , 549.9 ± 2.79 , 536.1 ± 2.09 , respectively, support the idea of two eucrites, A-880761, -881388 paring.

Acknowledgment:

We thank NIPR for Asuka samples.

References:

- [1] Yanai K. et al. (1993) *Proc. NIPR Symp. Antarct. Meteorites*, 6, 137-147. [2] Yanai K. (1993) *Proc. NIPR Symp. Antarct. Meteorites*, 6, 148-170.
- [3] Yamaguchi A. et al. (1997) *Proc. NIPR Symp. Antarct. Meteorites*, 10, 415-436. [4] *Meteorite Newsletter*, 11, #1 (2002) edited by Kojima H. and Imae N.
- [5] Eugster O. and Michel Th. (1995) *Geochim. et Cosmochim. Acta*, 59, 177-199. [6] Mart K. et al. (1966) *Naturforsch.*, 21a, 398-413. [7] Miura Y N. (1995) Doctor thesis presented to the University of Tokyo. [8] Miura Y. N. et al. (1993) *Geochim. et Cosmochim. Acta*, 50, 1357-1866. [9] Eugster O. et al. (1967) *Earth Planet Sci. Lett.* 2, 77-82. [10] Schultz L. (1986) *Mem. Natl. Inst. Polar Res. Spec. Iss.* 41, 319-327.

Presence of mature and fresh surfaces on new-born asteroid Karin. T. Sasaki¹, S. Sasaki¹, J. Watanabe², T. Sekiguchi², H. Kawakita³, T. Fuse⁴, N. Takato⁴, F. Yoshida², B. Dermawan⁵ and T. Ito², ¹Department of Earth & Planetary Science, The University of Tokyo, 7-3-1 Hongo, Bunkyo-ku, Tokyo 113-0033, Japan, ²National Astronomical Observatory of Japan, 2-21-1 Osawa, Mitaka, Tokyo 181-8588, Japan, ³Gunma Astronomical Observatory, 6860-86 Nakayama, Takayama, Gunma 377-0702, Japan, ⁴Subaru Telescope, National Astronomical Observatory of Japan, 650 North Aohoku Place, Hilo, HI 96720, USA, ⁵Department of Astronomy, Bandung Institute of Technology, Bandung 40132, Indonesia

Spectral mismatch between asteroids and meteorites:

There is a long-standing spectral mismatch between asteroids and meteorites. Although S-type asteroids are the most common among the inner-part main belt asteroids as well as near-Earth asteroids, reddened reflectance spectra and derived mineralogy of S-type asteroids are different from those of ordinary chondrites, the most common meteorites. Space weathering is thought to be able to explain the spectral mismatch [1,2]. Recent asteroid surveys have discovered a strong link between S-type asteroids and ordinary chondrites [3,4]. Multispectral observation of Ida by Galileo spacecraft showed that relatively fresh surface such as crater interiors and ejecta have reflectance like ordinary chondrites [1]. Furthermore, NEAR-Shoemaker spacecraft revealed an ordinary chondrite composition of S-type asteroid 433 Eros [5,6]. The laboratory experiments using high-energy pulse laser irradiation showed that the reflectance change forming S-type spectra is caused by formation of nanophase iron particles within vapour-deposited rim around regolith particles [7]. The degree of space weathering can be used to discuss the age of asteroids [7].

Recently, using numerical integration of asteroid orbits, Nesvorny *et al.* found a new-born group of asteroids named Karin cluster group, which is thought to be remnants of a recent breakup of only 5.8 million years ago [8]. Here, we observed the brightest asteroids 832 Karin in this group to consider the relation between the asteroid age and the effect of space weathering.

Observation of new-born asteroid Karin:

A near-infrared spectroscopic observation of Karin was performed by the 8-m Subaru telescope with Cooled Infrared Spectrograph and Camera for OHS (CISCO) on September 14 (UT) 2003. In order to obtain wide range spectrum in the near-infrared region, we used grisms named zJ (0.88-1.40 μm), JH (1.06-1.82 μm), and wK (1.85-2.51 μm). The integration time for Karin was 800 s for each grism i.e. 2400 s for each setting (zJ + JH + wK). In order to cancel telluric absorption features, a reference star (G2V star HIP3990) was observed just after Karin observation. And for the wavelength

identification, another reference star (A0 star SAO165395) was observed during Karin observation.

We observed Karin at 7:57-8:40 (UT), 8:46-9:29 (UT), and 10:45-11:50 (UT). The synodic rotational period of Karin is 18.348 hours, which was derived from the light-curve obtained by supporting observations (Fig.1). In comparison with the light curve, rotational phases of Karin in our observation are 0.30-0.34 (the first set), 0.35-0.38 (the second set), and 0.45-0.50 (the last set).

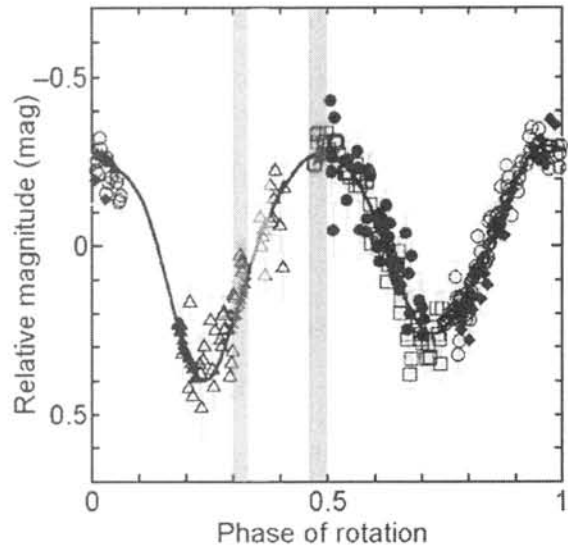


Figure 1 Light-curve of 832 Karin [9]. Based on data obtained by the 1.8-m VATT at the Vatican observatory at Mt. Graham, Arizona, by the 1-m Schmidt telescope at the Kiso observatory, Japan, and by the 40-cm telescope in Fukuoka University of Education, Japan. Total observing duration is nine nights from August to September 2003. The rotational period of this asteroid is 18.348 hours. The amplitude of the light-curve is 0.7 mag at the zero Solar-phase-angle. The zero phase of rotation is at 2004 July 31 0:00 UT. Our observation corresponds to the phase of rotations of three vertical lines.

Karin has heterogeneous surface:

Fig.2 shows the relative reflectance spectra of Karin for these three observation sets. Bottom, middle, and top spectra in Fig.2 are those of the first, the second, and the last observational sets, respectively. The difference in the airmass at the observations of the asteroid and the reference star was smaller than 0.1 for first set and second set. There is obvious difference between the top two and bottom spectra at wavelength between 0.9 and 1.4 μ m. Spectra of reference star SAO165395 were unchanged before the first set and after the second set of Karin observation: the difference of zJ band spectra in Fig.2 is not artifact. Large color changes with rotation have been hardly observed on asteroids, and this would be the biggest color change with rotational phase ever observed. This result suggests that Karin's surface is inhomogeneous for each rotational phase.

Mature and fresh surfaces on Karin, Discussion:

The shape of 0.8-2.5 μ m in the first set's spectrum is consistent with an S-type object. The latter two spectra can match typical spectrum of L6 ordinary chondrite. And the first set should be the reddened spectrum of the last set by space weathering. Our result indicates that Karin has two different surfaces, reddened and un-reddened surfaces, and the difference among spectra would reflect the degree of space weathering. These color changes were also derived by supporting observations, which observed Karin at B(0.44 μ m), V(0.54 μ m), R(0.63 μ m), and I(0.81 μ m), bands in visible wavelength [9]. Their result suggests that reflectance at phase 0.3 is more weathered than that at phase 0.5 and less weathered than that at phase 0.2.

The mature and fresh surfaces' spectra strongly stand up for the idea that space weathering is responsible for the mismatch between asteroid types and meteorite classes. The change of space weathering degree on Karin's surface can be explained if Karin is one of cone-shaped fragment at low-velocity impact forming the Karin family. Impact disruption experiments suggest that in the low-velocity impact regime ($v < 1$ km/s) the target is shattered into cone-shaped fragments, pointing towards the impact point [10]. In this case, only the base of this cone is mature surface darkened by space weathering, which is consistent with a feature of the light-curve of Karin described above. Probable sharp edged boundary between the cone base and cone side of the fragment could explain the observed change of the space weathering degree around phase 0.2-0.5. Around the phase 0.3-0.4, both matured and fresh surfaces would have been observed.

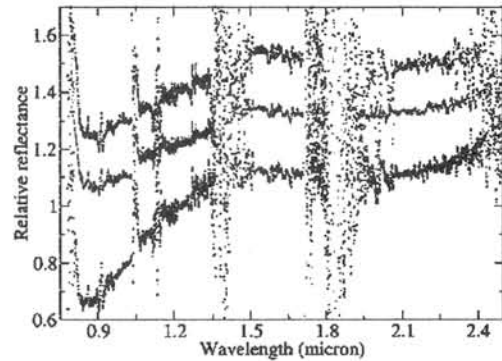


Figure 2 Relative reflectance spectra of 832 Karin: Bottom one is the spectrum of the first set of the night, middle one is that of the second set, and top one is that of the last set. Spectral data are smoothed by running average of 5 pixels, and top and bottom spectra are vertically shifted by 0.2 for clarity. Reflectance spectra of reference star SAO165395 were unchanged before the first set and after the second set of Karin observation.

References:

- [1] Chapman, C. R. (1996) *MAPS* **31**, 699-725,
- [2] Pieters, C. M. *et al.* (2000) *MAPS*. **35**, 1101-1107,
- [3] Binzel, R. P., Bus, S. J., Burbine, T. H. & Sunshine, J. M. (1996) *Science* **273**, 946-947, [4] Burbine, T. H. & Binzel, R. P. (2002) *Icarus* **159**, 468-499, [5] McFadden, L. A. *et al.* (2001) *MAPS* **36**, 1711-1726, [6] Bell, J. F. III *et al.* (2002) *Icarus* **155**, 119-144, [7] Sasaki, S., Nakamura, K., Hamabe, Y., Kurahashi, E. & Hiroi, T. (2001) *Nature* **410**, 555-557, [8] Nesvorný, D., Bottke, W. F. Jr, Dones, L. & Levison, H. F. (2002) *Nature* **417**, 720-722, [9] Yoshida, F. *et al.* (2004), submitted to PASJ, [10] Fujiwara, A. *et al.* (1989) in *Asteroid II* 240-265 (Univ. Arizona Press, Tucson).

Sodium-metasomatism in CAIs in the anomalous carbonaceous chondrite Ningqiang: Evidence for parent-body processes.

Mitsuhiro Sugita and Kazushige Tomeoka

Department of Earth and Planetary Sciences, Faculty of Science Kobe University, Nada, Kobe 657-8501, Japan. Correspondence authors' e-mail address: 026d860n@y04.kobe-u.ac.jp

Introduction:

Ningqiang has been described as an anomalous CV3 chondrite containing low abundances of Ca-Al-rich inclusions (CAIs) (~1.0 vol%) and bulk refractory lithophiles [1]. However, it was later found to be more closely related in petrography and chemistry to CK chondrites [2]. A more recent study by Lin and Kimura [3] reported that the abundance of CAIs in Ningqiang is higher (2.5 vol%) than the previous estimate and most CAIs are similar to those in Allende but less altered. In order to find a clue to the anomalous characteristics and possibly unique formation history of Ningqiang, we undertook a detailed mineralogical and petrographic study of this meteorite using a scanning electron microscope and an electron probe microanalyzer. We have found that Ningqiang shows unusual characteristics in CAIs and matrix that have not been reported previously. In contrast to the report by Lin and Kimura [3], most CAIs in Ningqiang contain abundant nepheline and show evidence for extensive alteration, which suggests that Ningqiang has experienced some unique secondary processes.

Petrography and Mineralogy:

Ca-Al-rich inclusions

We found 17 inclusions in the three thin sections (63, 37, and 52 mm² in area) that range in size from 80 to 580 μm with the average of 260 μm. They comprise ~1.7 vol% of the samples. All the inclusions are fine-grained, and no melilite-rich type A inclusions such as reported by Lin and Kimura [3] are present. Most inclusions can be divided into two types: (1) spinel-pyroxene-rich inclusions (7 out of 17), and (2) pyroxene-rich inclusions (9 out of 17). Spinel-pyroxene-rich inclusions are assemblages of concentric objects; each object has a core of spinel, surrounded by a rim (5-10 μm in thickness) of diopside; melilite, aluminous diopside and nepheline occasionally occur inside of the diopside rim. They correspond to the spinel-pyroxene inclusions that Lin and Kimura [3] described as the second most abundant type of inclusions. On the other hand, pyroxene-rich inclusions are unrimmed porous aggregates of fine grains (0.1-10 μm in size) of diopside and/or Ca-Mg-Fe-rich pyroxene, nepheline and occasional spinel, melilite and sodalite. Nepheline and sodalite have formed by replacing melilite. Inclusions of these two types occasionally contain small grains of perovskite, ilmenite and

hibonite. Only one inclusion (200X700 μm in size) did not fit into these two types. This is only one inclusion containing major amounts of melilite and spinel.

However, unlike melilite-rich type A inclusions, it is a porous aggregate of very fine grains (0.1-10 μm in size) of melilite, spinel, nepheline and sodalite.

In addition to these relatively large CAIs, we also found 21 smaller inclusions ranging in size from 15 to 60 μm from the matrix. They are angular to irregularly shaped porous aggregates of diopside and/or Ca-Mg-Fe-rich pyroxene and nepheline with minor variable amounts of melilite, ilmenite, perovskite, hibonite and Fe-rich olivine; they are mineralogically and texturally similar to the pyroxene-rich inclusions described above.

Matrix

The matrix consists mainly of fine grains of Fe-rich olivine that show a wide range in size and composition. There are mainly two populations in olivine grains; one is Fe-rich, relatively large (2-20 μm in size) and irregular in shape, and the other is Fe-poor, small (<1 μm) and equidimensional in shape. These characteristics do not resemble any of the matrix olivines in CV3 chondrites. Minor minerals include magnetite, troilite and Fe-Ni metal. In addition to these minor constituents, nepheline occurs pervasively as grains ranging in size from 0.1 to 5 μm. There are considerable variations in number density of nepheline grains on the scales of 0.1-1 mm.

The bulk composition of the matrix, obtained by using a defocused (100 μm-diameter) beam, is similar to mean CV3 matrix for most elements [4]. However, Na and Al are significantly higher (3.1 and 1.6 by factor, respectively) and variable in distribution. Plots of the analyses in terms of Na vs. Al show an apparent correlation of the two elements with a slope of approximately Na/Al=1 (in atomic proportion), which suggests that Na and Al in the matrix can be mainly explained by nepheline (Na₂Al₂Si₂O₈). X-ray chemical mapping shows that Na is mainly concentrated in the matrix, where it shows variable contents that are mostly correlated with those of Al. There is a tendency for a region having higher contents of Na and Al to show a higher abundance of nepheline grains.

Discussion:

The CAIs in Ningqiang that we studied are fine-grained and much smaller in size and lower in modal abundance (1.7 vs. 5.1 vol%) than those in CV3 chondrites. These characteristics are similar to those reported by Rubin et al. [1]. Although Rubin et al. did not report detailed mineralogy of the CAIs, the CAIs studied here contain abundant nepheline and minor amounts of melilite. In contrast, Lin and Kimura [3] reported that the CAIs in their samples show a significantly higher modal abundance and most CAIs are melilite-rich type A inclusions. These results suggest that Ningqiang is not a homogeneous rock but is composed of at least two different lithologies, refractory inclusion-rich and -poor. Our samples probably represent the refractory inclusion-poor lithology.

Rubin et al. [1] suggested, based on the low abundance of refractory inclusions, that Ningqiang formed relatively late in the solar nebula, after most refractory inclusions had already been incorporated into other objects. However, our study has revealed that most CAIs in Ningqiang are porous aggregates of fine grains and melilite grains in them have been extensively replaced by nepheline. In the matrix, nepheline grains are abundant, and small CAI fragments are also widely scattered. The nepheline grains and CAI fragments are likely to have resulted from disaggregation of porous, fine-grained CAIs. It has been known that CAIs in CV3 and CO3 chondrites show various degrees of alteration and contain a variety of secondary minerals including nepheline and sodalite [e.g., 5-8]. Most previous workers suggested that the feldspathoids formed by reaction of primary phases such as melilite and anorthite with the solar nebula gas. However, recent studies showed that CAIs in CO3 chondrites of higher petrologic subtypes tend to show higher degrees of Na-metasomatism [8-10], and thus suggested that, at least, part of the metasomatism occurred on the parent body. Tomeoka and Itoh [11] studied nepheline in chondrules in CO3 chondrites and suggested that it formed initially as

hydrous nepheline under the presence of aqueous fluids and was subsequently dehydrated after exhaustion of aqueous fluids on the meteorite parent body.

We suggest that the CAIs in the refractory inclusion-poor lithology of Ningqiang has experienced aqueous alteration and subsequent dehydration under the conditions similar to what Tomeoka and Itoh [11] proposed for CO3 chondrites. In those processes, most CAIs probably became fine-grained and porous, and during brecciation, they were disaggregated and mixed into matrix. Consequently, CAIs decreased in size and modal abundance, whereas the number density of small fragments of CAIs increased. In addition, we envisage that nepheline in the matrix also formed by precipitation from solutions that migrated through matrix during aqueous alteration. These results imply that Ningqiang has gone through low-grade aqueous alteration and subsequent dehydration at the early stage of heating on the meteorite parent body.

References:

- [1] Rubin A. E. et al. (1988) *Meteoritics* 23, 13-23.
- [2] Kallemeyn G. W. et al. (1991) *Geochim. Cosmochim. Acta* 55, 881-892.
- [3] Lin Y. and Kimura M. (2003) *Geochim. Cosmochim. Acta* 67, 2251-2267.
- [4] MacSween H. Y. Jr. and Richardson S. M. (1977) *Geochim. Cosmochim. Acta* 41, 1145-1161.
- [5] MacPherson G. J. and Grossman L. (1984) *Geochim. Cosmochim. Acta* 48, 29-46.
- [6] Wark D. A. (1986) *Earth Planet. Sci. Lett.* 77, 129-148.
- [7] Tomeoka K. et al. (1992) *Meteoritics* 27, 136-143.
- [8] Russell S. S. et al. (1998) *Geochim. Cosmochim. Acta* 62, 689-714.
- [9] Kojima T. et al. (1995) *Proc. NIPR Symp. Antarct. Meteorites* 8, 79-96.
- [10] Itoh D. and Tomeoka K. (1998) (Abstract) *Antarct. Meteorites* 23, 42-44.
- [11] Tomeoka K. and Itoh D. (2004) *Meteorit. Planet. Sci.* 39 (in press).

CL images of anorthite in meteorites. N.Sugiura¹ and A.Miyazaki¹, ¹Department of Earth and Planetary Science, Univ. of Tokyo.

Introduction:

Anorthite is the main target mineral in meteorites for Al-Mg dating by secondary ion mass spectrometry. Many anorthite grains in Ca-Al-rich inclusions (CAIs) show an initial Al ratio $^{26}\text{Al}/^{27}\text{Al}=5\times 10^{-5}$ which is called the canonical value. But some anorthite grains in CAIs are disturbed after the CAI formation, showing smaller initial Al ratios. It is not easy to distinguish the pristine anorthite and disturbed anorthite by usual petrographic studies. Al-Mg ages of anorthite in chondrules have been studied for some time [1]. But it is not yet clear if there is any definite systematic changes in the Al-Mg ages among chondrules. If there is a real difference among the chondrule ages, then it is not yet clear to what extent the Al-Mg age difference is attributed to the timing of chondrule formation and to what extent the ages had been affected by parentbody metamorphism. Cathodoluminescence (CL) is a powerful tool for detecting slight changes in mineral compositions and structure. Thus, CL of anorthite may provide valuable information on the formation and subsequent metamorphic alteration of anorthite.

Instrumental:

A panchromatic CL detecting system (Gatan Inc.) was attached to a scanning electron microscope. Slight modification was made to the system so that a RGB (red-green-blue) filter can be placed in front of the detector window. CL images were taken with the RGB filters and color images were synthesized from the RGB images using a software (photoshop, Adobe Co.) The use of color image (or at least blue-filtered image) is important for studying anorthite CL. This is because anorthite CL (mainly emitted in blue or green region) is rather weak and unfiltered CL images are often dominated by red CL emitted from olivine, pyroxene and spinel. The electron beam used for CL observation is ~ 0.5 nA and the high voltage applied to the photomultiplier is usually 1kV, although the voltage is often reduced to 0.9kV for red images. (Otherwise, the red signal is too strong.) Normally, RGB-filtered images were simply superposed to produce nearly natural color images. Comparison between CL images from different anorthite grains is made using such nearly natural color. However, comparison within an image is often made with enhanced blue (and green) color. This is because anorthite luminesces mainly in blue (or green) and hence difference in CL brightness is best seen in blue color. It is to be noted that out nearly natural color is not necessarily identical with that obtained by the luminoscope.

Anorthite grains in CAIs and chondrules were selected from from one CV (Sahara 98044), two CO (Yamato 81020 and Yamato 82094). One eucrite

(Asuka 881394) containing anorthite was also studied..

Results:

Primary anorthite in CAIs: A large (~ 1 cm) type B CAI in Sahara 98044 contains many anorthite grains in the core, which is considered to be primary in the sense that it was formed at the time of initial formation of the CAI. Based on the texture, this CAI seems to have experienced a shock event. CL of the primary anorthite is blue. Anorthite is known to often shows greenish CL which is due to a trace amount of Mn [e.g. 2]. The bluish color of the primary anorthite suggests that Mn (a volatile element) is depleted and that structural defects may be the main emitter of the CL. Difference in the CL brightness is often observed within an anorthite grain. In many cases the boundary between the two areas with different brightness is straight and the Mg concentration in the brighter area is smaller than that in the darker area. Such features were reported by [3,4] and are due to sector zoning during the growth of anorthite crystals. Although, each area of anorthite appears usually homogeneous in CL, slight heterogeneity of CL brightness was observed in the dark (Mg-rich) area of an anorthite grain. SIMS observation of Mg^+ ions showed that such area is heterogeneous with respect to the Mg concentration. Therefore, the slight heterogeneity in the CL brightness is probably due to heterogeneous distribution of Mg (which is known as a CL quencher in anorthite [3,4]). This suggests that the anorthite was somewhat disturbed by a secondary event. We note that the initial Al ratio of this anorthite is canonical, which means either the secondary event occurred early when abundant ^{26}Al was alive, or the secondary disturbance is not significant at the scale of SIMS analyses (20–30 μm).

In a rare case, a boundary between bright CL and dark CL areas was not straight and no systematic difference in the Mg concentrations was found in these areas. Elsewhere in this anorthite, non-luminescent areas are present. Such non-luminescent areas appear homogeneous in BEI image and are devoid of cracks that are normally quite abundant in anorthite. Based on this texture, we suggest that such non-luminescent areas may be maskelynite (or shock-melted glass). By inference, the bright CL area in this anorthite is suggested to be rich in structural defects formed by a shock event. Studies on shock effects on CL in plagioclase are rather limited [5] and further studies on CL in artificially shocked anorthite are needed to verify the above speculation.

Needle-shape anorthite suggesting rapid remelting is present in a CAI in Yamato 81020. The CL is purple and rather dark. The Mg concentration

is ~0.06 atomic %.

Secondary anorthite in CAIs: Secondary anorthite (which appears to have formed after the initial melting of compact CAIs) was found in Yamato 82094. It is located near the rim of a CAI. The CL color of the anorthite is somewhat white to greenish, suggesting that Mn may be present. The Mg concentration is ~0.03 atomic % and the CL is bright.

Anorthite in chondrules: So far, chondrules examined by CL color are limited and hence we caution that the following results may not be representative of the whole chondrule population. CL of anorthite (~0.4 atomic % Mg) in a type I chondrule in the Yamato 81020 is dark red. It is darker than pyroxene in CL. Anorthite (0.03 atomic % Mg) in a Al-rich chondrule in the Yamato 82094 luminesces brightly in blue. Anorthite (~0.4 atomic % Mg) in a type I chondrule in Yamato82094 luminesces somewhat faintly in blue. Anorthite (~0.4 atomic % Mg with a relatively high Na) in another type I chondrule luminesces very darkly in blue.

In summary, chondrule anorthite mainly luminesces in blue which may be attributed to structural defects. Reddish CL color in anorthite is usually attributed to Fe^{3+} . But Fe^{3+} should not be present in metal-containing chondrules and hence the emitter is not known. The blue CL is bright in Mg-depleted anorthite.

Achondrite: Anorthite with ~0.07 atomic % Mg in the Asuka 881394 luminesces dark red. This CL is dark in spite of the relatively small Mg concentration. Thus quantitative relationship between CL brightness and Mg concentration seems rather complicated.

Summary:

In the case of CAIs, usefulness of CL observation is evident. Sector zoning, slight heterogeneity in Mg distribution and shock effects may be found in primary anorthite. In addition, secondary anorthite may be distinguished by greenish color. In the case of chondrule anorthite, bright CL corresponds to low Mg concentrations. But more detailed CL observations and corresponding trace element measurements are needed for full understanding of the CL color and the brightness. It is not yet known if anorthite CL color in chondrules corresponds to the formation conditions and/or metamorphic conditions.

References:

- [1] Kita N.T. et al. (2000) GCA, 64, 3913-3922.
- [2] Gotze J. et al. (1999) Am. Min., 84, 1027-1032.
- [3] Hutcheon I.D. et al. (1978) Proc. Lunar Planet. Sci. Conf., 9th, 1345-1368. [4] Steele I.M. et al. (1997) GCA, 61, 415-423. [5] Kaus A. and Bischoff A. (2000) Meteor. Planet. Sci., 35, A86.

Heating conditions of chondrule precursors during shock-wave heating: constraints from sulfur isotopic compositions of chondrule troilites. S. Tachibana¹, G. R. Huss², H. Miura³, and T. Nakamoto³, ¹Dept. of Earth and Planetary Science, Univ. of Tokyo, ²Department of Geological Sciences and Center for Meteorite Studies, Arizona State Univ., ³Center for Computational Physics, Univ. of Tsukuba.

Introduction:

Chondrules would have formed by melting and subsequent cooling of solid precursors. Evaporation of volatile elements may have occurred from high-temperature chondrule melts during chondrule formation. Sulfur would thus have evaporated either from silicate melt or from Fe-S melt, immiscible with silicate melt, at chondrule-forming temperatures [e.g., 1], and would have recondensed onto chondrules during cooling as sulfide veneers around chondrules or as opaque assemblages such as those found in matrix or at chondrule rims [e.g., 2-4].

The sulfur isotopic compositions of chondrule troilites in Semarkona and Bishunpur (both LL3.1), measured by ion microprobe, are indistinguishable from troilites around chondrules or in matrix [5, 6]. The largest fractionation reported in [5, 6] was 2.7 ± 1.4 ‰/amu, while all other troilite grains had isotopic fractionations of <1 ‰/amu. Since some of chondrule troilites measured by [5, 6] are most likely primary troilites, which crystallized from Fe-S melt that did not evaporate completely during chondrule formation, the suppressed sulfur isotopic compositions can put some constraints on evaporation behavior of sulfur during chondrule formation. We have interpreted such suppressed isotopic fractionations of sulfur as results of i) rapid heating of precursors at temperatures below the silicate solidus and ii) diffusion-controlled evaporation through a surrounding silicate melt at temperatures above the silicate solidus [5, 6].

Shock-wave heating has been proposed as a plausible mechanism for abrupt heating of chondrule precursors [e.g., 7-11]. Chondrule precursors in the pre-shock region (i.e., before the shock front passing) are heated by radiation from the post-shock region, while they are heated by gas-drag in the post-shock region. Gas-drag heating is strong enough to melt solid grains and form chondrules for some shock parameters. The heating/cooling rate of precursors in the post-shock region is determined by energy transfer between gas and dust, radiative cooling of dust, and latent heat cooling due to evaporation of dust or melt.

In this study, we model evaporation behavior of sulfur from chondrule precursors and accompanying sulfur isotopic fractionation during shock-wave heating and attempt to put constraints on conditions for shock-wave heating.

Evaporation of sulfur from troilite and Fe-S melt:

Evaporation of troilite and Fe-S melt and accompanying sulfur isotopic fractionation are modeled in a Fe-S-H system that is open for gas-solid (or gas-liquid) reactions but is closed for the abundance of elements.

Because sulfur is more volatile than iron in the Fe-S system, preferential evaporation of sulfur occurs from troilite and Fe-S melt. Evaporation flux of sulfur from troilite and Fe-S melt can be described by the Hertz-Knudsen equation [e.g., 12]:

$$J = (\alpha_e P_i^{eq} - \alpha_c P_i) / (2\pi m_i kT)^{1/2},$$

where P_i^{eq} is the equilibrium vapor pressure of gas species i ($i = \text{H}_2\text{S}$, HS , and S_2), P_i is the vapor pressure of i , m_i is the molecular weight of i , k is the Boltzmann constant, T is the absolute temperature, and α_e and α_c are the evaporation and condensation coefficients. The evaporation and condensation coefficients ($0 \leq \alpha_e, \alpha_c \leq 1$) express kinetic barriers for evaporation and condensation. Here we assume that $\alpha_e = \alpha_c = \alpha$ for simplicity. The α for H_2S , HS , and S_2 , which have dependence on temperature and hydrogen pressure, are taken from experimental data of [12]. The equilibrium vapor pressures for S-bearing gas species for troilite and Fe-S melt are calculated from [13, 14]. Since iron is much more refractory than sulfur, evaporation of iron is not taken into account.

Isotopic fractionation of sulfur is assumed to occur for evaporation from Fe-S melt for simplicity. Instantaneous isotopic homogenization within Fe-S melt is also assumed. The square root of mass ratio is used for an isotopic fractionation factor for each sulfur-bearing gas species.

The proportions of solid phases (FeS or Fe) and melt in a bulk condensed phase and the composition of the melt at a certain temperature are determined based on the bulk composition of the condensed phase with the Fe-S binary phase diagram.

Evaporation of sulfur in the post-shock region was simulated by heating the Fe-S-H system at heating rates predicted in a shock wave heating model (initial number density of gas: $n_0 = 10^{13}$ - 10^{14} cm^{-3} ; a shock velocity: $v = 6$ - 10 km/s; an initial dust radius: $r = 10$ - 1000 μm). The dust/gas weight ratio for the pre-shock region was set to the solar dust/gas ratio (0.01). We used a temperature profile that forsterite particles would experience.

Evaporation in the pre-shock region was evaluated by changing heating rates (10 - 10^5 K/h) and temperatures just before the shock front passing (800 - 1200°C) as parameters.

Results and Discussion:

Post-shock region: The heating rate of chondrule precursors in the post-shock region ranges from $\sim 10^4$ to $\sim 10^7$ K/h at temperatures of 1000-1300°C, depending on shock parameters. It is found that little evaporation of sulfur occurs from solid troilite due to abrupt heating and sulfur evaporates mainly from Fe-S melt after temperature rises above the troilite liquidus. Although the isotopic composition of sulfur becomes heavier as evaporation proceeds, rapid heating prevent a large degree of sulfur evaporation and thus significant isotopic fractionation. Under the shock conditions in this study, isotopic fractionations in evaporation residues are at most 2.4 ‰/amu at temperatures below 1300°C. Such suppressed isotopic fractionations are consistent with the observation by [5, 6]. At temperatures above 1300°C, silicates begin (or have begun) to melt and evaporation of sulfur should occur through surrounding silicate melt, which would not produce a large degree of isotopic fractionation [5, 6]. Note that the pre-shock heating discussed below is not considered to elucidate the effect of gas-drag heating in the post-shock region.

It is also found that the degrees of isotopic fractionations for grains with different sizes are almost the same. The heating rate for a smaller grain is larger than that for a larger grain because smaller grains with larger surface/volume ratios are decelerated (i.e., heated) more efficiently by gas drag than larger grains. Rapid heating should suppress evaporation from smaller grains. On the other hand, evaporation occurs efficiently from smaller grains due to their larger surface/volume ratios. The effects of heating rate and evaporation, both of which are approximately proportional to the grain size, are thus canceled out [10], resulting in the similar degrees of evaporation and accompanying isotopic fractionations for grains with different sizes and different heating histories.

Pre-shock region: If radiative heating in the pre-shock region is relatively rapid ($>10^4$ K/h), the evaporation behavior of sulfur is almost the same as the one we discussed for the post-shock region for 100 μm -sized grains, i.e., isotopic fractionation of sulfur is suppressed (less than 3 ‰/amu) even if the pre-shock heating is considered.

However, in the case with the heating rates of 10^2 - 10^3 K/h for the pre-shock region, which have been predicted for radiative heating in shock-wave models [8, 9, this study], more sulfur evaporates due to prolonged heating time. If the temperature before the shock front passing reaches to $\sim 1000^\circ\text{C}$, isotopic fractionation can still be suppressed to less than 3 ‰/amu because most of sulfur evaporates from solid troilite. However, if the temperature of chondrule precursors is raised to 1100-1200°C in the

pre-shock region, sulfur evaporates from Fe-S melt before the shock-front passing, which results in sulfur isotopic fractionation of >3 ‰/amu, which is inconsistent with [5, 6]. If the temperature reaches to $>1200^\circ\text{C}$ in the pre-shock region, it would be difficult for chondrules to retain sulfur during chondrule formation.

References: [1] Yu Y. et al. (1996) In *Chondrules and the Protoplanetary Disk*, pp. 213-219. [2] Zanda B. et al. (1995) *Meteoritics*, 30, 605. [3] Lauretta D. S. et al. (2001) *GCA*, 65, 1337-1353. [4] Lauretta D. S. and Buseck P. R. (2003) *Meteoritics & Planet. Sci.*, 38, 59-80. [5] Tachibana S. and Huss G. R. (2002) *LPS XXXIII*, Abstract #1685. [6] Tachibana S. and Huss G. R. (2004) submitted to *GCA*. [7] Iida A. et al. (2001) *Icarus*, 153, 430-450. [8] Desch S. J. and Connolly H. C. (2002) *Meteoritics & Planet. Sci.*, 37, 183-207. [9] Ciesla F. J. and Hood L. L. (2002) *Icarus*, 160, 258-270. [10] Miura H. et al. (2002) *Icarus*, 158, 281-293. [11] Miura H. and Nakamoto T. (2004) submitted to *Icarus*. [12] Tachibana S. and Tsuchiyama A. (1998) *GCA* 62, 2005-2022. [13] Chase M. W. (1998) *NIST JANAF Thermochemical Tables*. New York, AIP. [14] Nagamori M. et al. (1970) *Trans JIM* 11, 190-194.

Magnesian granulitic clasts in some lunar meteorites from the feldspathic highlands.

Hiroshi Takeda¹, Addi Bischoff² and A. Yamaguchi³, ¹Research Inst., Chiba Inst. of Technology, ²Inst. fuer Planetologie, Muenster, Germany, ³National Inst. of Polar Res., Japan.

Introduction:

Lunar granulites are metamorphic rocks and occur as fragments in meteorites and sampled rocks from the Moon. Lindstrom and Lindstrom [1] studies eight granulites in the Apollo samples and proposed that they result from metamorphism of precursor anorthositic norites of the early lunar crust. Granulitic clasts are also abundant in many anorthositic lunar meteorites. A diagram of Mg' number = $Mg \times 100 / (Mg + Fe)$ atomic % in mafic minerals versus anorthositic content of plagioclases of these clasts demonstrates, that they are similar to those of the above-mentioned Apollo granulites [e.g., 2]. This report will mainly focus on granulitic breccias, because they are (a) widespread and (b) the most important magnesian feldspathic lithology in the lunar highlands [3]. The study of granulites will lead to a better understanding of the earliest history of the lunar highland crust.

Here, we report on the mineralogy of large granulitic clasts in three lunar meteorites, Yamato(Y) 86032 [4], Dhofar(Dho) 489 [5] and Dho 908 [6]. Y86032 and Dho 489 have been proposed to come from the far-side of the Moon, because they are not contaminated with KREEP components (e.g., very low Th) [7]. They may represent our best samples of the early lunar highland crust, because their Ar-Ar ages are as old as 4.3 to 4.4 Gyr [8,9].

Samples and experimental methods:

Dho 489 weighing 34.4 g is a crystalline matrix feldspathic breccia [5]. Three polished thin sections (PTSs, ,1, ,11 ,2-1) of Dho 489 were examined for comparisons. One PTS of Dho 908 (provisional name) from Institut fuer Planetologie, Germany and Y86032,45 from NIPR [4] were studied by an optical microscope and by electron microprobe (EPMA). Chemical compositions of minerals in the granulitic clasts were analyzed by the JEOL 733 EPMA equipment at the Ocean Res. Inst. of Univ. of Tokyo.

Results:

A granulitic clast found in Y86032, 45 shows a rectangular shape 1.5 x 0.84 mm in size, in which subrounded mafic silicates up to 0.11 x 0.07 mm in size are evenly distributed (Fig. 1). This texture is different from those of some Apollo granulites, which show remnants of breccia texture (granulitic breccias) [1]. Granulitic breccias also occur in lunar meteorites (see Table 1 in [10] or [11]). The compositions of olivine (Fo76.2) and pyroxene ($Ca_6Mg_{75}Fe_{19}$, $Mg'=80$) within the clast are magnesian and are similar to those of the magnesian granulites [1]. The plagioclase compositions

(An96.8) are similar to those in Dho 489. Modal abundance of plagioclase (74.3 vol. %), pyroxene (19.4), olivine (5.0) and augite (1.2) [4] indicates anorthositic norite affinity.

A spinel troctolite clast 4.1 x 1.3 mm in size in Dho 489,11 shows granulitic texture with elongated oval-shaped olivine crystals (up to 0.69 x 0.23 mm in size). The amount of plagioclase (72 vol. %, An96) is larger than that of olivine (27 %, Fo84). The recrystallized matrix textures of Dho 489,11 and ,2-1 are much finer grained than those reported previously (PTS ,1) [5]. The distribution of dark, fine crystalline matrices is similar to that of Dho 908.

A large, granulitic clast found in Dho 908 has sharp angular edges and is of triangular shape with 3.9, 3.1, 2.9 mm-sized sites. One corner is truncated by an 1.4 mm edge. Mafic silicates with joined subrounded elongated spherical shape up to 0.20 x 0.05 mm in size are evenly distributed in plagioclase of the entire clast (Fig. 2). Plagioclase has a modal abundance of 64 vol.%. The Fo84.5 and An96.1 values are also similar to those of these minerals in Dho 489 [9]. The Fo values of the olivine fragments in the breccia matrices range from 90-60.

In spite of the similarity of these large clasts, chemical compositions of mafic silicates in the fragmental breccia matrices of the three lunar meteorites are different. In Y86032 and Dho 908 are more ferroan mafic silicates as in many Apollo highland breccias than Dho 489. The Fos of the Dho 489 olivines are mostly higher than 70, except for only a few grains with Fo65, and two pyroxene grains with $Mg'=65$ and 36. The most abundant Fo contents agree with those of the spinel troctolite clast [9].

Discussion:

Many Apollo granulites have been recognized as metamorphosed breccias, because we can detect remnants of a brecciated texture on a large scale (e.g., 79215,55). Granulitic breccias result from brecciated rocks that have been thermally metamorphosed by the heat of large impacts (probably close to impact melt pools or sheets) causing solid state recrystallization [2,3]. Some lunar granulites such as 67016,111 show fairly uniform texture. Textures of meteoritic lunar granulites have been difficult to define, because of their small sizes.

Although the large crystalline clast in Dho 489 has a granulitic texture, we classified this rock as a spinel troctolite, because of their large grain size, undisturbed crystalline texture, and the presence of chromian spinel (pleonaste). The presence of spinel suggests its deep-seated crustal origin and excavation by a large basin-forming event [9,12]. This view is

in line with the proposal by Korotev *et al.* [3], that the type of magnesian anorthositic breccia was assembled by one or a small number of very large impacts. Such impacts penetrated to mid crust levels or deeper and produced thick ejecta deposits, and later basin-sized and large-crater events brought these rocks to the surface and distributed them widely. Other two granulitic clasts have finer texture, but their fairly uniform textures suggest that they may represent distinct types of precursor rocks. Higher modal abundance of plagioclase suggests that the precursor rocks approach the mineralogical composition of anorthositic troctolites and norites.

The absence of clasts of Mg-suite rocks such as troctolites, norites, or gabbros in these lunar meteorites is to be noted. Mixing of spinel troctolite with nearly pure anorthosite is required for Dho 489. Ferroan anorthosites were not abundant around the site Dho 489 derived from. In contrast, fragments in matrices of Y86032 and Dho 908 contain some ferroan anorthosite components.

The far-side connection was established in part by the low FeO, MgO, and Th concentrations obtained by the orbiting gamma-ray experiments [3]. Compositions of granulites more closely resemble the average composition of lunar highlands [1,3]. Based on the predominance of plutonic anorthositic norite precursors in rocks having the composition typical of the highlands, Lindstrom and Lindstrom [1] suggested that plutonic anorthositic norites were more abundant in the early lunar crust as is implied by their scarcity among pristine rocks from the Apollo missions [1]. The Y86032 granulite agrees with this proposal. We add anorthositic troctolites as an important lithology. The trace element data of Y86032 and Dho 489 [7] directly indicate towards a far-side origin of these rocks.

Magnesian feldspathic lunar meteorites are defined as "magnesian", because they contain a normative component of high-Mg' mafic silicates in the bulk composition [3]. Calculated olivine has a Fo content above 80. In the meteorites with the highest Mg', the main olivine-bearing lithologies are magnesian granulitic breccias [3] and spinel troctolite, and not Mg-suite lithologies of the Apollo rock collection. The average composition and the Th/Sm ratios of the magnesian granulitic breccias cannot be explained as a mixture of the above known plutonic rocks [3].

We interpret that the metamorphism took place before the impact event to form these breccias, as indicated by the old Ar-Ar ages of Y86032 and Dho 489 [8,9]. The earliest crustal rock formed on a Vesta-like body 4.562 Gyr ago such as Asuka 881394 [13], which has a kind of granulitic texture. Rocks formed, while the magma ocean was still active or the solidified crust was still hot. Intense bombardments of meteoroids also contributed to the granulite formation. The old Ar-Ar ages and magnesian nature of the anorthositic rocks support

such scenario. Large angular clasts as in Dho 908 and Y86032 were abundant lithologies when these fragmental breccias were formed. Thus, these granulites must have been important components of the earliest lunar highlands.

This study was carried out as parts of "Ground-based Res. Announcement for Space Utilization" (PI: K. Saiki) by Japan Space Forum and of a Grant-in-Aid for Japanese Ministry of Education, Sci. Culture and Tech. We thank Dr. T. Ishii and Mrs. M. Otsuki at ORI for EPMA, and Dr. M. Ohtake for PTS, Dho 489,11, Drs. D. D. Bogard, L. E. Nyquist, M. Ohtake, K. Saiki, T. Arai, K. Misawa, J. Haruyama, and K. Nakamura for discussions.

References:

- [1] Lindstrom M. M. and Lindstrom D. J. (1997) *JGR*, 91, D263-D276.
- [2] Takeda H. *et al.* (1997) *Proc. Lunar Planet. Sci. Conf.*, 20, 91-100.
- [3] Korotev R. L. *et al.* (2003) *Geochim. Cosmochim. Acta*, 67, 4895-4923.
- [4] Yamaguchi A. *et al.* (2004) *LPS XXXV*, #1474.
- [5] Takeda H. *et al.* (2003) *LPS XXXIV*, #1284.
- [6] Bischoff A. (2004) *Met. Bull.* (provisional).
- [7] Karouji Y., Ebihara M. and Yamaguchi A. (2004) *This volume*.
- [8] Bogard D. D. *et al.* (2000) *LPS XXXI*, #1138.
- [9] Takeda H. *et al.* (2004) *LPS XXXV*, #1222.
- [10] Bischoff *et al.* (1998) *Meteorit. Planet. Sci.*, 33, 1243-1243.
- [11] Ostertag *et al.* (1986) *Mem. Natl. Inst. Polar Res., Spec. Issue*, 41, 17 - 44.
- [12] Herzberg C. T. and Baker M. B. (1980) *Proc. Conf. Lunar Highlands Crust*, 113-132.
- [13] Nyquist L. E. *et al.* (2003) *Earth Planet. Sci. Lett.*, 214, 11-25.

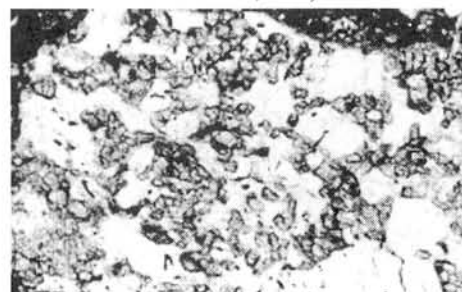


Figure 1. Photomicrograph of a granulitic clast in Y86032, 45 (width 1.3 mm).

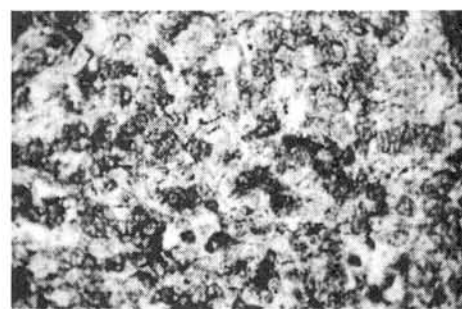


Figure 2. Photomicrograph of a granulitic clast in Dho 908 (width 1.3 mm).

Petrologic study of eucritic clasts in mesosiderites, Mount Padbury and Vaca Muerta.

M. Tamaki¹, A. Yamaguchi^{1,2}, K. Misawa^{1,2}, M. Ebihara³, H. Takeda⁴ ¹ Grad. Univ. Advanced Studies, 1-9-10 Kaga, Itabashi, Tokyo 173-8515, Japan. ² National Institute of Polar Research, 1-9-10 Kaga, Itabashi, Tokyo 173-8515, Japan. ³ Grad. School of Sci., Tokyo Metropolitan University, Hachioji, Tokyo, 192-0372, Japan. ⁴ Research Institute, Chiba Institute of Technology, Narashino 257-0016, Japan. (E-mail: tamaki@nipr.ac.jp)

Introduction:

Mesosiderites are stony-iron meteorites consisting of roughly equal proportions of silicates and Fe-Ni metal. The silicate fraction of mesosiderite mainly consists of pyroxene and plagioclase and is similar in mineralogy and chemical compositions to those in eucrites, igneous rocks from the crust of an HED parent body [1]. It is open to question whether or not silicate fraction of mesosiderites came from the same parent body as the HEDs. Most of the mesosiderites suffered severe thermal metamorphism, as indicated by petrographic, mineralogical and chronological evidence [2-5].

We performed geochemical and petrological studies of clasts in the least metamorphosed mesosiderites Mount Padbury and Vaca Muerta to better understand igneous and subsequent thermal histories.

Sample and analytical technique:

We selected two silicate clasts from Mount Padbury and Vaca Muerta. Polished thin sections of silicate clasts were examined optically and with scanning electron microscope. Minerals were analyzed with electron probe microanalyzers (JEOL JXM-8800 and 8200). Electron probe analysis was carried out at an accelerating voltage of 15kV with a beam current of 12-30nA. Counting time was 15-90 sec for each element. Major, minor and trace element abundances of bulk samples were determined by neutron-induced prompt gamma-ray analysis (PGA) and by instrument neutron activation analysis (INAA). Rare earth element (REE), Th and U were determined by inductively coupled plasma mass spectrometry (ICP-MS).

Petrology and mineralogy:

Basaltic clast from Mount Padbury

This clast displays a fine-grained (50 μ m in size) granular texture but has a relict subophitic texture with plagioclase laths (2mm long) and anhedral pyroxene grains (~1mm). Minor minerals include tridymite, chromite, ilmenite, Ca-phosphate, troilite, Fe-metal and baddeleyite (Table 1). Tridymite occurs as a massive interstitial phase between plagioclase and pyroxene, and as lathy to irregular discrete crystals. Pigeonite contains homogeneously distributed augite lamellae and is similar to that in type 5 eucrites [6]. The augite lamellae are thin (several μ m thick) and closely spaced. Pyroxene compositions are Wo₂En₃₅ - Wo₃₉₋₄₁En₂₉₋₃₀. Mg/Fe ratios of pigeonite are limited and are in the same range of those of other basaltic

clasts in mesosiderites [7] and basaltic eucrites [6]. Plagioclases are uniform in composition (An_{88.3-89.4}).

Gabbroic clast from Vaca Muerta

This clast shows a coarse-grained gabbroic texture, mainly composed of low-Ca pyroxene, plagioclase and tridymite. Minor minerals include chromite, Ca-phosphate, troilite and Fe-metal (Table 1). Low-Ca pyroxene has thin exsolution lamellae of augite (<2 μ m). Some augite occurs as a thick band (up to 100 μ m in width) in low-Ca pyroxene. Rim of pyroxene includes abundant augite, tridymite and troilite, with small amount of chromite, Ca-phosphate and Fe-Ni metal. Composition in the pyroxene rim is more Mg-rich than core. Low-Ca pyroxenes in the edge of clast contain irregular-shaped augites, abundant Ca phosphates and opaque minerals. Large tridymite grains occur between pigeonite and plagioclase, and small tridymite grains occur in the pigeonite rim. The titanium and calcium contents of large tridymite grains are lower than those of small tridymite grains.

Bulk chemistry:

Figure 1 shows CI-normalized REE patterns of Mount Padbury and Vaca Muerta clasts. The basaltic clast from Mount Padbury shows a relatively flat (CI \times 10) REE pattern similar to other basaltic clasts in mesosiderites [8,9] and basaltic eucrites [10]. The gabbroic clast from Vaca Muerta has very low REE concentrations. The pattern has a negative slope for LREE, a steep positive slope for HREE and a positive Eu anomaly (normalized Eu/Eu* = 83). This fractionated pattern is general characteristic in some gabbroic clasts [9-11]. The bulk molar Mg/(Mg+Fe) ratios of the basaltic clast from Mount Padbury and the gabbroic clast from Vaca Muerta are 0.38 and 0.58, respectively.

Discussion:

Basaltic clast from Mount Padbury

The remnant subophitic texture invokes relatively rapid cooling of the initial melt, analogous to most basaltic eucrites and basaltic clasts from mesosiderites. The metamorphic degree of pyroxene in the basaltic clasts is comparable to type 5 eucrite [6]. Peak metamorphic temperatures of type 5 pyroxene could have been ~1000 $^{\circ}$ C [12]. We applied two pyroxene geothermometry [13] to coexisting pigeonite and augite, and obtained equilibration temperatures of 833-932 $^{\circ}$ C. Texture and equilibration temperatures of pyroxene indicate that thermal history at > 800 $^{\circ}$ C of the basaltic clast and

basaltic eucrite might have been similar.

Gabbroic clast from Vaca Muerta

The presence of thick lamellae of augite indicates that the gabbroic clast experienced slow cooling after crystallization. The two-pyroxene equilibration temperature of low-Ca pyroxene and augite pairs is 904-1080 °C. This result shows that the clast may have experienced higher temperature and slower cooling rates than the basaltic clast from Mount Padbury. Small tridymite grains coexisting troilite in pyroxene rim would be formed by subsolidus reduction. Large tridymite grains would be formed by crystallization or by partial melting. Positive Eu anomaly is larger than those of cumulate eucrites [14]. This highly fractionated REE pattern may represent melting residue of preexisting cumulate.

In summary, the basaltic clast from Mount Padbury experienced rapid cooling similar to the basaltic eucrite. The gabbroic clast from Vaca Muerta experienced extensive reduction. The bulk compositions of the gabbroic clast may reflect SiO₂ rich melts.

Acknowledgements

We thank Western Australian Museum for supplying Mount Padbury clasts, and Mr. S. Inoue for supplying Vaca Muerta clasts from the Inoue collection.

References:

- [1] Mittlefehldt, D. W. (1979) *Geochim. Cosmochim. Acta* **43**, 1917-1935. [2] Powell, B. N. (1971) *Geochim. Cosmochim. Acta* **35**, 5-34. [3] Floran, R. J. (1978) *Proc. Lunar Planet. Sci. Conf.*, **9th**, 1053-1081. [4] Delaney, J. S. et al. (1981) *Proc. Lunar Planet. Sci. Conf.*, **12th**, 1315-1342. [5] Stewart et al. (1994) *Geochim. Cosmochim. Acta* **58**, 3487-3509. [6] Takeda, H. and Graham, A. L. (1991) *Meteorit.* **26**, 129-134. [7] Ikeda, Y. et al. (1990) *Proc. NIPR Symp. Antarct. Meteorites*, **3**, 99-131. [8] Rubin, A. E. and Jerde, E. A. (1988) *Earth Planet. Sci. Lett.* **87**, 485-490. [9] Rubin, A. E. and Mittlefehldt, D. W. (1992) *Geochim. Cosmochim. Acta* **56**, 827-840. [10] Warren, P. H. and Jerde, E. A. (1987) *Geochim. Cosmochim. Acta* **51**, 713-725. [11] Kimura, M. et al. (1991) *Proc. NIPR Symp. Antarct. Meteorites*, **4**, 263-306. [12] Yamaguchi, A. et al. (1996) *Icarus* **124**, 97-112. [13] Kretz, R. (1982) *Geochim. Cosmochim. Acta* **46**, 411-421. [14] Mittlefehldt, D. W. (1979) *Geochim. Cosmochim. Acta* **43**, 1917-1935.

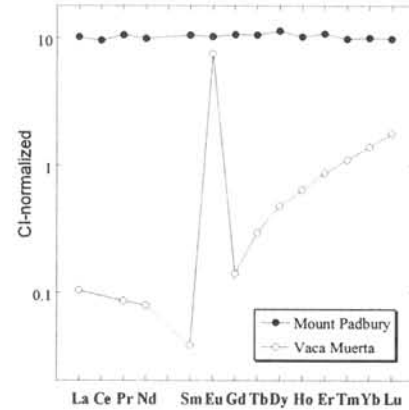


Figure 1. CI-normalized REE patterns of clasts from Mount Padbury and Vaca Muerta.

Table 1. Modal compositions of clasts from Mount Padbury and Vaca Muerta.

	M.P. basaltic clast	literature [7]	V.M. gabbroic clast	literature [7]
Modes (vol%)				
Pyroxene	52.9	42.9	42.6	39.0
Plagioclase	43.6	38.9	43.4	48.0
Silica	1.5	2.4	11.2	3.8
Ilmenite	0.4	0.2		
Chromite	0.5	0.5	0.6	0.3
Phosphate	0.2	+	0.6	0.3
Troilite	0.4	0.4	0.6	0.3
Fe-metal	0.3	0.2	0.5	+
Baddeleyite	+	+		
Total	99.6	85.5	99.5	91.7

Thermal history of Yamato 86753. T. Tomiyama¹ and K. Misawa^{1,2}, ¹Dept. of Polar Science, Grad. Univ. for Advanced Studies, 1-9-10 Kaga, Itabashi, Tokyo, 173-8515 JAPAN. (tomiyama@nipr.ac.jp) ²Antarctic Meteorite Research Center, National Institute of Polar Research, 1-9-10 Kaga, Itabashi, Tokyo, 173-8515 JAPAN.

Introduction:

The degrees of metamorphism of individual ordinary chondrites (OCs) reflect thermal histories on their parent bodies. The thermal structure of the OC parent body (i.e., the geological setting of each petrologic type of OC) is not well known, because metamorphic degree depends not only on metamorphic temperature but also on duration of metamorphism. Detailed study of thermal history is necessary for elucidating the thermal structure of the OC parent body. We performed two-pyroxene geothermometry, olivine-spinel (ol-sp) geothermometry and metallographic cooling rate estimates [1-3] on equilibrated L chondrites, to determine individual thermal histories. Isotopic analyses of the ⁵³Mn-⁵³Cr system in olivines have been done on Yamato (Y) 86753, a rapidly cooled L5 chondrite.

Experiments:

Polished thin-sections of equilibrated L chondrites were examined using an optical microscope, a scanning electron microscope (JEOL JSM-5900LV equipped with Oxford LINK ISIS EDS system) and an electron microprobe (JEOL JXA-8800M). Two-pyroxene geothermometry, ol-sp geothermometry and metallographic cooling rate estimate were applied to coexisting mineral pairs of interest.

For isotopic measurement, we prepared a polished potted-but sample of Y86753 (L5) with San Carlos olivines whose Mn/Cr ratio was obtained from neutron activation analysis. Olivines with very low Cr contents were identified in Y86753 using electron microprobe. Isotopic analyses were carried out for these olivines, using a secondary ion mass spectrometer (SHRIMP II). The primary O₂⁻ beam was accelerated to 10 kV with a current of 3-4 nA, focused into a spot of ~ 17 μm. The secondary ion counting was operated through slight energy filtering and collector slit of 180 μm width, resulting in a mass resolving power of M/ΔM ~ 3400. Repeated analyses on San Carlos olivine (n = 27) yield ⁵³Cr/⁵²Cr ratio of 0.11170 ± 0.00008 (95% c.l.). There was an instrumental mass fractionation of ~ 15 % favoring lighter isotope. Sensitivity factor of 2.06 for measured ⁵⁵Mn/⁵²Cr ratio was calculated from neutron activation data.

Results:

Two-pyroxene geothermometry [1] yields equilibration temperatures of 890-920 °C for high-Ca pyroxenes and 810-860 °C for low-Ca pyroxenes in L5-L6 chondrites. Pyroxenes in L4 chondrites were not chemically equilibrated. The ol-sp geothermometry [2] yields equilibration temperatures of 620 – 650 °C for most L4-L6 chondrites (Fig. 1). The ol-sp temperatures of Y86753 (~ 710 °C) are higher than those of other chondrites.

Fe-Ni metals in Y86753 were cooled at > 100 °C/Myr, whereas most Fe-Ni metals in other L4-L6 chondrites were cooled at 0.1-100 °C/Myr (Fig. 2). Ion probe analyses show that Y86753 olivines have ⁵⁵Mn/⁵²Cr ratios of up to ~ 280 (Fig. 3). There is no systematic relationship between ⁵³Cr excess and ⁵⁵Mn/⁵²Cr ratio.

Discussion:

The parent bodies of ordinary chondrites accreted in the early stages of the formation of the solar system [4]. After accretion, parent bodies might have been internally heated by sources such as the decay of short-lived radionuclides (e.g., ²⁶Al [5]). If such was the case, parent bodies should initially have had onion-shell structures, in which metamorphism increased with burial depth [6]. Metamorphic temperatures and cooling rates of OCs should then correlate with petrologic types.

Pyroxene geothermometry shows metamorphic temperatures of L4 chondrites were lower than those of L5 - L6 chondrites. This is partly consistent with a relationship between petrologic types and metamorphic temperatures. However, ol-sp temperatures and metallographic cooling rates show no significant relationship against petrologic types. Because a majority of OCs shows similar ol-sp temperatures and metallographic cooling rates, we consider that applied geothermometries and metallographic cooling rate estimates are somewhat insensitive to small differences in thermal histories.

Higher ol-sp temperature and higher metallographic cooling rate of Y86753 indicate that this chondrite experienced rapid cooling. Flash heating by shock is unlikely because Y86753 is only a weakly shocked chondrite (S2). We suggest that thermal structure of the L chondrite parent body was modified during thermal metamorphism and that Y86753 experienced different cooling histories from other chondrites. If there was a large scale impact event, thermal structure of the parent body could have been partly or totally disturbed, as suggested by [7]. In such case, some materials of OC parent body could have been excavated from the hot interior and cooled rapidly. Y86753 could be such a chondrite, which experienced this hot excavation.

The ⁵³Mn-⁵³Cr systematics of chondrules in un-equilibrated OC suggest that the formation of OC chondrules formed at ~ 4568 Ma [8]. Although most olivine in OCs crystallized during chondrule formation, Y86753 olivine does not retain ⁵³Cr excesses. The experimental data for Cr diffusion in olivine yielded an Arrhenius equation of $D = 2.28 \times 10^{-2} \exp(-E/RT) \text{ cm}^2/\text{s}$ with an activation energy of $E = 323 \text{ kJ/mol}$ [9]. The typical diffusion distance (\sqrt{Dt}) of Cr in olivine within 1 Myr exceeds typical grain

size of olivine (100 μm) at the temperature of ~ 790 $^{\circ}\text{C}$. Pyroxene temperatures of L5-6 chondrites are higher than this temperature, implying that the ^{53}Mn - ^{53}Cr system of olivine could be an open system during thermal metamorphism of highly equilibrated OCs. The ^{53}Mn - ^{53}Cr system of Y86753 olivine closed during the rapid cooling after hot excavation.

We can calculate the upper limit of ^{53}Mn - ^{53}Cr age of Y86753 olivine. Assuming that isochrones of ^{53}Mn - ^{53}Cr system are fixed at $(^{53}\text{Mn}/^{53}\text{Cr}, \delta^{53}\text{Cr}) = (0, 0)$, the closure age of ^{53}Mn - ^{53}Cr system in Y86753 olivine is calculated to be ≤ 4563 Ma. Y86753 suffered thermal metamorphism which prolonged more than ~ 5 Ma after chondrule formation, and cooled rapidly just after a large scale impact on the parent body.

References: [1] Kretz, R. (1982) GCA, 46, 411-421. [2] Fabriés, J. (1979) Contrib. Mineral. Petrol., 69, 329-336. [3] Willis, J. and Goldstein, J. I. (1981) PLPSC, 12B, 1135-1143. [4] Weidenschilling, S.J. (1988) Meteorites and the Early Solar System, Univ. Ariz. press, Tucson, 348. [5] Lee, T. et al. (1976) GRL, 3, 109-112. [6] Miyamoto, M. et al. (1981) PLPSC, 12B, 1145-1152. [7] Taylor, G. J. et al., (1987) Icarus, 69, 1-13. [8] Nyquist, L. et al. (2001) Meteoritics & Planet. Sci., 36, 911. [9] Ito, M. et al. (2004) LPSC, 35, #1324, [10] Lugmair, G.W. and Shukolyukov A. (1998) GCA, 62, 2863.

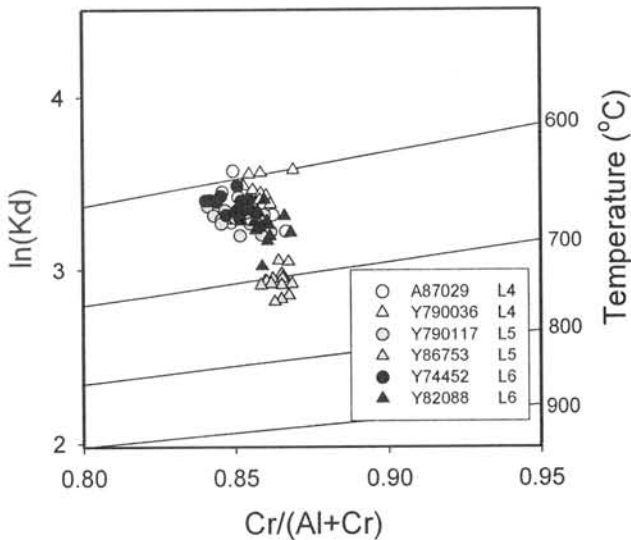


Fig. 1. Plots of Fe-Mg partition coefficients between coexisting ol-sp pairs against Cr/(Al+Cr) ratio of chromites, showing closure temperature of the ol-sp system [2].

$$Kd = \left(X_{\text{Mg}}^{\text{ol}} \cdot X_{\text{Fe}}^{\text{sp}} \right) / \left(X_{\text{Fe}}^{\text{ol}} \cdot X_{\text{Mg}}^{\text{sp}} \right)$$

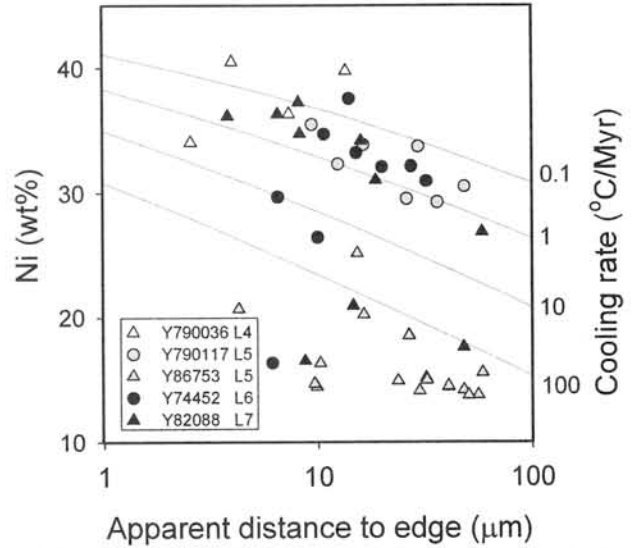


Fig. 2. Plots of Ni contents in taenite cores against the grain sizes, showing metallographic cooling rates [3]. Data for A87029 are not plotted because all analyses show too high Ni contents (> 44 wt%)

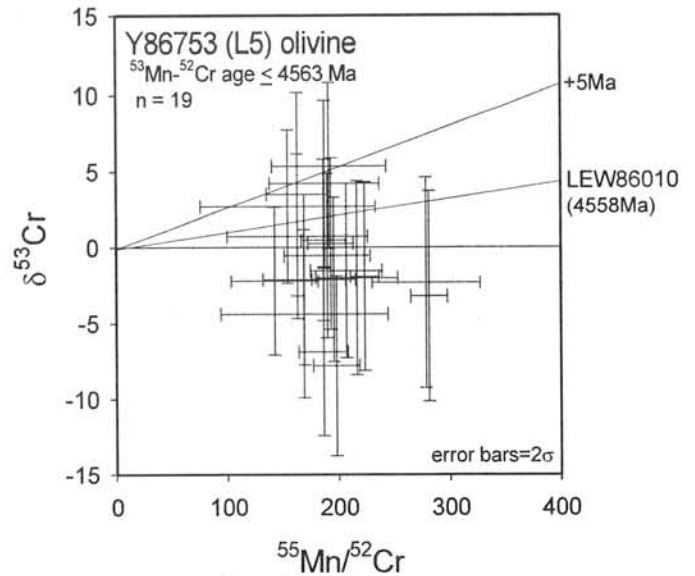


Fig. 3. The ^{53}Mn - ^{53}Cr systematics of Yamato 86753 (L5). The isochrones for LEW86010 Angrite and +5 Ma are also presented [10]. Error bars represent 2σ of means.

$$\delta(^{53}\text{Cr}) = \left[\left(\frac{^{53}\text{Cr}}{^{52}\text{Cr}} \right)_{\text{UNK}} / \left(\frac{^{53}\text{Cr}}{^{52}\text{Cr}} \right)_{\text{STD}} - 1 \right] \times 10^3$$

Heating experiments of the HaH 262 eucrite. A. Yamaguchi¹ and T. Mikouchi², ¹National Institute of Polar Research, Tokyo 173-8515, ²Department of Earth and Planetary Sciences, Graduate School of Science, University of Tokyo, Tokyo 113-0033.
(E-mail: yamaguch@nipr.ac.jp)

Introduction.

Eucrites are among the oldest igneous rocks formed 4.55-4.56 Ga ago, and probably make up most of the outer crust of the parent body, probably asteroid 4Vesta. The formation of eucritic crust occurred in a short period and subsequently, thermal metamorphism and impact events took place in a crustal scale, which disturbed textures, mineral chemistries and isotopic ages [1-4]. Almost all eucrites are metamorphosed in a varying degree [1,2]. In most cases, the metamorphism occurred at the temperatures below the solidus (~900-1000°C) [1]. Recent studies [3,4] showed that some eucrites such as Ibitira and EET90020 experienced peak temperatures over the solidus of eucrites at ~1060°C [5]. The high temperature metamorphism may have caused the formation of secondary minerals and redistribution of trace elements, disturbance of some isotopic ages, and probably changed the original igneous textures [3,4]. It appears that this process was related to shock events when the crust was still hot. Also, some eucritic clasts in mesosiderites could have experienced remelting induced by heating during metal-silicate mixing event [6]. To better understand textural and chemical changes of eucrites during high temperature metamorphism, we have performed heating experiments of an unbrecciated eucrite, Hammadah al Hamra (HaH) 262 near the solidus

Heating experiments and analytical techniques.

We prepared a thin slice (~5 x 3 x 1 mm) of HaH262 and placed it inside the Pt foil suspended in an alumina tube of a vertical 1 atm gas-mixing furnace. So far we have performed two runs at 1050 and 1100 °C. In each run, heating time was for 24 hours and the sample was quenched in air. Experimental temperatures were measured with thermocouples calibrated by using a melting point of gold (1064.4°C). Gas mixture of CO₂-H₂ was used to control the oxygen fugacity, and each gas flow rate was monitored by a mass flow meter. We employed the oxygen fugacity of logfO₂=IW-1 for the experiment, which was measured by an oxygen electrolytic zirconia cell (SIRO₂ C700+).

Polished thick sections of the starting material and recovered samples were examined by optical and scanning microscopy, and with a micro-Raman spectroscopy and an electron microprobe. The modes of phases were determined by X-ray mapping of electron microprobe.

HaH262

Our entire slab of HaH262 (4.6 x 3.0 cm)

shows an igneous texture. It displays a subophitic to ophitic texture composed of plagioclase lath (~0.15 x 0.7 mm) and anhedral pyroxene (~0.6 mm) (Fig. 1). Minor minerals include ilmenite, chromite, Ca-phosphate, and troilite. Recrystallized mesostasis interstitially occurs in plagioclase and pyroxene crystals, and is mainly composed of fine-grained quartz. Pyroxene has a remnant Ca zoning like those found in type 4 eucrite (e.g., Stannern, [1]), and shows a cloudy appearance due to the presence of minor oxide minerals. Metallic Fe and troilite in many cases occur along healed crack. Pyroxene compositions are Wo_{5.4}En_{33.9}-Wo_{42.4}En_{28.8}. Plagioclase is chemically zoned from An_{91.4}Or_{0.4} to An_{75.6}Or_{1.5}, and has minute inclusions (mainly silica minerals) in the cores. The texture and mineral chemistry indicate that HaH262 is a typical ordinary eucrite. The absence of brecciation textures, and the low degree of shock metamorphism and weathering [7] make HaH262 a suitable starting sample for the heating experiments.

Results

In the sample heated at 1050°C for 24 hours under IW-1, we could not find any detectable textural changes at present. Chemical compositions of plagioclase (An_{91.3}Or_{0.33}-An_{76.7}Or_{1.6}) and pyroxenes are also unchanged.

In the sample heated at 1100°C for 24 hours under IW-1, the sample is clearly melted (>10 vol%) with abundant vugs (~10 vol%) but still roughly preserve original basaltic texture (Fig. 2). Thus, the solidus temperature of this eucrites is between 1050 and 1100 °C, consistent to crystallization experiments with ordinary eucrites [5].

The melting mainly occurs along the boundaries between pyroxene and plagioclase. We did not observe recrystallized mesostasis. Ilmenite also was melted although we observed a few tiny phases rich in Ti. It is likely these phases are almost totally melted. Instead, we observed aggregates of fine-grained cristobalite laths that could have been formed during quenching. Plagioclase crystals roughly show original lath shape, but are complexly corroded by melt and contain narrow channels of melts. Pyroxene is mostly melted with rounded to subrounded core, surrounded by fine crystals of newly formed pyroxenes formed during quenching.

Chemical compositions of plagioclase are An_{91.8}Or_{0.2} to An_{81.2}Or_{1.35} slightly narrower than those of the unheated sample, probably due to the preferential melting of the Na-rich rim near the mesostasis. The chemical compositions of relict pyroxene are unchanged by heating. The partial

melt is slightly enriched in TiO_2 (0.79-1.75 wt%) and has a high $\text{Fe}^{\#}=\text{Fe}/(\text{Fe}+\text{Mg})$ (0.78). The content of CaO (10.5-11.2 wt%) is similar to those of ordinary eucrites, and that of Al_2O_3 (9.7-10.5 wt%) is slightly lower than those of ordinary eucrites such as Juvinas. Comparison with the bulk data of HaH262 is in progress.

Discussion

Our experiments showed that disequilibrium melting of the HaH262 eucrite occur at between 1050-1100°C. Minor minerals such as silica minerals, ilmenite, and Ca-phosphate are almost totally melted at 1100°C. The similar results were given by shock experiments at 20GPa preheated at ~900°C [8].

EET90020 and Ibitira experienced peak temperature over the solidus according to mineralogical and geochemical studies. Mineralogical evidence suggests that the heating event occurred in a short period at ~900-1000°C. The temperature went up around 1060°C, and cooled rapidly (several degrees per day) because of the presence of disequilibrium phases [3]. Wadhwa et al. [6] suggested that the basaltic inclusions of mesosiderites also experienced similar thermal history above 900-1000°C.

Our 1100°C experiments showed that the a few tens of percent of melting do not destroy the original igneous texture if the heating event was short and the cooling rate was rapid (i.e., by impact). This explains the presence of relict basaltic texture observed in recrystallized eucrite, Ibitira and eucritic inclusions in Mt. Pudbury [9,10].

Yamaguchi et al. [3] suggested that large tridymite and Ti-rich spinels in EET90020 were crystallized from partial melts formed by shock events. The partial melt of the 1100°C experiment is not so enriched in TiO_2 , compared to results of shock-partial melting [8]. It may be possible that some Ti-rich phase could be a likely phase to be crystallized although it depends of the redox conditions [8]. The concentration of such elements strongly depends on the degree of partial melting, and mineral assemblages. Our experiments are preliminary, and we are planning to perform melting experiments between 1050 and 1100 °C.

References

- [1] Takeda H. and Graham A.L. (1991) *Meteoritics* 26, 129-134. [2] Yamaguchi A. et al. (1996) *Icarus* 124, 97-112. [3] Yamaguchi A. et al. (2001) *GCA* 65, 3577-3599. [4] Floss C. et al. (2000) *AMR* 13, 222-237. [5] Stolper E.M. (1977) *GCA* 41, 587-611. [6] Wadhwa M. et al. (2003) *GCA* 67, 5047-5069. [7] Grossman J.N. (2000) *MAPS* 35, A199-A225. [8] Yamaguchi A. et al. (2002) in *High Pressure Shock Compression of Solids V.*, 29-45. [9] Steele I.M. and Smith J.V. (1976) *EPSL* 7, 833-835. [10] Tamaki M. et al. (2003) *this volume*.

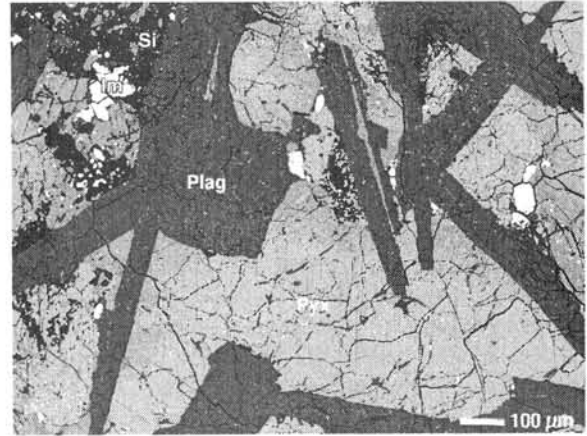


Fig. 1. Backscattered electron image (BEI) of unheated HaH262, showing a basaltic texture. There is recrystallized mesostasis (upper left) mainly composed of fine-grained silica (black, Si) minerals. Pyx = pyroxene; Plag = plagioclase; Im = ilmenite

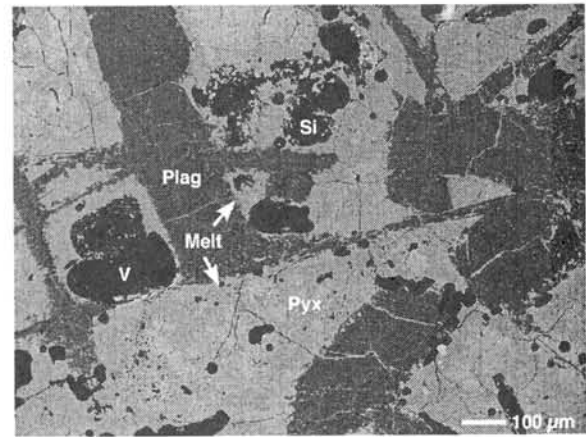


Fig. 2. BEI of the sample heated at 1100 °C for 24 hours under the IW-1 condition, showing a remnant basaltic texture. Plagioclase lath is complexly corroded by melt. V: vugs filled with epoxy.

Aqueous alteration effects on argon-rich noble gases in the Ningqiang carbonaceous chondrite: an experimental study.

Y. Yamamoto¹, R. Okazaki² and T. Nakamura²,

¹Department of Earth and Planetary Sciences, Graduate school of Sciences, Kyushu University, Hakozaki, Fukuoka 812-8581, Japan. ²Department of Earth and Planetary Sciences, Faculty of Sciences, Kyushu University, Hakozaki, Fukuoka 812-8581, Japan.

Introduction:

Ningqiang is an ungrouped carbonaceous chondrite because of its low abundance of refractory lithophile elements. Some petrologic, oxygen isotopic, and thermoluminescence suggest that Ningqiang is similar to the oxidized CV3 chondrites [e.g., 1]. This chondrite contains very primitive materials like dark inclusions with radiation damaged silicates [2] and also contains Ar-rich noble gases [3].

Ar-rich noble gases, one of the components of primordial noble gases, are contained in some classes of anhydrous carbonaceous chondrites and unequilibrated ordinary chondrites [e.g., 4, 5]. The Ar-rich noble gases are characterized by the high $^{36}\text{Ar}/^{132}\text{Xe}$ and $^{84}\text{Kr}/^{132}\text{Xe}$ ratios relative to Q gas [6]. The $^{36}\text{Ar}/^{132}\text{Xe}$ and $^{84}\text{Kr}/^{132}\text{Xe}$ ratios are variable between meteorites, and thus unique composition has not been defined. Recently, it was reported that the Ar-rich noble gases in Ningqiang were removed by light HF/HCl etching, accompanied by loss of amorphous rims coated around fine-grained olivine and pyroxene. These results suggest that Ar-rich noble gases are located in the amorphous rims [3]. In contrast to some classes of anhydrous carbonaceous chondrites and unequilibrated ordinary chondrites, carbonaceous chondrites that experienced aqueous alteration contain little amount of Ar-rich noble gases, whereas contain Q gas dominantly [e.g., 7]. Q gas is in phase Q that is carbonaceous materials in matrix and rims around chondrules. The elemental composition of Q gas distributes in the narrower range than that of Ar-rich noble gases.

In order to understand the relation between the abundance of Ar-rich noble gas contents and the degree of aqueous alteration that meteorites have experienced in their parent bodies, we performed an experimental aqueous alteration on Ningqiang.

Experimental method:

A piece of Ningqiang weighing 300mg was crushed into μm -sized particles and loaded into pressurized vessel with 15g liquid water. Sample and water were kept at 200°C (estimated internal water vapor pressure is 15 atms.). After 10 days, half of the sample (150mg) was recovered and the rest of the sample (150mg) was kept being soaked for another 10 days.

Natural Ningqiang sample and altered ones soaked for 10 and 20 days were analyzed for mineralogy and noble gases. Mineral composition before and after alteration was analyzed by powder X-ray diffraction (XRD) method with Rigaku

RAD-IIA at Kyushu University. Noble gases were extracted at the temperatures of 300, 700, 1000, 1300 and 1850°C. The concentrations and isotopic ratios of the noble gases were determined with a mass spectrometer (modified MM5400) at Kyushu University. To confirm homogeneity of noble gas elemental and isotopic compositions in samples, stepped pyrolysis analyses were performed on two and three fractions (each fraction was weighing about 10mg.) prepared from the 10- and 20-day sample, respectively. The results discussed below are averages of these fractions. For natural Ningqiang, five fractions (each fraction was weighing about 2mg.) were analyzed by total melting because of the same reason as above. A stepped pyrolysis analysis was performed on 23.2mg of natural Ningqiang at the temperature described above. In each samples, noble gases released at 300°C were considered the adsorbed air on the basis of their isotope ratios, and then are not considered in the following discussion.

Results and Discussion:

XRD patterns show that the natural sample consists of olivine, low-Ca pyroxene, magnetite and iron sulfide, among which olivine is the dominant phase. The results of noble gas analyses indicate that the $^{36}\text{Ar}/^{132}\text{Xe}$, $^{84}\text{Kr}/^{132}\text{Xe}$ and $^{20}\text{Ne}/^{132}\text{Xe}$ ratios of total gas in natural Ningqiang are 220, 1.3 and 31, respectively. The result of stepped pyrolysis reveals that the noble gases released at around 1000°C have high $^{36}\text{Ar}/^{132}\text{Xe}$ and $^{84}\text{Kr}/^{132}\text{Xe}$ ratios and are in the range of Ar-rich noble gases contained in enstatite chondrites [8] and ureilites [9]. On the other hand, noble gases released at temperatures higher than 1300°C have low ratios and are in the range of Q gas [10] (Fig. 1).

Aqueous alteration for 10 days:

XRD pattern of the sample altered for 10 days shows that intensities of olivine, low-Ca pyroxene and iron sulfide decrease. This indicates that olivine, low-Ca pyroxene and iron sulfide were decomposed during 10 days alteration. The presence of reflections at 7.28Å and 2.70Å indicate that phyllosilicate and hematite were formed, respectively. Magnetite content in the 10-day sample is equivalent to that in the natural sample. Noble gas analyses show that 10-day alteration removes 90%, 72% and 61% of ^{36}Ar , ^{84}Kr and ^{132}Xe in natural Ningqiang, respectively, whereas less proportion (28%) of ^{20}Ne is removed. These indicate that the altered phases had contained greater amounts of Ar, Kr and Xe than

those remaining in the 10-day sample. The $^{36}\text{Ar}/^{132}\text{Xe}$ and $^{84}\text{Kr}/^{132}\text{Xe}$ ratios are reduced to 59 and 0.9, respectively (Fig. 1), whereas $^{20}\text{Ne}/^{132}\text{Xe}$ ratio increases to 57. Calculated $^{36}\text{Ar}/^{132}\text{Xe}$ and $^{84}\text{Kr}/^{132}\text{Xe}$ ratios of noble gases removed by the 10-day alteration are 323 and 1.5, respectively (Fig. 1). These values are higher than those of natural Ningqiang. This leads that noble gases removed by the 10-day aqueous alteration are enriched in Ar and Kr relative to Xe, compared with natural sample. The results of 10-day sample indicate that the Ar-rich noble gases are located in materials that are susceptible to weak aqueous alteration by the neutral water for 10 days. In contrast to noble gases removed by the 10-day alteration, the $^{36}\text{Ar}/^{132}\text{Xe}$ and $^{84}\text{Kr}/^{132}\text{Xe}$ ratios of the noble gases remaining in the sample are in the range of Q gas [10]. This is consistent with previous work done for Allende [11]. This indicates that phase Q is much more resistant to aqueous alteration than the host phases of Ar-rich noble gases. This result confirms that chondrites experienced aqueous alteration, like CM chondrites, do not have Ar-rich noble gases, although it has large amounts of Q gas.

Aqueous alteration for 20 days:

In the sample altered for 20 days, phyllosilicate content is equivalent to those in the 10-day sample, while hematite content increases. The presence of reflection at 3.50\AA in the XRD pattern indicates that anhydrite formed in the 20-day sample. The concentrations of ^{36}Ar and ^{132}Xe are essentially equivalent to those in the 10-day sample. These indicate that almost all of the Ar-rich noble gases were lost from its host phases by aqueous alteration within 10 days.

The concentration of ^{40}Ar is six times larger than that in the 10-day sample. The concentrations of ^{36}Ar and ^{40}Ar released at $700\text{-}1000^\circ\text{C}$ increase by two and ten times, respectively, compared with those in the 10-day sample. The $^{40}\text{Ar}/^{36}\text{Ar}$ ratio of noble gases released at $700\text{-}1000^\circ\text{C}$ also increased from 8.2 to 37, and shifted toward atmospheric values (296, [12]). The concentration of ^{84}Kr is also 8% higher compared with that in the 10-day sample. The excesses of ^{40}Ar and ^{84}Kr in the 20-day sample can be accounted for by absorption or incorporation of atmospheric noble gases into phases that formed by aqueous alteration.

Our results from natural, 10- and 20-day altered samples suggest that major portion of primordial noble gases were lost from primitive hydrous asteroids during low-temperature aqueous alteration. It is confirmed that hydrated chondrites without the Ar-rich noble gases still retain Q-gas, like CM chondrites.

References:

[1] Rubin A. E. et al. (1988) *Meteoritics*, 23,

13-23. [2] Zolensky M. et al. (2003) *Meteorit. Planet. Sci.*, 38, 305-322. [3] Nakamura T. et al. (2003) *Meteorit. Planet. Sci.*, 38, 243-250. [4] Schelhaas N. et al. (1990) *Geochim. Cosmochim. Acta* 54, 2869-2882. [5] Miura Y. N. et al. (2002) *Proc. NIPR Symp. Antarct. Meteorites*, 27, 96-97. [6] Wacker J. F. and Marti K. (1983) *Earth Planet. Sci. Lett.*, 62, 147-158. [7] Nakamura T. et al. (1999) *Geochim. Cosmochim. Acta*, 63, 241-255. [8] Crabb J. and Anders E. (1981) *Geochim. Cosmochim. Acta*, 45, 2443-2464. [9] Wacker J. F. (1986) *Geochim. Cosmochim. Acta*, 50, 633-642. [10] Busemann H. et al. (2000) *Meteorit. Planet. Sci.*, 35, 949-973. [11] Nakasho et al. (2000) *Antarct. Meteorite Res.*, 13, 135-140. [12] Ozima M. and Podosek F. A. (2002) In *Noble gas geochemistry*, pp.12.

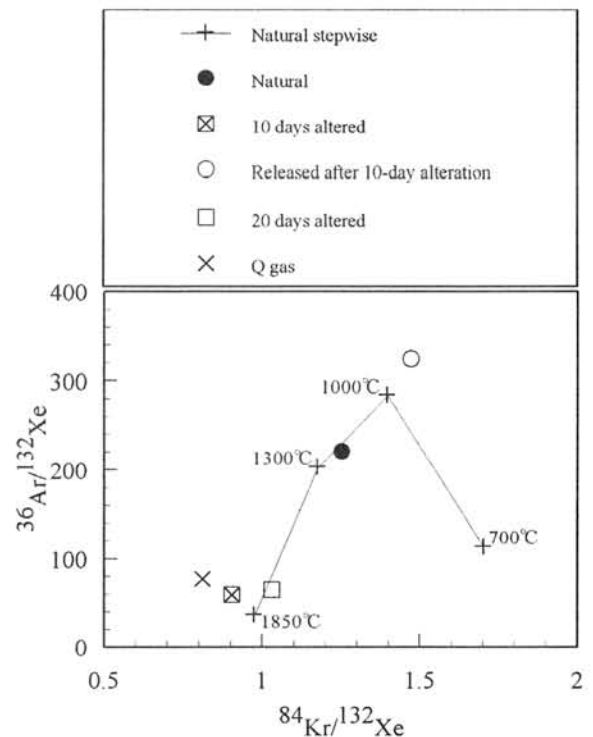


Figure 1. Noble gas elemental compositions of released gases by the stepped pyrolysis of natural sample, and aqueous alteration for 10 and 20 days. The value of Q gas is from Busemann et al. (2000) [10].

Pb isotopic study of Kobe (CK4) meteorite K. Yamashita¹, N. Nakamura^{1,2} and L.M. Heaman^{3, 1}
 Department of Earth and Planetary Sciences, Kobe University, Nada, Kobe 657-8501, Japan, ² Graduate School of Science and Technology, Kobe University, Nada, Kobe 657-8501, Japan, Department of Earth and Atmospheric Sciences, University of Alberta, 1-26 ESB, Edmonton, AB T6G 2E3, Canada.

Introduction

The Kobe meteorite is a carbonaceous chondrite, which fell on September 26, 1999. It has been classified as CK4 based on its petrological and oxygen isotopic characteristics [1, 2]. Although detailed petrological and geochemical studies have already been undertaken on this meteorite, geochronological research using radiogenic isotopes is still in its infancy (e.g. [3]). In this study, the Pb isotopic systematics of whole rock powders and hand picked separates (see below for details) prepared from two different specimens of Kobe meteorite (C-4-1 and C-4-a) was investigated in order to constrain the timing of thermal events (i.e. metamorphic and/or shock events) which this meteorite may have experienced.

Sample and analytical procedure

The powder aliquots of whole rock sample (WR) were prepared from Kobe C-4-1. After washing the exterior of the meteorite with distilled acetone under ultrasonic agitation, the meteorite was gently crushed using an Al-oxide mill. The crushed sample was subsequently sieved to obtain the 75-150µm and <75 µm fractions, and the procedure was repeated until the entire sample was <150µm. Three aliquots of whole rock powder (labeled as Kobe-1, -2 and -3) were prepared. To avoid contamination from the environment, crushing and sieving was conducted under clean air conditions. In addition to the whole rock powders, samples with distinct appearances under the binocular microscope were hand picked from a coarsely crushed Kobe C-4-a. The sample labeled as "matrix" is a collection of fine-grained, whitish-gray fragments dominated by matrix material, although it may contain traces of chondrule fragments. Other hand picked fractions (CH-1, CH-2, FR-3, FR-4, FR-5, GRS-1 and GRS-2) include dark brown-black fragment or a collection of such fragments (DF or dark fragments hereafter) which appears to be, at least in part, fragments of chondrule(s). Pb was extracted from the samples using HBr-HNO3 chemistry. The blank levels were 6-11 pg during the earlier part of the work (i.e. when the whole rock powders were processed), and 0.5-1.0 pg when the remainder of the samples were processed.

Results and discussion

The ²⁰⁷Pb-²⁰⁶Pb/²⁰⁴Pb isotopic signatures for the whole rock powders and matrix are shown in figure 1. These samples show a range in the ²⁰⁶Pb/²⁰⁴Pb and ²⁰⁷Pb/²⁰⁴Pb ratios of 9.68~10.90 and 10.58~11.25, respectively. A Pb-Pb age of 4407 +/- 21 Ma is

calculated from the slope of a regression line constructed to pass through all analyses.

It is noteworthy that the slope is largely controlled by the isotopic composition of the leachates, with the residues clustering in a very narrow Pb isotope range. For this reason, it is important for us to track down the possible phases that were dissolved during the leaching procedure. Shown in figure 2 are the ²⁰⁸Pb-²⁰⁷Pb/²⁰⁶Pb isotopic signatures for the whole rock and the matrix. It is clear from this figure that the signatures of the leachates define a linear trend, with a slope that corresponds to Th/U ratio of ~2 (t = 4.4 Ga). Such a linear trend can be interpreted as a result of mixing between (I) phase(s) with significant Pb but no U and Th, and (II) phase(s) with high Th/Pb and U/Pb ratios with Th/U ratio of ~2. Previous petrological/mineralogical studies have revealed that this meteorite contains Fe-Ni sulfide and chlorapatite in the matrix and the chondrules. Since sulfides are not expected to contain U nor Th, and chlorapatite is generally enriched in U and Th with respect to Pb and have Th/U ratio of ~1.5 (as opposed to merrillite which has Th/U ratio of ~11.67; [4]), these two phases may be responsible for the leachate linear relationship defined in figure 2. If this is the case, the 4407 +/- 21 Ma age can be interpreted as the formation age of the sulfide-chlorapatite or, to be more conservative, the age when sulfide and chlorapatite last equilibrated.

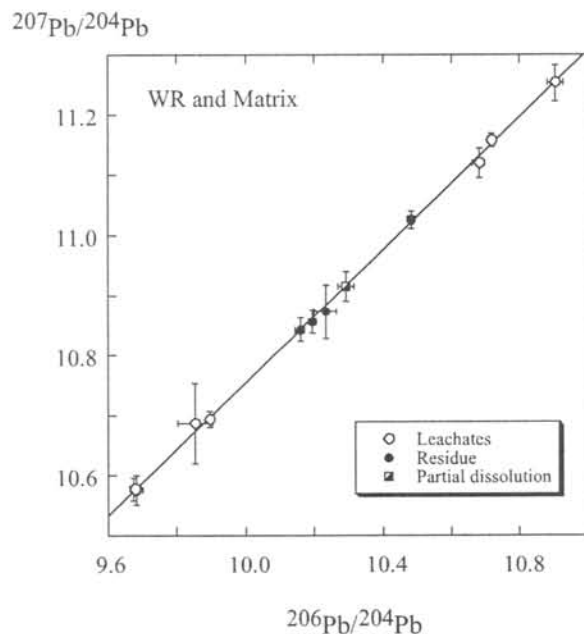


Figure 1. ²⁰⁶Pb/²⁰⁴Pb vs. ²⁰⁷Pb/²⁰⁴Pb plot for whole rock and matrix from Kobe meteorite sample C-4-a.

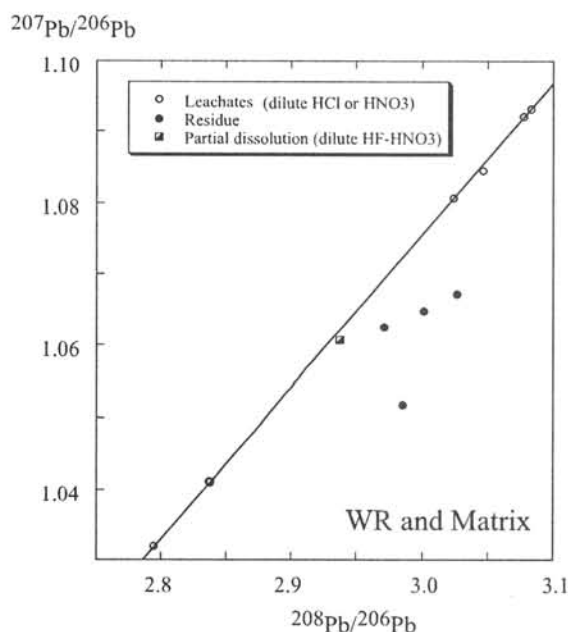


Figure 2. $^{208}\text{Pb}/^{206}\text{Pb}$ vs. $^{207}\text{Pb}/^{206}\text{Pb}$ plot for whole rock and matrix.

Unlike the leached residues of the whole rock powders and the matrix, the isotopic signatures of the dark fragments are highly variable, ranging from 10.28 to 14.39 for $^{206}\text{Pb}/^{204}\text{Pb}$ ratio and 10.92 to 13.89 for $^{207}\text{Pb}/^{204}\text{Pb}$ ratio (Figure 3).

These data also define a linear trend, but the slope of the line is steeper than the line defined by the whole rock/matrix, yielding a Pb-Pbage of 4512 ± 17 Ma. This age indicates that Pb from at least this part of the meteorite did not completely equilibrate with the rest of the meteorite during the ~ 4.4 Ga thermal event. However, when compared with the age of chondrules from other carbonaceous chondrites, the age of these dark fragments is clearly younger, and their Pb isotopic ratios are considerably less radiogenic (e.g. [5, 6]). If these dark fragments indeed represent fragments of chondrules, one possible explanation for its young age and lower isotopic composition may be contamination by less radiogenic Pb from the matrix during the ~ 4.5 Ga thermal event. This is in accord with the relatively high Pb concentration of these fragments. It remains, however, unclear at this stage whether this thermal event is directly related to the metamorphic event reported by Tachibana et al. [7]

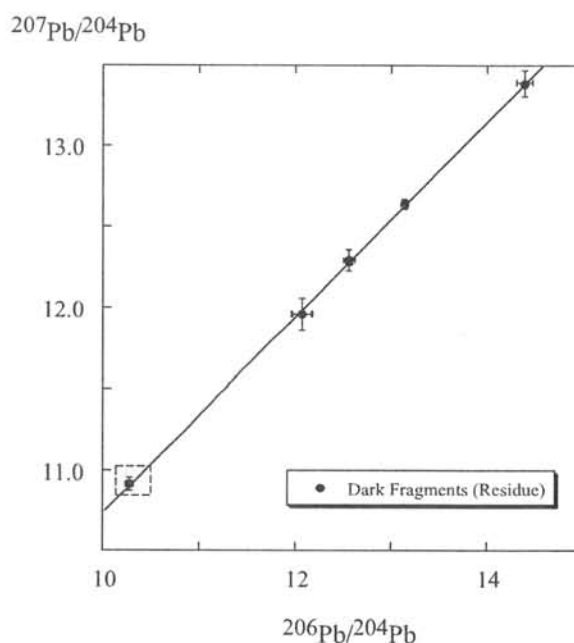


Figure 3. $^{206}\text{Pb}/^{204}\text{Pb}$ vs. $^{207}\text{Pb}/^{204}\text{Pb}$ plot for six leached dark fragments. The gray box in the figure represents the range of the isotopic composition defined by the residues of the whole rock powders and the matrix.

Concluding remarks

The Pb isotopic signatures of whole rock powders, matrix and dark fragments (at least in part chondrule?) from the Kobe CK4 meteorite have revealed two distinct ages, likely related to separate thermal events at ~ 4.5 Ga and ~ 4.4 Ga. The former age is younger than the age of chondrules determined from less metamorphosed carbonaceous chondrites [5, 6]. Although this age may be related to the age of metamorphism, details on the nature of this metamorphism remain uncertain at this stage and will require further investigation. Judging from the model Th/U ratio, the younger ~ 4.4 Ga age most likely represents the formation age of chlorapatite and sulfide, if not the age when these phases last equilibrated.

References

- [1] Nakamura, N., Ebihara, M., Hirota, Y., Oura, Y., Yoneda, S., Kojima, H., Tomeoka, K., Kojima, T., Komura, K., Clayton, R.N., Mayeda, T.K. and Wang, D. (2000) *Lunar Planet. Sci.* XXXI (abstract 1234).
- [2] Tomeoka, K., Kojima, T., Kojima, H. and Nakamura, N. (2000) *Antarctic Meteorite*, XXV, 160-162.
- [3] Tamaki, M., Hirota, Y., Nakamura, N., Yamashita, K. and Kojima, H. (2001) *Antarctic Meteorite*, XXVI, 138-139.
- [4] Goreva, J.S., Burnett, D.S. (2001) *Meteoritics and Planetary Science*, 36, 63-74.
- [5] Amelin, Y., Krot, A.N., Hutcheon, I.D. and Ulyanov, A.A. (2002) *Science*, 297, 1678-1683.
- [6] Chen, J.H. and Tilton, G.R. (1976) *Geochim. Cosmochim. Acta*, 40, 635-643.
- [7] Tachibana, Y., Kitamura, M., Hirajima, T. and Nakamura, N. (2002) *Geochem. J.*, 36, 323-332.

Camel Donga 040: A CV Chondrite Genomict Breccia With Unequilibrated And Metamorphosed Material. M.E. Zolensky¹, E.K. Tonui^{1,2}, A.W.R. Bevan³, L. Le⁴, R.N. Clayton⁵, T.K. Mayeda⁵ and M. Norman⁶; ¹ARES, NASA Johnson Space Center, Houston, TX 77058, USA (michael.e.zolensky@nasa.gov); ²Institute of Geophysics, UCLA, Los Angeles, CA 90095, USA; ³Western Australian Museum, Perth, WA 6000, Australia; ⁴Lockheed Martin, Houston, TX, 77058, USA; ⁵University of Chicago, Chicago, IL, 60637, USA; ⁶Australian National University, Canberra, ACT, 0200, Australia.

Camel Donga 040 was collected as two extremely rusty, and bleached stones (55g total) in Western Australia in 1988. It is a breccia of two lithologies, which we call 1 and 2.

Description: Both lithologies share the following characteristics. (1) Abundant matrix-supported chondrules up to 1 mm across, some with well-developed fine-grained or igneous rims. (2) Abundant smaller lithic fragments and (in lithology 1) one amoeboid olivine aggregate. (3) Abundant troilite and pentlandite, but no pyrrhotite. (4) Very rare metal with compositions Fe 0.49-63 Ni 0.51-37; this rarity no doubt arises from the advanced terrestrial weathering. (5) We observed no magnetite, possibly due to weathering. (6) The matrix is predominantly olivine, with no evidence of preterrestrial aqueous alteration products, although the terrestrial weathering makes analysis of the matrix by the microprobe a difficult task.

Analysis for oxygen isotopes (by RNC and TKM) yielded identical results for both (separated) lithologies, namely $\delta^{18}\text{O}$: +0.18 to -0.01; $\delta^{17}\text{O}$: -4.39 to -4.48, and $\Delta^{17}\text{O}$: -4.46. The lithologies have remarkably different olivine compositions: those in lithology 1 are Fa1-49, with a peak at Fa3, while lithology 2 olivines have the more restricted range Fa23 to Fa42, and a pronounced peak at Fa35. Lithology 1 low-Ca pyroxenes are Fs2-11 and lithology 2 are Fs2-25; not nearly so different as the olivines.

Mineralogy, chondrule sizes and oxygen isotope compositions suggest a classification of the entire meteorite as CV [1], although CK cannot entirely be ruled

out [2&3] on the basis of these data alone. To better discriminate between CV and CK, solution ICPMS analyses of the material carefully separated from the clasts were made by MN at ANU. Previous work [2&3] has generally indicated that averaged CK chondrites have slightly lower contents of refractory lithophiles and volatile siderophiles and chalcophiles than do the CVs. However, the compositions of CVs and CKs are actually rather similar on a meteorite-by-meteorite basis. Nevertheless, the ICPMS results reveal that Camel Donga 040 lithologies 1 and 2 are *both* most compatible with a classification as CV.

Discussion: The mineralogies of both Camel Donga 040 lithologies are generally consistent with the oxidized Allende-like subgroup of the CVs, although with significant differences from typical CVs. Lithology 1 is unusually unequilibrated (based on the olivine compositions) compared to typical oxidized CV3s. The simplest explanation for lithology 2 is that it was material identical to lithology 1 which has been thermally metamorphosed. If this is true then this lithology is the first (or among the first) recognized example of a genomict breccia containing metamorphosed CV material in addition to the unmetamorphosed precursor lithology.

In an attempt to determine the peak metamorphic temperature of lithology 2, we have compared the compositional ranges of olivines and low-Ca pyroxenes to those in laboratory-heated Allende samples [5&6]. The best match is in the range 1100-1200°C, although the lithology 2 matrix and chondrule textures do not show significant recrystallization, requiring that the

hypothesized heating was rather brief. These results are also tentative since the laboratory heating experiments were performed under a reducing atmosphere for less than 1 month-long experimental runs, and are of uncertain realism.

Camel Donga 040 deserves further investigation as it appears to be a rare combination of pre- and post-metamorphic carbonaceous chondrite material from the same asteroid, permitting detailed examination of the mineralogic and compositional changes attending asteroidal metamorphism. Finally, we note that Greenwood et al. [7] have recently suggested that CK chondrites are in reality metamorphosed oxidized CV3 materials.

This idea can be tested by further analyzing Camel Donga 040.

Acknowledgements: We thank Alan Rubin, Michael Weisberg, and Naoya Imae for valuable discussions.

References: [1] Krot et al. (1995) *Meteoritics and Planetary Science* **30**, 748-776; [2] A.E. Rubin, pers. com. 2002; [3] Kallemeyn et al. (1991) *Geochim. Cosmochim. Acta* **55**, 881-892; [4] Krot et al. (1998) *Meteoritics and Planetary Science* **33**, 1065-1085; [5] Zolensky et al (1994) *Lunar and Planetary Science XXV*, 1567-1568; [6] Hiroi et al. (1994) *19th Symposium on Antarctic Meteorites*, 194-197; [7] Greenwood et al. (2004) *Lunar and Planetary Science XXXV*, 1446.

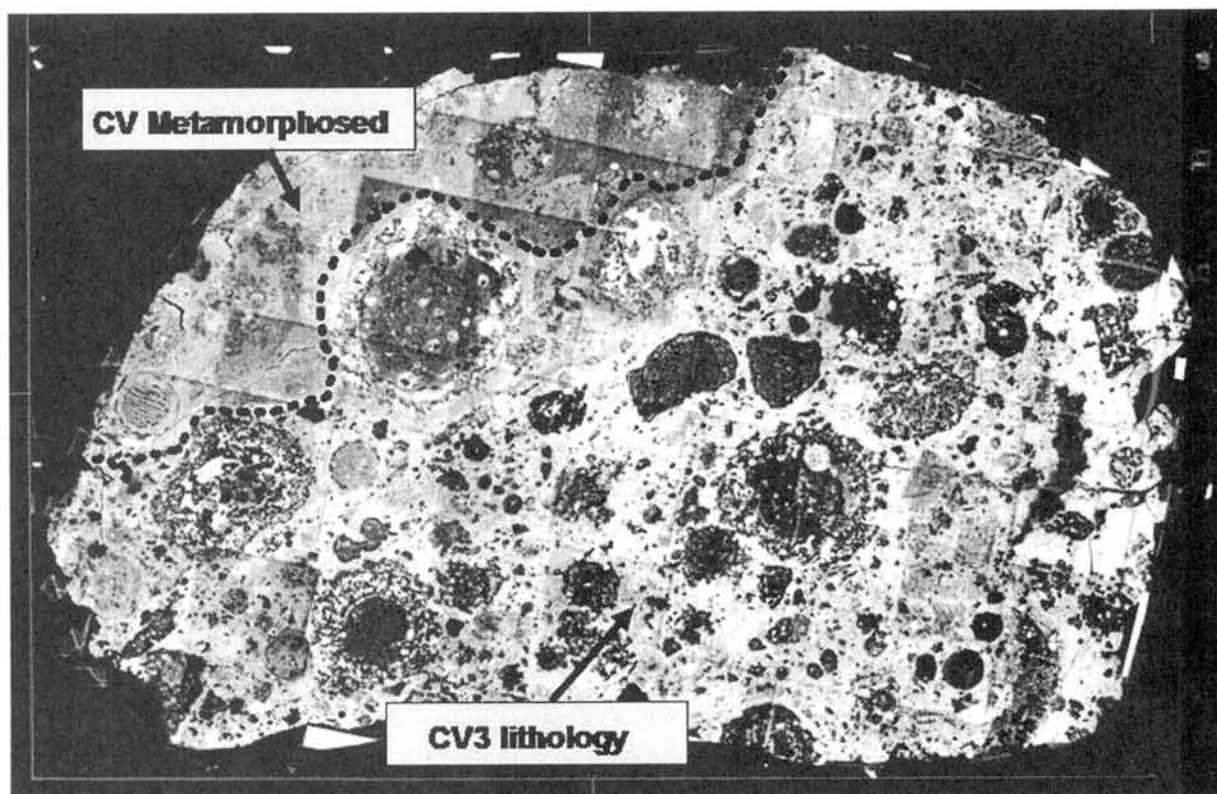


Figure 1. Backscattered electron image of a thin section of Camel Donga 040. The two lithologies are labeled, and are separated by a dotted line. View measures approximately 2 cm across.

AUTHOR INDEX

- ✓ Abe M.37
 ✓ Arai T.4
 ✓ Bérczi Sz.1
 ✓ Bevan A. W. R.95
 ✓ Bischoff A.83
 ✓ Bobrov A. V.42
 ✓ Buchanan P. C.27
 ✓ Busemann H.6
 ✓ Chokai J.4, 39, 46
 ✓ Christen F.6
 ✓ Clayton R. N.95
 △ Dermawan B.75
 ✓ Dreibus G.8, 23
 ✓ Ebihara M.29, 68, 85
 ✓ Eugster O.6
 △ Fabriczy A.1
 △ Földi T.1
 ✓ Fritz J.10
 ✓ Fujiwara A.37
 ✓ Fukuoka T.12
 ✓ Fukushi Y.12
 ✓ Funaki M.14
 △ Fuse T.75
 ✓ Granovsky L. B.42
 ✓ Greshake A.10
 △ Hargitai H.1
 ✓ Heaman L. M.93
 △ Hegyi S.1
 ✓ Hillegonds D. J.60
 ✓ Hiyagon H.15, 31
 ✓ Honda M.64
 △ Hudoba Gy.1
 ✓ Huss G. R.81
 ✓ Ikeda Y.17
 △ Illés E.1
 ✓ Imae N.19, 58, 62
 ✓ Ishizaki N.21
 ✓ Ito T.75
 ✓ Jagoutz E.8, 23
 ✓ Johnson J. A.25
 ✓ Jotter R.23
 △ Józsa S.1
 ✓ Jull A. J. T.25
 ✓ Kaiden H.27
 ✓ Karouji Y.29
 ✓ Kawakita H.75
 △ Kereszturi A.1
 ✓ Kimura M.15, 31, 33, 62
 ✓ Kita N. T.33, 54
 ✓ Kitajima F.35
 ✓ Kitajima Y.35
 ✓ Kitazato K.37
 ✓ Koizumi E.4, 39, 44, 46, 52
 ✓ Kojima H.41, 58
 △ Komatsu M.46
 △ Kovács Zs.1
 ✓ Kubny A.23
 ✓ Kusakabe M.41, 50
 △ Le L.44, 95
 ✓ Lorenzetti S.6
 ✓ Marakushev A. A.42
 ✓ Maruyama S.41
 ✓ Mase K.35
 ✓ Matsuzaki H.64
 † Mayeda T. K.95
 ✓ McHargue L. R.25
 ✓ McKay G.39, 44
 ✓ Mikouchi T.4, 39, 44, 46, 52, 89
 ✓ Misawa K.85, 87
 △ Miura H.48, 81
 ✓ Miura Y. N.50, 72
 ✓ Miyamoto M.4, 39, 46, 52
 △ Miyazaki A.79
 ✓ Monkawa A.4, 39, 46, 52
 ✓ Morishita Y.33
 △ Mörtl M.1
 ✓ Nagai H.64
 ✓ Nagao K.50, 70, 73
 △ Nakajima H.31
 ✓ Nakamoto T.48, 54, 81
 △ Nakamura A. M.37
 ✓ Nakamura N.93
 ✓ Nakamura T.35, 91
 ✓ Nakamuta Y.56

✓ Ninagawa K.	58
✓ Nishiizumi K.	25, 60
✓ Noguchi T.	62
✓ Noguti M.	64
△ Norman M.	95
✓ Nyquist L. E.	66
✓ Okamoto C.	68
✓ Okazaki R.	91
✓ Osawa T.	70
✓ Ozima M.	72
✓ Park J.	73
✓ Podosek F. A.	72
△ Roskó F.	1
✓ Saito J.	37
△ Saito Y.	12
✓ Sasaki S.	75
✓ Sasaki T.	75
△ Schwandt C.	44
△ Seki K.	72
△ Sekiguchi T.	75
△ Setoguchi M.	64
✓ Shih C.-Y.	66
△ Shimoda G.	17
△ Sik A.	1
✓ Stöffler D.	10
✓ Sugita M.	77
✓ Sugiura N.	50, 79

✓ Sugiyama K.	52
△ Syono Y.	14
△ Szakmány Gy.	1
✓ Tachibana S.	54, 81
✓ Tachikawa O.	46
△ Takato N.	75
✓ Takeda H.	66, 83, 85
✓ Tamaki M.	85
✓ Tazawa Y.	12
✓ Tomeoka K.	21, 77
✓ Tomiyama T.	87
× Tonui E. K.	95
△ Tóth Sz.	1
× Watanabe J.	75
△ Weidinger T.	1
✓ Weisberg M. K.	31
✓ Yada T.	12
✓ Yamada I.	46
✓ Yamaguchi A.	29, 68, 83, 85, 89
✓ Yamamoto Y.	91
✓ Yamashita K.	93
✓ Yanai K.	58
× Yoshida F.	75
✓ Zartman W.	23
✓ Zinovieva N. G.	42
✓ Zolensky M. E.	95

